

Montana Tech Library

Digital Commons @ Montana Tech

Graduate Theses & Non-Theses

Student Scholarship

Spring 5-2023

Optimization of Porosity in Cold Spray Produced Copper and Zinc Coatings

Cameron Hughes

Follow this and additional works at: https://digitalcommons.mtech.edu/grad_rschr



Part of the [Other Materials Science and Engineering Commons](#)

Recommended Citation

Hughes, Cameron, "Optimization of Porosity in Cold Spray Produced Copper and Zinc Coatings" (2023). *Graduate Theses & Non-Theses*. 300.

https://digitalcommons.mtech.edu/grad_rschr/300

This Thesis is brought to you for free and open access by the Student Scholarship at Digital Commons @ Montana Tech. It has been accepted for inclusion in Graduate Theses & Non-Theses by an authorized administrator of Digital Commons @ Montana Tech. For more information, please contact sjuskiewicz@mtech.edu.

Optimization of Porosity in Cold Spray Produced Copper and Zinc Coatings

by
Cameron Hughes

A thesis submitted in partial fulfillment of the
requirements for the degree of

Masters in Material Science and Engineering

Montana Tech

2023



Abstract

Since its invention in 1981, the cold spray (CS) additive manufacturing (AM) process has been studied and optimized to produce well-adhered, dense material coatings. CS can operate at a wide range of temperatures if the feed material remains in a solid state. Copper and zinc were studied to characterize and understand the effects of heating element voltage, travel speed, and standoff distance on deposit porosity, grain size, microhardness, and coating thickness. Samples were sprayed on 3.2 mm x 25 mm x 150 mm 6061 aluminum substrates. Sections were taken from the middle of the samples to represent steady-state conditions. Sample sections were polished and imaged with optical microscopy before being etched and imaged again. Sample sections were repolished for Vickers microhardness testing. Results from the copper CS deposits show that porosity, grain size, and microhardness can be controlled in the variable range, (69%-100% voltage to a heating element, 33-251 mm/min travel speed, and 4.2-15.2 mm standoff distance) of the study however, copper porosity results exclude travel speed as a variable which goes against other research in the field, suggesting some physical phenomenon was not accounted for in the study. Results from the zinc CS deposits show that porosity can be controlled in the variable range of the study and that optimal processing parameters to produce minimal porosity (1.5%) are 94% heating element voltage, 69 mm/min nozzle travel speed, and 9.7 mm standoff distance. There was no correlation in zinc grain size data or microhardness data from any of the tested processing parameters. Thickness results from both tested materials indicate a strong correlation with the studied processing parameters and thickness can be controlled.

Keywords: Cold Spray, Additive Manufacturing, Porosity Optimization, Microstructure, Grain Size, Microhardness, Deposit Thickness

Dedication

I wish to dedicate this work to my mom and dad for all their support and love and to thank Savannah Sparley for supporting me through all the hard work that was involved in this project, for staying by my side during late hours, and for agreeing to marry me. Without the constant support of these beloved people, I am hesitant to think about where I might be now.

Acknowledgements

I thank and acknowledge my committee chair and research advisor, Dr. Sudhakar Vadiraja, for his valuable guidance, knowledge, and commitment to high quality teaching. I also thank my committee members: Dr. Peter Lucon, Dr. Nathan Huft, and Dr. Richard LaDouceur for their invaluable expertise, time, and advice on the research. I wish to thank Dr. Courtney Young for getting me into the metallurgy program, Dr. Avimanyu Das for supporting me as a student both in classes and clubs, and Dr. Jerome Downey for encouraging me to pursue the master's program.

Additional appreciation goes to Steven Hansen, Morgan Ashbaugh, Jay Yoder, Josef Fields, Andrew Woods, and Zach Hein for their immense help in sample synthesis, Cristina Stefanescu and Gary Wyss for their time and expertise on the TESCAN SEM, and Dr. Hrudaya Biswal for grammar edits.

This research was sponsored by the Combat Capabilities Development Command Army Research Laboratory and was accomplished under Cooperative Agreement Number W911NF-20-2-0163. The views and conclusions contained in this document are those of the authors and should not be interpreted as representing the official policies, either expressed or implied, of the Combat Capabilities Development Command Army Research Laboratory or the U.S. Government. The U.S. Government is authorized to reproduce and distribute reprints for Government purposes notwithstanding any copyright notation herein.

Table of Contents

ABSTRACT	II
DEDICATION	III
ACKNOWLEDGEMENTS	IV
LIST OF TABLES	VIII
LIST OF FIGURES	IX
LIST OF EQUATIONS	XVIII
1. INTRODUCTION.....	1
1.1. General	1
1.2. Cold Spray	2
1.3. Specific Objectives.....	3
2. BACKGROUND	4
2.1. Bonding Mechanism.....	4
2.2. Cold Spray Variables.....	5
2.2.1. Particle Velocity	5
2.2.2. Particle Feed Rate.....	9
2.2.3. Particle Temperature	10
2.2.4. Gas Pressure	10
2.2.5. Gas Temperature	11
2.2.6. Gas Type	13
2.2.7. Nozzle Standoff Distance.....	15
2.2.8. Nozzle Travel Speed	16
2.2.9. Nozzle Angle and Path	16
2.2.10. Substrate Temperature.....	18
3. METHODS	19
3.1. Metallography.....	19

3.2.	<i>ImageJ Contrast Analysis</i>	21
3.3.	<i>Design of Experiments</i>	25
3.4.	<i>Procedure</i>	28
3.4.1.	Cold Spraying Samples	28
3.4.2.	Sectioning Samples	32
3.4.3.	Polishing Samples	33
3.4.4.	Imaging of Samples.....	34
3.4.5.	Etching Samples.....	35
3.4.6.	Microhardness	36
4.	RESULTS.....	38
4.1.	<i>Powder Size Analysis</i>	38
4.2.	<i>Powder Feed System</i>	42
4.3.	<i>Micrographs</i>	44
4.3.1.	Un-Etched Copper.....	44
4.3.2.	Etched Copper	48
4.3.3.	Un-Etched Zinc	51
4.3.4.	Etched Zinc	54
4.4.	<i>Microhardness</i>	57
4.5.	<i>Deposit Thickness</i>	58
4.6.	<i>Design of Experiments</i>	58
4.6.1.	Copper	59
4.6.1.1.	Porosity	59
4.6.1.2.	Grain Size	63
4.6.1.3.	Microhardness.....	72
4.6.1.4.	Thickness	75
4.6.1.5.	Copper Validation	84
4.6.2.	Zinc	85
4.6.2.1.	Porosity	85

4.6.2.2.	Grain Size and Microhardness	90
4.6.2.3.	Thickness	92
4.6.2.4.	Zinc Validation.....	96
5.	DISCUSSION.....	97
5.1.	<i>Powder Sieve Analysis</i>	97
5.2.	<i>Powder Feed System</i>	98
5.3.	<i>Copper</i>	98
5.3.1.	Porosity	98
5.3.2.	Grain Size.....	103
5.3.3.	Microhardness.....	105
5.3.4.	Thickness	107
5.4.	<i>Zinc</i>	109
5.4.1.	Porosity	109
5.4.2.	Grain Size and Microhardness	110
5.4.3.	Thickness	111
6.	CONCLUSIONS	111
7.	FUTURE WORK	112
8.	BIBLIOGRAPHY	114
9.	APPENDIX A: SEM PORE ANALYSIS.....	127
10.	APPENDIX B: MODEL DIAGNOSTIC GRAPHS.....	143
11.	APPENDIX C: RAW DATA	150

List of Tables

Table I: Average percent error between ImageJ grain analysis and Heyn line intercept grain analysis for various lower threshold limits	23
Table II: Initial design of experiments produced by the Design Expert software	27
Table III: Design of experiments adjusted to reflect instrument precision.....	28
Table IV: Copper Powder Sieve Analysis	38
Table V: Zinc Powder Sieve Analysis	38
Table VI: Vickers hardness data for runs in the DOE for both copper and zinc samples.	57
Table VII: Deposit Thickness data for runs in the DOE for both copper and zinc samples.	58
Table VIII: Copper porosity ANOVA table	60
Table IX: Copper grain size ANOVA table at 75% heating element voltage	64
Table X: Copper grain size ANOVA table at 80% heating element voltage.....	67
Table XI: Copper deposit thickness ANOVA table with 75% heating element voltage...	75
Table XII: Copper deposit thickness ANOVA table with 80% heating element voltage..	76
Table XIII: Copper CS validation statistics with 75% heating element voltage	85
Table XIV: Copper CS validation statistics with 80% heating element voltage	85
Table XV: Zinc porosity ANOVA table.....	86
Table XVI: Zinc deposit thickness ANOVA table	93
Table XVII: Zinc CS validation statistics.....	97
Table XVIII: Copper CS grain size analysis.....	150
Table XIX: Zinc CS grain size analysis.....	154
Table XX: CS Vickers microhardness data	156
Table XXI: CS Porosity Analysis Data	165

List of Figures

Figure 1: SEM images of tin particle impacts at and above critical velocity studied by Lienhard et al.	8
Figure 2: SEM images of zinc particle impacts at and above critical velocity studied by Lienhard et al.	9
Figure 3: Molecular velocity distribution of nitrogen gas that flattens and widens as temperature increases.....	13
Figure 4: Coating profile sketch from Cai et al.....	15
Figure 5: Example image showing the CS nozzle work angle.....	17
Figure 6: Example image showing the CS nozzle travel angle.....	18
Figure 7: Depiction of porosity analysis and manual thresholding 1) unaltered image, 2) greyscale applied, 3) auto threshold settings with scratches and noise, 4) hand thresholding with filtered out scratches and noise.....	22
Figure 8: Picture depicting the Feret maximum and Feret minimum dimensions (Sympatec, accessed 2023).....	23
Figure 9: Depiction of the grain analysis process, 1) unaltered image, 2) 8-bit mask applied, 3) "find edges" process highlights enclosed areas of contrast, 4) overlay map of the analyzed particles 16- 600 μm^2	24
Figure 10: Central composite design matrix with cube points at the corners, star points outside the design space, and the center point of the design with run numbers (edited from Hetzner et al., 2021, accessed 2023).	25
Figure 11: Variac voltage versus Gas temperature	26
Figure 12: CS set up showing A) the standoff distance gantry, B) the powder recapture apparatus, C) the linear motion track, D) the feed hopper, and E) the variable transformer	29
Figure 13: Copper CS deposits in accordance with the experimental design to minimize statistical bias	30

Figure 14: Zinc CS deposits in accordance with the experimental design to minimize statistical bias	31
Figure 15: Copper and Zinc CS remade samples. Copper samples are in the following order, Run 3, 6, 7, 14, Validation 1, Validation 2. Zinc samples are in the following order, Run 14, Validation 1, Validation 2.....	32
Figure 16: Diagram showing where sections were taken out of samples to represent steady state operations and an arrow denoting the nozzle travel direction	32
Figure 17: Schematic of the orientation of how the sample sections were mounted in phenolic mounting medium and the orientation of the CS nozzle and travel direction.....	33
Figure 18: Example cross section where imaging for porosity averaging was taken and the orientation of the CS nozzle and travel direction	35
Figure 19: Schematic diagram showing where microhardness measurements were taken for samples as well as sufficiently thick samples and the orientation of the CS nozzle and travel direction.....	37
Figure 20: Copper powder cumulative % passing versus Particle size (μm) with a d50 size of $22\mu\text{m}$	39
Figure 21: Copper powder sieve analysis using linear interpolation with a d50 size of $22\mu\text{m}$ and d80 size of $26\mu\text{m}$	39
Figure 22: Zinc powder cumulative % passing versus Particle size (μm) with a d50 size of $22\mu\text{m}$ and a bimodal particle distribution	40
Figure 23: Zinc powder sieve analysis using linear interpolation with a d50 size of $22\mu\text{m}$ and a d80 size of $50\mu\text{m}$	40
Figure 24: SEM image of copper particles showing a jagged pinecone like structure with many nodules protruding from the particles surface	41
Figure 25: SEM image of large zinc particles with a round irregular geometry among smaller round zinc particles.....	41

- Figure 26: In-house RuSonic CS machine with separate feed hopper and heating element controlled through a variable transformer..... 42
- Figure 27: New powder feed system design with the hopper with vibratory motor mount (left), interchangeable feed nozzle (middle), and air intake (right) 43
- Figure 28: 3D resin powder feed hopper, feed nozzle, and air intake nozzle, attached to the Rusonic CS machine with arrows to denote the powder flow path and air intake path..... 44
- Figure 29: Un-etched image comparison between copper Run 3 (A1), Run 1 (A2), Run 7 (B1), Run 18 (B2). From 1 to 2, heating element voltage increases from 80% to 94%. From A to B, standoff distance decreases from 13.0 mm to 6.5 mm. Travel speed remains the same, at 206 mm/min 46
- Figure 30: Un-etched image comparison between copper Run 6 (C1), Run 13 (C2), Run 14 (D1), Run 11 (D2). From 1 to 2, heating element voltage increases from 80% to 94%. From C to D, the standoff distance increases from 13.0 mm to 6.5 mm. Travel speed remains the same, at 69 mm/min 47
- Figure 31: SEM image of copper CS run 8 showing the presence of pores in the deposit opposed to the presence of surface contaminants or oxides..... 48
- Figure 32: Microstructural comparison between copper Run 3 (A1), Run 1 (A2), Run 7 (B1), Run 18 (B2). From 1 to 2, heating element voltage increases from 80% to 94%. From A to B, the standoff distance decreases from 13.0 mm to 6.5 mm. Travel speed remains the same, at 206 mm/min 49
- Figure 33: Microstructure comparison between copper Run 6 (C1), Run 13 (C2), Run 14 (D1), Run 11 (D2). From 1 to 2, heating element voltage increases from 80% to 94%. From C to D, the standoff distance decreases from 13.0 mm to 6.5 mm. Travel speed remains the same, at 69 mm/min 50
- Figure 34: Un-etched image comparison between Zinc Run 3 (A1), Run 1 (A2), Run 7 (B1), Run 18 (B2). From 1 to 2, heating element voltage increases from 75% to 94%. From A to B, the standoff

distance decreases from 13.0 mm to 6.5 mm. Travel speed remains the same, at 206 mm/min
 52

Figure 35: Un-etched image comparison between Zinc Run 6 (C1), Run 13 (C2), Run 14 (D1), Run 11 (D2). From 1 to 2, heating element voltage increases from 75% to 94%. From C to D, the standoff distance increases from 13.0 mm to 6.5 mm. Travel speed remains the same, at 69 mm/min
 53

Figure 36: SEM image of zinc CS run 11 showing the presence of pores in the deposit opposed to the presence of surface contaminants or oxides..... 54

Figure 37:Microstructural comparison between Zinc Run 3 (A1), Run 1 (A2), Run 7 (B1), Run 18 (B2). From 1 to 2, heating element voltage increases from 75% to 94%. From A to B, the standoff distance decreases from 13.0 mm to 6.5 mm. Travel speed remains the same, at 206 mm/min
 55

Figure 38: Microstructure comparison between Zinc Run 6 (C1), Run 13 (C2), Run 14 (D1), Run 11 (D2). From 1 to 2, heating element voltage increases from 75% to 94%. From C to D, the standoff distance increases from 13.0 mm to 6.5 mm. Travel speed remains the same, at 69 mm/min
 56

Figure 39: Copper graph plotting Porosity (%) versus Heating element voltage (%) 61

Figure 40: Predicted versus actual plot for the linear copper porosity model..... 61

Figure 41: Copper porosity leverage versus run, showing runs 6, and 14 higher than the rest due to these runs being performed at the same voltage setting as the two that were null in the data set62

Figure 42: Interaction plot of copper porosity versus heating element voltage at the travel speed midpoint indicating that porosity decreases as heating element voltage is increased for a standoff of 13.0 mm (red) and porosity increases as heating element voltage is increased for a standoff of 6.5 mm (black) 63

Figure 43: Predicted versus actual plot for the quadratic copper grain size model with the 75% heating element voltage data 65

Figure 44: Copper grain size leverage versus Run showing the model leveraging run 16 higher than other runs, with the 75% heating element voltage data.....	65
Figure 45: Interaction plot of grain size versus heating element voltage at the travel speed midpoint with the 75% heating element voltage data indicating that grain size increases as heating element voltage is increased for a standoff of 13.0 mm (red) and grain size decreases as heating element voltage is increased for a standoff of 6.5 mm (black).....	66
Figure 46: Predicted versus actual plot for the quadratic copper grain size model with the 80% heating element voltage data	68
Figure 47: Copper grain size leverage versus Run showing the model leveraging runs 10 and 16 higher than other runs, with the 80% heating element voltage data.....	68
Figure 48: Interaction plot of grain size versus heating element voltage at the travel speed midpoint with the 80% heating element voltage data indicating that grain size increases for both high (206 mm/min, red) and low (69 mm/min, black) travel speeds with low travel speeds producing larger grains as heating element voltage is increased.....	69
Figure 49: Copper CS grain size versus deposit thickness for runs 8, 10, 11, 13, and 14	70
Figure 50: Copper CS Feret ratio and grain gize for 75% heating element voltage data.....	71
Figure 51: Copper CS Feret ratio and grain size for 80% heating element voltage sample rerun data	72
Figure 52: Copper CS graph plotting Vickers microhardness (HV) versus Heating element voltage (%)	73
Figure 53: Copper microhardness versus thickness of the deposit	74
Figure 54: Copper graph plotting Thickness (μm) versus Heating element voltage (%) showing an increase in thickness as heating element voltage increases	77
Figure 55: Predicted versus actual plot for the copper deposit thickness with the 75% heating element voltage data.....	78

- Figure 56: Copper thickness leverage versus Run showing the model leveraging runs, with the 75% heating element voltage data..... 78
- Figure 57: Interaction plot of copper thickness versus travel speed at the heating element midpoint with the 75% heating element voltage data indicating that thickness decreases for both high (13.0 mm, red) and low (6.5 mm, black) standoff distances as heating element voltage is increased79
- Figure 58: Copper deposit thickness 3D response surface with the 75% heating element voltage data showing that the thickest deposits can be created at slow travel speed (69 mm/min) and high heating element voltage (94%) 79
- Figure 59: Predicted versus actual plot for the copper deposit thickness with the 80% heating element voltage data..... 81
- Figure 60: Copper thickness leverage versus Run showing the model leveraging runs, with the 80% heating element voltage data..... 81
- Figure 61: Interaction plot of copper thickness versus travel speed at the heating element midpoint with the 80% heating element voltage data indicating that thickness increases for both high (13.0 mm, red) and low (6.5 mm, black) standoff distances and heating element voltage is increased82
- Figure 62: Interaction plot of thickness versus heating element voltage at the standoff distance midpoint with the 80% heating element voltage data indicating that thickness increases for both high (206 mm/min, red) and low (69 mm/min, black) travel speeds and that low travel speeds create the thicker deposits as heating element voltage is increased 82
- Figure 63: 3D Response surface of thickness showing heating element voltage versus travel speed at the standoff distance midpoint with the 80% heating element voltage data showing that the thickest deposits can be created at slow travel speed (69 mm/min) and high heating element voltage (94%) 83
- Figure 64: Interaction plot of thickness versus travel speed at the heating element voltage midpoint with the 80% heating element voltage data indicating that thickness decreases for both high (13.0 mm, red) and low (6.5 mm, black) standoff distances as heating element voltage is increased84

Figure 65: Zinc graph plotting Porosity (%) versus Heating element voltage (%)..... 87

Figure 66: Predicted versus actual plot for the zinc porosity model..... 87

Figure 67: Zinc porosity model Leverage versus Run that shows the model leveraging runs 8, and 20 higher than the other runs 88

Figure 68: Interaction plot of zinc porosity versus heating element voltage at the standoff distance midpoint indicating that porosity decreases for both high (206 mm/min, red) and low (69 mm/min) travel speeds as heating element voltage is increased..... 89

Figure 69: Zinc deposit porosity 3D response surface showing that lowest porosity can be created at slow travel speed (69 mm/min) and high heating element voltage (94%) 89

Figure 70: Zinc porosity model optimized for a minimal porosity of 1.4% suggesting operating at high heating element voltage (94%), low travel speed (69 mm/min), and a standoff distance of 9.7 mm 90

Figure 71: Zinc graph plotting Feret ratio and grain size versus heating element voltage 91

Figure 72: Zinc graph plotting microhardness (Vickers) versus deposit thickness 92

Figure 73: Zinc Excel graph plotting Thickness (μm) versus Heating element voltage (%)..... 93

Figure 74: Predicted versus actual plot for the zinc deposit thickness model..... 94

Figure 75: Zinc thickness leverage versus Run that shows the model leveraging runs 8 and 20 above reasonable bounds..... 94

Figure 76: Interaction plot of zinc thickness versus heating element voltage at the standoff distance midpoint indicating that thickness increases for both high (206 mm/min, red) and low (69 mm/min, black) travel speeds with low travel speed producing thicker deposits, as heating element voltage is increased 95

Figure 77: Zinc deposit thickness 3D response surface showing that the thickest deposits can be created at slow travel speed (69 mm/min) and high heating element voltage (94%)..... 96

Figure 78: Cu run 8 SEM pore analysis area 1 127

Figure 79: Cu run 8 SEM pore analysis area 1 spot 1..... 127

Figure 80: Cu run 8 SEM pore analysis area 1 spot 2.....	128
Figure 81: Cu run 8 SEM pore analysis area 1 spot 3.....	128
Figure 82: Cu run 8 SEM pore analysis area 1 spot 4.....	129
Figure 83: Cu run 8 SEM pore analysis area 1 spot 5.....	129
Figure 84: Cu run 8 SEM pore analysis area 1 spot 6.....	130
Figure 85: Cu run 8 SEM pore analysis area 1 spot 7.....	130
Figure 86: Cu run 8 SEM pore analysis area 2	131
Figure 87: Cu run 8 SEM pore analysis area 2 spot 1.....	131
Figure 88: Cu run 8 SEM pore analysis area 2 spot 2.....	132
Figure 89: Cu run 8 SEM pore analysis area 2 spot 3.....	132
Figure 90: Cu run 8 SEM pore analysis area 2 spot 4.....	133
Figure 91: Cu run 8 SEM pore analysis area 2 spot 5.....	133
Figure 92: Cu run 8 SEM pore analysis area 2 spot 6.....	134
Figure 93: Cu run 8 SEM pore analysis area 2 spot 7.....	134
Figure 94: Zn run 11 SEM pore analysis area 1.....	135
Figure 95: Zn run 11 SEM pore analysis area 1 spot 1	135
Figure 96: Zn run 11 SEM pore analysis area 1 spot 2.....	136
Figure 97: Zn run 11 SEM pore analysis area 1 spot 3	136
Figure 98: Zn run 11 SEM pore analysis area 1 spot 4.....	137
Figure 99: Zn run 11 SEM pore analysis area 1 spot 5.....	137
Figure 100: Zn run 11 SEM pore analysis area 1.....	138
Figure 101: Zn run 11 SEM pore analysis area 1 spot 6.....	138
Figure 102: Zn run 11 SEM pore analysis area 1 spot 7	138
Figure 103: Zn run 11 SEM pore analysis area 2.....	139
Figure 104: Zn run 11 SEM pore analysis area 2 spot 1	139
Figure 105: Zn run 11 SEM pore analysis area 2 spot 2.....	140

Figure 106: Zn run 11 SEM pore analysis area 2 spot 3.....	140
Figure 107: Zn run 11 SEM pore analysis area 2 spot 4.....	141
Figure 108: Zn run 11 SEM pore analysis area 2 spot 5.....	141
Figure 109: Zn run 11 SEM pore analysis area 2 spot 6.....	142
Figure 110: Zn run 11 SEM pore analysis area 2 spot 7.....	142
Figure 111: Cu Porosity Model Diagnostics.....	143
Figure 112: Cu Grain Size 75 Heating Element Voltage Model Diagnostics.....	144
Figure 113: Cu Grain Size 80 Heating Element Voltage Model Diagnostics.....	145
Figure 114: Cu Thickness 75 Heating Element Voltage Model Diagnostics	146
Figure 115: Cu Thickness 80 Heating Element Voltage Model Diagnostics	147
Figure 116: Zn Porosity Model Diagnostics.....	148
Figure 117: Zn Thickness Model Diagnostics	149

List of Equations

Critical Velocity Equation (1).....	6
Root Mean Square Velocity (2)	13
Hall-Petch Equation (3)	20
Vickers Hardness (4).....	37

1. Introduction

1.1. General

Material science is an important field of study that investigates how the properties, processing, and structure of a material affect its performance. The study of materials is broad, covering three primary categories of materials: ceramics, polymers, and metals. Each of these categories has subclasses for materials such as composites and thin films. The way a material is processed can have a drastic effect on the final properties of a product. Additive manufacturing (AM), for example, is a form of material processing to produce a part through layer-by-layer addition of material. Software is used to develop a path based on the geometry of the final component that will guide the feed delivery to the AM system. In general, AM methodologies can be grouped into three categories based on their feed stock delivery: wire feed systems, powder bed systems, and powder feed systems (W. E. Frazier, 2014). The capabilities of AM technology to create full components have continued to increase since its discovery in the 1980s (Alkhimov et al., 1981).

A popular example of a wire feed AM system is polymer wire 3D printer. This process works by heating a polymer wire in a nozzle and depositing the melted strand onto a platform (American Society for Metals (ASM) Handbook Volume 24). The nozzle moves along the path, pulling, heating, and depositing more strands on top of one another eventually completing the desired part.

Laser powder bed fusion (LPBF) is an AM powder bed process where a laser is pathed along a bed of powder contained by a stage that can be lowered. The laser melts the powder, that then resolidifies to form the initial layers of a component. Next, the stage is lowered, and more

powder is added to the stage, covering the initial resolidified layer. The laser moves along the path again to create more layers of material (ASM Handbook Volume 24).

Powder feed systems are structured in such a way that a powder is injected into the AM process stream to then be adhered to a substrate. Plasma arc spraying is one such AM technique. Powdered material is injected into a plasma arc, usually through a carrier gas, melted and splattered onto a substrate. Layers are built by splattered material along the desired path. Cold spraying (CS) is another such technique based on adding powder into a process stream. In the CS process, the powder is accelerated to supersonic velocities in a gas stream. Upon reaching a critical velocity, the powder particles will deform when colliding with a substrate and adhere to the substrate (Alkhimov et al., 1981; Assadi et al., 2003; Bae et al., 2009; Gilmore et al., 1999; Li and Li, 2003; Prashar and Vasudev, 2021; Schmidt et al., 2006; Vinay et al, 2021; Wong et al., 2010; Wu et al., 2005).

1.2. Cold Spray

CS is a relatively new AM processing method, with its origin in 1981 Russian wind tunnel experiments which examined the interaction of particles on gas flow with a body. The researchers found that some particles had adhered into their test piece through metallurgical bonding (Alkhimov et al., 1981). CS offers several advantages over other AM methods such as requiring little to no substrate preparation and providing minimal thermal heat input into the substrate. The namesake of the process comes from the low temperatures that are used relative to the melting point of the material being sprayed. These lower temperatures allow the grains in the sprayed material to remain solid during flight in the gas stream and only change during impact with a substrate. However, there is no defined temperature for the CS of materials, and it is distinctly different from thermal spraying, where the powder is deposited in a molten droplet

state. The CS process itself has a cold working effect where stress is added to the grain structure, increasing strength, and decreasing ductility. This makes coatings produced via CS strong but brittle. CS research involving the spray of two elements is sparse, with relevant research focusing on spraying mixed metal powders onto carbon fiber substrates (Che et al., 2017) or graphite (Ling et al., 2019). The goal of this research is to spray elemental copper and zinc onto metal substrates to optimize an in-house CS unit for low porosity. Copper has a melting point at 1084 °C and commonly cold sprayed between 400-600 °C (Fukumoto et al., 2007; Kim and Lee, 2021; Ling et al., 2019; Yin et al., 2018). Zinc has a melting point at 420 °C and is commonly cold sprayed between 200-400 °C (Lapushkina et al., 2020; Marzbanrad et al., 2021; Vinay et al., 2021).

1.3. Specific Objectives

For the purposes of this research, optimization to minimize porosity is important to study as porosity produced via CS materials results in a decrease in the material properties when compared to conventionally wrought materials.

The closer a CS deposit is to zero porosity, the better the material properties. The results of this research can then be later applied to concurrent research into three-dimensional modeling of the gas flow out of the CS nozzle. Additionally, the effects of gas temperature, travel speed, and standoff distance on CS of deposits produced by the K205 nozzle and a low-pressure in-house system are presently unknown. This study attempts to better understand these effects.

The research surrounding the K205 CS nozzle is limited and research focuses on the CS of materials onto polymer substrates (Tsai et al., 2021, 2023; Akin et al., 2020). While this research did not examine the effect of nozzle geometry on the CS of Cu and Zn particles, it can provide data for future investigation into the K205 nozzle design and the in-house low pressure

CS system. CS is typically performed with a convergent-divergent nozzle to obtain supersonic flow, but this geometry alone is not sufficient to obtain supersonic flow in the gas stream. The supplied pressure, or stagnation pressure, and nozzle throat area ratio determine the Mach number as the end of the CS nozzle. Nozzle throat area ratio refers to the ratio of the nozzle exit area to the nozzle throat area. Nozzles with a low throat area ratio require higher temperatures for particles in the gas stream to reach a particle velocity above the minimum adhesion velocity (Jodoin, 2002).

2. Background

2.1. Bonding Mechanism

There are two forms of particle bonding in the CS process: 1) Mechanical interlocking and 2) metallurgical bonding. Mechanical interlocking (Hussain et al., 2009) described the behavior when particles adhere to either the substrate or the material that is deformed from previous particle impacts. The particles are attached where movement is severely restricted. Analogously, one can think about the behavior of adhesives for binding materials together. Rougher surfaces allow adhesives to form and fill in many of the surface features of a substrate that lock the adhesive to the surface. On the other hand, metallurgical bonds are formed in CS when the atoms in particles are brought close enough together that the atoms bond to one another. Metallurgical bonds are a classification of chemical bonds (Gilbert et al., 2020) where the proximity of the atoms to one another creates an overlap in the outermost valence shell electrons and the electrons are shared across the metal.

The true bonding in CS deposits is a mixture of the two mechanisms and depends heavily on material flow and the velocity of the particles in the gas stream. In more recent CS research (Kumar et al., 2021; Vinay et al., 2021; Assadi et al., 2003; Bae et al., 2009) the synergistic

effects of temperature, strain, and flow stress at the impact point have been termed as Adiabatic Shear Instability (ASI). Research by Hamid Assadi et al. suggests that the velocity needed to create ASI at the interface of the particles and the substrate also lies near the critical velocity of materials.

2.2. Cold Spray Variables

Many variables affect the powder coating resulting from the CS process. The variables include particle velocity, gas pressure, particle feed rate, substrate temperature, particle temperature, gas composition, substrate hardness, and nozzle-substrate rotation (Schmidt et al., 2006). Optimizing towards deposition efficiency (DE) is typical for CS research. However, DE only shows the fraction of successfully adhered feed material to total material sprayed but neglects porosity and the potential for material to fail because of a high porosity.

2.2.1. Particle Velocity

Increasing the particle velocity while exceeding the minimum velocity to adhere, or critical adhesion velocity, determines if a particle will successfully adhere and can decrease deposit porosity. Exceeding the critical velocity to the point where particle collision obliterates the substrate mass more than what it adhered, or erosion velocity (Lienhard et al., 2022; Schmidt et al., 2006; Sun et al., 2020), will increase the porosity of the coating. As the particle velocity increases, so does the available kinetic energy of each particle which deforms the particle and makes it adhere onto a substrate. Particle velocity cannot be directly controlled and is controlled using other processing variables. For instance, increasing the gas pressure will increase the particle velocity as there is more force being applied to the solid particles in the gas stream. However, increasing feed rate can decrease the velocity of particles in the gas stream as the force

has to be applied across more particles in flight and more mass in the gas stream needs to be accelerated to, or above, critical velocity.

D. L. Gilmore et. al. (1999) looked at the importance of particle velocity on DE, and concluded that DE increases as particle velocity increases, which has held true across multiple studies and materials. H Assadi, et al. (2003) studied the bonding mechanism in CS by using numerical modeling of particle impacts as well as experimental results. Their results suggested that particle bonding is due to adiabatic shear instability at or above critical velocity. Additionally, interface temperature and strain produced via modeling suggested that particle temperature and particle density play an important role in determining the critical velocity needed for successful CS.

Wu et. al. (2005) measured particle velocities in aluminum kinetic spraying and characterized the deposit. Their findings showed that particle velocity increased with gas pressure and temperature and that deposition efficiency increased as particle velocity increased. The authors also noted that there may be multiple critical velocities needed in a CS process, one for adhesion to the substrate, and one for adhesion to other deposited particles.

Schmidt et al. (2006) developed a generalized parameter window for the CS process. From their research, they developed and refined an equation (**Eqn. 1**) for the critical velocity of a material based on melting temperature, tensile strength, and specific heat capacity.

$$v_{crit} = \sqrt{\frac{F_1 * 4 * \sigma_{TS} * (1 - \frac{T_i - T_{ref}}{T_{mel} - T_{ref}})}{p} + F_2 * c_p * (T_{mel} - T_i)} \quad (1)$$

Where σ_{TS} is tensile strength, p is particle density, c_p is specific heat capacity, T_i is impact temperature, T_{mel} is melting temperature, T_{ref} is initial reference temperature, and F_1 and F_2 are correction factors of 4.8 and 1.2 respectively. F_1 is a mechanical property-based correction

factor and F_2 is a thermal-based correction factor and they are generated by correlating calculated and experimentally determined critical velocities.

Tianyu et al. (2020), studied the deposition mechanisms for CS processing experimentally and numerically. They investigated both spherical copper and spherical aluminum powders (+15-45 μm) sprayed onto an aluminum substrate to a thickness of 3 mm. They used air as the carrier gas with a pressure of 0.8-1.1 MPa, heated to 400 °C with a nozzle standoff distance and travel speed of 10 mm and 4 mm/s, respectively. The gas type and pressure were selected to achieve an approximate particle velocity of 500 m/s for aluminum and 400 m/s for copper. Metallography was performed to characterize the microstructures of the CS deposits. Under the experimental conditions, the copper deposit had a porosity of 8.78% with voids found near the particle boundaries, while the aluminum deposit was considered almost fully dense and was comparable to wrought aluminum. CS of copper was then modeled for higher temperatures and higher particle velocities. Under both high gas temperature and high particle velocity, deposit porosity would decrease because of increased particle deformation during impact with the substrate. Both high temperatures and particle velocities produced high maximum equivalent plastic strain which ensured a high bond strength. Aluminum particles behaved in the same fashion.

Particles in the CS process can be accelerated to a point where they will no longer adhere to the substrate and instead erode and/or bounce off the substrate surface. Jasper Lienhard et al. (2022) examined the transition from a critical adhesion velocity to an erosion velocity. Lienhard used laser induced particle impact tests (LIPIT) to accelerate single zinc particles and single tin particles above their accepted critical velocities of approximately 350 m/s and 530 m/s, respectively. With tin, particle melting was observed around 400 m/s while at 480 m/s, large

portions of the particle were ejected from the impact. Between 600 m/s and 900 m/s, fragments of the original particle were observed in a noticeable crater. At 940 m/s and 1160 m/s, no tin appeared in the resulting crater and the tin melted on impact and ejected itself off the substrate (**Figure 1**).

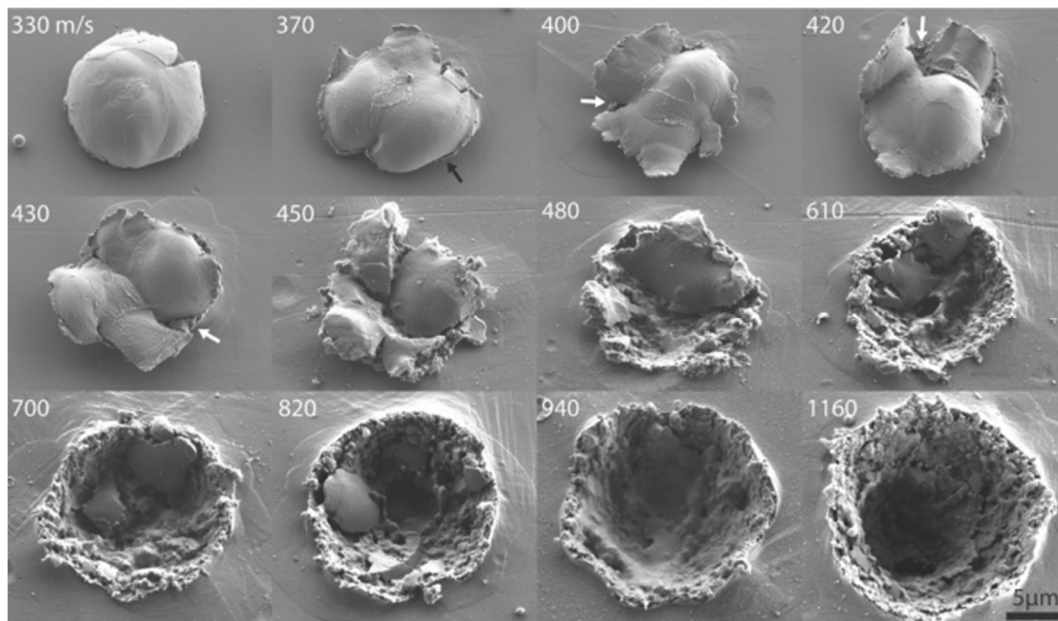


Figure 1: SEM images of tin particle impacts at and above critical velocity studied by Lienhard et al.

Melting in the zinc particles was not observed until around 730 m/s. At 930m/s and 1020m/s, the particles seemed to melt entirely, and collapse inwards. At 1140 m/s and 1230m/s, the particles completely collapsed into the crater formed during impact (**Figure 2**). Lienhard found that the erosion velocities of tin and zinc occurred when the temperature associated with the particle/substrate impact surpassed the melting temperature of both elements.

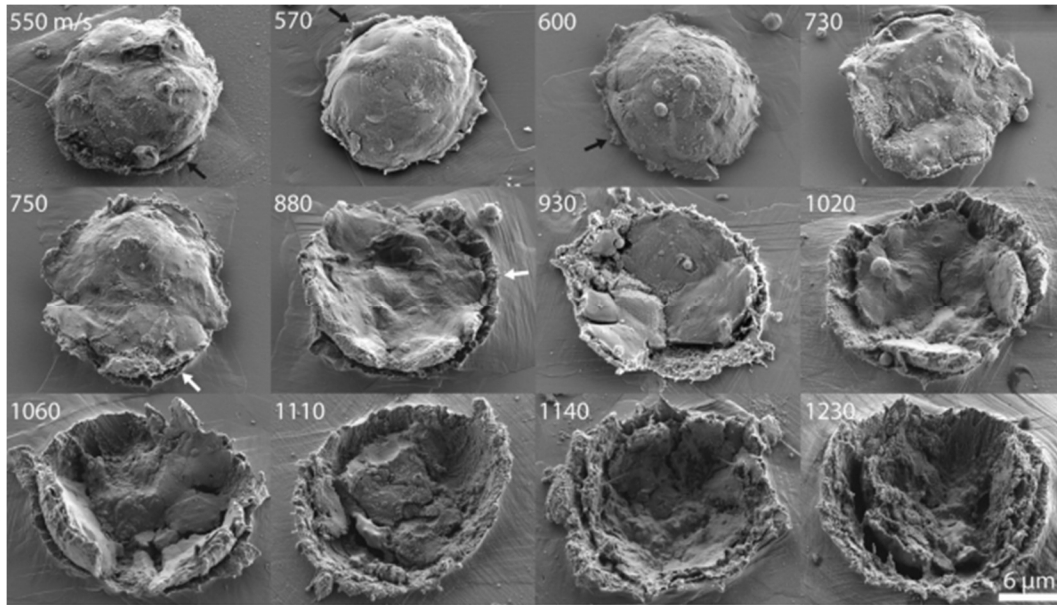


Figure 2: SEM images of zinc particle impacts at and above critical velocity studied by Lienhard et al.

2.2.2. Particle Feed Rate

Higher feed rates decrease the overall velocity of the gas plume, and therefore the inflight particles, reducing the chance of particles to reach the critical velocity needed for deposition. Meyer et al. (2016) examined the effect of feed rate on the CS process under low pressure, between 0.5 MPa and 1 MPa, and how it affected the particle acceleration before impact. They found that an optimal feed rate exists for materials. Furthermore, they observed that dense materials lose more velocity overall as feed rate increases.

Klinkov et al. (2019) studied the impact of nozzle velocity and feed rate on deposition efficiency and total deposit mass. They discovered that increasing powder feed rate also decreases the particle velocity, potentially reducing particles to below critical velocity and therefore reducing deposition efficiency.

2.2.3. Particle Temperature

As particle temperature increases, so does the thermal energy contained within the particle that is used in deformation when impacting a substrate and already adhered particles. Additionally, large impact temperatures can be observed in CS and can be near the melting point of low melting temperature materials. In some cases, melting can be observed via material flow in the coating as particles momentarily melt during impact (Legoux et al., 2007; Lienhard et al., 2022). As such, increasing particle temperature can reduce the critical velocity needed to achieve CS. The particle can be preheated to a predetermined temperature before entering the gas stream. The gas stream, however, has the potential to reduce the temperature of the particles that are in flight towards the substrate. While increasing particle temperature can increase the deposition efficiency of CS, the effects from gas temperature may nullify the single effect of particle preheating temperature.

M. Faizan-Ur-Rab, et al. (2016) investigated the application of a 3D model to estimate the temperature, velocity, and position of titanium particles in the CS process. The model predicted that larger titanium particles would reach higher temperatures than smaller particles. It also predicted that preheating of the metal powder would increase the deposition efficiency. However, the model was only compared against other research performed by R. Lupoi (2014) and experiments were not performed Faiozan-Ur-Rab et al.

2.2.4. Gas Pressure

Gas pressure is one of the variables that directly affects the particle velocity and helps determine whether successful CS will take place. Higher gas pressures produce higher particle velocities than lower gas pressures (Yin et al., 2018). As particle velocity approaches and exceeds critical velocity, up to a point, DE increases but will decrease as particle velocity

reaches erosion velocity where more material is obliterated from the substrate, than adheres to it. Gas pressure can also impact the final coating porosity in a similar way to how it affects DE. When the energy of the system is increased, particles deform more easily, and close the gaps left by previous particle impacts that would form pores near the edges of adhered particles.

Goldbaum et. al. (2011), investigated the effects of carrier gas type, gas temperature, and gas pressure on CS Ti and Ti-6Al-4V. They also looked at how the conditions of substrate temperature, powder size, and powder temperature affected the deposit. They found that both gas temperature and pressure increased the particle velocity which in turn increased the deposition onto the substrate. It was also noted that smaller particles achieved higher velocities and adhered better to the substrate.

2.2.5. Gas Temperature

Gas temperature is another variable that has a substantial impact on successfully achieving a CS process, as gas temperature influences both particle velocity and the ability for particles and substrate to deform. Carrier gas can preheat the substrate before particles are introduced to the gas stream, which allows the substrate to deform easier than at room temperature. Additionally, the gas temperature is imparted to the particles in the gas stream, allowing in-flight particles to deform more when impacting the substrate. This increased temperature must also be considered from a cooling perspective. Particles that impact the substrate at an increased temperature will cool and produce internal stresses because of the cooling (Assadi et al., 2003, Schmidt et al., 2009). This stress in the deposit can result in the deposit being brittle and able to be easily removed from the substrate.

Wang et al (2008) studied the effect of gas composition, gas temperature, and gas pressure on the microstructure and corrosion resistance of titanium coatings. They found that

increasing gas temperature and pressure lowers the porosity of the produced coating. Furthermore, they discovered that the use of compressed air as a carrier gas introduced severe porosity into the titanium microstructure due to the titanium reactivity when compared to nitrogen as a carrier gas. Additionally, they observed that the CS coatings with higher density were also more corrosion resistant than carbon steels, which can provide more protection to a substrate and lending the opportunity for CS titanium coatings to be used as a corrosion resistant layer.

Lapushkina et al. (2020) attempted to optimize the CS of Zn on steel surfaces for increased corrosion resistance properties by varying the carrier gas temperature and pressure. They found that for the tested parameters, the highest corrosion resistance was found at a temperature of 320 °C and 2.5 MPa, however it is noteworthy to mention that these settings were the highest within the design matrix. They also pointed out that further optimization of gas temperature and pressure parameters may exist outside the scope of Lapushkina's research, potentially leading to even better corrosion resistance properties.

Building on these findings, Marzbanrad, Toyserkani, and Jahed (2021) looked at the effects of a zinc CS interlayer on an AZ31B-H24 magnesium alloy substrate to minimize the thermal stresses resulting from differences in thermal expansion coefficients. They found that carrier gas temperatures and the heat generated by particle impacts increase the overall temperature of synthesized coatings and components. However, they also observed that residual thermal stresses were still observed at the interface of the zinc coating and magnesium alloy substrate, and that fractography showed cracks nucleating at and along the interface, and perpendicularly through the substrate.

2.2.6. Gas Type

It has been found (Stokes et al., 2022; Suo et al., 2015) that lighter gases can be accelerated to higher velocities. This comes about from the kinetic molecular theory of gases (Yoshio, 2012) where the average root mean square velocity of a gas particle is proportional to the temperature of the gas particle and the mass of the gas particle,

$$v_{rms} = \sqrt{\frac{3RT}{m}} \quad (2)$$

where v_{rms} is the root mean square velocity, R is the gas constant, T is temperature, and m is molecular weight. This proportionality comes from equating the average kinetic energy of a gas particle to its thermal energy. This velocity refers to the average velocity of an amount of gas at some temperature, but the velocities form a distribution that gets wider and flatter as temperature increases. The distribution, known as the Maxwell-Boltzmann distribution (Roy et al., 2021) shows the fraction of molecules at some velocity **Figure 3**.

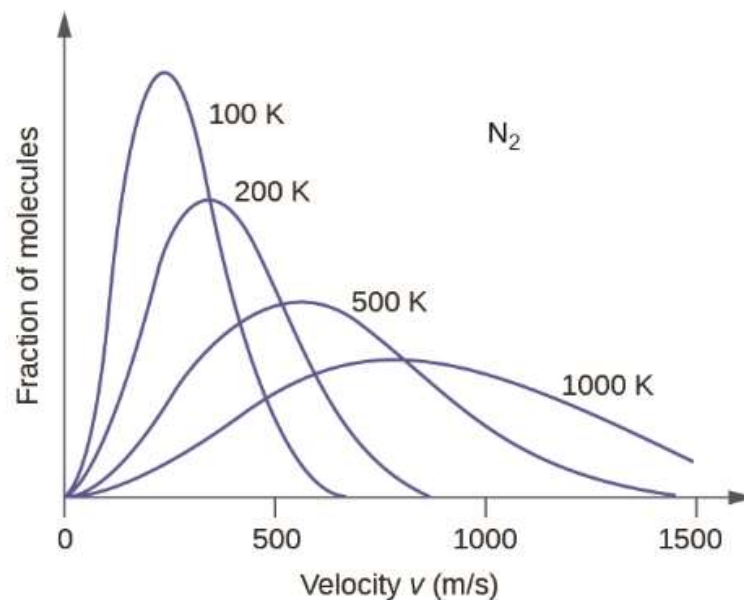


Figure 3: Molecular velocity distribution of nitrogen gas that flattens and widens as temperature increases

Gas type is also important when considering nozzle geometry and design, as the absolute velocity of the gas stream will change despite the Mach number remaining constant. A desired Mach number can be achieved through pressure ratios and the nozzle design (Jodoin, 2002). Because Mach numbers are ratios of the speed of flow to the speed of sound and the speed of sound of gases is dependent on density, low density gases will have a higher absolute velocity while maintaining a consistent Mach number. Materials with higher critical adhesion velocities may require lighter gases such as nitrogen or helium for the particles to reach the required velocity to adhere.

In 2021, Kim and Lee studied the effect of carrier gas composition on copper CS deposits. The CS was performed at room temperature with nitrogen gas and helium gas. They examined the microstructure of the copper powder and samples created by both gases. Deposits made with nitrogen gas had a grain size of 3.14 μm and a yield strength of 340 MPa while deposits made with helium gas had a grain size of 0.92 μm and a yield strength of 415 MPa. Furthermore, the research found that the helium gas produced a more refined microstructure, resulting in a higher yield strength.

Additionally, Zhou (2021) researched microstructural control of CS Ti coatings to control the porosity, microhardness, and corrosion resistance of the coating. They varied gas species, stand-off distance, spray angle, powder geometry, and nozzle type. They found that helium gas was the most effective in eliminating porosity, however N_2 gas can be used with higher gas temperature and pressure to achieve a similar result. Zhou's research indicated that irregular particle shapes formed more dense coatings than medium and large spherical particles. It was found that as gas temperature, pressure, and powder temperature increases, porosity of the coatings decreases which resulted in a higher microhardness and better corrosion resistance.

2.2.7. Nozzle Standoff Distance

As the particles exit the nozzle and gas stream of a CS unit, there is a brief period where they continue to accelerate, after which the particles will quickly decelerate (Gilmore et al., 1999). Depending on the pressure of the gas stream, the distance when particles begin to decelerate will change. If the CS nozzle is positioned where in-flight particles are still accelerating when they collide with the substrate, they might not be above the critical velocity. Conversely, if the nozzle is positioned far away, where particles have accelerated and begun decelerating, the particle may drop below the critical velocity. The standoff distance is material, gas, and application dependent and must be controlled to produce layers in the CS process whereas when layers are built the standoff distance decreases by the build height of the layer. The nozzle standoff distance also determines the distribution of deposited particles due to the shape of the gas stream and results in the final geometry of the product.

Cai et al (2012) researched the effect of nozzle standoff distance and the distance between the nozzle path, known as scanning step, on CS coating uniformity(**Figure 4**). Nozzle standoff distance determines not only deposition efficiency but also deposit shape. The scanning step determines the overall roughness of a CS coating, which must be used in gross tolerance to final dimensions.

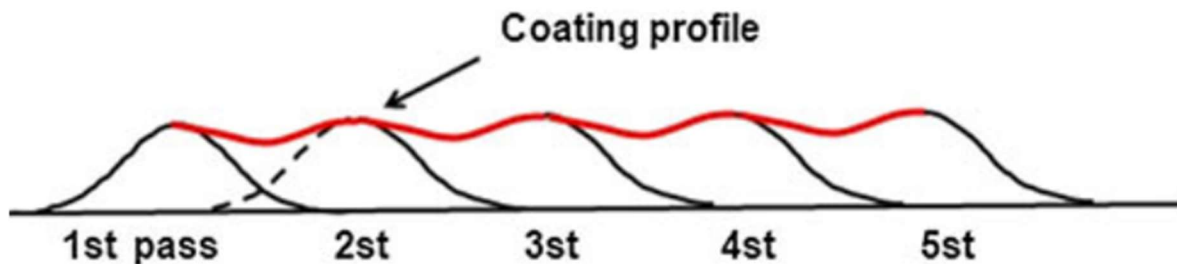


Figure 4: Coating profile sketch from Cai et al

2.2.8. Nozzle Travel Speed

Nozzle travel speed strongly interacts with other processing variables. When nozzle speed is low, gas temperature can provide heat input into a substrate for longer periods of time. This heat input can thermally soften the substrate and any material that has already been deposited allowing for more deformation. Additionally, low nozzle speeds allow for more particle feed to be sprayed per unit length traveled, which can increase the deposit height. Conversely, high nozzle speeds provide the opposite effect where less powder can be sprayed per unit length and gas temperature cannot transfer as much heat into the substrate. Klinkov et al. (2019) studied nozzle velocity and feed rate on deposition efficiency and total deposit mass. They observed that by increasing nozzle travel speed, the deposition efficiency decreases as the substrate was not as hot due to more spread-out particle impacts providing less energy through impact and less energy from the gas stream was transferred to the substrate. Klinkov reported that increasing powder feed rate also decreases the particle velocity, potentially reducing particles to below critical velocity and therefore reducing deposition efficiency.

2.2.9. Nozzle Angle and Path

Nozzle angle refers to the work angle that the CS nozzle makes with the substrate with many studies having a work angle of 90° , or normal, to the substrate (**Figure 5**). Nozzle travel angle refers to the angle of the nozzle, oriented to the direction of spray (**Figure 6**).

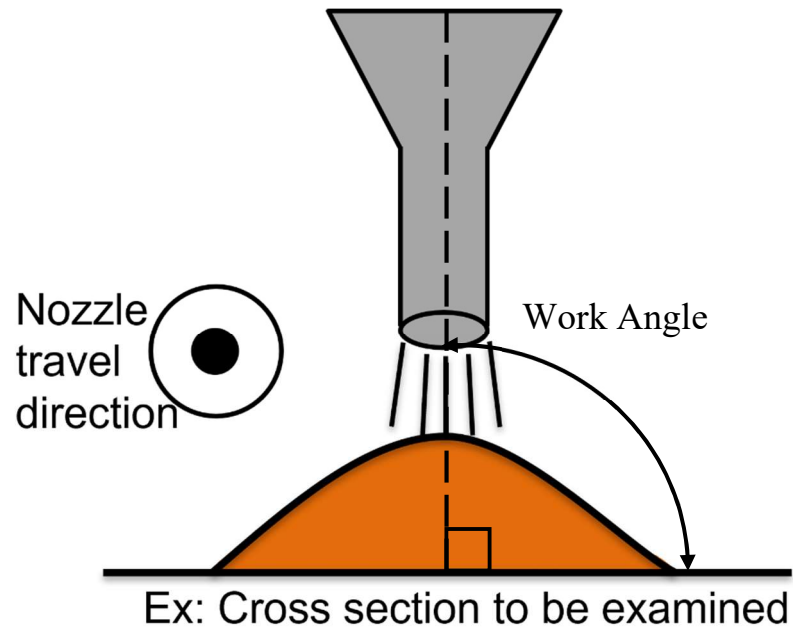


Figure 5: Example image showing the CS nozzle work angle

The nozzle angle affects particle velocity by adding a vector to total velocity. This can result in particles having a total velocity exceeding critical velocity, but not being adhered to the substrate because neither velocity vector is about the critical velocity needed to deposit. Nozzle path refers to the movement that the nozzle will take. It is important to consider deposition profile overlap when using CS along complex paths. Yin et al (2018) used nozzle path to compare the anisotropy produced in CS parts and components. They found that while changing the travel path can minimize the effect of both microstructural and mechanical anisotropy within CS components, it cannot eliminate it completely. To further address the issue of anisotropy, Yin et al. suggested using a cross-hatching strategy when spraying layers, which can reduce mechanical property anisotropy. Post-deposition heat treatment can also reduce anisotropy.

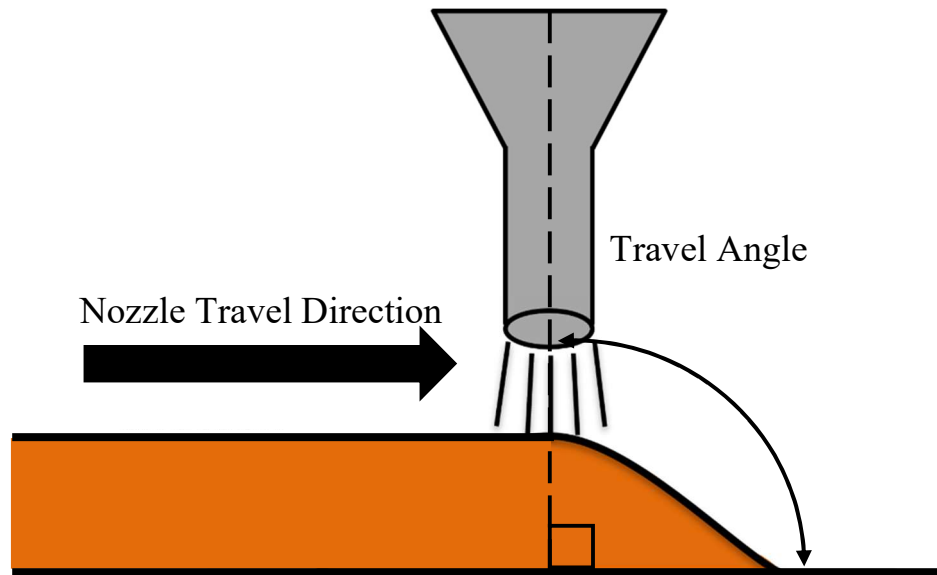


Figure 6: Example image showing the CS nozzle travel angle

Later research performed by Hutasoit et al (2021) examined aluminum CS produced parts and studied the effects of build orientation and heat treatment on physical properties and corrosion resistance. It was found that porosity of the deposit decreases when the parts are sintered and are more corrosion resistant than typical wrought aluminum when oriented vertically with the CS nozzle.

Vargas-Uscategui et al. (2021), attempted to create titanium walls produced via the CS process through toolpath planning and optimization of the travel speed, work angle, and corner radius of the spray path. They found that varying the nozzle work angle with respect to the plate, had a high level of control over the geometry and could potentially allow for sharper features to be produced. However, the walls that the researchers produced exhibited higher porosity (20-30% near the edge) which was attributed to unoptimized processing parameters.

2.2.10. Substrate Temperature

Substrate temperature can increase or decrease DE by having the substrate deform during particle impacts. This deformation of the substrate is important in CS processes, as particle-

substrate and particle-particle deformation allow for adiabatic shear instability to form in addition to the metallurgical bond. M. Fukumoto et al. (2007) examined the effect of substrate heating on CS of copper particles and found that increasing substrate temperature increased deposition efficiency independently of other gas processing parameters. Legoux, Irissou, and Moreau (2007) studied the effect of substrate temperature specifically on the formation of CSed aluminum, zinc, and tin coatings and found that the gas temperature greatly affected the surface temperature before particle impact. Aluminum had a higher deposition efficiency as temperature increased while zinc decreased and tin remained the same, which was attributed to the low melting point of the metals.

3. Methods

3.1. Metallography

Examining the microstructure and crystallographic grains of a material can give conclusions about the material properties of the material (Vander et al., 2004). To observe the crystal grains, the material must be either roughly polished and etched to reveal a macrostructure or polished to a point where almost no scratches are visible under diffused light optical microscopy and etched to reveal a microstructure.

Typically, there is an accepted list of polishing steps that must be performed to produce a surface finish acceptable for viewing under optical microscopy. However, there are no definitively correct steps in so much as good polishing practices are performed (ASM Handbook Volume 9). When applying pressure to the sample onto the polishing medium, the pressure generally needs to lessen after each polishing step and the sample must be rotated 90 degrees. When the sample is rotated 90 degrees, scratching the surface in the orientation perpendicular with the previous step, removes the scratches created by that previous step. If the sample is not

rotated, then the scratches created by the previous polishing step can be exaggerated and may still be present in progressive steps. These exaggerated scratches are difficult to remove as progressive polishing steps remove less and less material from the surface of the sample, and it is important to eliminate scratches early by this 90-degree rotation.

There are several polishing mediums to be considered when preparing samples for microstructural analysis. The rough polishing steps are usually performed with silica carbide paper and the finer polishing steps are performed with a suspension of particles in liquid applied to a soft cloth. The cloth provides a gentler polishing action by allowing the suspension of particles to be brushed against the sample surface. The fibers of the cloth make the finer polishing more resistant to changes in the pressure being applied to the sample.

After polishing to the degree where scratching is infrequent or non-existent, the sample can be etched with a selection of reagents based on the material of the sample. ASM Handbook Volume 9 has a selection guide for etchants based on the material being studied. In general, etchants work by selectively corroding the less corrosive resistant features on the sample surface, the edges, and boundaries of crystallographic grains. This selective corrosion provides a contrast between the grain boundary and the bulk material of the crystal grain. This contrast provides the means to analyze the size of crystal grains which have a direct correlation to the mechanical properties of the material. For example, grain size is related to the yield strength via the Hall-Petch equation,

$$\sigma_y = \sigma_o + \frac{k}{\sqrt{d}} \quad (3)$$

where σ_y is the yield strength, d is the average grain diameter, and both σ_o and k are material constants. Using this equation, smaller grain sizes would result in higher yield strengths, however the yield strength of the deposits is not being examined in this study.

3.2. ImageJ Contrast Analysis

There are several methods to obtain porosity measurements of CS produced deposits. The most common technique in CS research is using the freeware, ImageJ. The second most common technique is Archimedes method and oil penetration (Zhou 2021), but that method was not chosen due to time constraints. ImageJ takes images and analyzes features based on contrast in values between pixels. Images were taken at fifty times magnification. Images were cropped during analysis to avoid the edges of the deposit. Images are converted into greyscale using an 8-bit mask and then contrast thresholds are adjusted to determine what should and should not be included in the analysis. Proper thresholding of images is important to separate true features from discoloration, stains, and remnant scratching from polishing (**Figure 7**). Once an image has gone through thresholding, ImageJ will count how many pixels are white and/or black and provide an area percentage that will correlate to the feature being analyzed. The measuring of contrasting pixel measurement makes ImageJ ideal for measuring both porosity and grain size and the process can be seen step-by-step in **Figure 7**. The image conversion and auto-thresholding process was automated with Jpor, an ImageJ extension created by Clayton Grove and Dougal Jerram (2010).

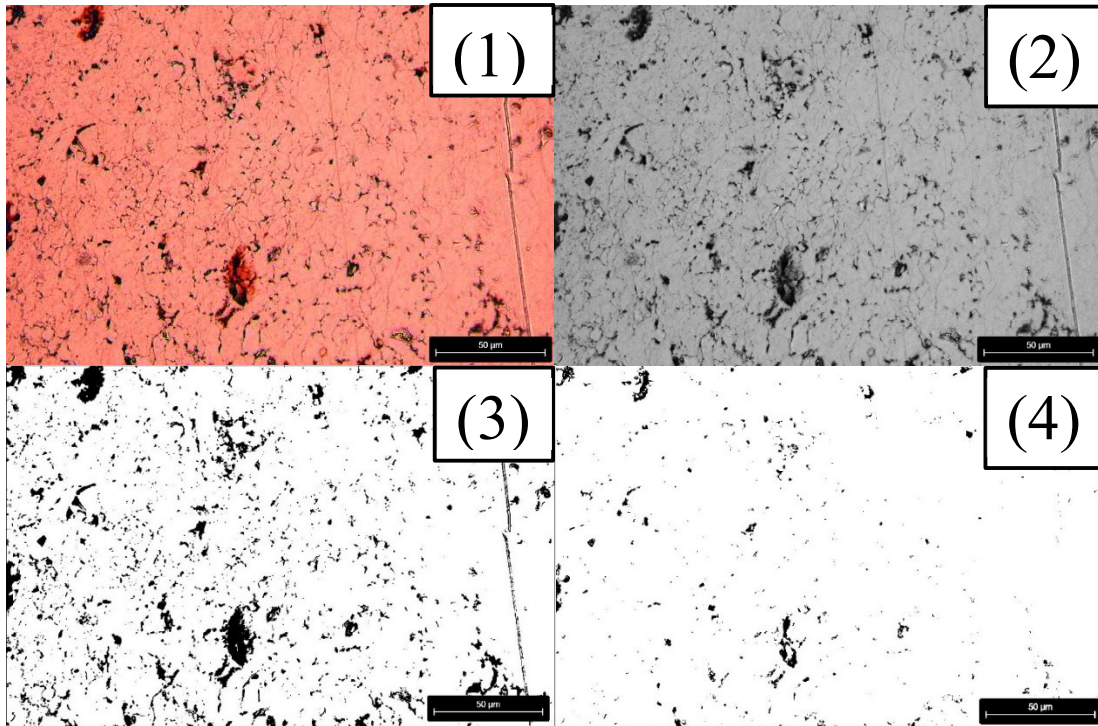


Figure 7: Depiction of porosity analysis and manual thresholding 1) unaltered image, 2) greyscale applied, 3) auto threshold settings with scratches and noise, 4) hand thresholding with filtered out scratches and noise

However, ImageJ is not necessarily representative of the bulk characteristics of the sample and is instead representative of the cross section being examined. The measurements obtained from this technique allow for comparison across samples but are not quantitative of the bulk material. ImageJ has analysis limitations as the thresholds for each image are not the same and have to be adjusted manually. Manual thresholding could result in overestimation or underestimation of porosity due to surface particles being counted as pores or pores being considered particles. ImageJ has additional imaging settings to accurately produce a grain size that is like an American Society for Testing and Materials (ASTM) accepted method such as the Heyn intercept method. When analyzing a feature, the ImageJ program accumulates pixel area in the bounds are $0 \mu\text{m}^2$ to Infinity. The accumulation of pixels is noise and will be overrepresented at the low range. At the high range, grains can be clumped together due to a single pixel breaking the contrast producing excessively large grain sizes. To correct clumping behavior, both a low and high range were identified that produced grain sizes close to the line intercept method of

grain analysis. $16 \mu\text{m}^2 - 600 \mu\text{m}^2$ was used for copper grain analysis and $32 \mu\text{m}^2 - 600 \mu\text{m}^2$ was used for zinc grain analysis based on the lowest average percent error when compared to the line intercept method **Table I**. The grain analysis method is shown in **Figure 9**.

The Feret diameter and Feret minimum can be obtained through grain analysis. The Feret diameter refers to the largest distance within an enclosed area, or grain, and the Feret minimum refers to the smallest distance within an enclosed area, or grain (**Figure 8**). By dividing the Feret diameter by the Feret minimum, an “aspect ratio”, or length to width ratio, can be obtained for an analyzed grain.

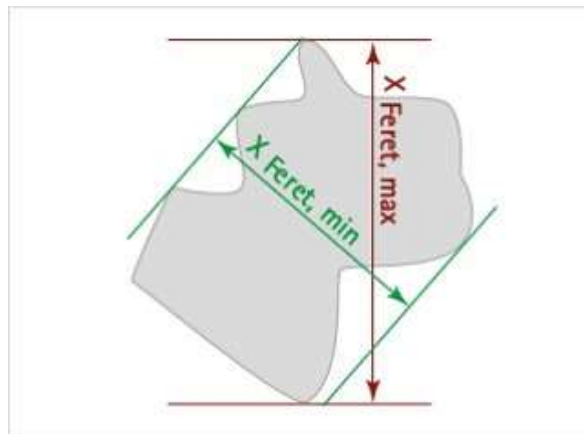


Figure 8: Picture depicting the Feret maximum and Feret minimum dimensions (Sympatec, accessed 2023)

Table I: Average percent error between ImageJ grain analysis and Heyn line intercept grain analysis for various lower threshold limits

	Copper	Zinc
Lower threshold	Average % Error	Average % Error
$64 \mu\text{m}^2$	77.19%	-22.10%
$32 \mu\text{m}^2$	29.69%	3.95%
$16 \mu\text{m}^2$	10.74%	24.46%
$8 \mu\text{m}^2$	18.88%	40.30%
$4 \mu\text{m}^2$	32.79%	51.77%
$2 \mu\text{m}^2$	43.19%	61.35%

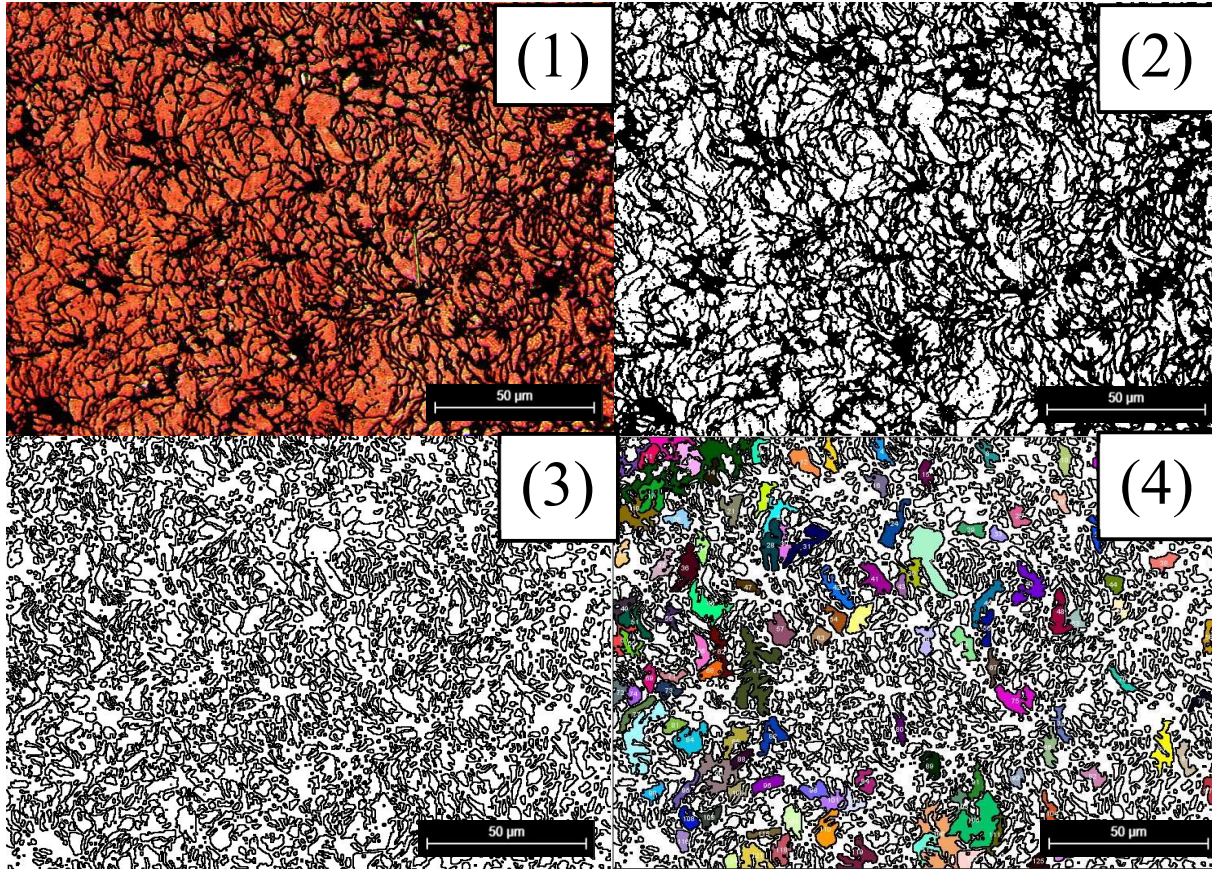


Figure 9: Depiction of the grain analysis process, 1) unaltered image, 2) 8-bit mask applied, 3) "find edges" process highlights enclosed areas of contrast, 4) overlay map of the analyzed particles 16-600 μm^2

The Heyn intercept method measures grain size from micrographs and is governed by ASTM E112. Several lines are drawn across the image and every time a grain boundary intersects with the line, it is counted. Then the grain size can be approximated by dividing the number of intersections by the known length of the line to produce an average length of a line that passes through a grain. The line length is then assumed to be representative as an equiaxed grain within the microstructure. This method was used to produce a grain size and compared with ImageJ analysis to find the low and high area ranges, limiting the low and high range of areas for analysis does bias against small and large grains.

3.3. Design of Experiments

The Design Expert program was used to create a series of experiments, their run order, and analyze the statistical interactions among the chosen variable effects. A three variable central composite design (**Figure 10**) was chosen to minimize runs and examine the quadratic effects of the chosen process variables, resulting in 40 total experiments, 20 experiments per feed stock material used as shown in **Table II**.

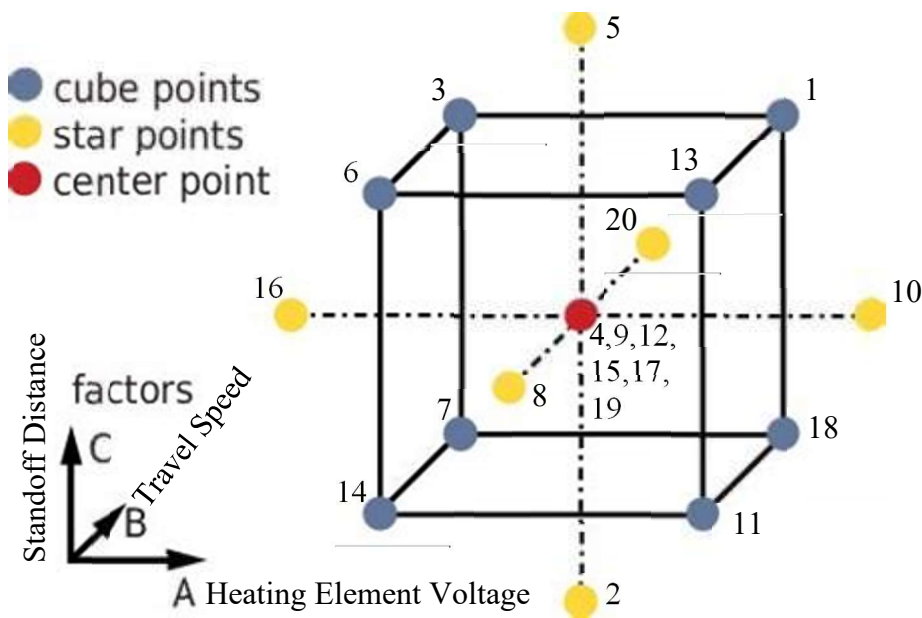


Figure 10: Central composite design matrix with cube points at the corners, star points outside the design space, and the center point of the design with run numbers (edited from Hetzner et al., 2021, accessed 2023).

There are many variables that will affect the porosity of the produced sample via the CS process, such as gas pressure and gas type, and were kept consistent across the copper and zinc powders. Variable ranges were selected based on a brief explorative study of the CS machine and parameters. Machine settings were found that would produce samples for both copper and zinc powders. The design of experiments (DOE) is limited to the precision of the instruments used to verify process settings and therefore the design was adjusted to reflect this limitation. The corrected design can be seen in **Table III**. Both **Table II** and **Table III** are sorted by Run which

refers to the order in which the experiments must be performed to minimize statistical bias in the resulting models.

The variables were chosen with machine limitation and ease of control considered. Control of gas temperature is indirect by instead controlling the voltage to a variac that controls the heating element of the RuSonic CS unit. Gas temperature was examined via thermocouple (**Figure 11**) and the data was fit with a quadratic regression.

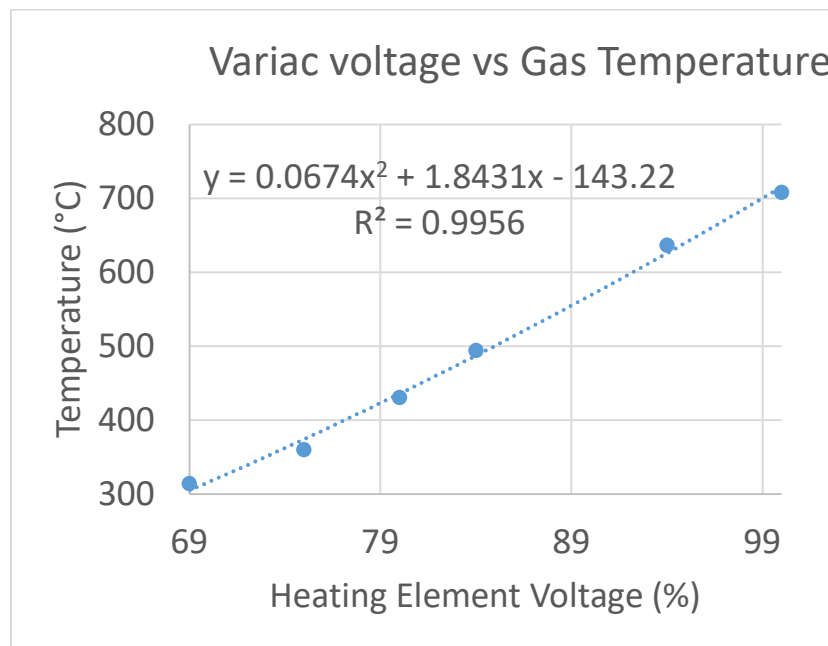


Figure 11: Variac voltage versus Gas temperature

Standoff distance was directly controlled and verified using calipers. Travel speed was also directly controlled using a welding track with digital display for the speed. The weld track speed digital read out is in inches/minute which was verified by timing over a set distance of 10 inches. It was found that the weld track read out was slightly incorrect and is faster than displayed. This is corrected for in the corrected experimental design (**Table III**) and changed to mm/min.

Table II: Initial design of experiments produced by the Design Expert software

Uncorrected DOE				
Standard	Run #	Heating Element (%)	Indicated Travel Speed (mm/min)	Standoff Distance (mm)
8	1	93.5	191	13.0
13	2	84.3	127	4.2
7	3	75.0	191	13.0
19	4	84.3	127	9.7
14	5	84.3	127	15.2
5	6	75.0	64	13.0
3	7	75.0	191	6.4
11	8	84.3	20	9.7
17	9	84.3	127	9.7
10	10	99.8	127	9.7
2	11	93.5	64	6.4
15	12	84.3	127	9.7
6	13	93.5	64	13.0
1	14	75.0	64	6.4
18	15	84.3	127	9.7
9	16	68.7	127	9.7
20	17	84.3	127	9.7
4	18	93.5	191	6.4
16	19	84.3	127	9.7
12	20	84.3	234	9.7

Table III: Design of experiments adjusted to reflect instrument precision

Corrected DOE				
Standard	Run #	Heating Element (%)	Actual Travel Speed (mm/min)	Standoff Distance (mm)
8	1	94	206	13.0
13	2	84	137	4.2
7	3	75	206	13.0
19	4	84	137	9.7
14	5	84	137	15.2
5	6	75	69	13.0
3	7	75	206	6.5
11	8	84	33	9.7
17	9	84	137	9.7
10	10	100	137	9.7
2	11	94	69	6.5
15	12	84	137	9.7
6	13	94	69	13.0
1	14	75	69	6.5
18	15	84	137	9.7
9	16	69	137	9.7
20	17	84	137	9.7
4	18	94	206	6.5
16	19	84	137	9.7
12	20	84	251	9.7

3.4. Procedure

3.4.1. Cold Spraying Samples

CS took place on 6061 aluminum substrates that measured 150 mm x 25 mm x 3.2 mm which was chosen to provide contrast between the feed materials. An air compressor was used to achieve a pressure of approximately 8 bar for each run. Each substrate was roughly prepared with 400-grit sandpaper to provide more sites for particle deformation and bonding based on the work of Singh et al.(2017). Next, each substrate was placed into the powder capture apparatus, on top of scaffolding to allow the CS nozzle to be moved in accordance with the design of experiments (**Figure 12**). Both the nozzle work angle and travel angle were oriented approximately 90 degrees to the substrate.

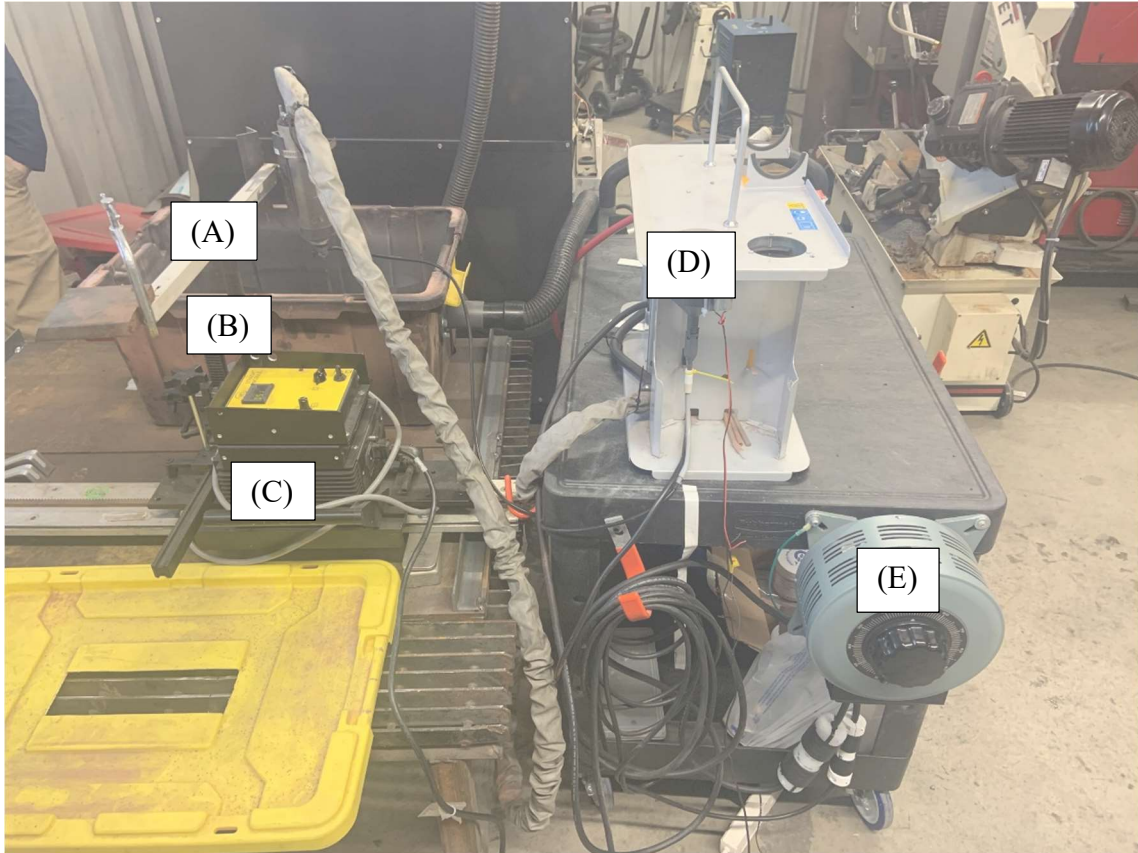


Figure 12: CS set up showing A) the standoff distance gantry, B) the powder recapture apparatus, C) the linear motion track, D) the feed hopper, and E) the variable transformer

Experiments were conducted with the following steps in accordance to the settings of the run number in the DOE:

1. Powder was added to the feed hopper.
2. Standoff distance was verified with calipers and feeler gauges.
3. Travel speed was set on the linear motion track.
4. The process gas was turned on and allowed to flow through the nozzle.
5. The vibratory motor was turned on.
6. The variable transformer was set to the percent voltage allowed.
7. The linear motion track was allowed to travel across the substrate.

When stopping a run the following steps were performed:

1. The linear motion track is halted.
2. The variable transformer is turned down completely.
3. The vibratory motor is turned off.
4. The process gas is shut off.

All CS samples can be seen in **Figure 13** and **Figure 14**, with the top left being Run 1 and increasing in number left to right, top to bottom.

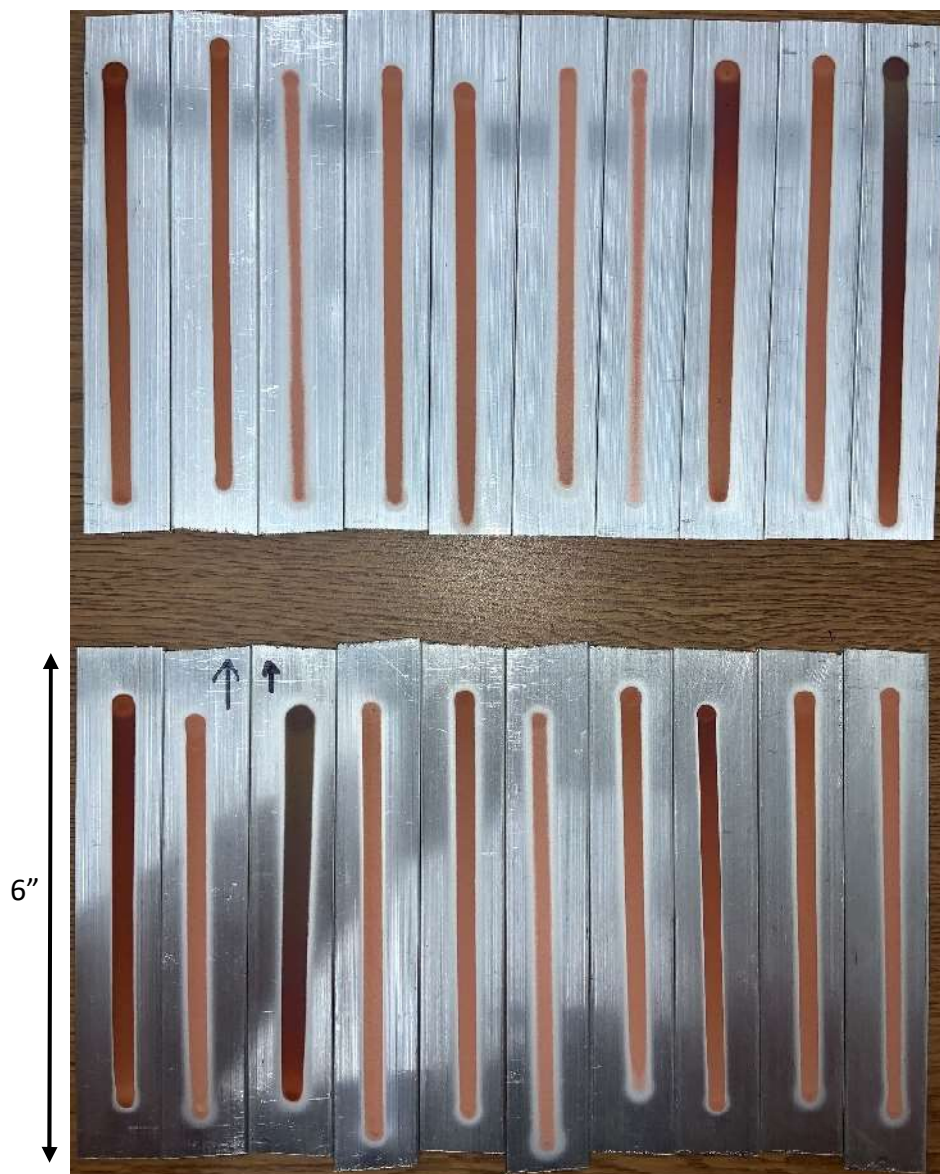


Figure 13: Copper CS deposits in accordance with the experimental design to minimize statistical bias



Figure 14: Zinc CS deposits in accordance with the experimental design to minimize statistical bias

The 75% heating element voltage runs had to be adjusted in the statistical design and were remade with a heating element percent of 80% to produce data for a complete design. Visual inspection of zinc run 14 showed deposit irregularities that were inconsistent with the other runs, and it was determined the powder feed rate was nonuniform during run 14 and the sample was remade. These additional samples and the samples produced to validate the model can be seen in **Figure 15**.

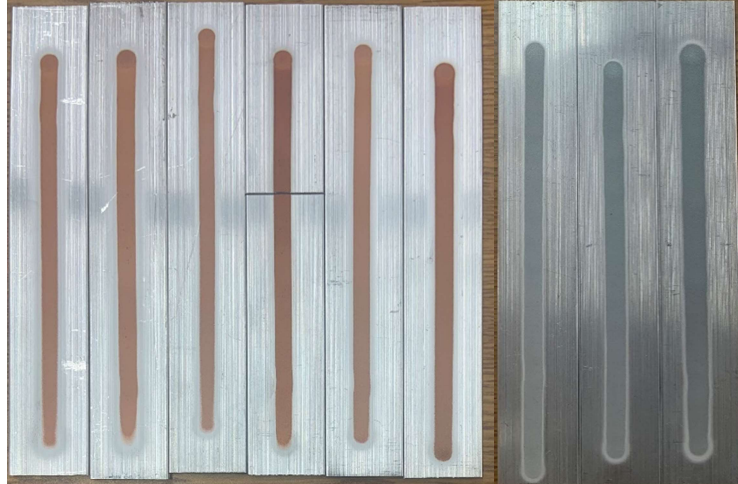


Figure 15: Copper and Zinc CS remade samples. Copper samples are in the following order, Run 3, 6, 7, 14, Validation 1, Validation 2. Zinc samples are in the following order, Run 14, Validation 1, Validation 2

3.4.2. Sectioning Samples

Each CS sample produced was sectioned near the middle of the substrate (**Figure 15**) to analyze results that would be representative of steady state operating conditions.

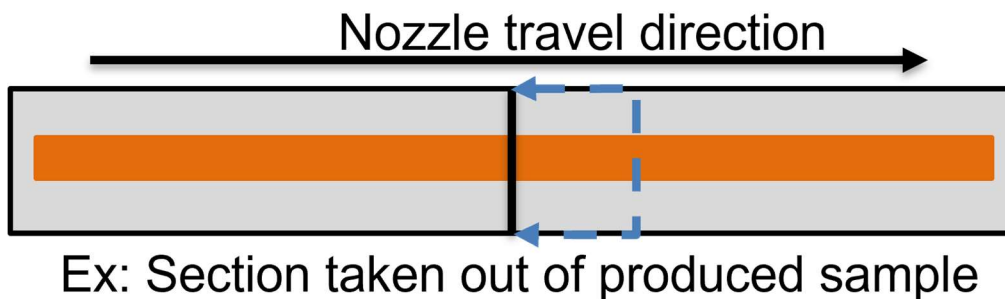


Figure 16: Diagram showing where sections were taken out of samples to represent steady state operations and an arrow denoting the nozzle travel direction

When performing the preliminary study, the produced copper coatings delaminated when cut with a fixed-speed wet abrasive saw. As a result, the copper samples were cut with a fluid-based copper saw with more gentle cutting action and 180 rotations per minute. The zinc samples however were adhered enough to the aluminum substrates and were able to be cut on the wet abrasive saw.

The sections of the samples were then mounted into phenolic mounting compound and were oriented to view the cross section of the produced coatings. A LECO MX400 was used to mount the samples, which heated the compound and sample to 176 °C under 29 MPa pressure and cured under these settings for three minutes. The cross section (**Figure 17**) allows for viewing of porosity, grain size, and performing microhardness testing in a representative sample and allows for comparison across experiments. Because the samples were produced with the nozzle oriented normally to the substrate, particle deformation is expected to occur in the same direction. The chosen cross-section orientation also enables the viewing of particle-substrate deformation and particle-particle deformation and can illustrate the evolution of grain size over substrate thickness.

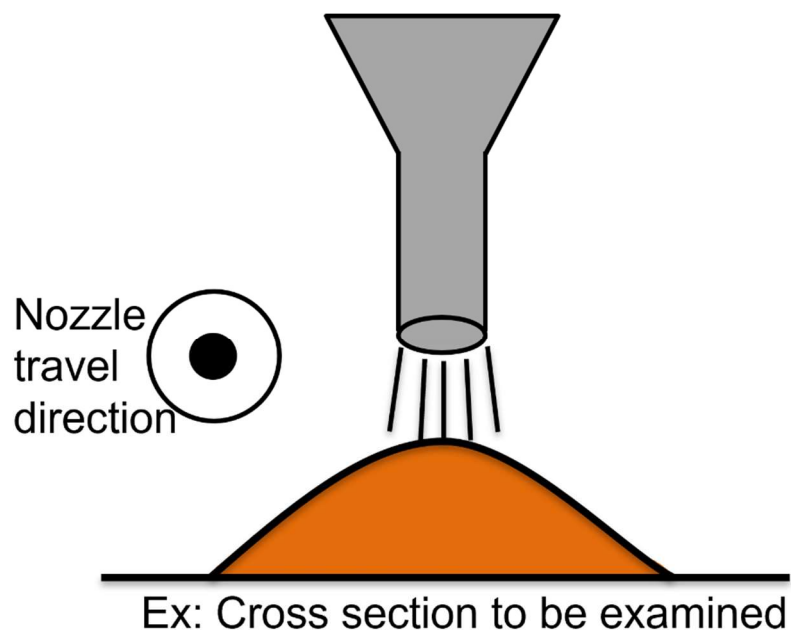


Figure 17: Schematic of the orientation of how the sample sections were mounted in phenolic mounting medium and the orientation of the CS nozzle and travel direction

3.4.3. Polishing Samples

The copper samples were polished with 240-grit silica paper, 320-grit silica paper, 400-grit silica paper, 600-grit silica paper, 5 μm alumina suspension, 3 μm alumina suspension,

0.5 μm alumina, and 0.05 μm alumina suspension, all acquired from Pace Technologies®. The alumina suspension polishing steps were performed on Pace Technologies® NYPAD and MICROPAD polishing pads with the final polishing size, 0.05 μm , being performed on a vibratory polisher. The vibratory polisher ran for 30 minutes on each sample at a frequency of 128 Hz, the point at which the samples began to travel on the polisher pad via the vibrational frequency.

The zinc samples were polished in a similar manner except the 5 μm alumina suspension was replaced with 1200-grit silica paper and the 0.05 μm polish was performed by hand. This change was adopted because the initial polishing of the zinc samples produced rounded features on the sample surface that were quickly oxidized. Produced polished samples had a mirror-like finish and were clear of most scratches.

3.4.4. Imaging of Samples

Once the samples were polished, the cross sections were imaged at the center of the deposit and at several points across the deposits at ten times magnification. Imaging was performed with a Leica DM750P with Leica DMC5400 camera using the ten times and fifty times lenses. Due to some deposits being thin, where moving the microscope view to a location not containing the original image displayed the edge of the deposit, three representative images were taken for averaging porosity across the deposit with contrast analysis. Thicker deposits were imaged five times to average results across the deposit. **Figure 18** shows the scheme for imaging on the sample cross sections.

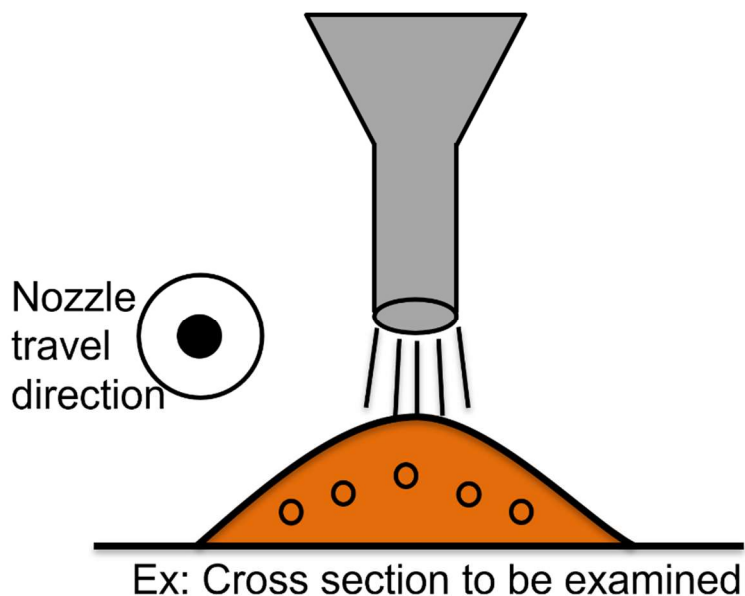


Figure 18: Example cross section where imaging for porosity averaging was taken and the orientation of the CS nozzle and travel direction

Imaging was done with the substrate oriented to the right of the image, and deposit build direction to the left. Pores were analyzed before etching due to the selective corrosion near the grain boundaries that would appear in contrast, which would prevent contrast analysis.

The zinc samples were imaged immediately after final polishing to prevent surface oxidation. Approximately one hour after final polishing, the sample surfaces were oxidized to the point where representative imaging could not be performed and the final polishing step had to be redone.

3.4.5. Etching Samples

Klemm's II reagent was chosen for copper etching and 0.5% nital was selected for zinc etching, based off ASM Handbook Volume 9 selection of etchants for copper and zinc. The Klemm's II reagent was purchased from Pace Technologies® and had a composition of 25% sodium thiosulfate, 5% potassium metabisulfite, and 70% water. The 0.5% nital was produced in house by diluting 0.5 mL of HNO₃ into 100 mL of de-ionized water.

Care was taken to avoid over-etching and the required repolishing of the sample surface to remove the over-etched surface. The Klemm's II reagent was applied to the copper sample deposits with a cotton swab that had one end submerged in the reagent. The copper surface was gently swabbed, periodically checking the sample surface after rinsing with deionized water and ethanol to ensure that the sample was not over-etched and grain boundaries appeared. Over-etching a polished sample would result in a burned appearance under microscope.

Initially, zinc etching was performed with only 0.5% nital but did not produce a sufficient etch to determine zinc grains from contrast with the rest of the sample surface. However, Klemm's II reagent is also suitable for zinc and zinc alloys and was applied to the CS zinc samples to improve grain contrast. Then, the zinc samples were etched with 0.5% nital for adequate contrast for grain analysis.

After etching the sample surfaces, imaging was performed again in the same fashion as before with some additions. Copper runs 8, 10, 11, 13, and 14 all were sufficiently thick coatings such that the entire cross section could not be seen from the widest point to substrate at fifty times magnification, and additional images were taken of the crystal grains, proceeding close to the substrate, and progressively getting further away until the edge of the deposit could be seen. This was done to see how grain size changes with deposit thickness.

3.4.6. Microhardness

Micro-indentation hardness testing was performed to obtain Vickers hardness measurements. Microhardness measurements were taken on freshly polished samples to be representative of the bulk material. In **Figure 19**, the red circles show the testing spots to suggest an average microhardness of the deposit and green circles show the testing spots and suggest a microhardness measurement as a function of deposit thickness for copper runs 8, 10, 11, 13, and

14. Micro-indentations were done using a Leco LM 300AT using a Vickers diamond-shaped indenter. The force used in the microhardness testing of copper varied between 300 gram-force (gf) and 50 gf depending on the thickness of the substrate and varied between 25 gf and 10 gf for zinc. Higher loading produces larger diamond indents, and therefore would produce an indent too large for some of the deposits. For Vickers microhardness, it is accepted that for force between 1 gf and 100 gf there is a 3% error within the measurement. Vickers microhardness is based on the following equation, therefore the mass used is not standardized in the testing. $F_{(gf)}$ is the force applied in units of gram-force, and d_v is the average indent diagonal length in μm (micron).

$$HV = 1854.4 * \frac{F_{(gf)}}{d_v^2 (um)} \quad (4)$$

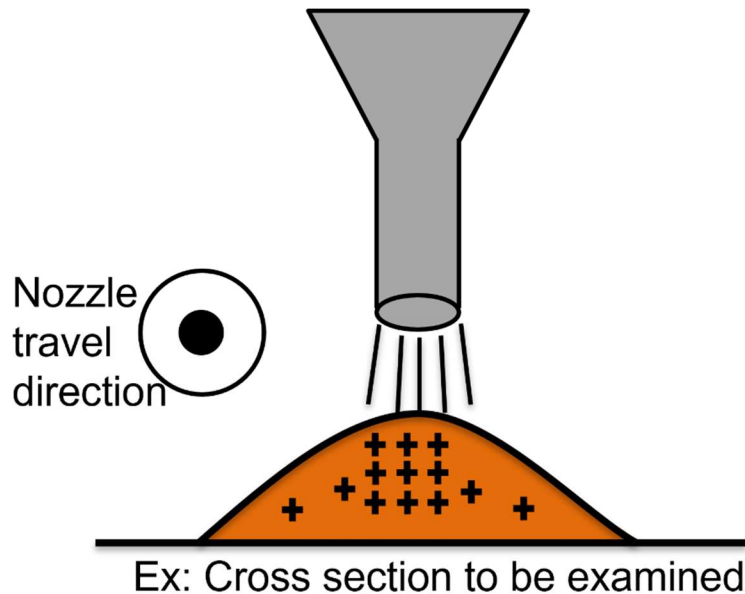


Figure 19: Schematic diagram showing where microhardness measurements were taken for samples as well as sufficiently thick samples and the orientation of the CS nozzle and travel direction

4. Results

4.1. Powder Size Analysis

A commercial off the shelf powder was procured. Sieving was performed on both powders, Cu and Zn, with mesh sizes of +106 μm , +53 μm , +45 μm , and +20 μm , with particles smaller than 20 μm being separated into a bottom pan, with 10 g's of force, for five minutes (ASTM E11). A large portion of powder was between the +45 μm and +20 μm meshes and an additional +25 μm mesh was added to the sieve stack. The powder retained on each sieve was recorded and tabulated, shown in **Table IV** and **Table V**.

Table IV: Copper Powder Sieve Analysis

	Pre-powder weight (g)	Post-powder weight (g)	Weight of powder (g)	Weight %	Cum. weight %	Cum. passing %	Size (μm)
Initial boat	50.0031	0.0000	50.00				
+106 μm	63.3382	63.4191	0.0809	0.19%	0.19%	99.81%	106
+53 μm	64.8311	65.9639	1.1328	2.64%	2.83%	97.17%	53
+45 μm	66.1298	68.5612	2.4314	5.66%	8.49%	91.51%	45
+25 μm	63.3862	64.2681	0.8819	2.05%	10.54%	89.46%	25
+20 μm	65.2098	91.4591	26.2493	61.12%	71.66%	28.34%	20
PAN	46.2264	58.3987	12.1723	28.34%	100.00%	0.00%	0
		Total	42.9486	100%			

Table V: Zinc Powder Sieve Analysis

	Pre-powder weight (g)	Post-powder weight (g)	Weight of powder (g)	Weight %	Cum. weight %	Cum. passing %	Size (μm)
Initial boat	50.0096	0.0000	50.01				
+106 μm	63.3240	65.1384	1.8144	3.64%	3.64%	96.36%	106
+53 μm	64.7836	71.7083	6.9247	13.88%	17.52%	82.48%	53
+45 μm	66.1815	69.2333	3.0518	6.12%	23.63%	76.37%	45
+25 μm	63.2398	65.5777	2.3379	4.69%	28.32%	71.68%	25
+20 μm	65.2939	83.5854	18.2915	36.66%	64.98%	35.02%	20
PAN	45.1227	62.5961	17.4734	35.02%	100.00%	0.00%	0
		Total	49.8937	100%			

Figure 20 and Figure 22 are histograms showing the particle size distribution versus cumulative percent passing. Figure 21 and Figure 23 show the graphical analysis and linear interpolation used to find the 50% passing size (d50) and 80% passing size (d80).

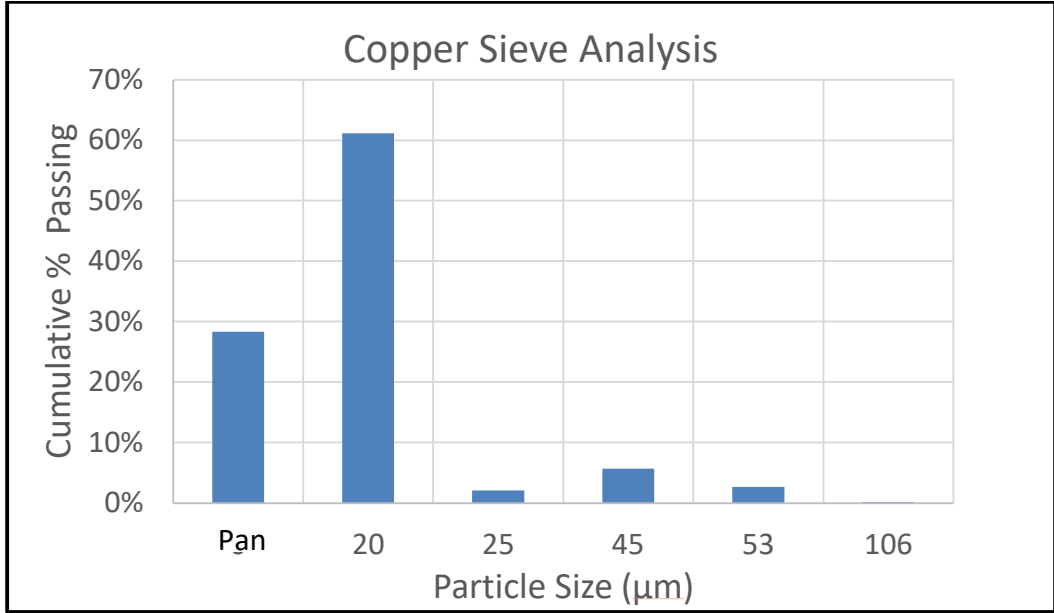


Figure 20: Copper powder cumulative % passing versus Particle size (µm) with a d50 size of 22µm

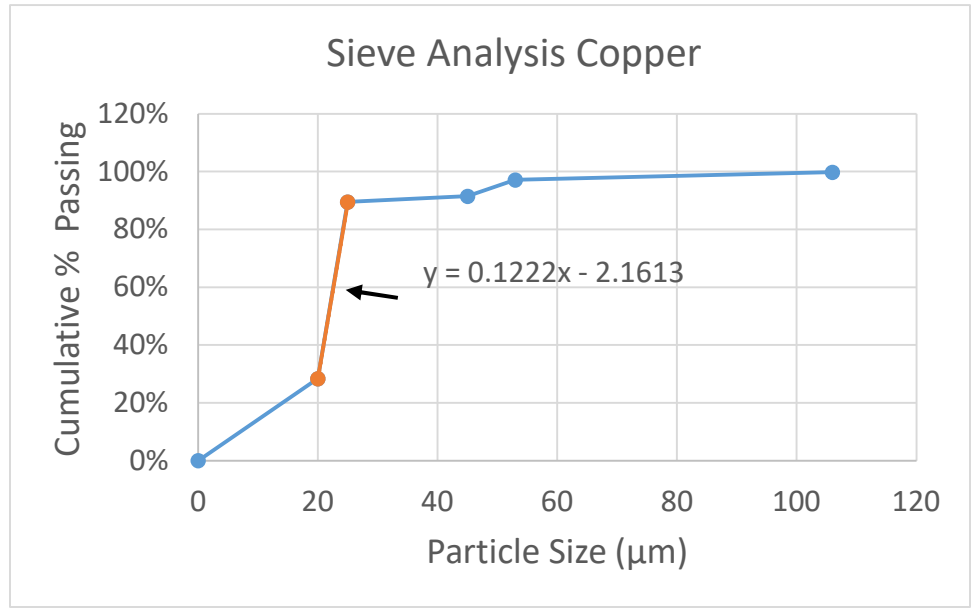


Figure 21: Copper powder sieve analysis using linear interpolation with a d50 size of 22µm and d80 size of 26 µm

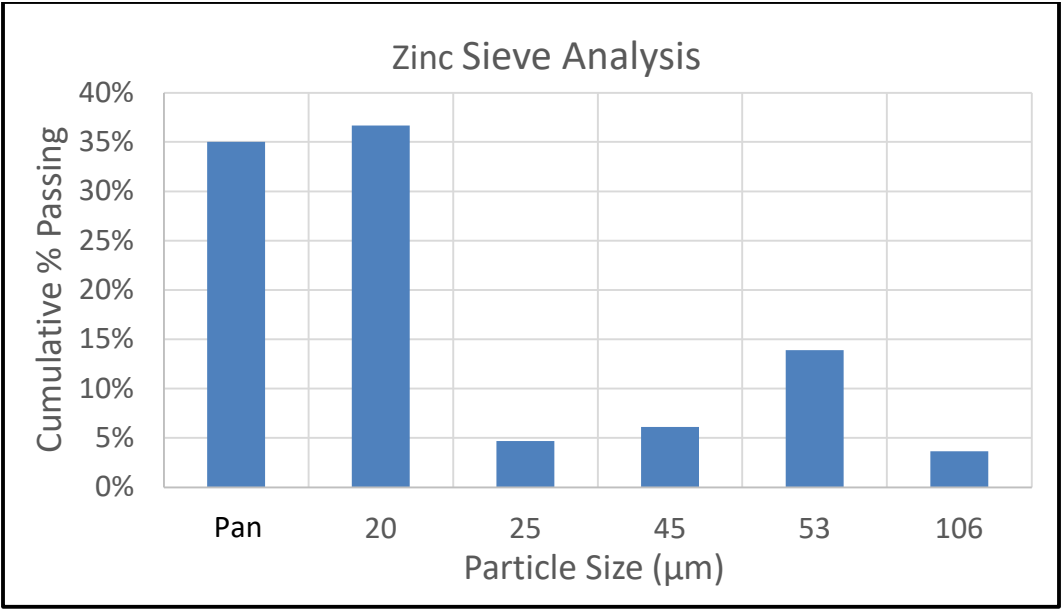


Figure 22: Zinc powder cumulative % passing versus Particle size (µm) with a d50 size of 22 µm and a bimodal particle distribution

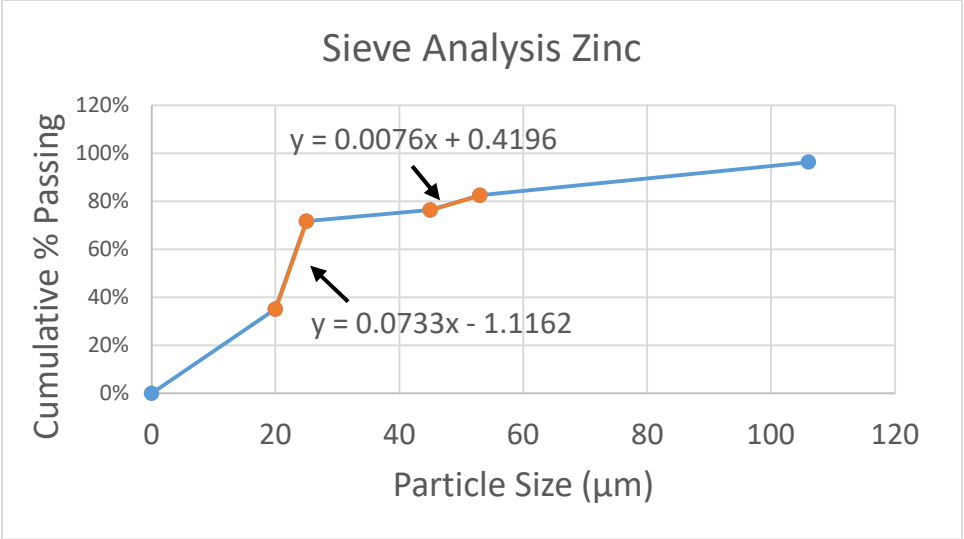


Figure 23: Zinc powder sieve analysis using linear interpolation with a d50 size of 22 µm and a d80 size of 50 µm

Scanning electron microscopy (SEM) was performed on a MIRA3 TESCAN and used to verify particle shape (**Figure 24** and **Figure 25**), to verify that the holes observed later in the porosity analysis are pores and not oxides or inclusions within the substrate, and to check for the presence of mechanical twin grains. The results of the pore energy dispersive x-ray analysis are presented in Appendix A: SEM Pore Analysis. The copper particles appeared to have a pinecone like geometry while the zinc particles had a round irregular geometry.

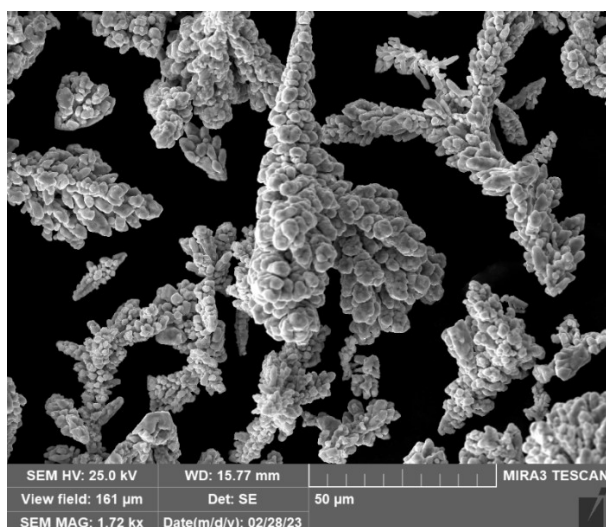


Figure 24: SEM image of copper particles showing a jagged pinecone like structure with many nodules protruding from the particles surface

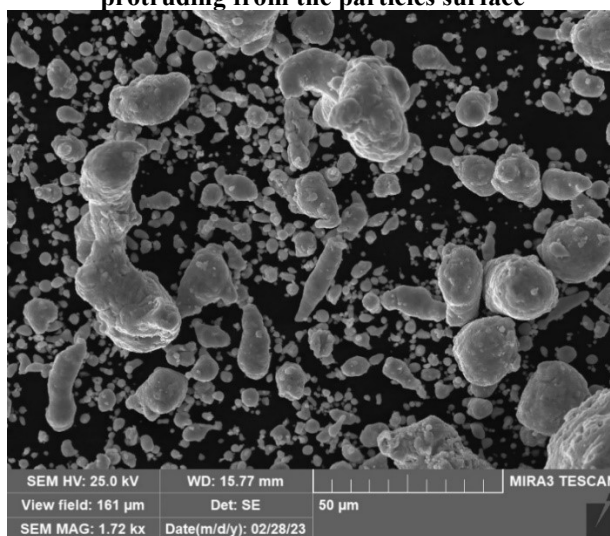


Figure 25: SEM image of large zinc particles with a round irregular geometry among smaller round zinc particles

4.2. Powder Feed System

To create consistent samples, a feed rate and system must be used that provides a consistent flow of powder into the gas stream. The RuSonic CS machine (**Figure 26**) used in this research was performing inconsistently and not maintaining the feed rate set on the machine, resulting in samples not suitable for study. The produced coatings would initially be consistent, however the actuator used to allow powder into the gas stream and pressure effects from the gas stream itself resulted in clogging. Additionally, powder would leak from the chamber and into the process stream, greatly exaggerating the feed rate and producing thick deposits.



Figure 26: In-house RuSonic CS machine with separate feed hopper and heating element controlled through a variable transformer

To resolve the powder feed issues, a new powder hopper, feed nozzle, and air intake nozzle (**Figure 27** and **Figure 28**) were designed in SolidWorks and 3D printed on a Formlabs 3L printer with Tough 2000 resin and a layer thickness of 50 μm . An orifice was drilled through the feed nozzle which aided in controlling the powder feed rate into the gas stream by allowing a

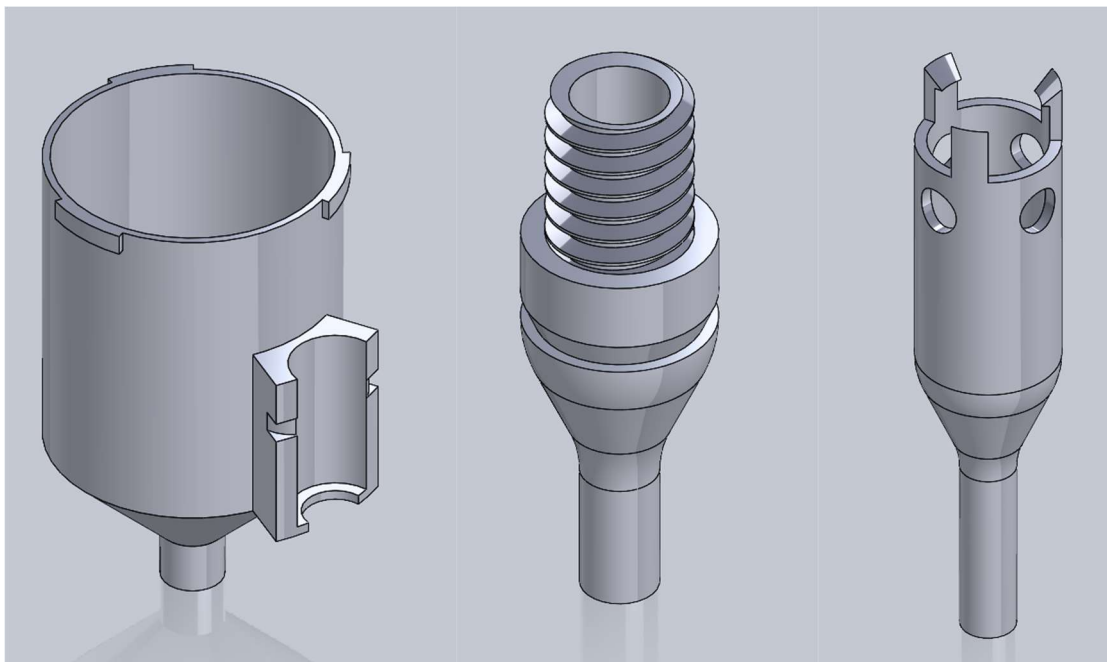


Figure 27: New powder feed system design with the hopper with vibratory motor mount (left), interchangeable feed nozzle (middle), and air intake (right)

small cross section of material to fall into the process stream. A hole size diameter of 0.6 mm was chosen to produce the copper samples for this study and a hole size diameter of 1.5 mm was used to produce the zinc samples. A vibrator motor was attached to the powder chamber to further ensure powder would move through the feed nozzle. The feed rate for both feed nozzles was measured by collecting powder that flowed out of the nozzle with the feed system on over a period of five minutes, averaging over three runs. The 0.6 mm nozzle resulted in a feed rate of 2.2 g/min for copper powder and the 1.5 mm nozzle resulted in a feed rate of 1.7 g/min for the zinc powder.

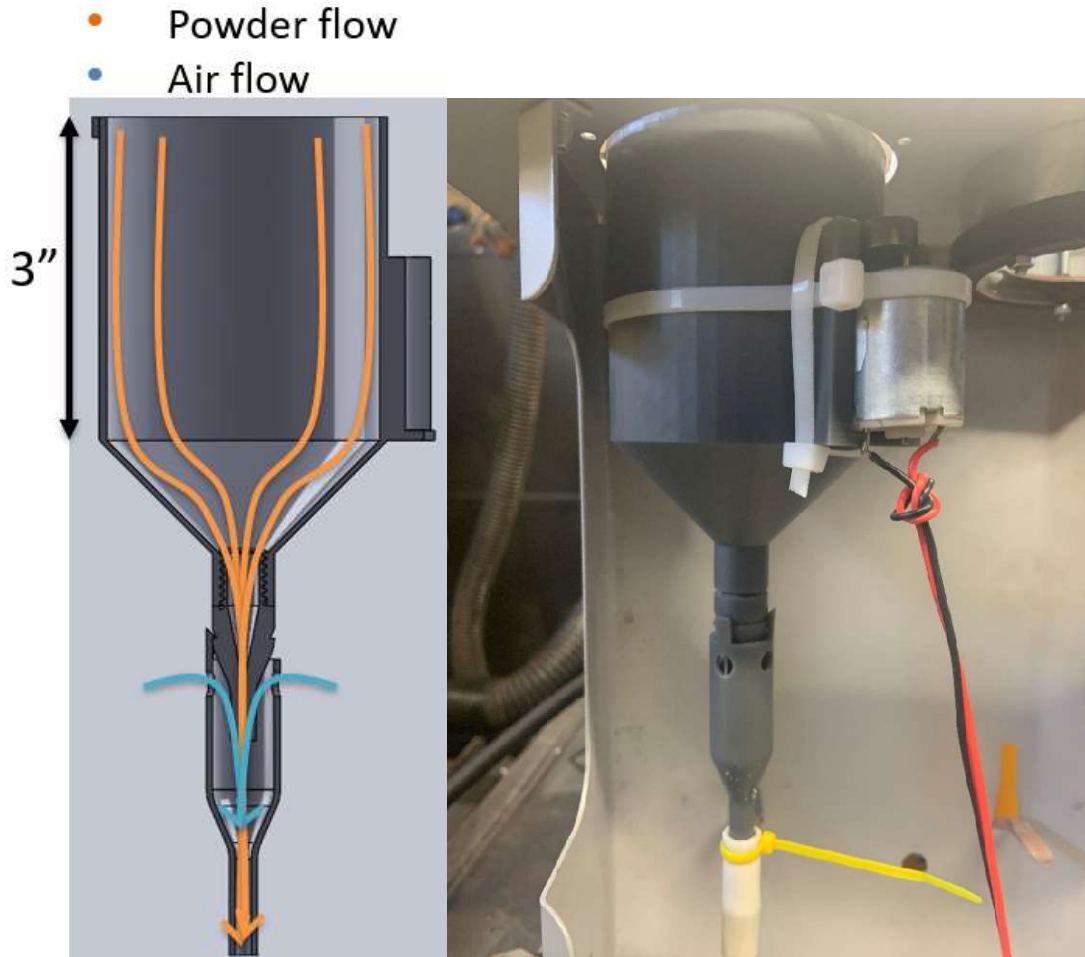


Figure 28: 3D resin powder feed hopper, feed nozzle, and air intake nozzle, attached to the Rusonic CS machine with arrows to denote the powder flow path and air intake path

4.3. Micrographs

4.3.1. Un-Etched Copper

Obtaining quality images to perform analysis on proved difficult due to the presence of a gap between the substrate and the deposit. Few copper particles adhered to the substrate, in which other copper particles were able to adhere to the few that did adhere to the substrate. The gap between the substrate and deposit was detrimental to the polishing and imaging of the deposits because it collected polishing media, which would later leak out when the sample was rinsed and stained the edges of both the substrate and the deposit. Particles in the crevices would settle of the sample. Despite images being taken with varying brightness, it likely did not affect

results as image processing relied on contrast between features and the surface and when turned into greyscale, thresholding corrected for brightness variation. The copper CS samples produced by runs 3 and 7, were too thin to analyze. As such, the samples produced with a heating element voltage of 75%, were rerun with a heating element voltage of 80% to produce deposits in which all samples in the design could be analyzed. These rerun samples were important for image comparison as they represent corner points in the design and were used to compare parameter effects in **Figure 29** and **Figure 30**. **Figure 31** shows the SEM image taken for pore verification where holes can be readily seen on the sample surface of copper run 8.

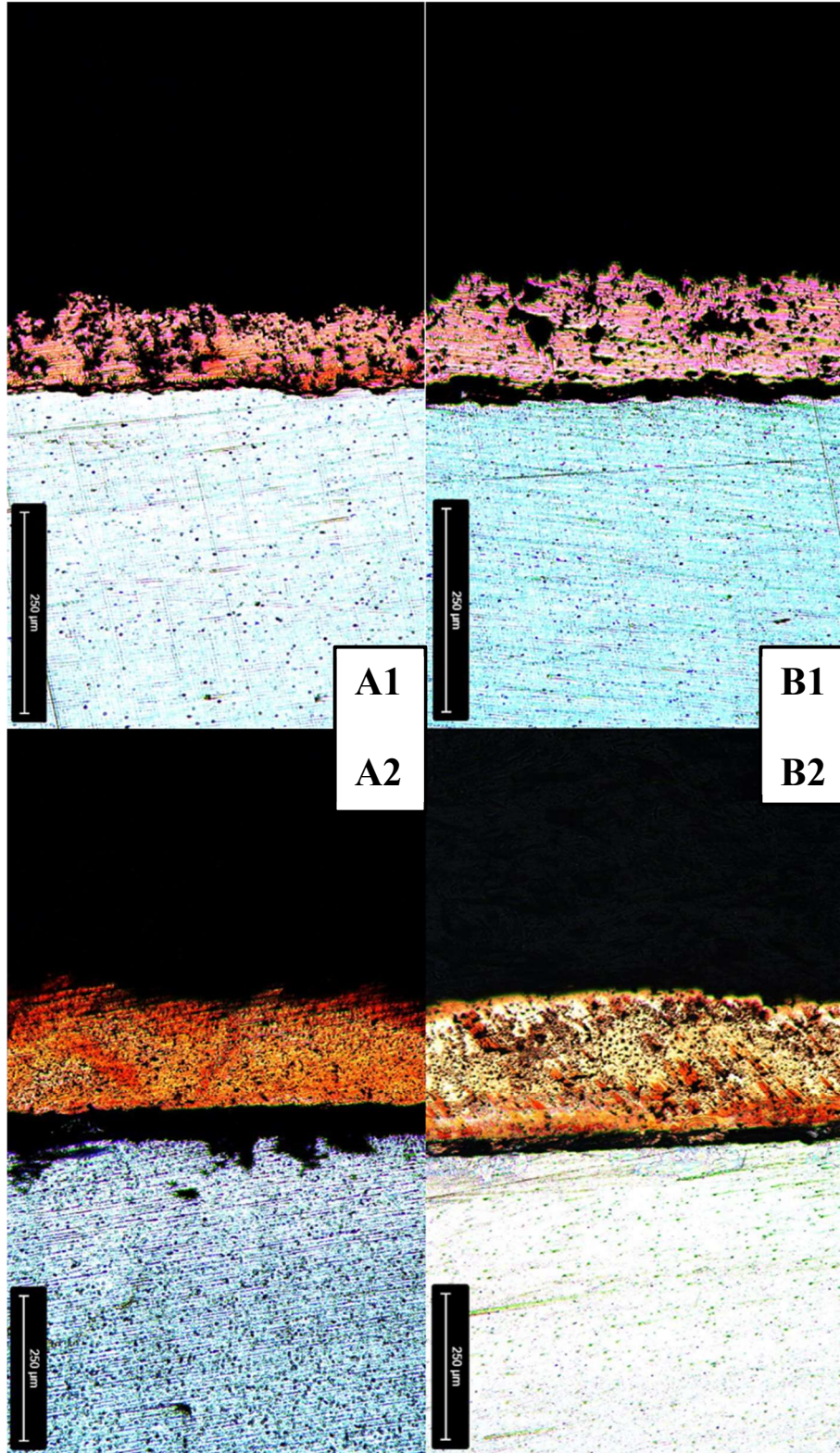


Figure 29: Un-etched image comparison between copper Run 3 (A1), Run 1 (A2), Run 7 (B1), Run 18 (B2). From 1 to 2, heating element voltage increases from 80% to 94%. From A to B, standoff distance decreases from 13.0 mm to 6.5 mm. Travel speed remains the same, at 206 mm/min

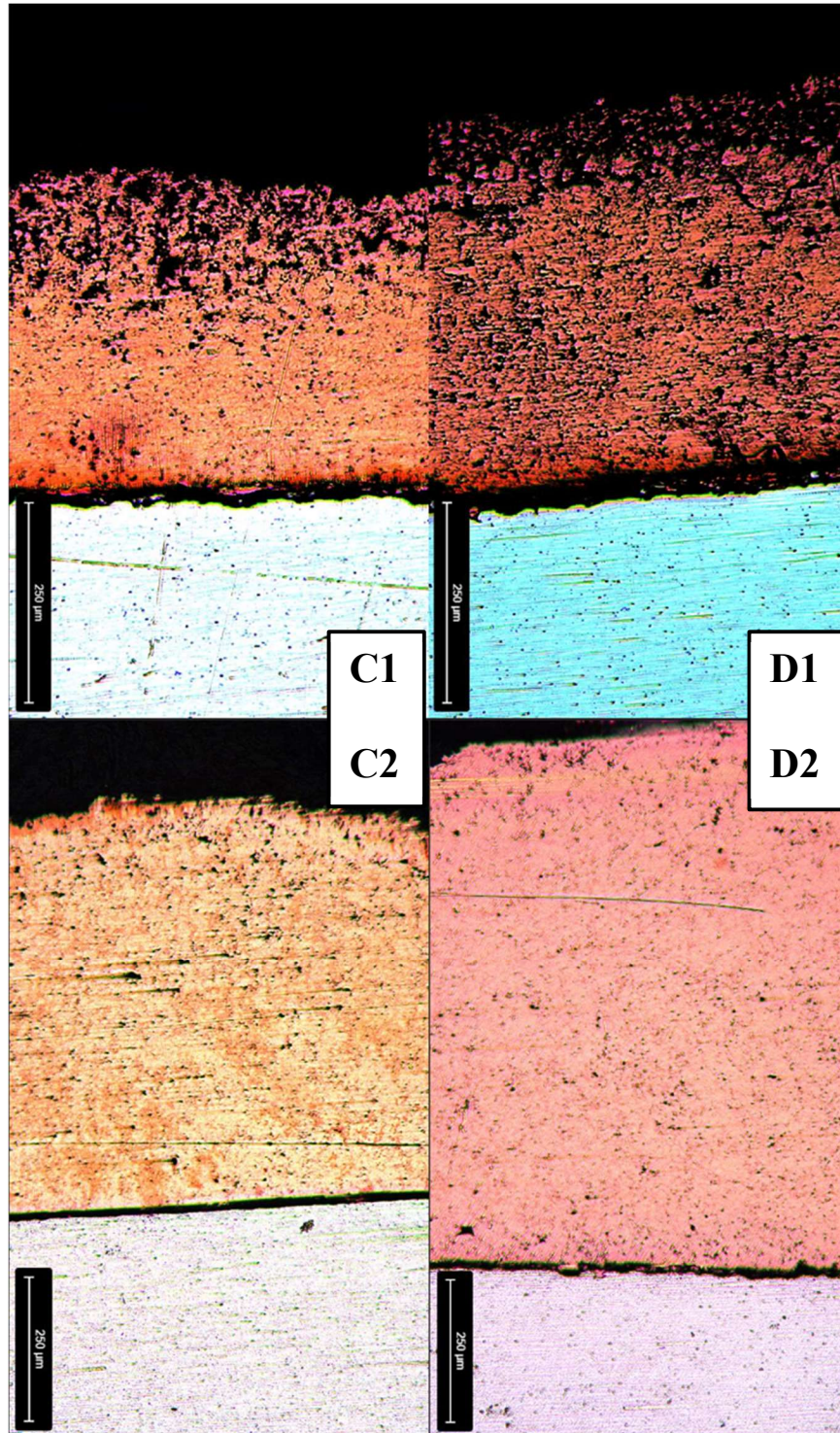


Figure 30: Un-etched image comparison between copper Run 6 (C1), Run 13 (C2), Run 14 (D1), Run 11 (D2). From 1 to 2, heating element voltage increases from 80% to 94%. From C to D, the standoff distance increases from 13.0 mm to 6.5 mm. Travel speed remains the same, at 69 mm/min

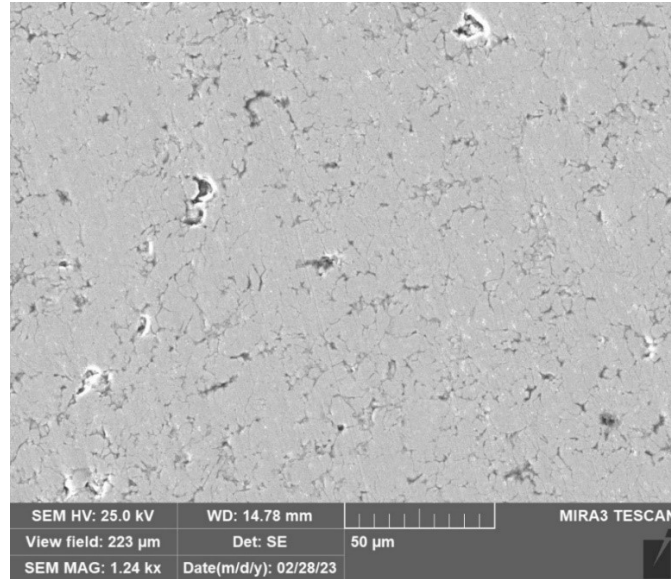


Figure 31: SEM image of copper CS run 8 showing the presence of pores in the deposit opposed to the presence of surface contaminants or oxides

4.3.2. Etched Copper

Images for the copper grain size were batch analyzed with digital image correlation performed using ImageJ and the following image processing steps: made binary to turn the image into black and white, invert the selection, de-speckle the image to reduce noise, find edges of features, invert again, and analyze the image with a known pixel to micron conversion of 3.97 pixels/ μm . This distance was based on measuring the scalebar in ImageJ, which measures the distance of the scalebar in pixels and then setting the pixel distance to a known unit distance. This was also used to measure deposit thickness from the tip of the deposit to the substrate. When analyzing particles, the software was set to analyze a collective area of $16 \mu\text{m}^2$ to $600 \mu\text{m}^2$. The range of values was found by comparing the results from the analysis with the Heyn intercept method, and selecting the area based on the lowest average percent error between the two analysis techniques. Image analysis was performed at fifty times magnification. **Figure 32** and **Figure 33** show the corner points of the design to draw comparisons between microstructures.

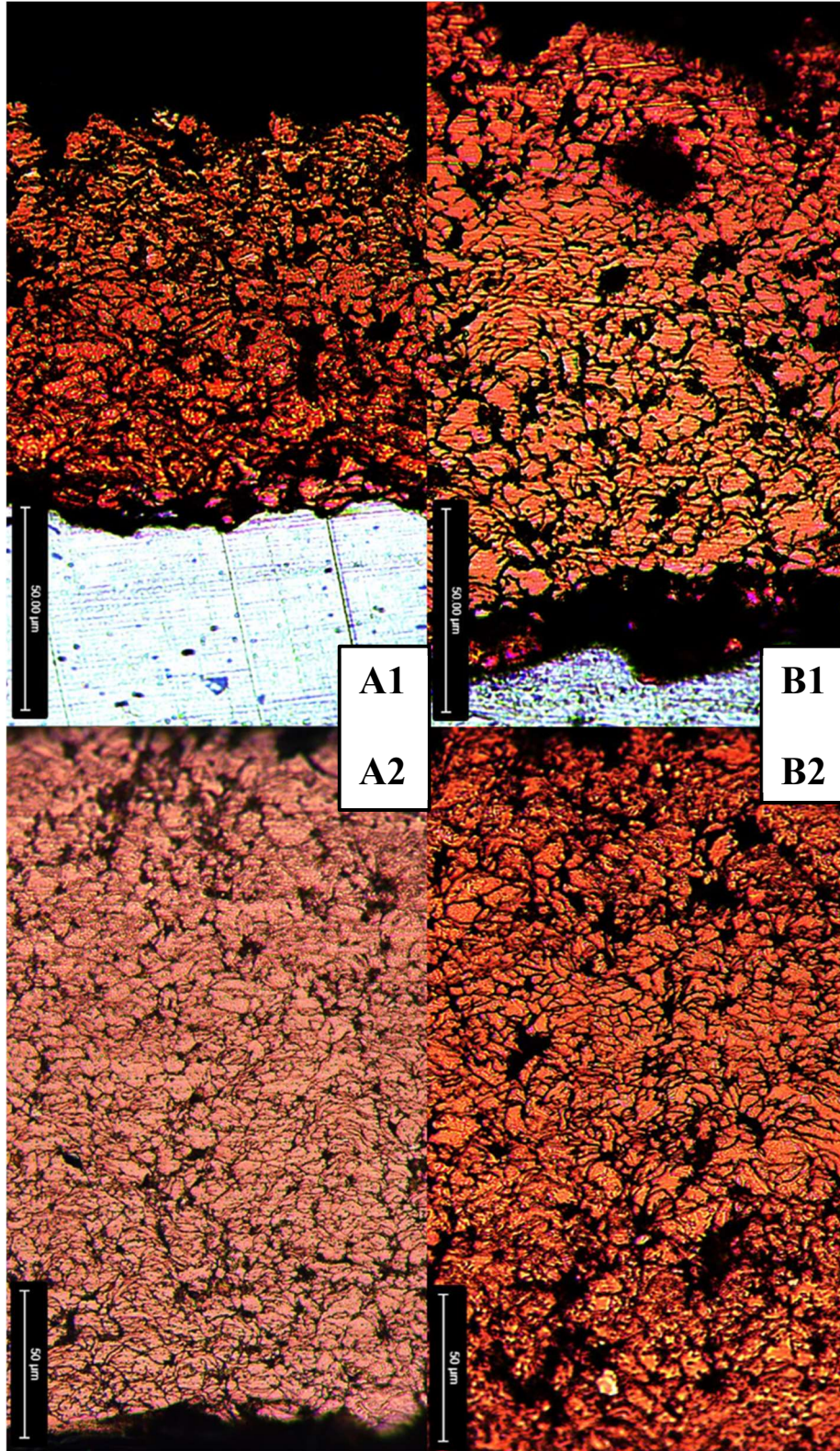


Figure 32: Microstructural comparison between copper Run 3 (A1), Run 1 (A2), Run 7 (B1), Run 18 (B2). From 1 to 2, heating element voltage increases from 80% to 94%. From A to B, the standoff distance decreases from 13.0 mm to 6.5 mm. Travel speed remains the same, at 206 mm/min

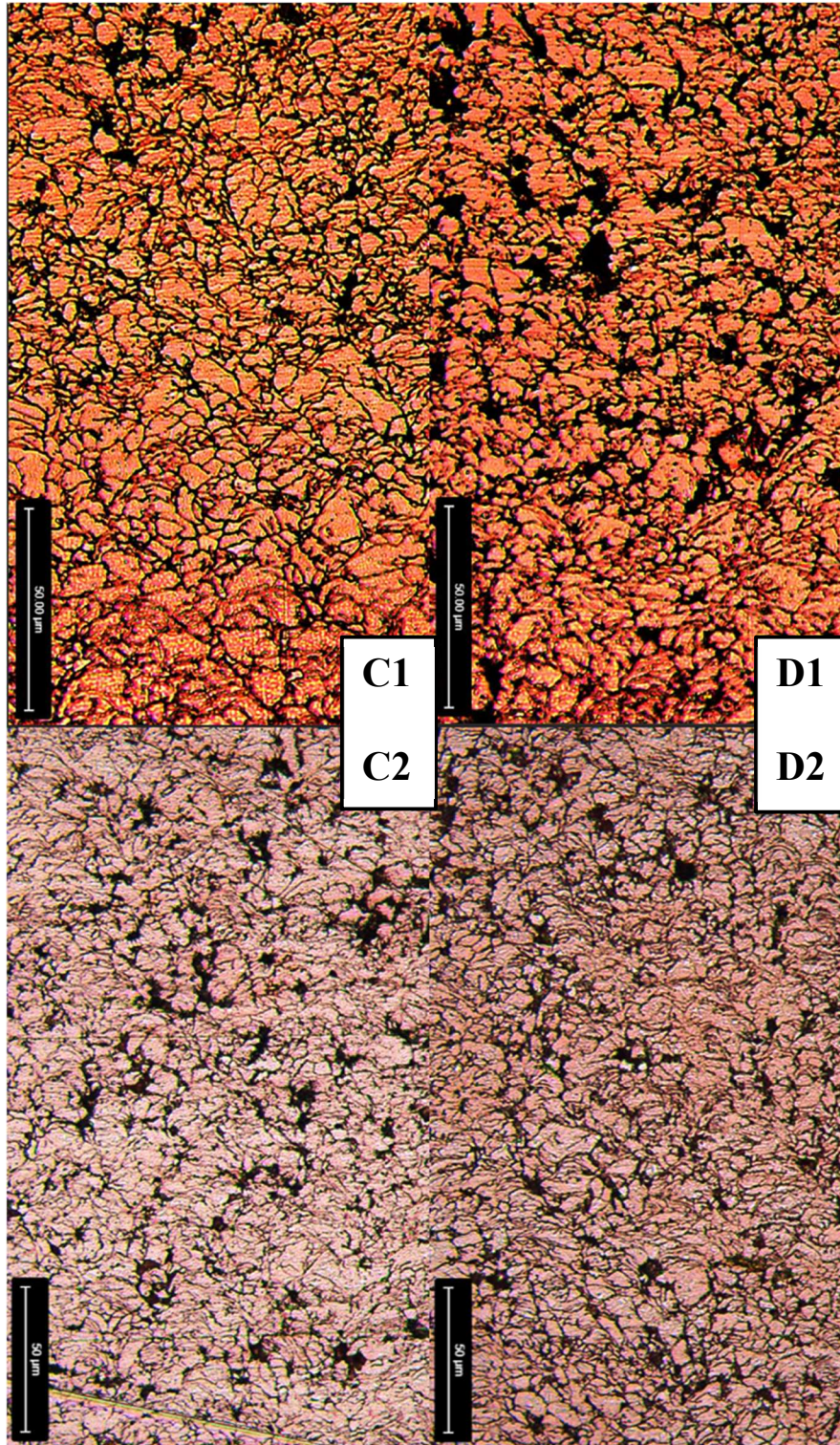


Figure 33: Microstructure comparison between copper Run 6 (C1), Run 13 (C2), Run 14 (D1), Run 11 (D2). From 1 to 2, heating element voltage increases from 80% to 94%. From C to D, the standoff distance decreases from 13.0 mm to 6.5 mm. Travel speed remains the same, at 69 mm/min

4.3.3. Un-Etched Zinc

Imaging the zinc samples followed the same practices as the copper samples and had much of the same issues with pores collecting polishing medium which produced some staining and particles on the surface. Zinc, however, had the extra challenge of quickly oxidizing within an hour of the final polishing step. The thin oxide layer was filtered out through contrast thresholding, however some samples had to be repolished and re-imaged due to the oxidation creating excessive interference with the contrast of actual pores. Additionally, polishing with a cloth without any polishing medium present and while wet, would produce scratches in the samples surface. The scratches from the polishing cloth were shallow enough to be filtered out in thresholding. Image comparison between parameter effects are shown in **Figure 34** and **Figure 35**. **Figure 36** shows the SEM image taken for pore verification where holes can be readily seen on the sample surface of zinc run 11.

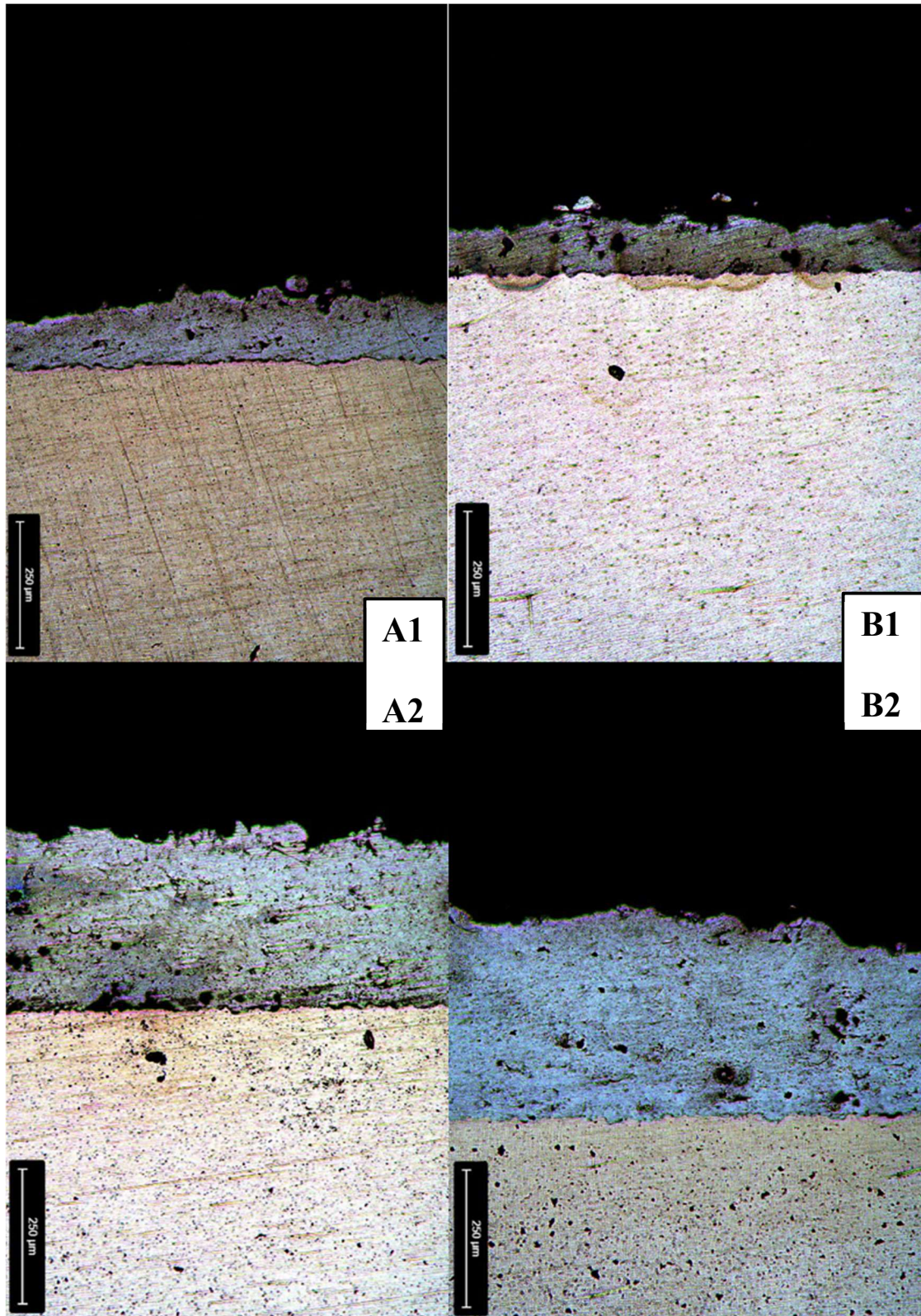


Figure 34: Un-etched image comparison between Zinc Run 3 (A1), Run 1 (A2), Run 7 (B1), Run 18 (B2). From 1 to 2, heating element voltage increases from 75% to 94%. From A to B, the standoff distance decreases from 13.0 mm to 6.5 mm. Travel speed remains the same, at 206 mm/min

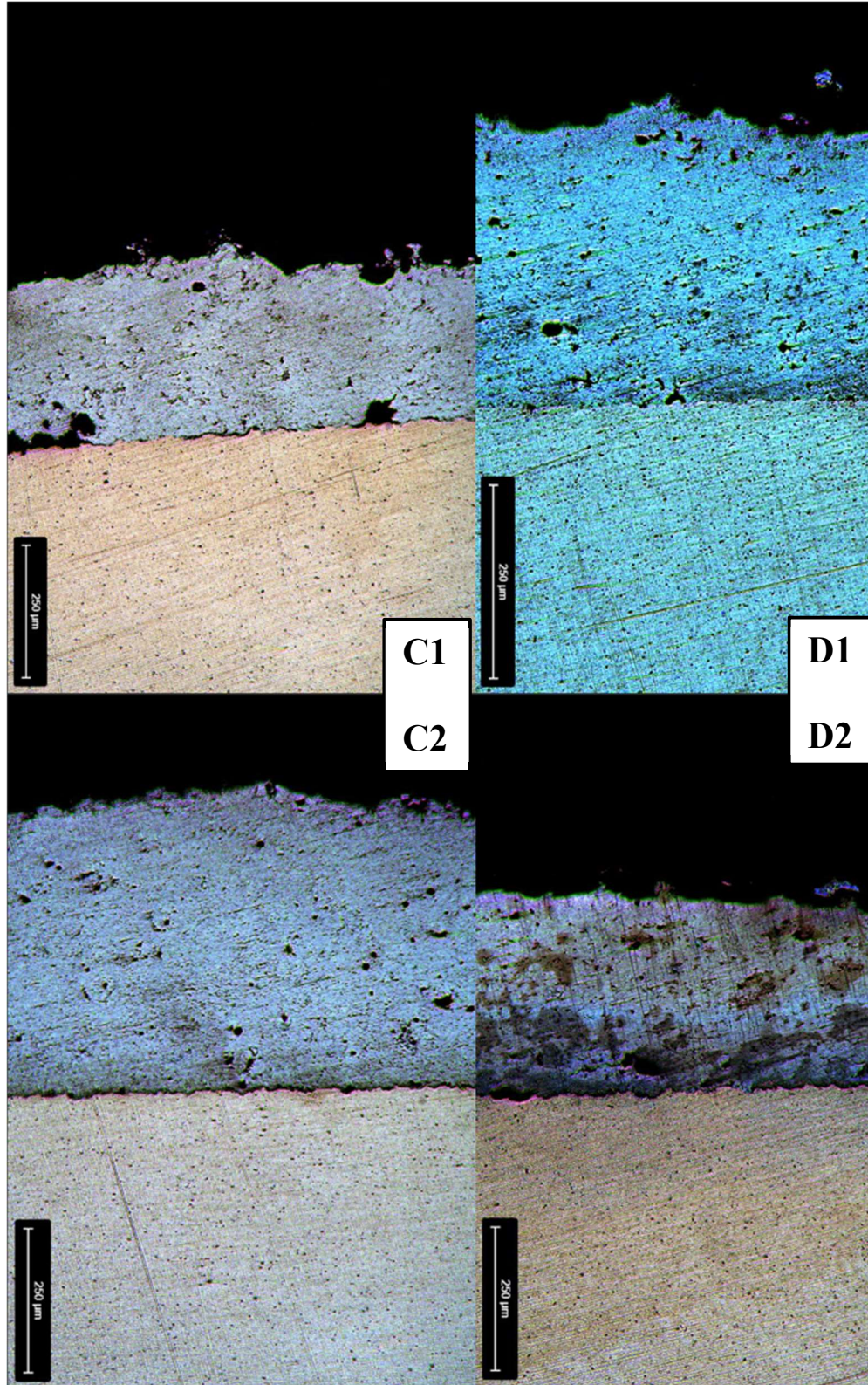


Figure 35: Un-etched image comparison between Zinc Run 6 (C1), Run 13 (C2), Run 14 (D1), Run 11 (D2). From 1 to 2, heating element voltage increases from 75% to 94%. From C to D, the standoff distance increases from 13.0 mm to 6.5 mm. Travel speed remains the same, at 69 mm/min

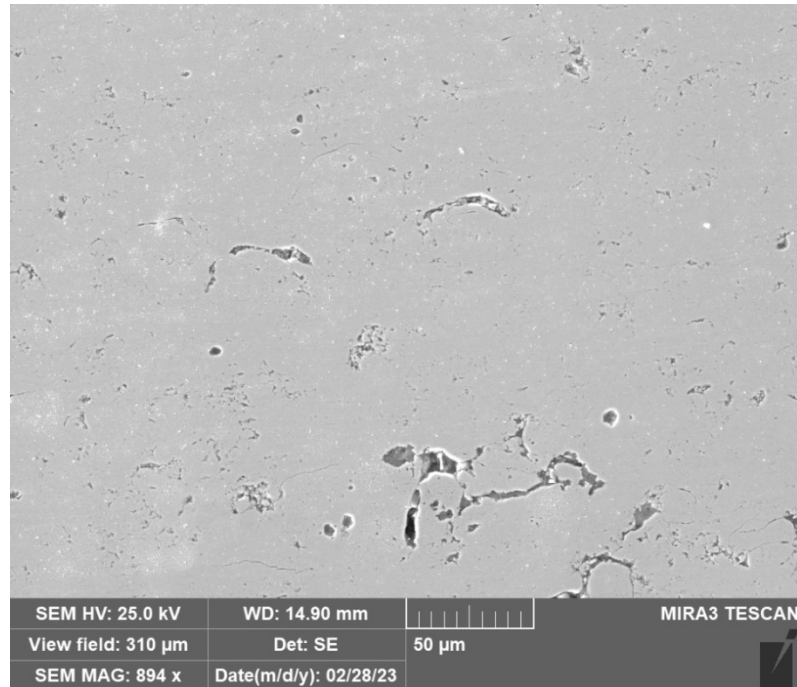


Figure 36: SEM image of zinc CS run 11 showing the presence of pores in the deposit opposed to the presence of surface contaminants or oxides

4.3.4. Etched Zinc

Images for the zinc grain size were batch analyzed with digital image correlation performed using ImageJ and same image processing techniques as copper except the zinc samples went through an initial Gaussian blur with a value of 1.4 to filter out noise. When analyzing grains, the software was set to analyze a collective area of $32 \mu\text{m}^2$ to $600 \mu\text{m}^2$. The range of values was also found by comparing the results from the analysis with the Heyn intercept method. Image analysis was performed fifty times magnification. **Figure 37** and **Figure 38** show the corner points of the design to draw comparisons between microstructures.

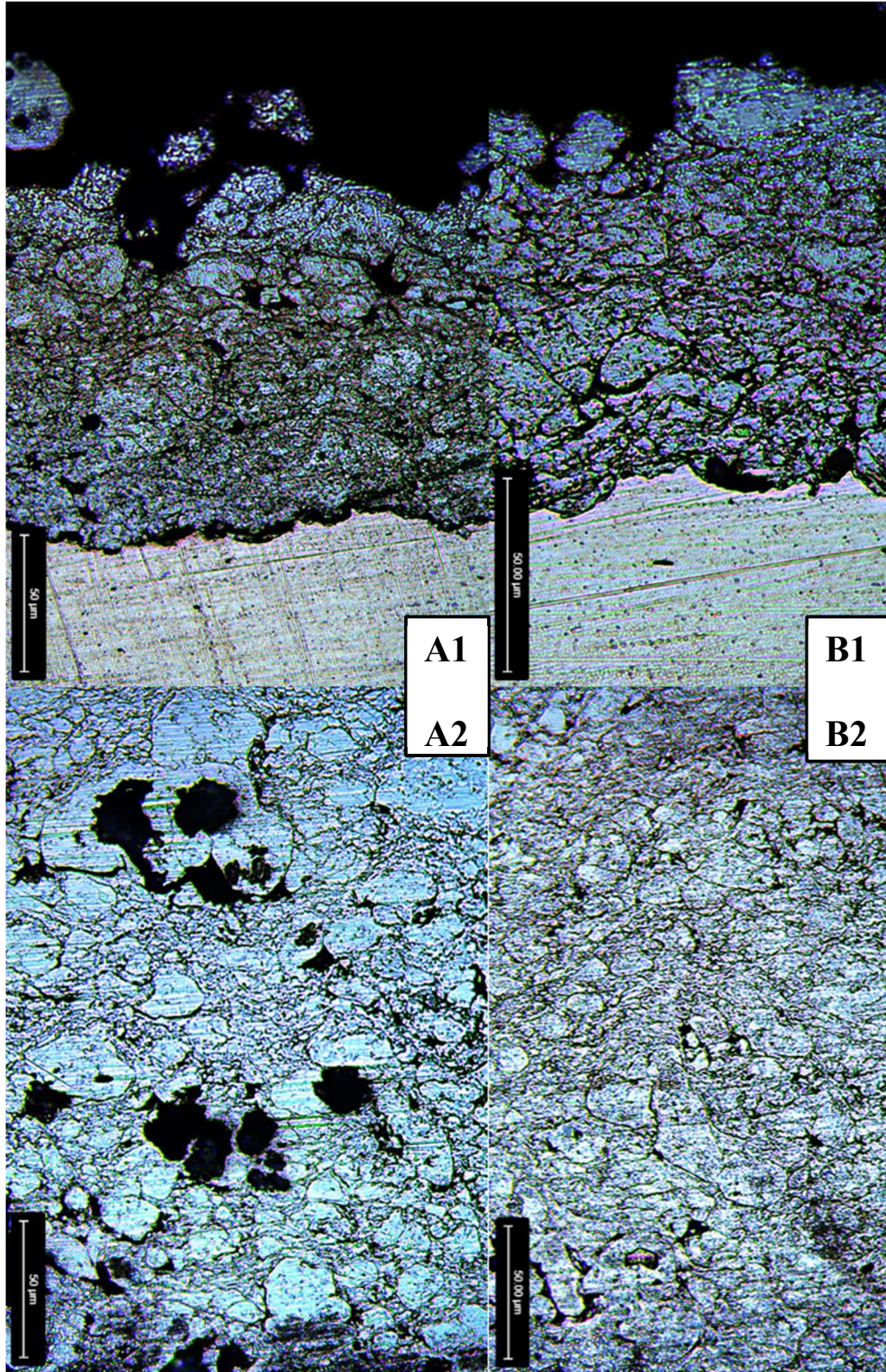


Figure 37: Microstructural comparison between Zinc Run 3 (A1), Run 1 (A2), Run 7 (B1), Run 18 (B2). From 1 to 2, heating element voltage increases from 75% to 94%. From A to B, the standoff distance decreases from 13.0 mm to 6.5 mm. Travel speed remains the same, at 206 mm/min

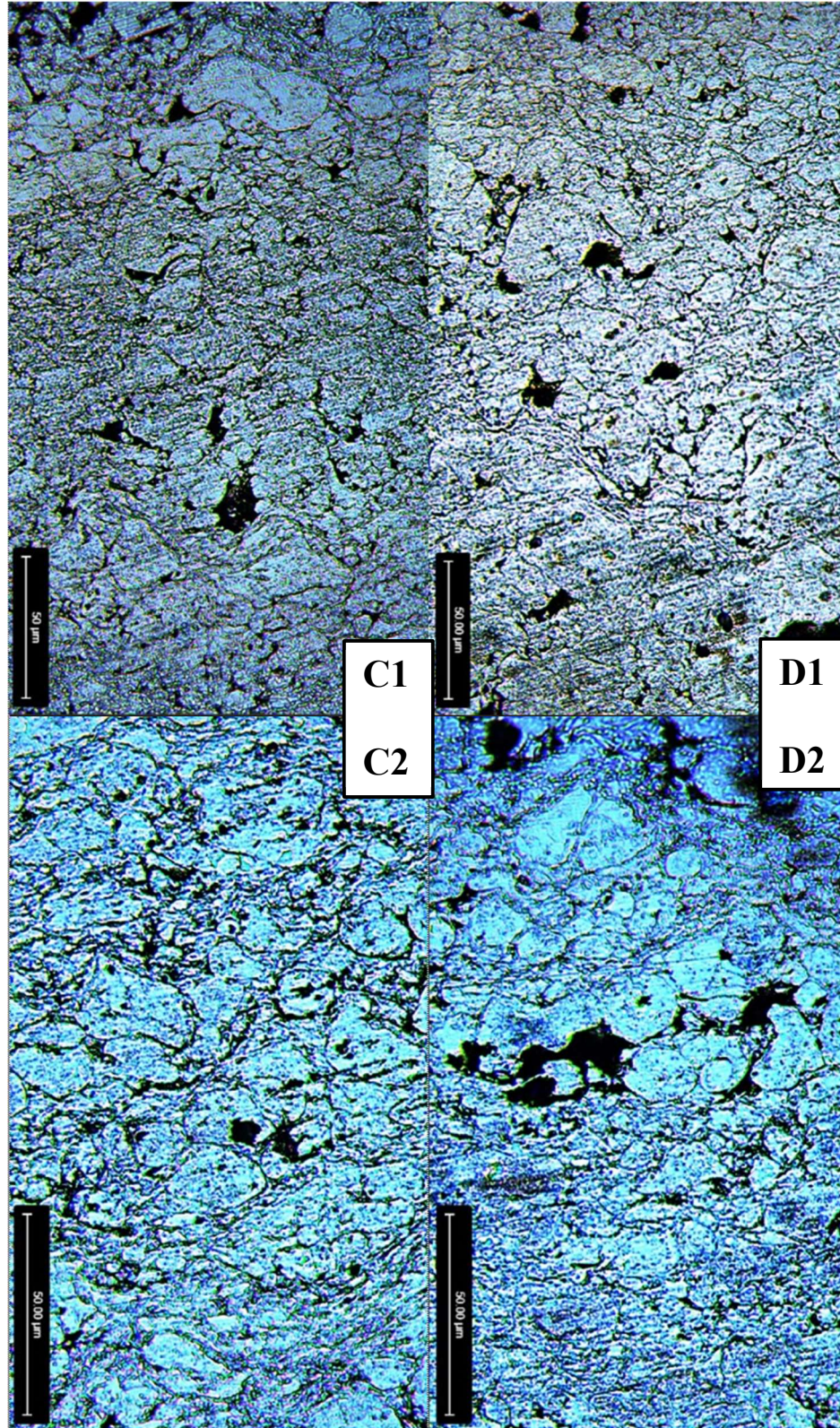


Figure 38: Microstructure comparison between Zinc Run 6 (C1), Run 13 (C2), Run 14 (D1), Run 11 (D2). From 1 to 2, heating element voltage increases from 75% to 94%. From C to D, the standoff distance increases from 13.0 mm to 6.5 mm. Travel speed remains the same, at 69 mm/min

4.4. Microhardness

Microhardness data is displayed in **Table VI**. Additionally, copper re-run samples 3, 6, 7, and 14 had an average Vickers hardness value of 68.8 HV, 64.0 HV, 50.6 HV, and 65.5 HV, respectively. Runs 8, 10, 11, 13, and 14 were sufficiently thick, where at fifty times magnification the deposits were thicker than the image view and the Vickers hardness was tested across the thickness of the deposit.

Table VI: Vickers hardness data for runs in the DOE for both copper and zinc samples.

Run #	Vickers Hardness	
	Copper	Zinc
1	66.6	35.9
2	65.9	35.4
3	NA	28.6
4	72.9	33.6
5	69.6	36.7
6	52.6	36.0
7	49.4	32.8
8	66.2	35.1
9	68.6	33.5
10	73.2	31.4
11	61.9	35.7
12	69.4	35.3
13	68.8	34.1
14	54.7	35.3
15	63.1	27.5
16	75.8	35.6
17	71.5	35.4
18	76.1	33.0
19	73.5	37.7
20	61.5	33.9
3-2	68.8	-
6-2	64.0	-
7-2	50.6	-
14-2	65.5	-

4.5. Deposit Thickness

Deposit thickness data is displayed in **Table VII**. Additionally, copper Re-Run samples 3, 6, 7, and 14 had a thickness of 105 μm , 385 μm , 128 μm , and 453 μm , respectively.

Table VII: Deposit Thickness data for runs in the DOE for both copper and zinc samples.

Run #	Thickness (μm)	
	Copper	Zinc
1	204	337
2	110	384
3	42	144
4	151	296
5	135	235
6	180	336
7	57	112
8	1339	931
9	373	265
10	505	332
11	968	360
12	254	199
13	710	550
14	608	381
15	245	111
16	121	40
17	243	244
18	250	393
19	281	184
20	114	147
3-2	105	-
6-2	385	-
7-2	128	-
14-2	453	-

4.6. Design of Experiments

After obtaining and inputting data into the Design Expert software, the software used response surface methodology to generate an ANOVA table and fit statistics. When examining the ANOVA table, it is important to look at the p-values of the data set, as the p-value is an

indicator of confidence in the model. A p-value of less than 0.05 is desired, which means that there is a 95% confidence that the examined parameter is important to the data set. When a p-value is greater than 0.05, it does not necessarily mean that the parameter is not important, but its uncertainty is higher. Also, if the model produced was to consider the synergistic variable of heating element voltage and standoff distance, to be significant (p-value < 0.05) and the variable of heating element voltage to be not significant (p-value >0.05), the variable of heating element voltage must still be included in the model. An adequate precision (Adeq Precision) is desired to be above a value of 4, which signifies that there is separation between data points and noise.

4.6.1. Copper

4.6.1.1. Porosity

Due to runs 3 and 7 of the copper design being exceedingly thin or non-existent, their data were ignored and taken as null values in the modeling. The resulting linear model ANOVA is presented in **Table VIII** with a model p-value of 0.052 making it not significant as p-values of <0.05 are considered significant, and a lack of fit p-value of 0.608. The lack of fit describes how well the model fits the data points. If the lack of fit is significant (p-value <0.05) than the data is not being described well by the model. The p-value being slightly out of range does not dismiss the model, and the produced model was still considered. The adequate precision of the model is 6.8 meaning there was a high enough statistical power to differentiate between the signal and noise. The model had an adjusted R^2 value of 0.29 and a coefficient of variance (C.V.) of 27.5%. The adjusted R^2 gives a measure of how the data fits the produced model and adjusts based on the variance in the data. The C.V. is a ratio of the standard deviation to the average of the data set and how much the data varies from that average. A model was also produced using the data acquired from the copper reruns at 80% heating element voltage, however, the resulting p-value

of the model was 0.142 without the suggestion of a data transform. That model was not considered.

Table VIII: Copper porosity ANOVA table

Source	Sum of Squares	df	Mean Square	F-value	p-value	
Model	166.08	3	55.36	3.3	0.052	not significant
A - Heating Element Voltage	31.37	1	31.37	1.87	0.193	
C - Standoff Distance	111.31	1	111.31	6.63	0.022	
AC	51.83	1	51.83	3.09	0.101	
Residual	235.03	14	16.79			
Lack of Fit	142.23	9	15.8	0.8515	0.608	not significant
Pure Error	92.8	5	18.56			
Std. Dev.	4.1					
Mean	14.9					
C.V.%	27.5					
R²	0.41					
Adjusted R²	0.29					
Adeq Precision	6.8					

Diagnostic graphs were generated based on the modeling. **Figure 40** shows the predicted versus actual plot which shows a comparison between the models predicted values and the actual values in the data set. The further away from the line a point is, the higher its residuals values. **Figure 41** shows the leveraging that the model had on the data set in which runs 6 and 14 are leveraged more than the other runs. The high leveraging of runs 6 and 14 is because the runs were at the same heating element voltage as runs 3 and 7. With runs 3 and 7 being null in the data set, more value is put on the other two runs that produced results at the same heating element voltage setting. Although these runs are outside of reasonable bounds, the produced model was not discarded because the leverage diagnostic only shows how important specific runs were to the model. Other diagnostic graphs for the models can be seen in Appendix B:

Model Diagnostic Graphs. **Figure 39** shows an graph of the data with a slight decreasing trend in the 6.5 mm standoff samples and a slight increasing trend in the 13.0 mm standoff samples.

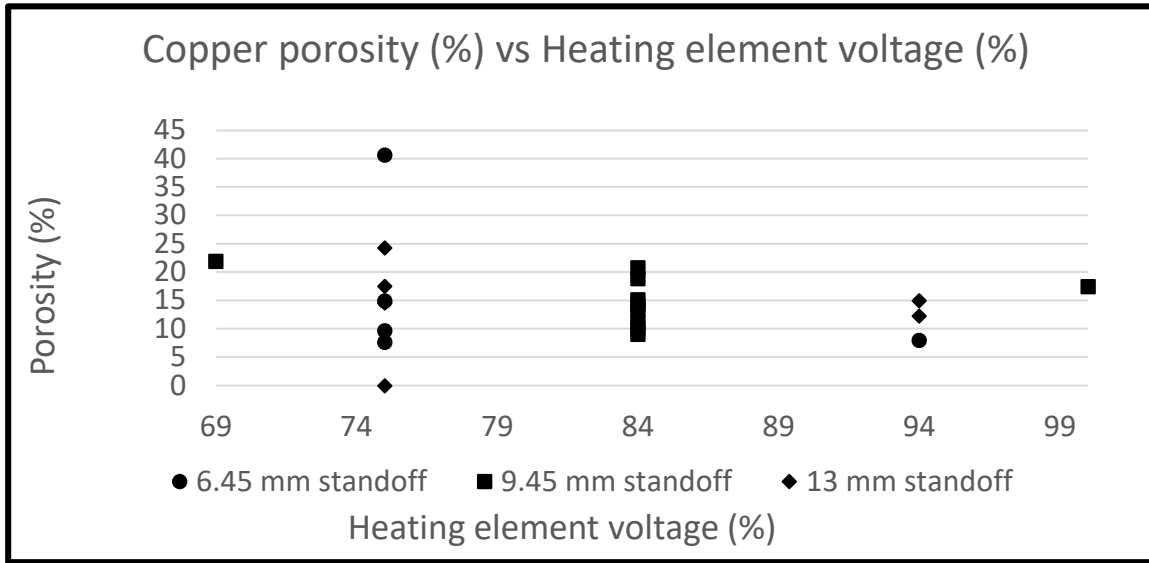



Figure 39: Copper graph plotting Porosity (%) versus Heating element voltage (%)

Porosity

Color points by value of Porosity:
 7.67  24.32

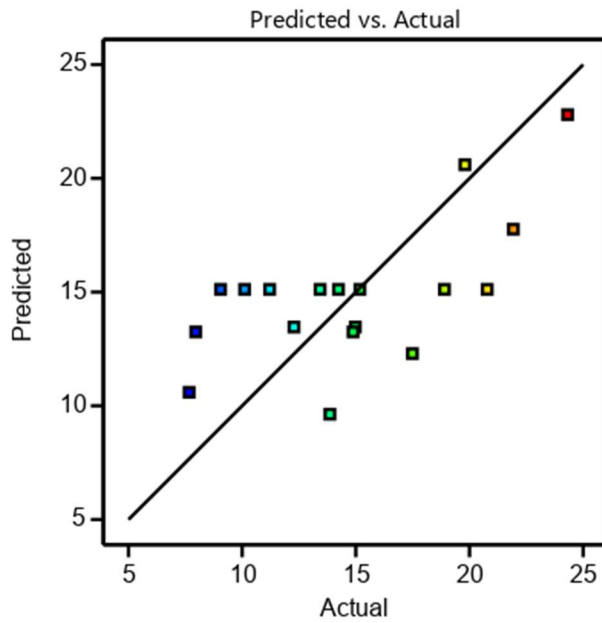


Figure 40: Predicted versus actual plot for the linear copper porosity model

Porosity

Color points by value of Porosity:

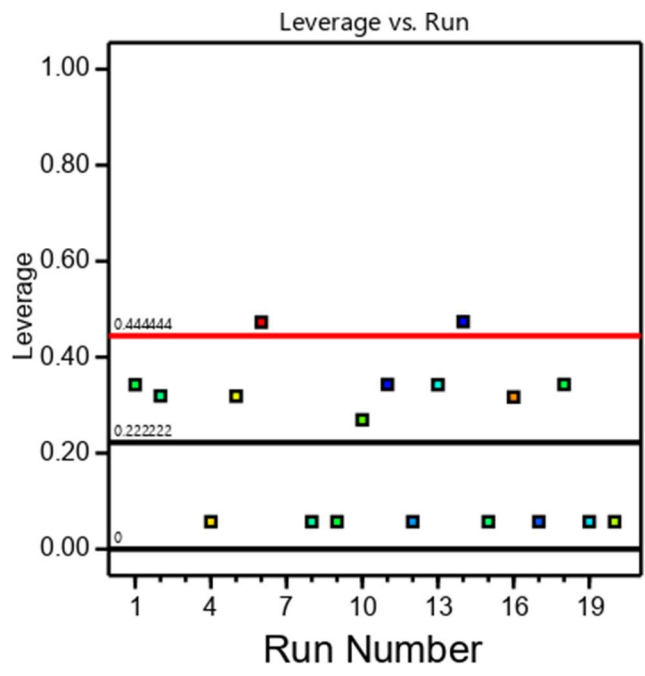
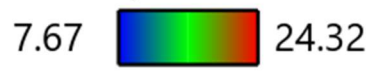


Figure 41: Copper porosity leverage versus run, showing runs 6, and 14 higher than the rest due to these runs being performed at the same voltage setting as the two that were null in the data set

Figure 42 shows the interaction of heating element voltage on the porosity of a copper CS deposit, varying standoff distance. The model displayed indicates that as heating element voltage was increased, porosity decreased when there was a standoff distance of 13.0 mm (red) and increased with a standoff distance of 6.5 mm (black).

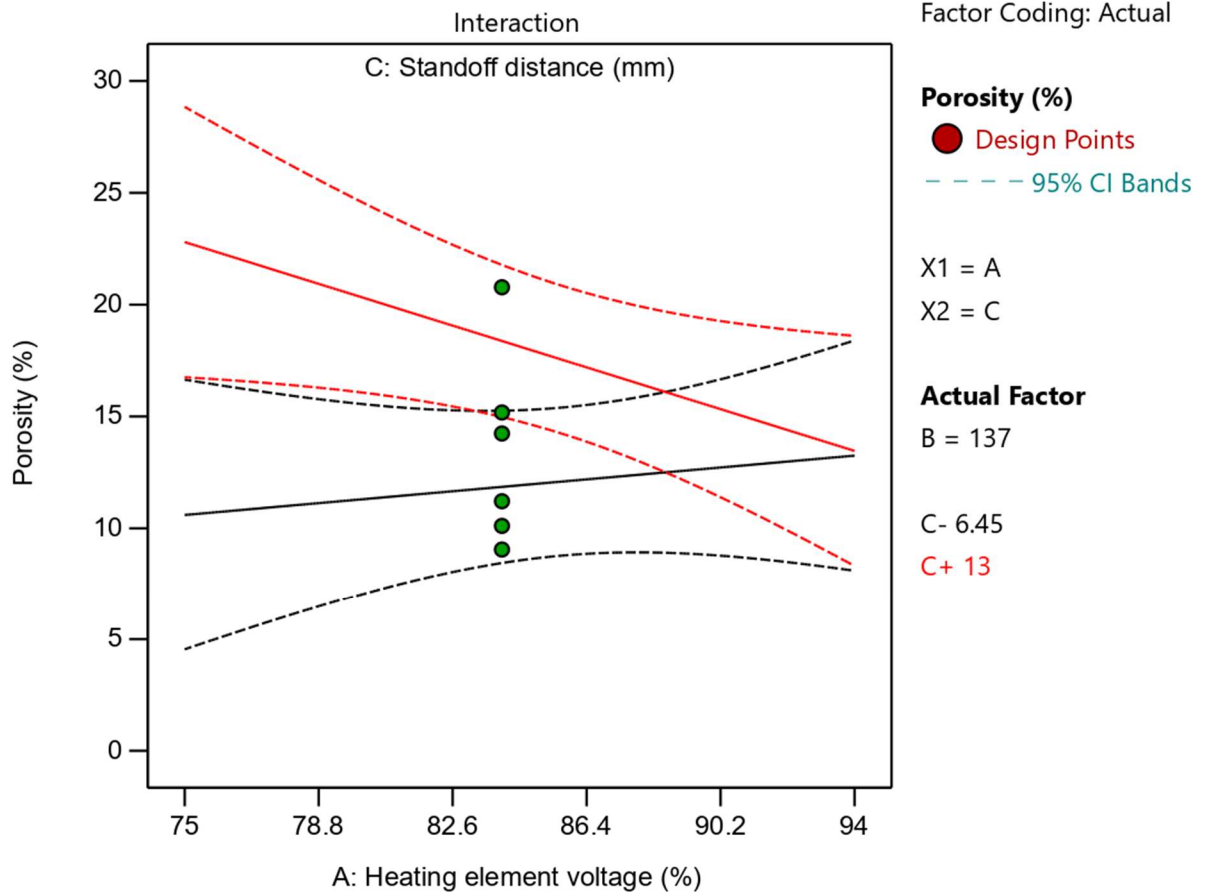


Figure 42: Interaction plot of copper porosity versus heating element voltage at the travel speed midpoint indicating that porosity decreases as heating element voltage is increased for a standoff of 13.0 mm (red) and porosity increases as heating element voltage is increased for a standoff of 6.5 mm (black)

4.6.1.2. Grain Size

Runs 3 and 7 were omitted from the grain size model as analysis of little to no particles would not produce a grain size that is representative of the deposit. **Table IX** shows that the copper deposit grain size data was able to produce a quadratic model with p-value of 0.056, meaning the model is considered not significant and a has lack of fit p-value of 0.496. This p-value does not discard the model because p-values are a measure of statistical confidence. The model had a confidence interval of 0.944. The model had an adjusted R^2 value of 0.33 and a C.V.

of 9.7%. The adequate precision of the model is 5.7 meaning there was a high enough statistical power to differentiate between the signal and noise.

Table IX: Copper grain size ANOVA table at 75% heating element voltage

Source	Sum of Squares	df	Mean Square	F-value	p-value	
Model	1.86	4	0.4654	3.06	0.056	not significant
A - Heating Element Voltage	0.4105	1	0.4105	2.7	0.124	
C - Standoff Distance	0.1116	1	0.1116	0.7342	0.407	
AC	0.9207	1	0.9207	6.06	0.029	
A²	0.6403	1	0.6403	4.21	0.061	
Residual	1.98	13	0.152			
Lack of Fit	1.24	8	0.1556	1.06	0.496	not significant
Pure Error	0.7	5	0.1464			
Std. Dev.	0.4					
Mean	4.0					
C.V.%	9.7					
R²	0.49					
Adjusted R²	0.33					
Adeq Precision	5.7					

Diagnostic graphs were generated based on the modeling. **Figure 43** shows the predicted versus actual plot which shows a comparison between the models predicted values and the actual values in the data set. **Figure 44** shows that the model leveraged runs 16, making those results more important when generating a model. Interestingly, run 16 had the lowest value from the DOE for heating element voltage at 69% and even if the run was outside of reasonable bounds, that does not immediately discard the produced model. Other diagnostic graphs for the models can be seen in Appendix B: Model Diagnostic Graphs

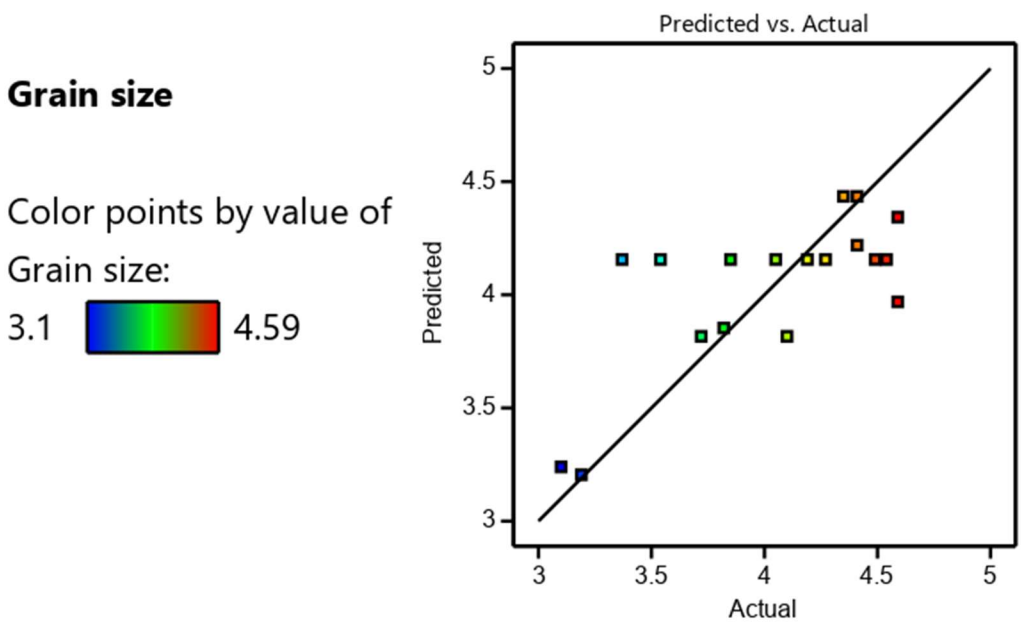


Figure 43: Predicted versus actual plot for the quadratic copper grain size model with the 75% heating element voltage data

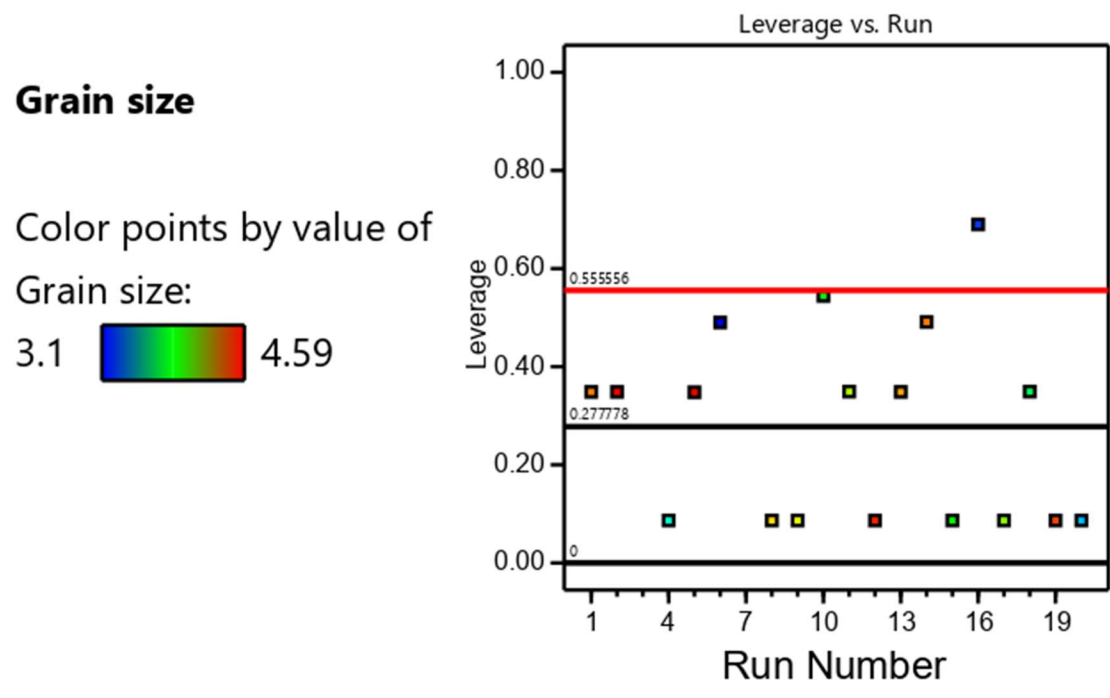


Figure 44: Copper grain size leverage versus Run showing the model leveraging run 16 higher than other runs, with the 75% heating element voltage data

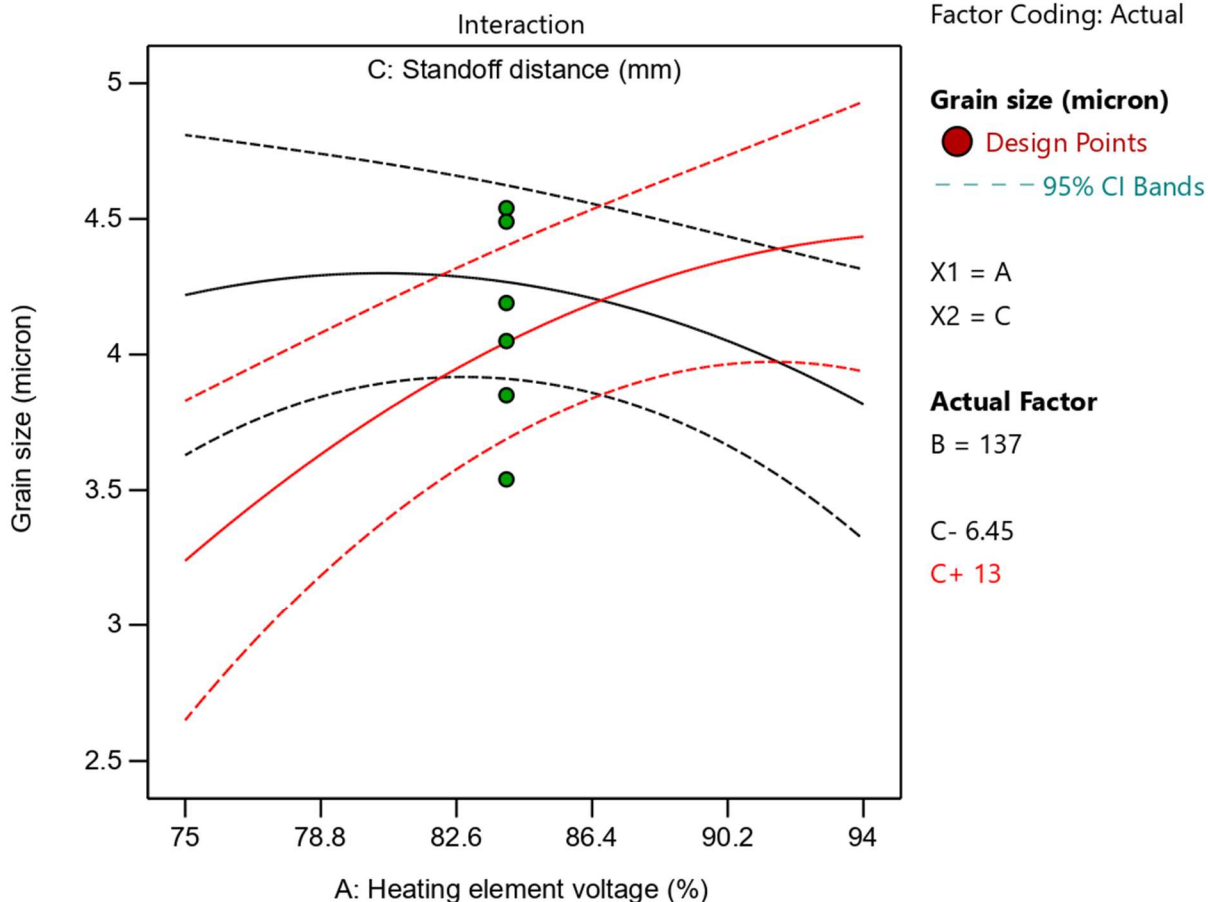


Figure 45: Interaction plot of grain size versus heating element voltage at the travel speed midpoint with the 75% heating element voltage data indicating that grain size increases as heating element voltage is increased for a standoff of 13.0 mm (red) and grain size decreases as heating element voltage is increased for a standoff of 6.5 mm (black)

Figure 45 shows the interaction of heating element voltage on the grain size of a copper CS deposit, varying standoff distance. The model displayed indicates that grain size increased with high heating element voltage at a standoff 13.0 mm (red) and decreased with high heating element voltage at a standoff of 6.5 mm (black). When the 80% heating element voltage was used instead of the 75% heating element voltage, a different model was generated as shown in **Table X**, including travel speed as opposed to standoff distance.

Table X: Copper grain size ANOVA table at 80% heating element voltage

Source	Sum of Squares	df	Mean Square	F-value	p-value	
Model	1.96	3	0.6528	4.09	0.025	significant
A - Heating Element Voltage	0.6372	1	0.6372	4	0.063	
B - Travel Speed	1.05	1	1.05	6.56	0.021	
A²	0.5386	1	0.5386	3.38	0.085	
Residual	2.55	16	0.1594			
Lack of Fit	1.82	11	0.1654	1.13	0.477	not significant
Pure Error	0.7	5	0.1464			
Std. Dev.	0.4					
Mean	4.0					
C.V.%	10.0					
R²	0.43					
Adjusted R²	0.33					
Adeq Precision	7.7					

Table X shows that the copper deposit grain size data was able to produce a quadratic model with p-value of 0.025, meaning the model is significant and a lack of fit p-value of 0.477. The model had an adjusted R² value of 0.33 and a C.V. of 10.0%. The adequate precision of the model is 7.7 meaning there was a high enough statistical power to differentiate between the signal and noise. Diagnostic graphs were generated based on the modeling. **Figure 46** shows the predicted versus actual plot which shows a comparison between the models predicted values and the actual values in the data set. **Figure 47** shows that the model leveraged runs 10 and 16, making those results more important to the model.

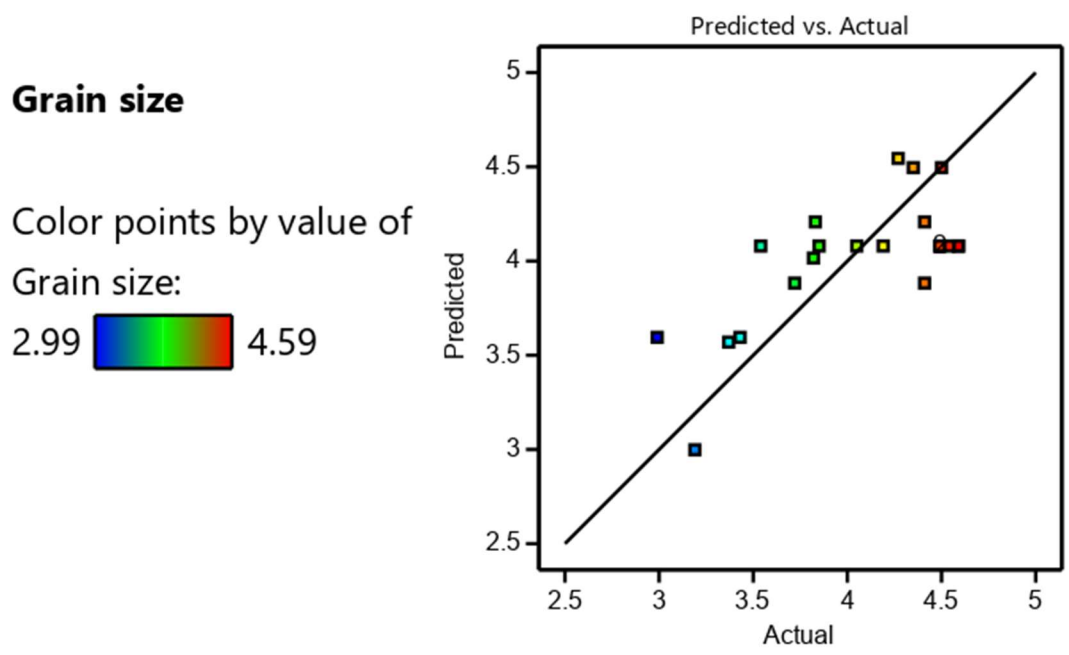


Figure 46: Predicted versus actual plot for the quadratic copper grain size model with the 80% heating element voltage data

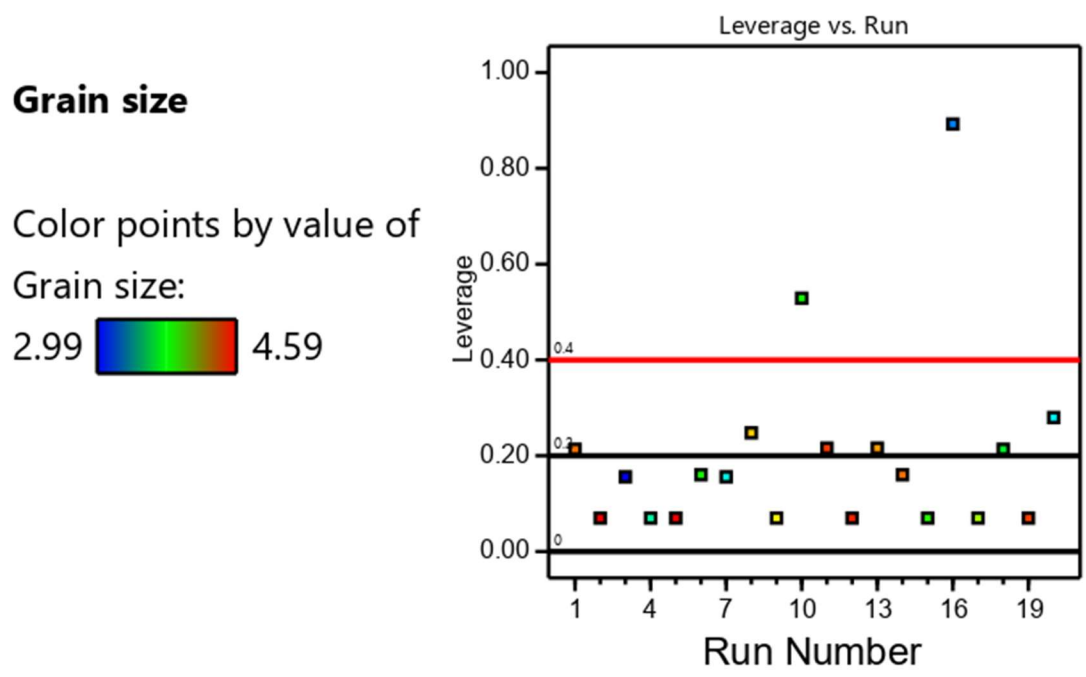


Figure 47: Copper grain size leverage versus Run showing the model leveraging runs 10 and 16 higher than other runs, with the 80% heating element voltage data

Figure 48 shows the interaction of heating element voltage on the grain size of a copper CS deposit, varying standoff distance. The model displayed indicates that grain size increased with high heating element voltage for both travel speeds of 69 mm/min (black) and 206 mm/min (red).

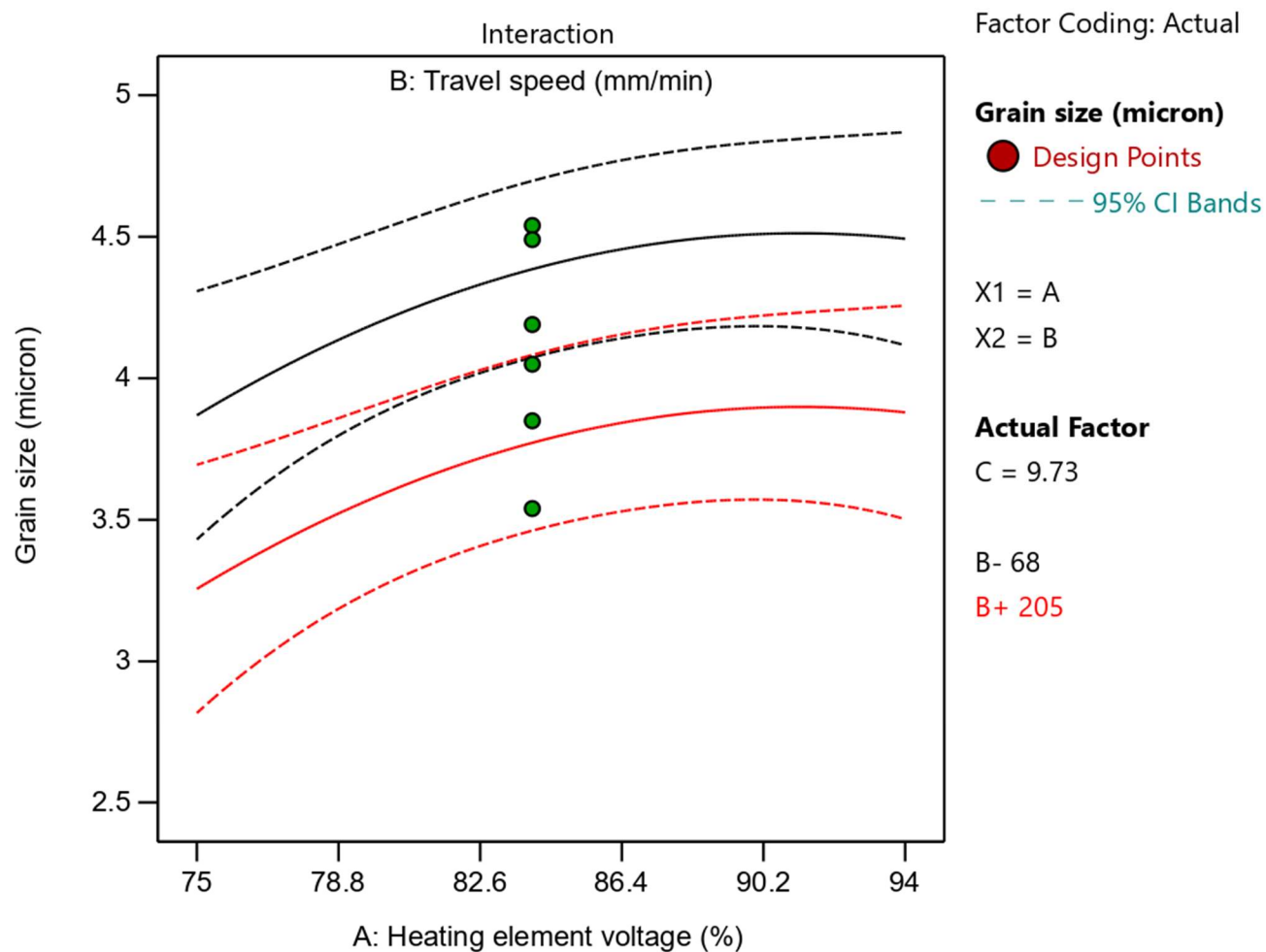


Figure 48: Interaction plot of grain size versus heating element voltage at the travel speed midpoint with the 80% heating element voltage data indicating that grain size increases for both high (206 mm/min, red) and low (69 mm/min, black) travel speeds with low travel speeds producing larger grains as heating element voltage is increased

4.6.1.2.1. Grain Size versus Thickness

For the sufficiently thick copper CS deposits, runs 8, 10, 11, 13, and 14, the grain size was analyzed in several spots getting progressively further away from the substrate to examine if

grain size would change with thicker CS deposits. The results of the grain size analysis can be seen in **Figure 49**. For runs 8, 10, and 13 grain size increased further away from the substrate, however the values from Run 13 only varied by +/-0.01 and did not actually produce a significant trend. The grain sizes of runs 11 and 14 decreased further away from the substrate.

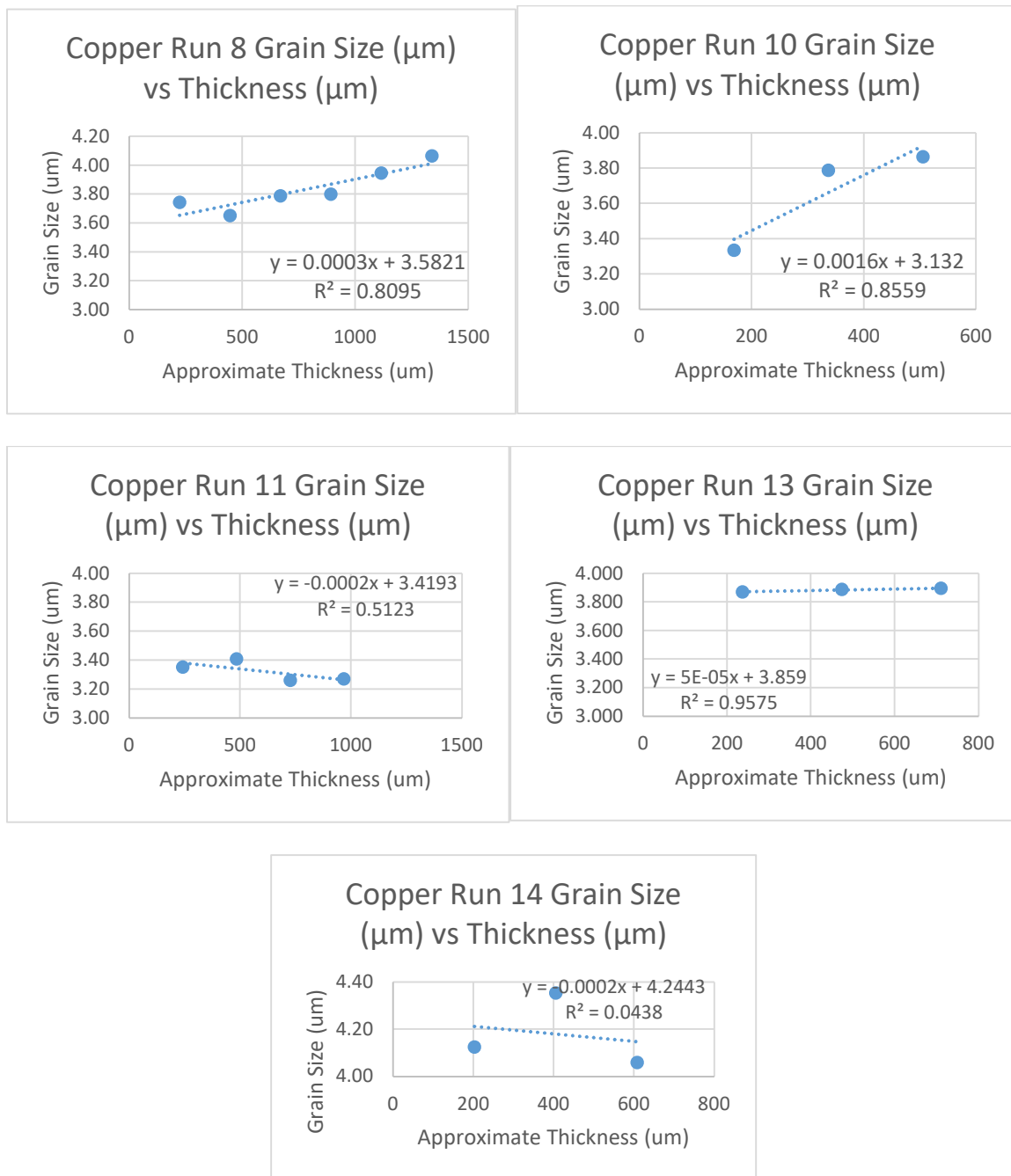


Figure 49: Copper CS grain size versus deposit thickness for runs 8, 10, 11, 13, and 14

4.6.1.2.2. Feret Ratio

As part of the grain size analysis, the Feret diameter and Feret minimum were obtained. The Feret diameter is the longest distance between two points on the edge of a grain and the Feret minimum is the shortest distance between two points on the edge of a grain (**Figure 8**). These values are not sensitive to the inside geometry and a Feret distance may lie outside of the volume of a grain itself. These distances were used to get an approximate understanding of the aspect ratio of a grain by dividing the Feret diameter, longest distance, by the Feret minimum shortest distance. The results were plotted in **Figure 50** which shows that despite changes in grain sizes between samples, the ratio of the longest dimension of a grain by the shortest dimension remained relatively constant for the system at approximately 1.91:1.

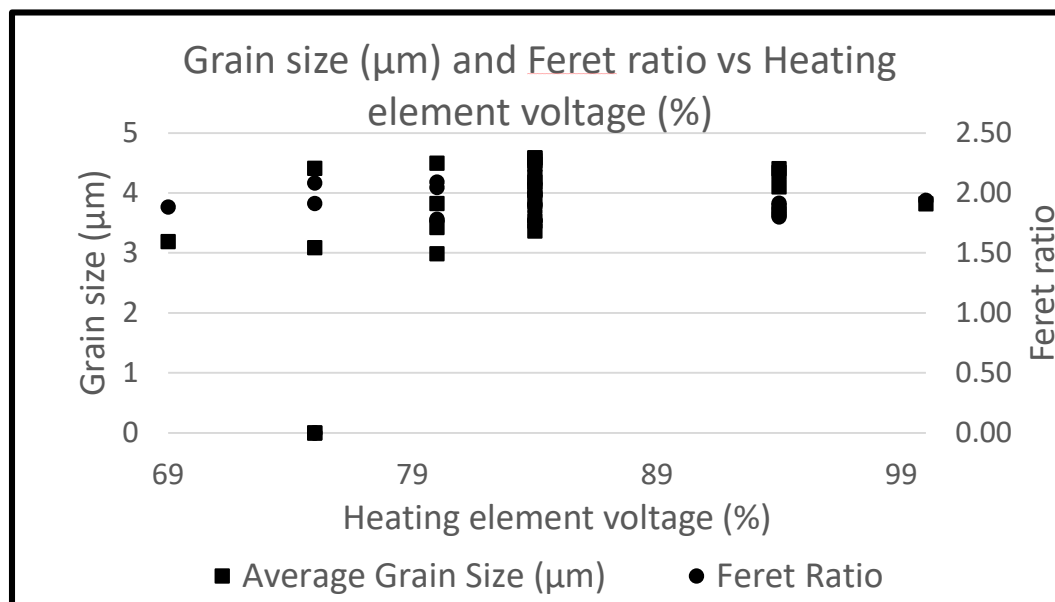


Figure 50: Copper CS Feret ratio and grain gize for 75% heating element voltage data

When considering the data produced from the 80% heating element voltage samples, the average Feret ratio was 1.90:1. The data from the four runs produced at 80% heating element voltage can be seen in **Figure 51**.

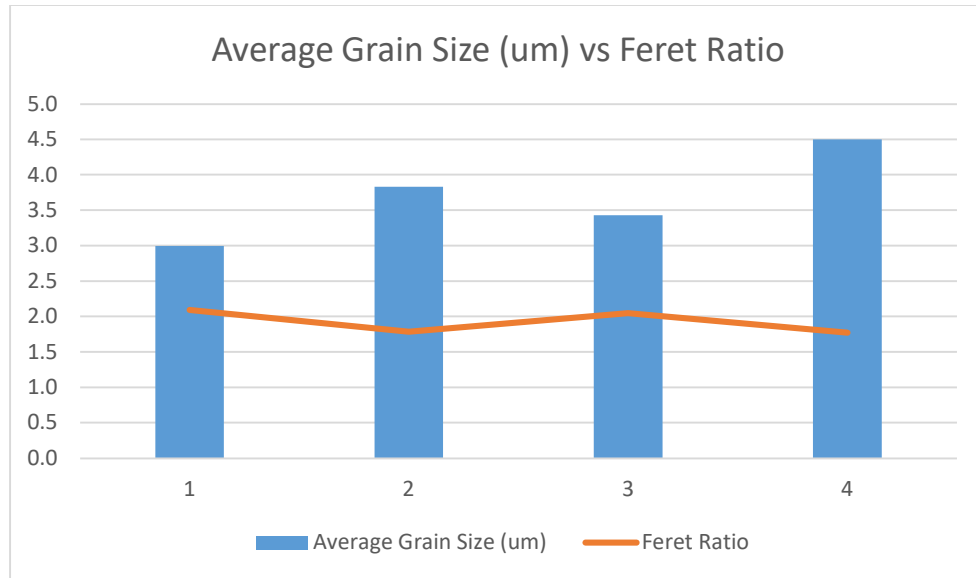


Figure 51: Copper CS Feret ratio and grain size for 80% heating element voltage sample rerun data

4.6.1.3. Microhardness

When the copper microhardness data was input into the design, the model ignored all processing variables as none of them seemed significant in affecting microhardness. Plotting the data (**Figure 52**), a slight increasing trend can be seen but with a large variation between midpoint heating element voltage runs. A change in microhardness was tested for the sufficiently thick samples and those results can be seen in **Figure 53**. As per ASTM standard E92, microhardness testing with 100 gf or less produces a 3% error between measurements. For Run 8, the error between values produced little to no trend in the microhardness moving away from the substrate. Runs 10 and 14 both showed trends of microhardness getting lower, moving away from the substrate. Runs 11, 13, and 14 with 80% heating element voltage, all trended with microhardness increasing, moving away from the substrate.

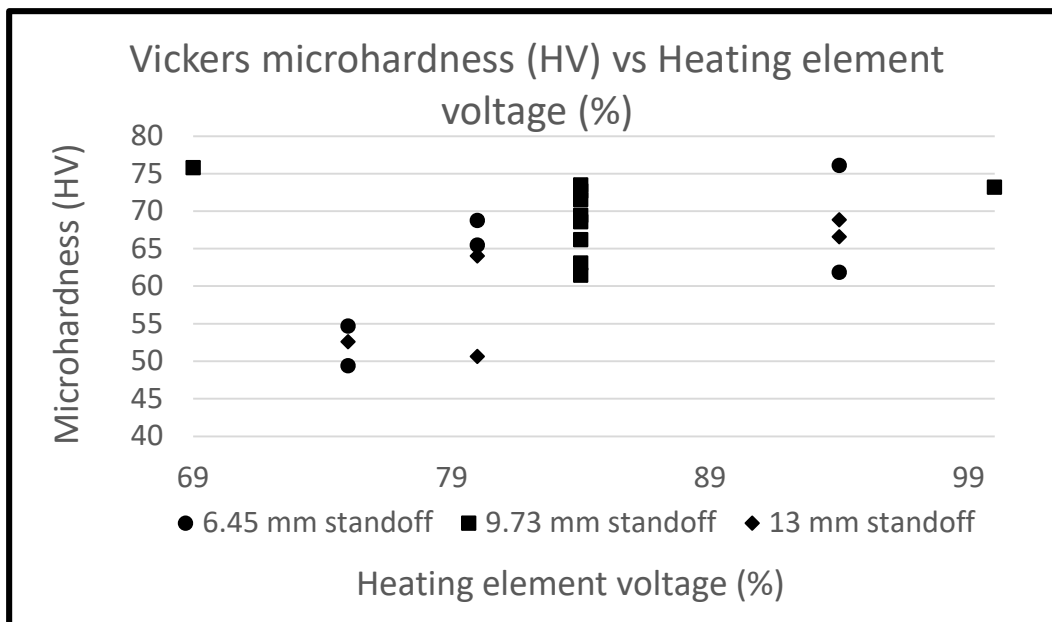


Figure 52: Copper CS graph plotting Vickers microhardness (HV) versus Heating element voltage (%)

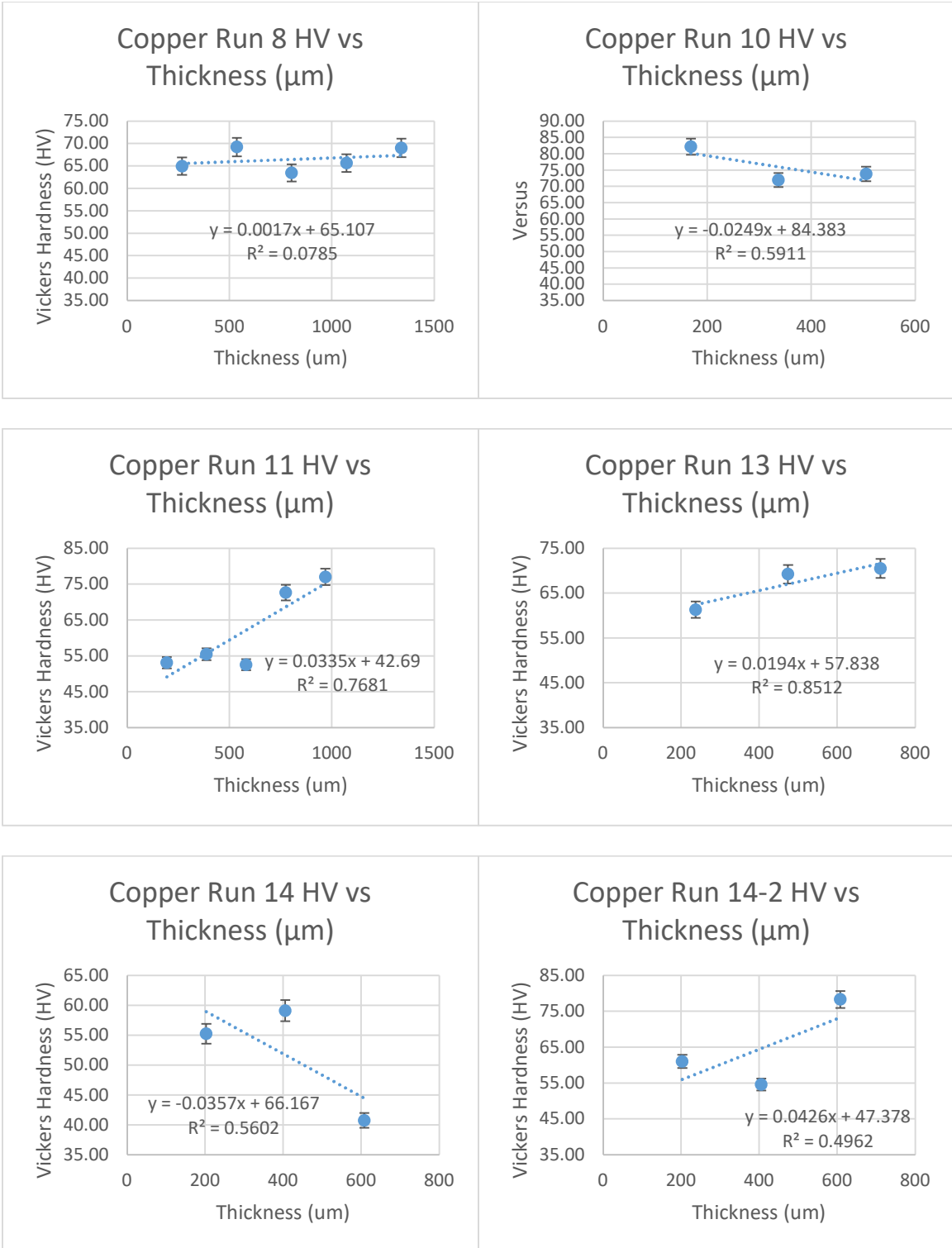


Figure 53: Copper microhardness versus thickness of the deposit

4.6.1.4. Thickness

As shown in **Table XI** and **Table XII**, both lower heating element voltage settings, 75% and 80%, produced significant deposit thickness models. For both models, standoff distance had significant quadratic effects despite the linear effect of standoff distance not being significant (p-values of 0.17 for 75% heating element voltage and 0.53 for 80% heating element voltage). Both models required the use of a logarithmic transform to the data set to produce a significant model. The 75% heating element voltage model had an adjusted R^2 value of 0.88 and a C.V. of 6%. The 80% heating element voltage model had an adjusted R^2 value of 0.91 and a C.V. of 4%. The adequate precision of the 75% heating element voltage model was 18 and for the 80% heating element voltage was 21, meaning there was a high enough statistical power to differentiate between the signal and noise.

Table XI: Copper deposit thickness ANOVA table with 75% heating element voltage

Source	Sum of Squares	df	Mean Square	F-value	p-value	
Model	13.64	5	2.73	27.72	<0.001	significant
A - Heating Element Voltage	3.88	1	3.88	39.47	<0.001	
B - Travel Speed	8.39	1	8.39	85.24	<0.001	
C - Standoff Distance	0.2064	1	0.2064	2.1	0.170	
B²	0.4758	1	0.4758	4.84	0.045	
C²	0.9568	1	0.9568	9.72	0.008	
Residuals	1.38	14	0.0984			
Lack of Fit	0.9531	9	0.1059	1.25	0.424	not significant
Pure Error	0.4244	5	0.0849			
Std. Dev.	0.3					
Mean	6					
C.V.%	6					
R²	0.91					
Adjusted R²	0.88					
Adeq Precision	18					

Table XII: Copper deposit thickness ANOVA table with 80% heating element voltage

Source	Sum of Squares	df	Mean Square	F-value	p-value	
Model	9.87	5	1.97	41.32	<0.001	significant
A - Heating Element Voltage	2.13	1	2.13	44.64	<0.001	
B - Travel Speed	6.82	1	6.82	142.73	<0.001	
C - Standoff Distance	0.0197	1	0.0197	0.412	0.531	
B²	0.6194	1	0.6194	12.96	0.003	
C²	0.75	1	0.75	15.7	0.001	
Residuals	0.6689	14	0.0478			
Lack of Fit	0.2444	9	0.0272	0.3199	0.934	not significant
Pure Error	0.4244	5	0.0849			
STd. Dev.	0.2					
Mean	6					
C.V.%	4					
R²	0.94					
Adjusted R²	0.91					
Adeq Precision	21					

Diagnostic graphs were generated based on the modeling. **Figure 55** shows the predicted versus actual plot which shows a comparison between the models predicted values and the actual values in the data set. **Figure 56** shows that the model is not leveraging any run outside of reasonable bounds. **Figure 57** shows the interaction between deposit thickness and travel speed at 84% voltage to the heating element. The deposit thickness decreased with faster travel speeds and increased with slower travel speeds for both standoff distances of 6.5 mm and 13.0 mm. The interaction data also suggest that a standoff distance of 6.5 mm produced thicker deposits at slower travel speeds than a standoff distance of 13.0 mm. **Figure 54** shows an graph of the thickness data versus heating element voltage. A trend can be seen where thickness increases as heating element voltage increases which is like the interaction plot in **Figure 62**.

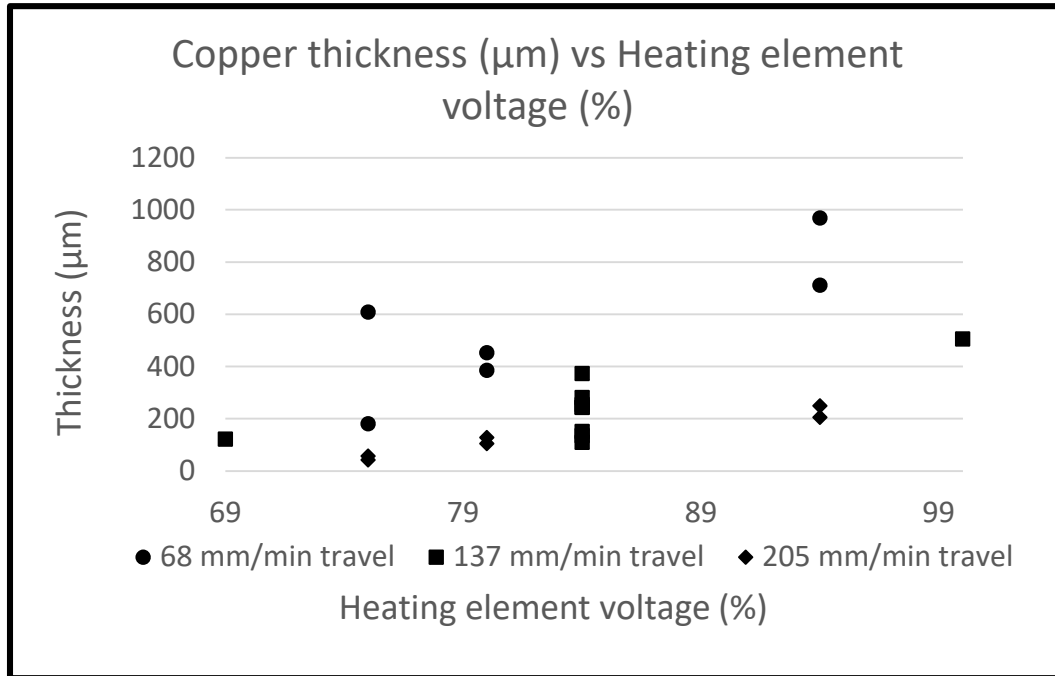


Figure 54: Copper graph plotting Thickness (μm) versus Heating element voltage (%) showing an increase in thickness as heating element voltage increases

Figure 58 is a 3D response surface of deposit thickness showing the effect of heating element voltage and travel speed with the middle standoff setting. The response surface indicates that 75% heating element voltage and a travel speed of 206 mm/min produced the thinnest deposits while 94% heating element voltage and a travel speed of 69 mm/min produced the thickest deposits. Other diagnostic graphs for the models can be seen in Appendix B: Model Diagnostic Graphs.

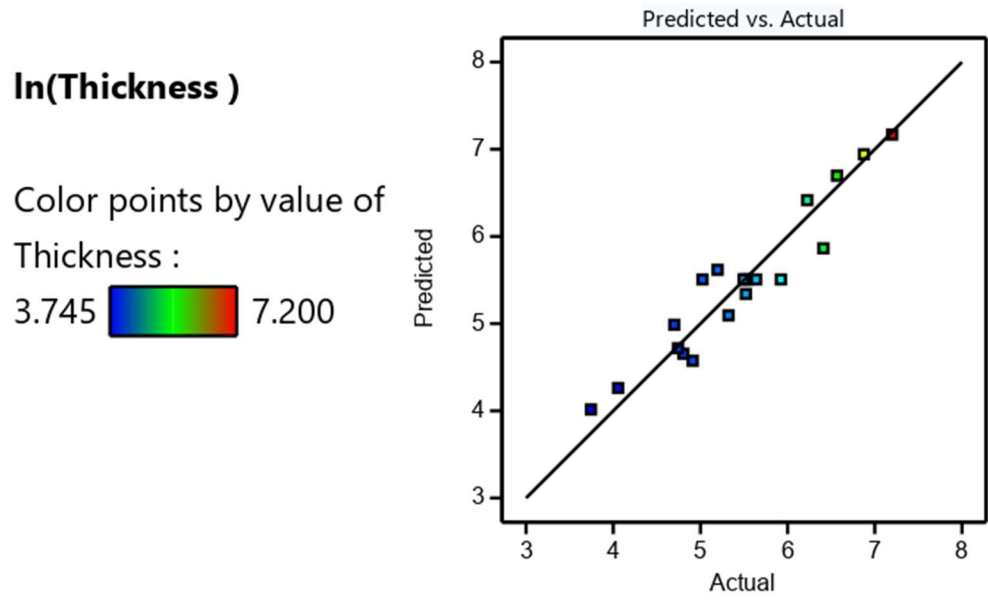


Figure 55: Predicted versus actual plot for the copper deposit thickness with the 75% heating element voltage data

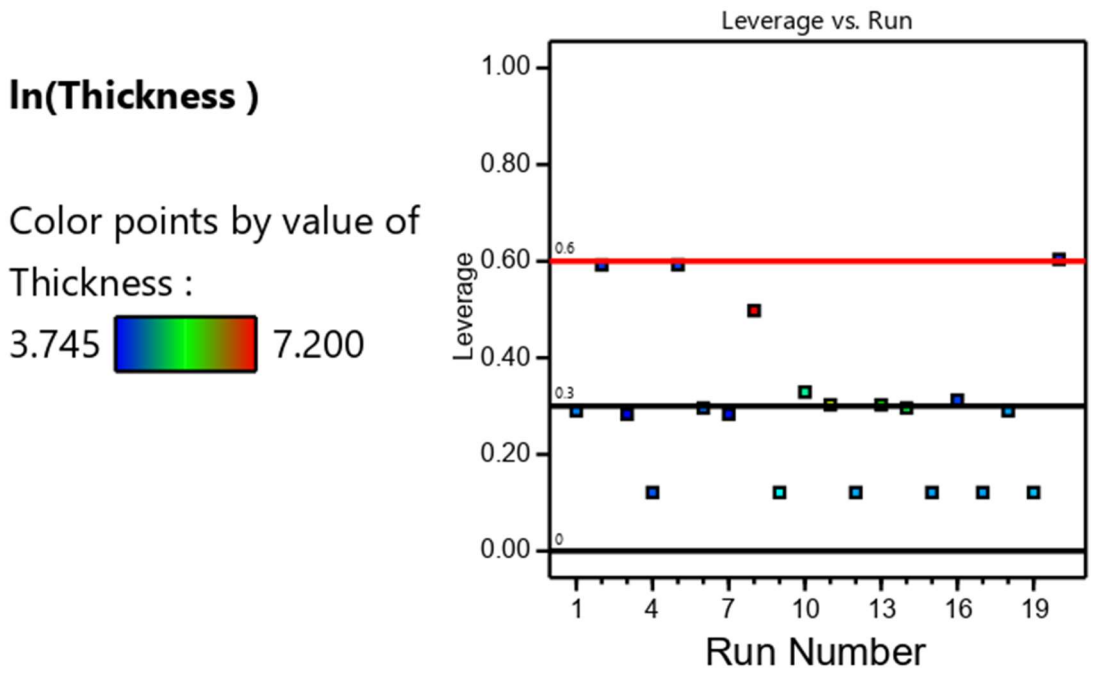


Figure 56: Copper thickness leverage versus Run showing the model leveraging runs, with the 75% heating element voltage data

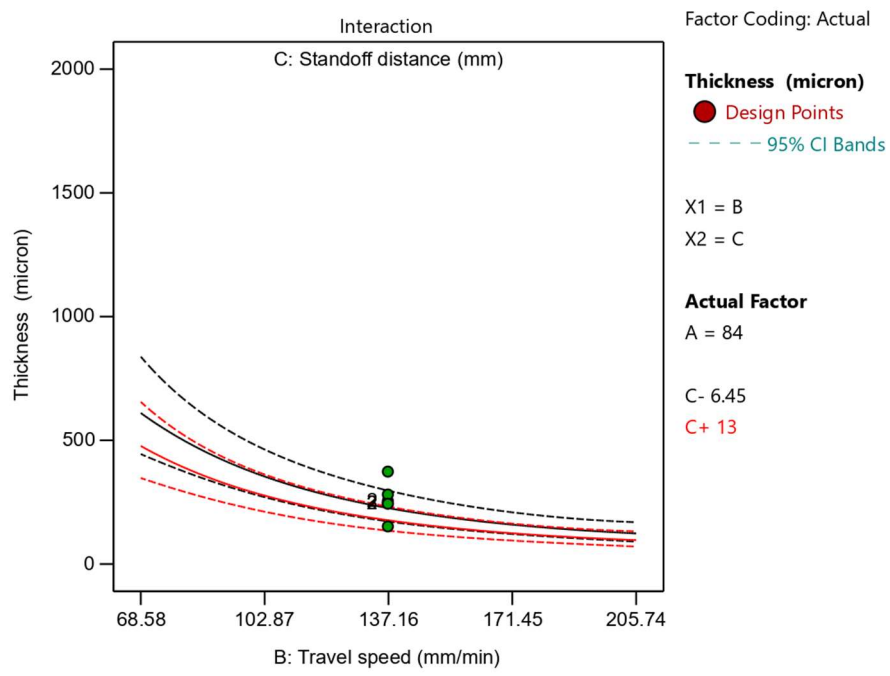


Figure 57: Interaction plot of copper thickness versus travel speed at the heating element midpoint with the 75% heating element voltage data indicating that thickness decreases for both high (13.0 mm, red) and low (6.5 mm, black) standoff distances as heating element voltage is increased

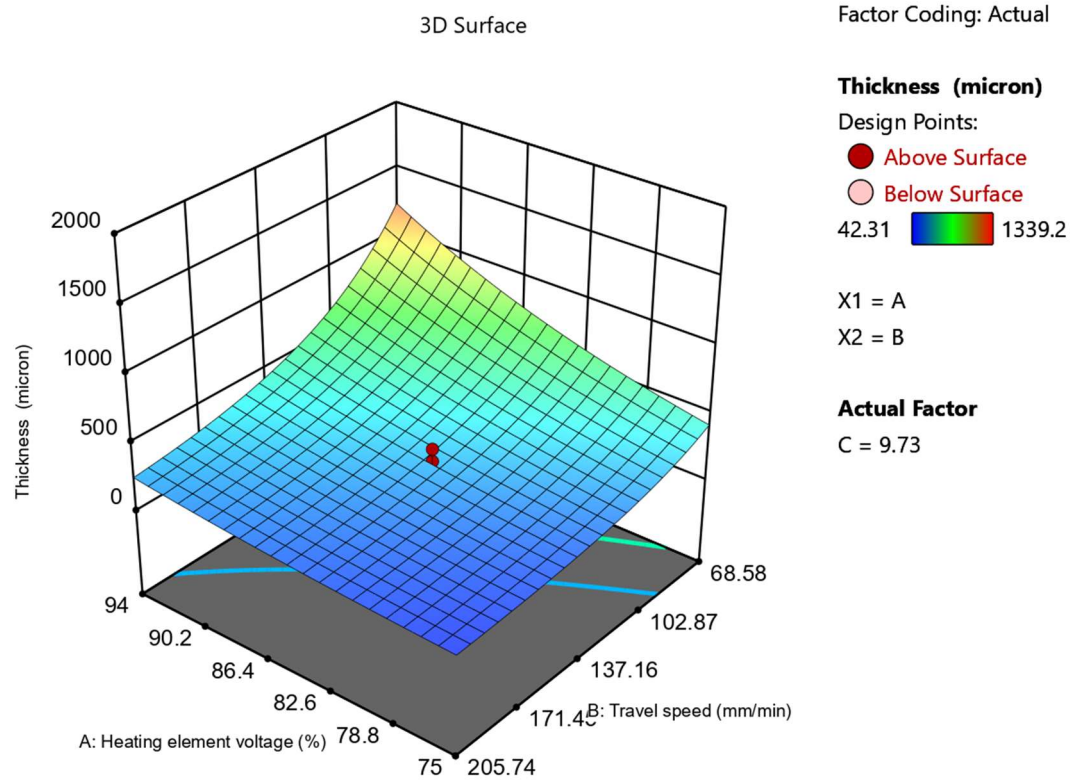


Figure 58: Copper deposit thickness 3D response surface with the 75% heating element voltage data showing that the thickest deposits can be created at slow travel speed (69 mm/min) and high heating element voltage (94%)

Figure 59 shows the predicted versus actual plot which shows a comparison between the models predicted values and the actual values in the data set. **Figure 60** indicates that the model is leveraging runs 2, 5, and 20 to the upper limit of reasonable bounds. **Figure 61** shows the interaction between travel speed and heating element voltage with the midpoint standoff distance. The interaction data suggest that for either standoff distance 6.5 mm or 13.0 mm, deposit thickness increased as the heating element voltage increased. The interaction plot between heating element voltage and travel speed with midpoint standoff distance (**Figure 62**) indicates that for either travel speed, 69 mm/min or 206 mm/min, deposit thickness increased as heating element voltage increases. The plot also shows that slower travel speeds increased deposit thickness much more than faster travel speeds. Travel speed and heating element voltage effects can also be seen in the 3D response surface in **Figure 63**. In **Figure 64**, the interaction of travel speed and standoff distance with the midpoint heating element voltage shows that increasing travel speed, for either standoff distance setting, decreased the deposit thickness.

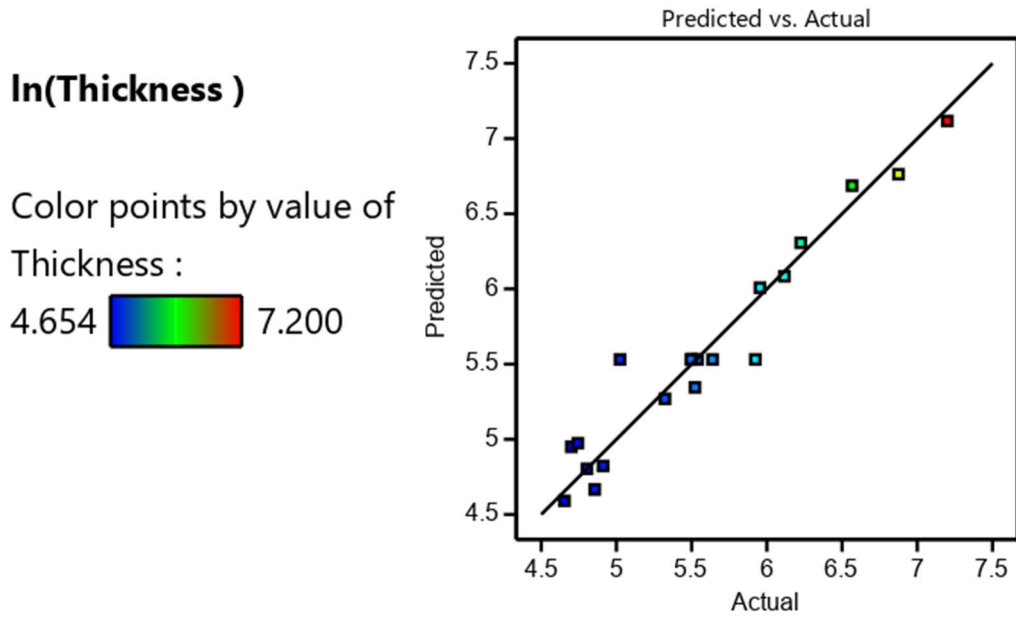


Figure 59: Predicted versus actual plot for the copper deposit thickness with the 80% heating element voltage data

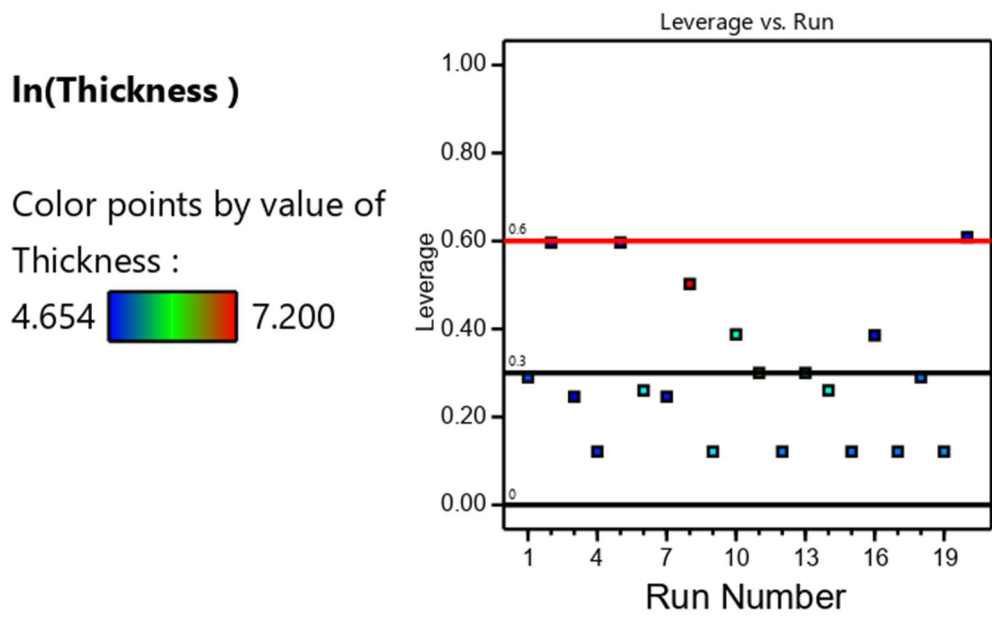


Figure 60: Copper thickness leverage versus Run showing the model leveraging runs, with the 80% heating element voltage data

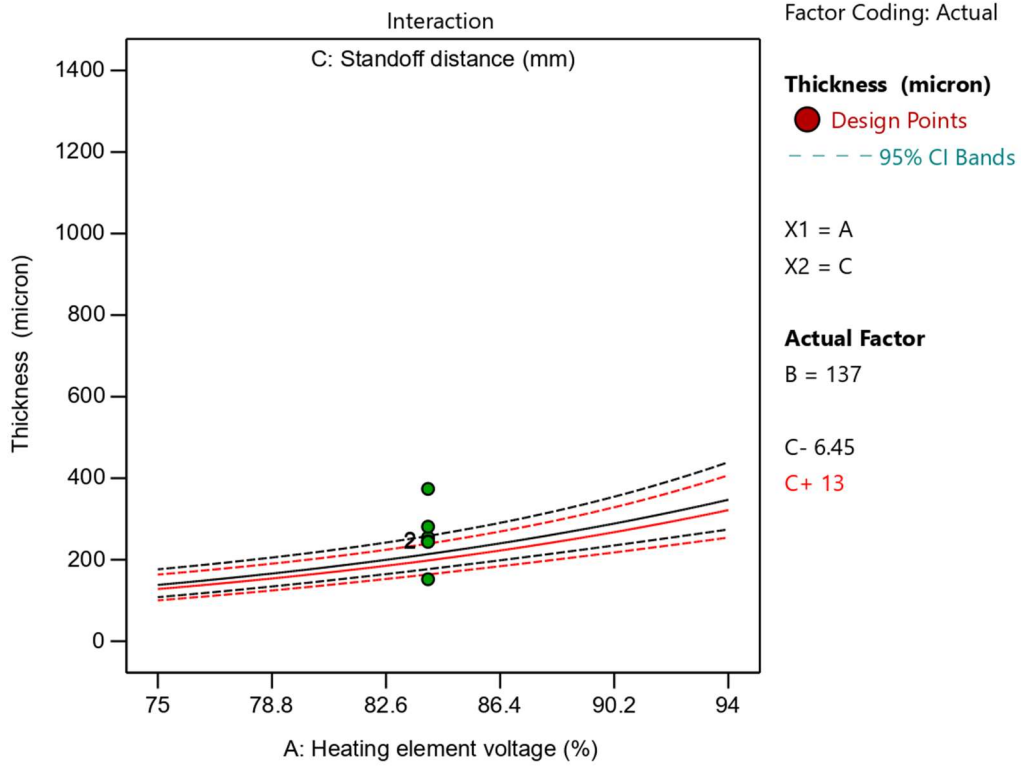


Figure 61: Interaction plot of copper thickness versus travel speed at the heating element midpoint with the 80% heating element voltage data indicating that thickness increases for both high (13.0 mm, red) and low (6.5 mm, black) standoff distances and heating element voltage is increased

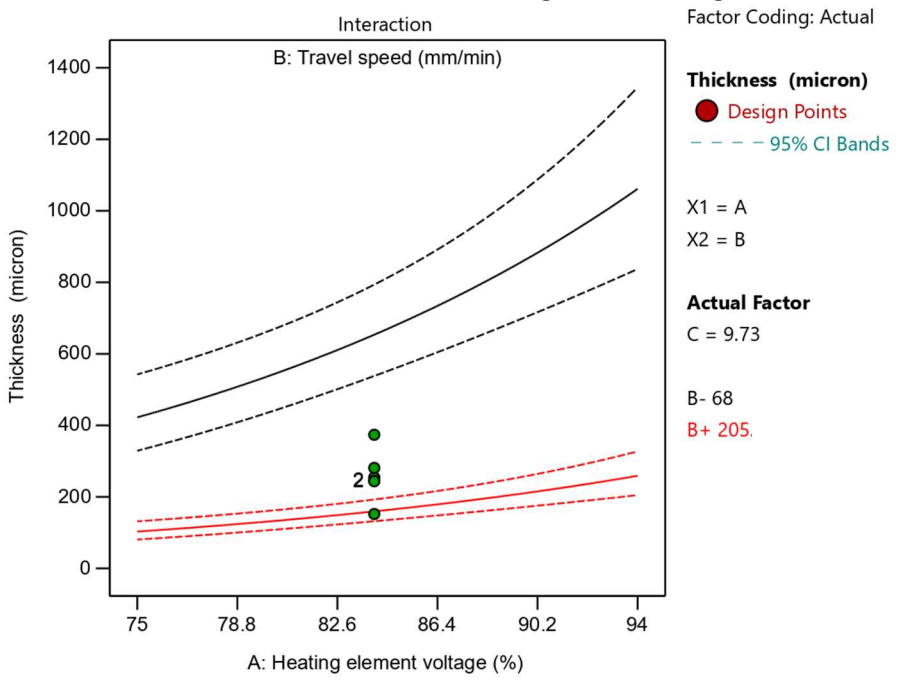


Figure 62: Interaction plot of thickness versus heating element voltage at the standoff distance midpoint with the 80% heating element voltage data indicating that thickness increases for both high (206 mm/min, red) and low (69 mm/min, black) travel speeds and that low travel speeds create the thicker deposits as heating element voltage is increased

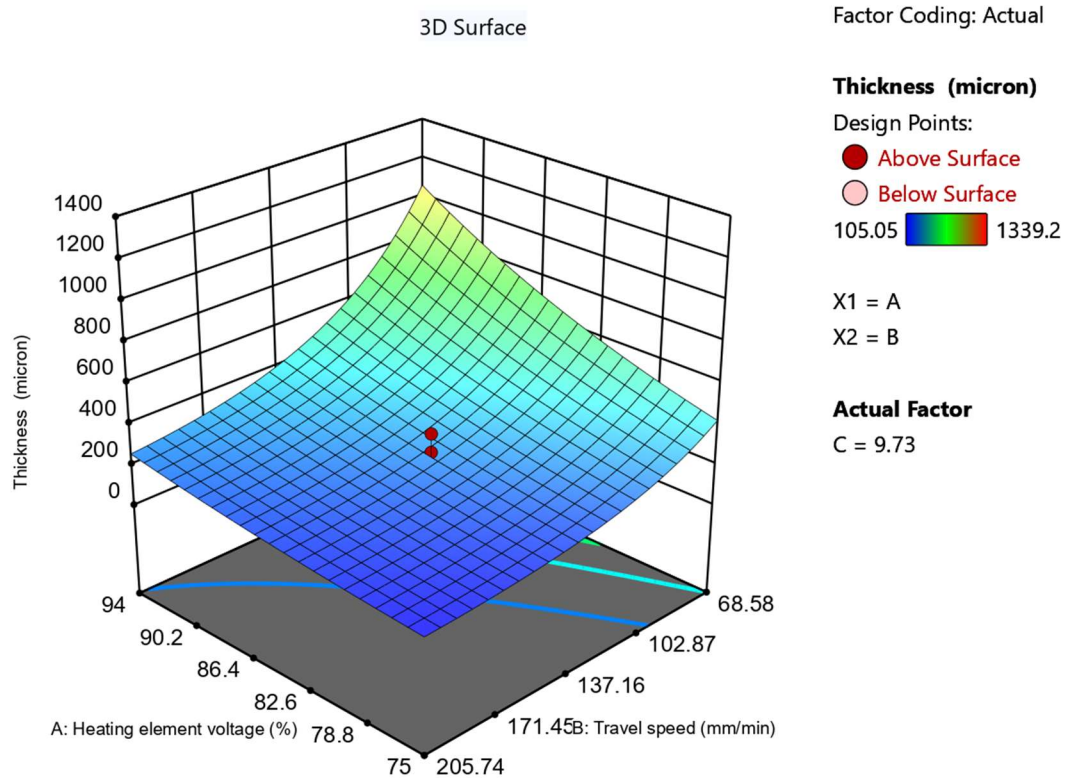


Figure 63: 3D Response surface of thickness showing heating element voltage versus travel speed at the standoff distance midpoint with the 80% heating element voltage data showing that the thickest deposits can be created at slow travel speed (69 mm/min) and high heating element voltage (94%)

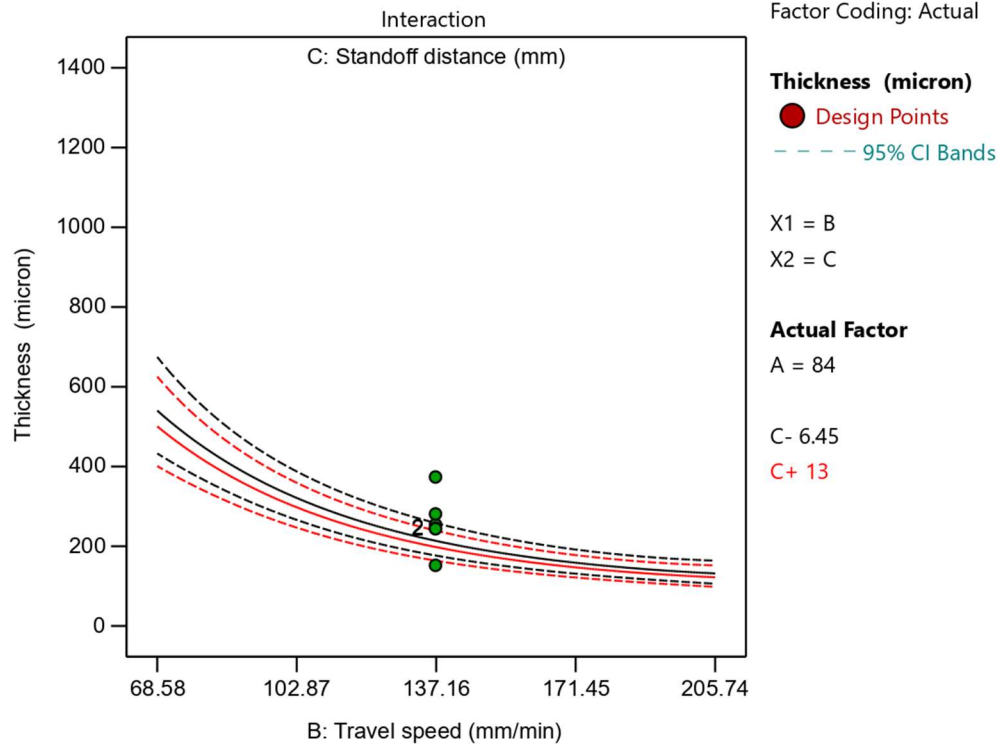


Figure 64: Interaction plot of thickness versus travel speed at the heating element voltage midpoint with the 80% heating element voltage data indicating that thickness decreases for both high (13.0 mm, red) and low (6.5 mm, black) standoff distances as heating element voltage is increased

4.6.1.5. Copper Validation

Two copper samples were produced at settings contained within the design. Validation sample 1 was made at 90% heating element voltage, 151 mm/min travel speed, and 11.2 mm standoff distance. Validation sample 2 was made at 81% heating element voltage, 101 mm/min travel speed, and 8.0 mm standoff distance. Porosity, grain size, thickness, and microhardness data were obtained for these samples to validate the produced models. **Table XIII** shows the validation data for the copper models produced with 75% heating element voltage. **Table XIV** shows the validation data for the copper models produced with 80% heating element voltage.

Table XIII: Copper CS validation statistics with 75% heating element voltage

	Response	Std Dev	95% PI low	Data Mean	95% PI high
Val. 1	Porosity (%)	4.1	6.0	7.1	24.1
	Microhardness (HV)	7.2	48.8	80.0	80.0
	Thickness (µm)	96	139	203	577
	Grain Size (µm)	0.4	3.2	3.0	5.0
Val. 2					
	Porosity (%)	4.1	6.0	14.7	24.1
	Microhardness (HV)	7.2	48.8	71.4	80.0
	Thickness (um)	96	139	194	577
	Grain Size (um)	0.4	3.3	3.6	5.0

Table XIV: Copper CS validation statistics with 80% heating element voltage

	Response	Std Dev	95% PI low	Data Mean	95% PI high
Val. 1	Porosity (%)	3.7	5.2	7.1	21.5
	Microhardness (HV)	7.7	48.5	80.0	82.4
	Thickness (µm)	62	166	203	453
	Grain Size (µm)	0.4	3.2	3.0	5.0
Val. 2					
	Porosity (%)	3.7	6.7	14.7	22.9
	Microhardness (HV)	7.7	46.6	71.4	80.9
	Thickness (µm)	73	195	194	528
	Grain Size (µm)	0.4	3.2	3.6	5.0

4.6.2. Zinc

4.6.2.1. Porosity

Table XV shows the statistical ANOVA results for the natural log model of zinc porosity. The model is significant and has a p-value of 0.001 and a lack of fit of 0.337. The model considered heating element voltage and travel speed significant as well as the quadratic effect of travel speed but did not consider standoff distance significant. The model had an adjusted R² value of 0.55 and a C.V. of 34.5%. The adequate precision of the model is 10.2 meaning there was a high enough statistical power to differentiate between the signal and noise.

Table XV: Zinc porosity ANOVA table

Source	Sum of Squares	df	Mean Square	F-value	p-value	
Model	3.99	3	1.133	8.75	0.001	significant
A - Heating Element Voltage	1.19	1	1.19	7.85	0.013	
B - Travel Speed	2.31	1	2.31	15.21	0.001	
B²	1.4	1	1.4	9.23	0.008	
Residual	2.43	16	0.1521			
Lack of Fit	1.87	11	0.1704	1.33	0.337	not significant
Pure Error	0.6	5	0.1119			
STd. Dev.	0.4					
Mean	1.1					
C.V.%	34.5					
R²	0.62					
Adjusted R²	0.55					
Adeq Precision	10.2					

Diagnostic graphs were generated based on the modeling and **Figure 66** shows the predicted versus actual plot which shows a comparison between the models predicted values and the actual values in the data set. **Figure 67** shows the leveraging of the model and indicates runs 8 and 20 were leveraged more in the creation of the model. Although these runs were outside of reasonable bounds, the produced model was not immediately discarded. Other diagnostic graphs for the models can be seen in Appendix B: Model Diagnostic Graphs. **Figure 65** shows a graph of the data and there is downward trend in data as heating element voltage increases like the interaction plot in **Figure 68**.

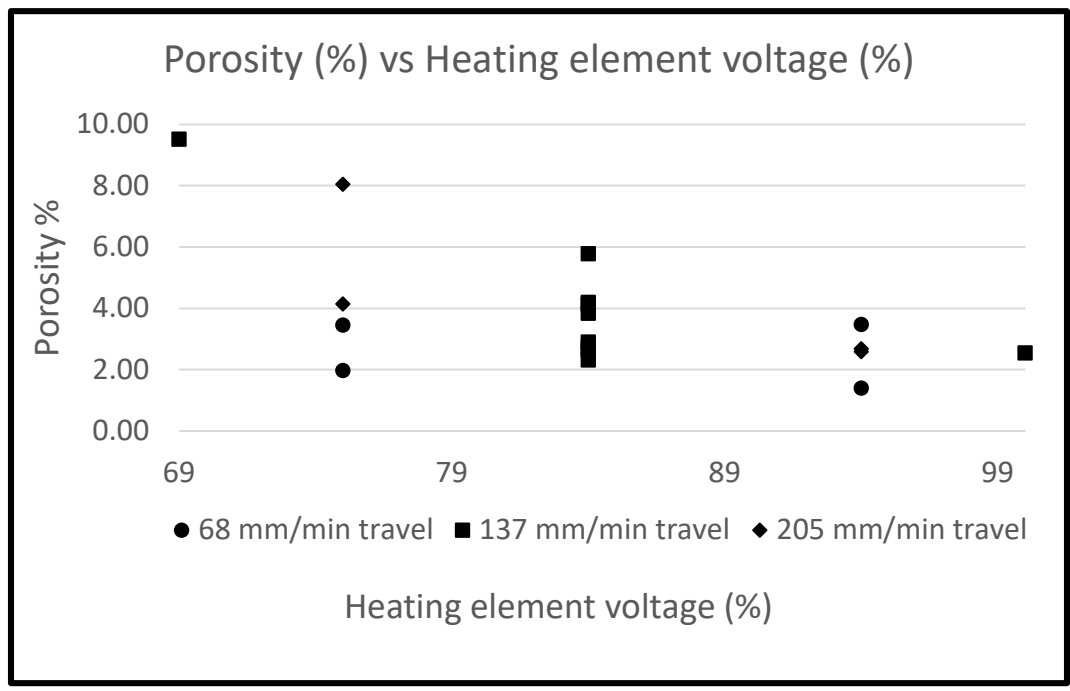


Figure 65: Zinc graph plotting Porosity (%) versus Heating element voltage (%)

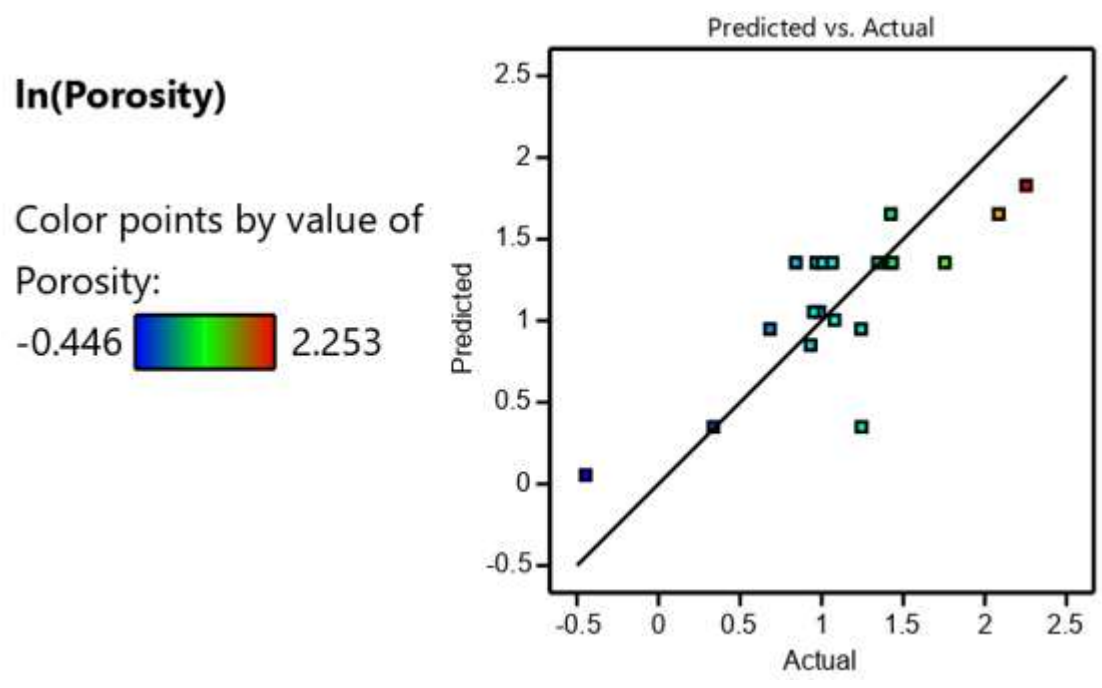


Figure 66: Predicted versus actual plot for the zinc porosity model

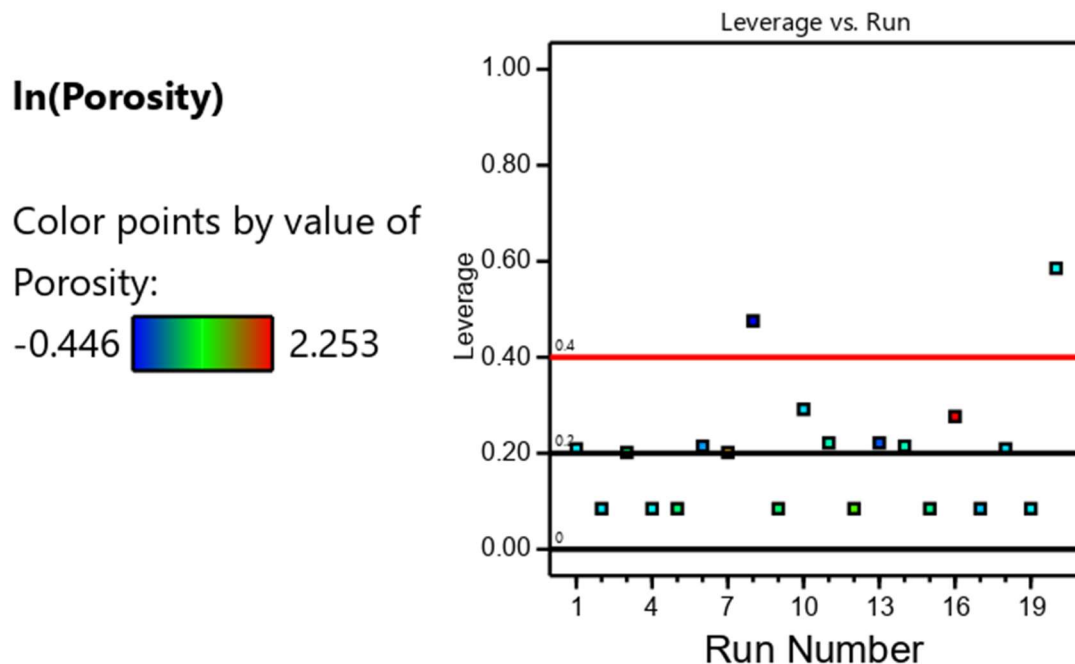


Figure 67: Zinc porosity model Leverage versus Run that shows the model leveraging runs 8, and 20 higher than the other runs

Figure 68 shows the resulting interaction plot from the natural logarithm zinc porosity model. The plot shows heating element voltage effect on deposit porosity at a midpoint standoff distance and varied travel speed of 69 mm/min and 206 mm/min, respectively, and suggests that porosity decreased with increasing heating element voltage for both travel speeds. The slower travel speed produced less porous deposits compared to the higher travel speed. This behavior can also be observed in Figure 69, where the 3D response graph shows how porosity is affected by heating element voltage versus travel speed.

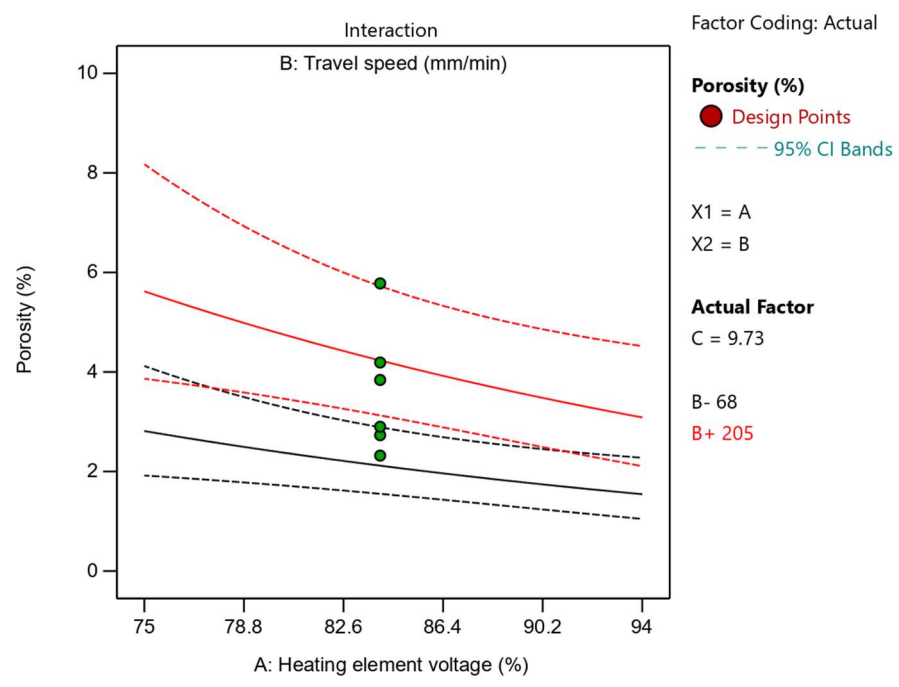


Figure 68: Interaction plot of zinc porosity versus heating element voltage at the standoff distance midpoint indicating that porosity decreases for both high (206 mm/min, red) and low (69 mm/min) travel speeds as heating element voltage is increased

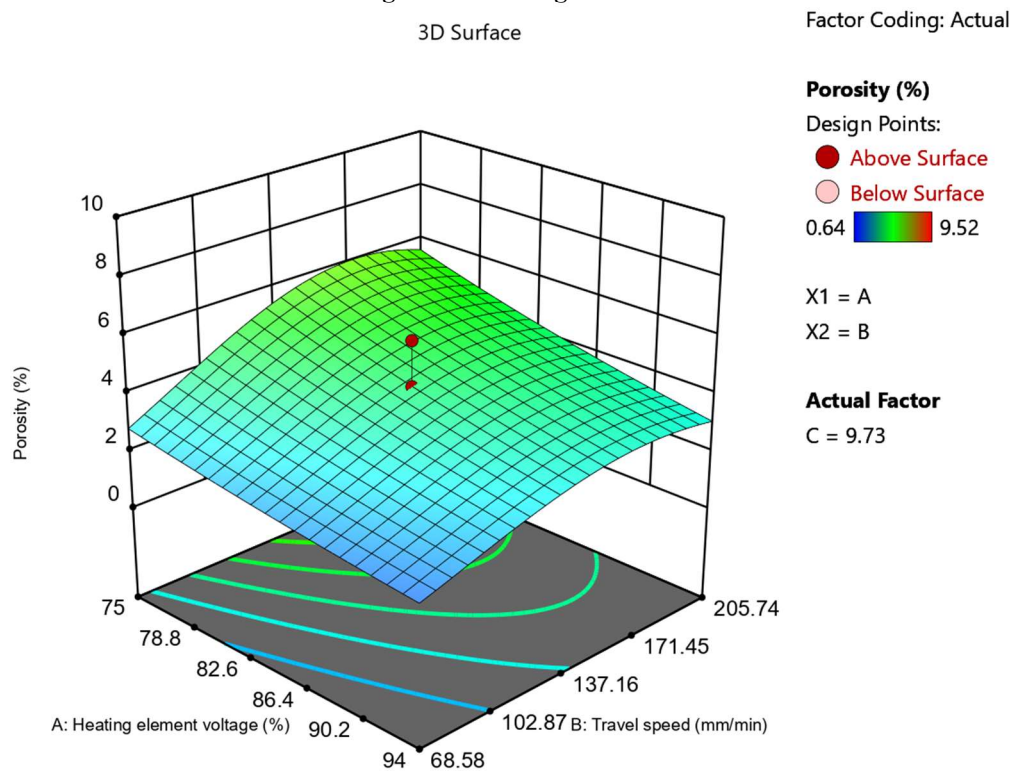


Figure 69: Zinc deposit porosity 3D response surface showing that lowest porosity can be created at slow travel speed (69 mm/min) and high heating element voltage (94%)

The model was then used to determine the parameters that would produce a deposit of minimum porosity. The results of this optimization are shown in **Figure 70**, where heating element voltage is 94%, travel speed is 69 mm/min, with a standoff distance of 9.7 mm, would potentially result in a zinc deposit porosity of 1.4%.

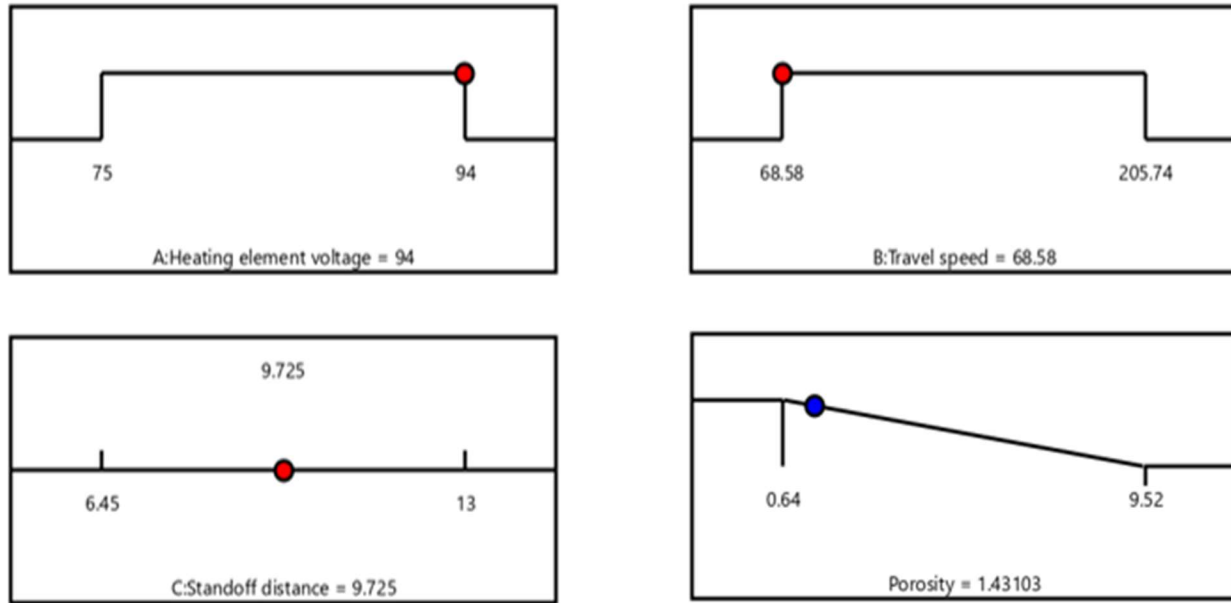


Figure 70: Zinc porosity model optimized for a minimal porosity of 1.4% suggesting operating at high heating element voltage (94%), low travel speed (69 mm/min), and a standoff distance of 9.7 mm

4.6.2.2. Grain Size and Microhardness

For the zinc CS deposits, both the grain size and microhardness data could not be modeled with the tested processing parameters as the statistical analysis performed by the Design-Expert software excluded all the processing parameters from modeling. The average zinc grain in a deposit was 6.0 μm in size. The Feret ratio of the grains could still be examined despite the lack of a trend within the data set itself.

4.6.2.2.1. Feret Ratio

The ratio of the Feret diameter to the Feret minimum for the zinc grains was 1.92:1 on average, which stayed consistent across multiple grains and grain sizes (**Figure 71**).

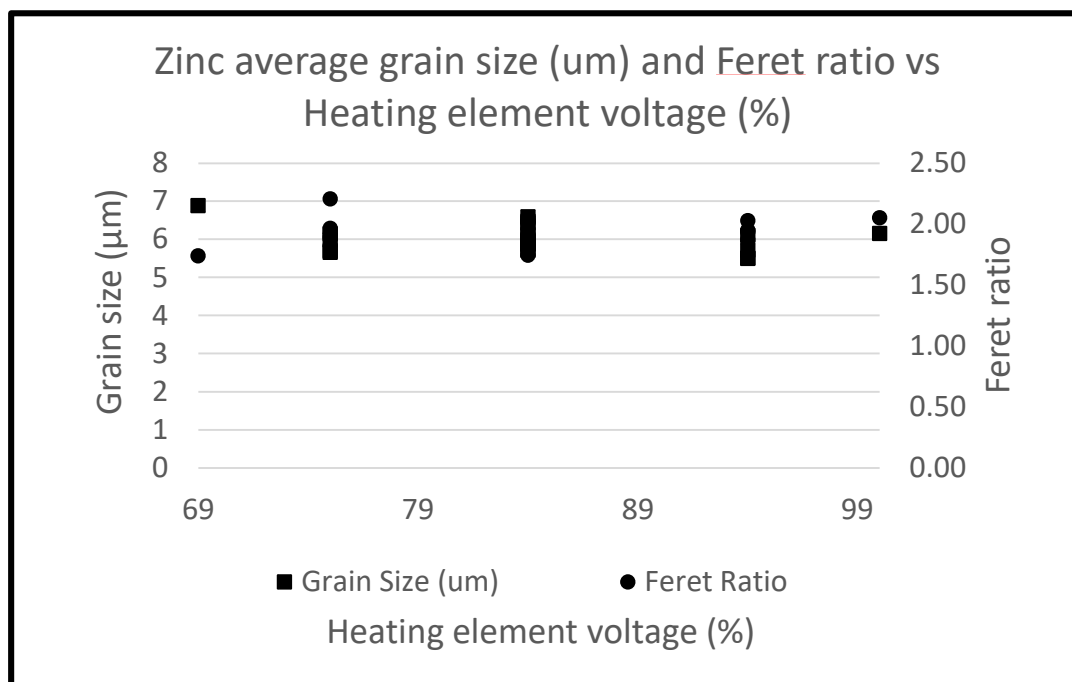


Figure 71: Zinc graph plotting Feret ratio and grain size versus heating element voltage

4.6.2.2.2. Microhardness versus Thickness

Similarly, to the copper CS deposits, the same runs produced thicker deposits which had their microhardness measured across the thickness of the deposit, progressively getting further away from the substrate. There was no observed trend in any of the runs that were analyzed. When taking the error inherent in the microhardness testing, 3% (Herrmann, 2011), the tests were consistent with one another as subsequent tests laid within the bounds of the error (**Figure 72**).

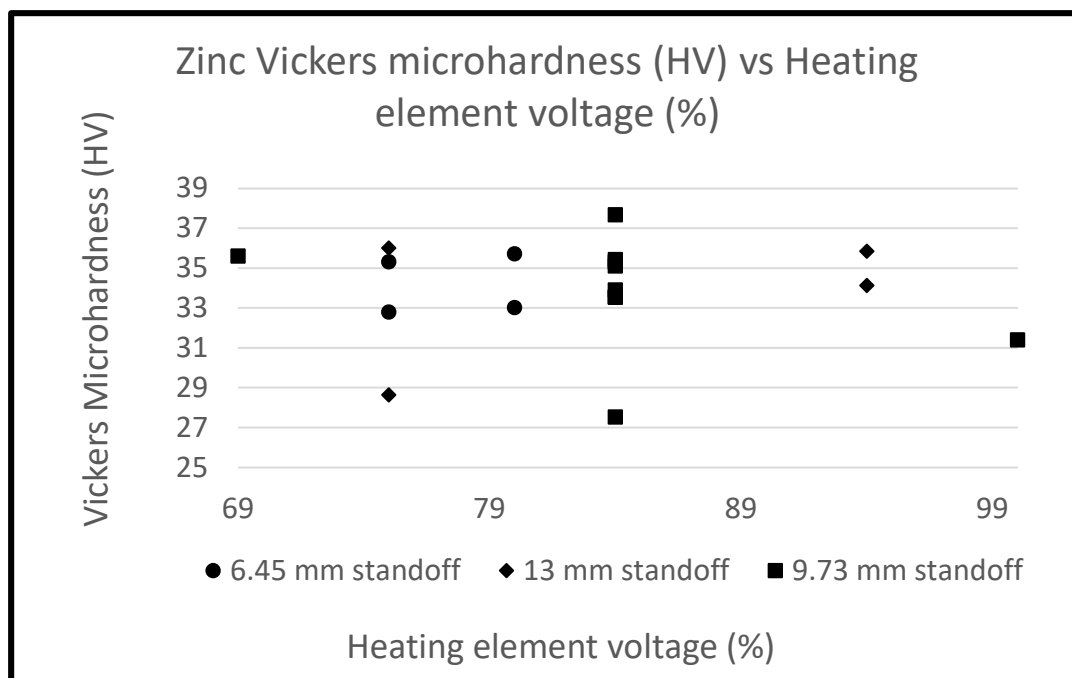


Figure 72: Zinc graph plotting microhardness (Vickers) versus deposit thickness

4.6.2.3. Thickness

As shown in **Table XVI**, the zinc deposit thickness data produced a square root modified model with heating element voltage, travel speed, and a quadratic travel speed affect that are significant. The model has a p-value of less than 0.001, and a lack of fit of 0.266. The model had an adjusted R^2 value of 0.68 and a C.V. of 18%. The adequate precision is 12, meaning there was a high enough statistical power to differentiate between the signal and noise. **Figure 74** shows the predicted versus actual plot which shows a comparison between the models predicted values and the actual values in the data set. **Figure 75** shows the leveraging of the zinc deposit thickness model where runs 8 and 20 are leveraged more than other runs. Although runs 8 and 20 are outside of reasonable bounds, the produced model was not immediately discarded. Other diagnostic graphs for the models can be seen in Appendix B: Model Diagnostic Graphs.

Table XVI: Zinc deposit thickness ANOVA table

Source	Sum of Squares	df	Mean Square	F-value	p-value	
Model	378.17	3	126.06	14.27	<0.001	significant
A - Heating Element Voltage	115.67	1	115.67	13.1	0.002	
B - Travel Speed	246.64	1	246.64	27.93	<0.001	
B²	84.83	1	84.83	9.6	0.007	
Residual	141.32	16	8.83			
Lack of Fit	112.92	11	10.27	1.81	0.266	not significant
Pure Error	28.4	5	5.68			
STd. Dev.	3					
Mean	17					
C.V.%	18					
R²	0.73					
Adjusted R²	0.68					
Adeq Precision	12					

Figure 73 shows a graph of the thickness data versus heating element voltage. A trend can be seen where thickness increases as heating element voltage increases which is like the interaction plot in Figure 76.

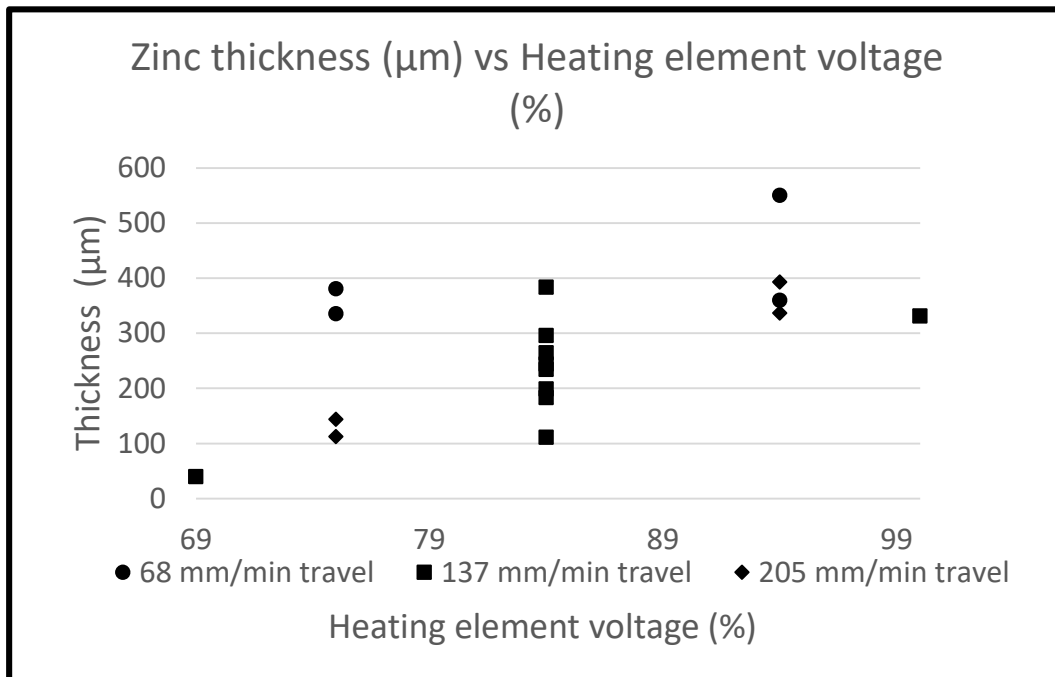


Figure 73: Zinc Excel graph plotting Thickness (µm) versus Heating element voltage (%)

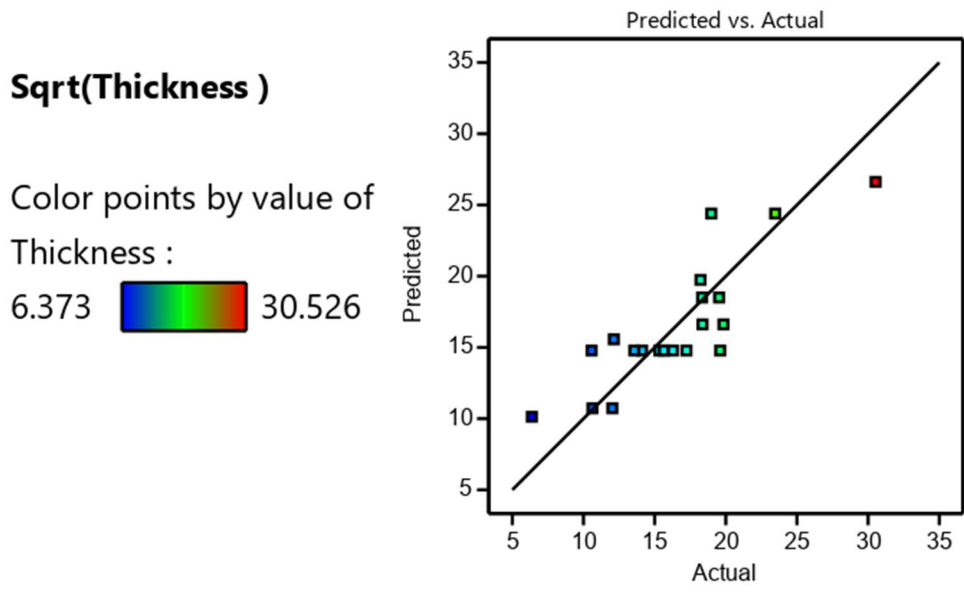


Figure 74: Predicted versus actual plot for the zinc deposit thickness model

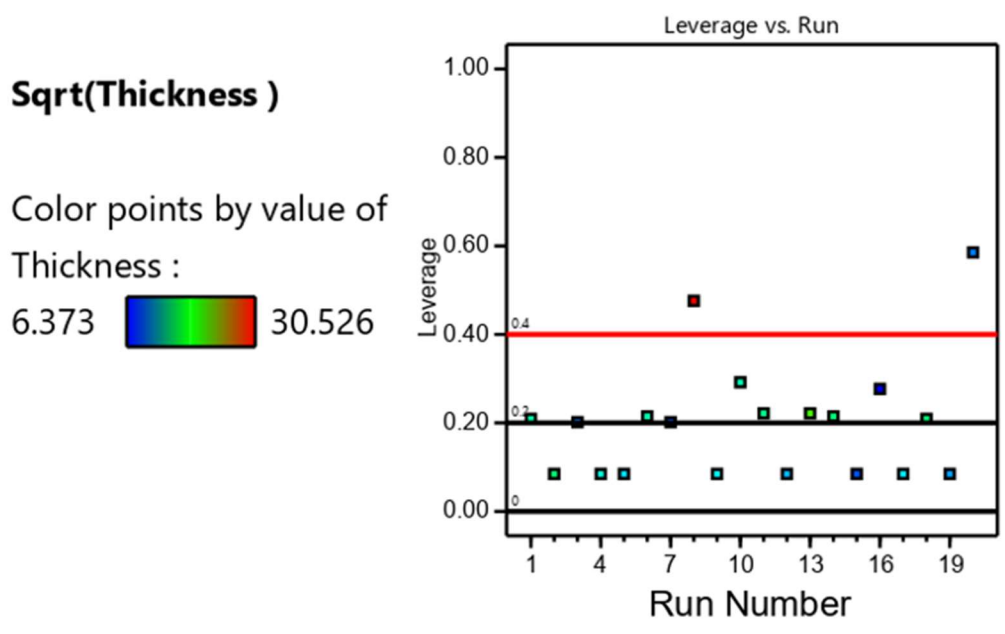


Figure 75: Zinc thickness leverage versus Run that shows the model leveraging runs 8 and 20 above reasonable bounds

Figure 76 shows the interaction of heating element voltage on deposit thickness with standoff distance of 9.7 mm, with varying travel speeds at 69 mm/min and 206 mm/min. The plot shows that increasing heating element voltage for both travel speeds increased deposit

thickness, while the slower travel speed produced thicker deposits than the faster travel speed.

This behavior can also be seen in **Figure 77**, the 3D response surface of deposit thickness versus heating element voltage and travel speed. The response surface suggests that the thickest deposits were produced from high heating element voltage and slow travel speed.

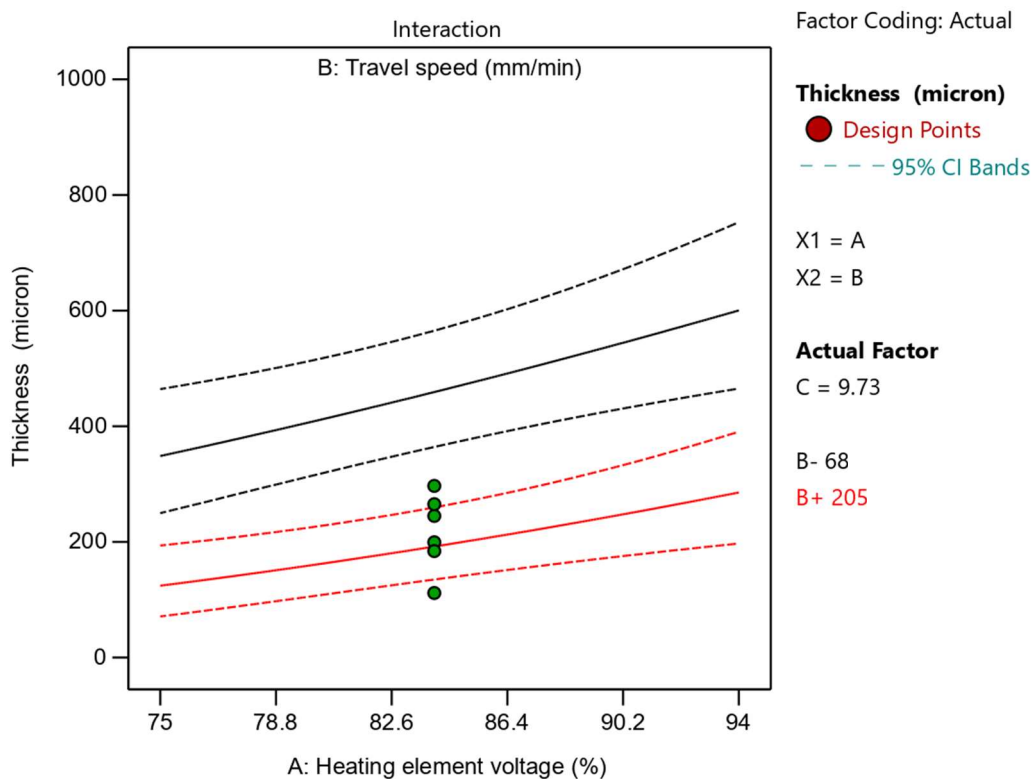


Figure 76: Interaction plot of zinc thickness versus heating element voltage at the standoff distance midpoint indicating that thickness increases for both high (206 mm/min, red) and low (69 mm/min, black) travel speeds with low travel speed producing thicker deposits, as heating element voltage is increased

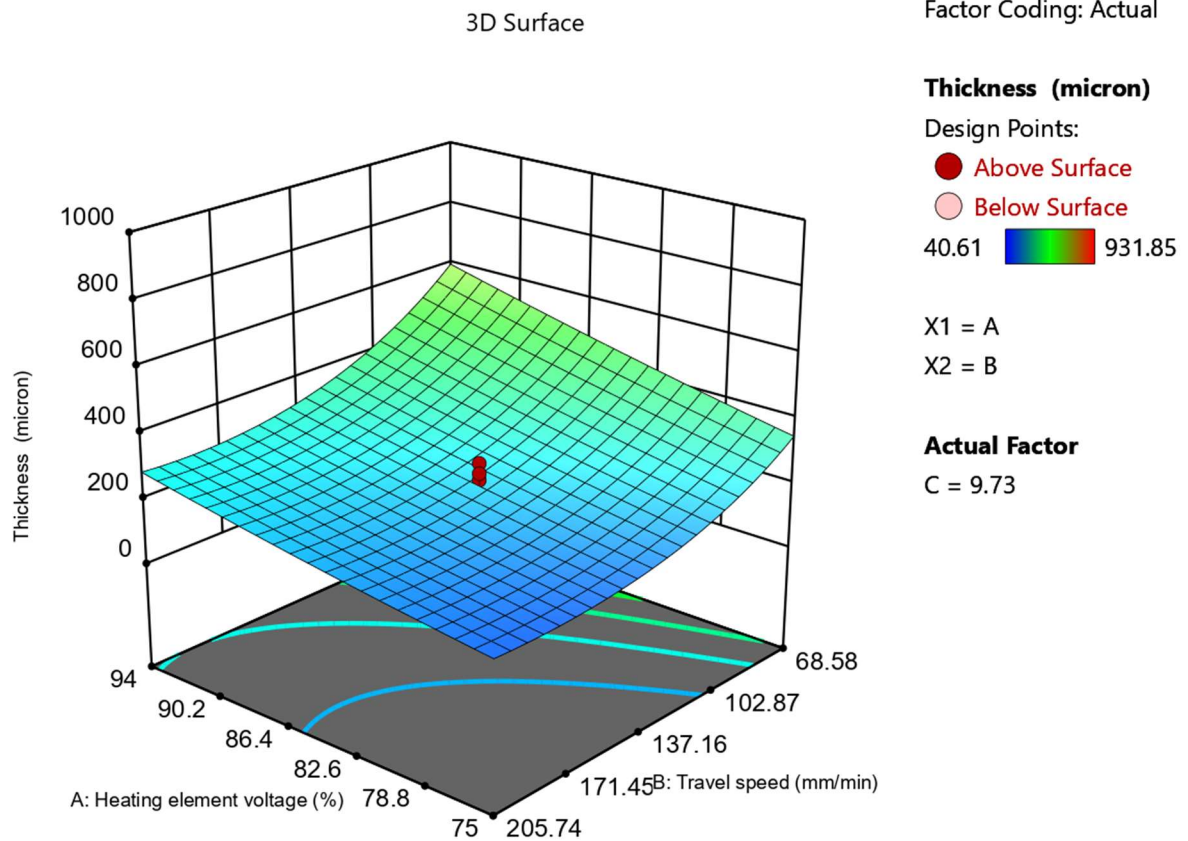


Figure 77: Zinc deposit thickness 3D response surface showing that the thickest deposits can be created at slow travel speed (69 mm/min) and high heating element voltage (94%)

4.6.2.4. Zinc Validation

Two zinc samples were produced at settings contained within the design. Validation sample 1 was made at 90% heating element voltage, 151 mm/min travel speed, and 11.2 mm standoff distance. Validation sample 2 was made at 81% heating element voltage, 101 mm/min travel speed, and 8.0 mm standoff distance. Porosity, grain size, thickness, and microhardness data were obtained for these samples to validate the produced models. Table XVII shows the validation data for the zinc models.

Table XVII: Zinc CS validation statistics

	Response	Std Dev	95% PI low	Data Mean	95% PI high
Val. 1	Porosity (%)	1.5	1.4	2.5	8.2
	Microhardness (HV)	2.5	28.7	32.9	39.6
	Thickness (μm)	95	86	369	509
	Grain Size (μm)	0.4	5.2	6.1	6.8
Val. 2					
	Porosity (%)	1.4	1.4	4.3	7.
	Microhardness (HV)	2.5	28.7	34.5	39.6
	Thickness (μm)	99	100	402	536
	Grain Size (μm)	0.4	5.2	5.9	6.8

5. Discussion

5.1. Powder Sieve Analysis

The powder retained on each sieve was recorded and tabulated, shown in **Table IV** and **Table V**. Linear interpolation was performed on the cumulative percent passing data, for copper between 89.5% and 28.3% to obtain a 50% passing size (d50) of 22 μm and an 80% passing size (d80) of 24 μm . For zinc, the interpolation was performed twice, one between 71.7% and 35.0% to obtain a d50 of 22 μm , and one between 82.5% and 76.4% to obtain a d80 of 50 μm . Due to the d50 and d80 being obtained via interpolation of the cumulative percent passing data, the values represent the average size of a particle and not necessarily a discrete particle size that is observed. As seen in **Figure 24** and **Figure 25**, the Cu powder had a jagged pinecone like structure with nodules coming off of the particles and the Zn powder was round but irregular with a bimodal particle size distribution.

The geometry of the Cu particle is interesting when considering the angle at which the particle may collide with the deposit and/or substrate. If the particle were to collide, oriented

such that a point or sharp feature were to strike first, the forces during collision may result in the nodules splaying outward. The nodules splaying could potentially create pores in the deposit that are hard for subsequent particle collisions to reach and close. The Zn particles having a bimodal distribution may also affect porosity as an adhered large particle may obstruct the path of a smaller particle, preventing the closing of pores.

5.2. Powder Feed System

For the powder to reach the required velocity to perform the CS process, it must be introduced into a gas stream and accelerated to the required velocity. However, the method of delivering the powder to the gas stream must be considered as too much powder will result in most of the particles not achieving their critical velocity as more mass will need to be accelerated. High feed rates can also result in clogging which would result in sporadic and non-uniform CS coatings. Low feed rates do not suffer from clogging but deposit material more slowly than high feed rates. . A single pass of the CS gun with low feed rate has, by nature of the lower feed rate, few particles adhered to the surface of the substrate per unit length under the nozzle, assuming all particles adhered successfully. A larger orifice diameter, 1.6 mm, was needed for the zinc powder to improve material flow. However, the zinc did not flow consistently into the process stream and deposition profile varied during experiments, even with the 1.6 mm orifice hole. The 0.6 mm nozzle resulted in a feed rate of 2.2 g/min for copper powder and the 1.6 mm nozzle resulted in a feed rate of 1.7 g/min for the zinc powder.

5.3. Copper

5.3.1. Porosity

A trend can be generally observed across the CS deposit thickness, that porosity increased away from the substrate material. The gap (**Figure 29** and **Figure 30**) between the deposit and

the substrate indicates poor adhesion and lack of metallurgical bonding between particles and the substrate, however a deposit was still able to be formed despite this minimal adherence. The gap would suggest that the dominate bonding mechanism for the deposits was a weak mechanical interlocking and not metallurgical bonding. The presence of the gap between deposit and substrate prevented analysis of potentially interlocked material and determination of the actual bonding mechanism of the deposit. During a preliminary study of the Cu CS system with high feed rates, it was observed that the deposit would begin to peel off the substrate entirely after the sample was made. During observation of the weakly adhered Cu samples, a gap between deposit and substrate was observed. The formation of this gap is thought to resultant from thermal contraction or from elastic recovery of adhered particles, but the exact mechanism is unknown.

Due to the CS processing parameters for runs 3 and 7 producing extremely thin “deposits” and considering the d80 size of the copper powder being 24 μm , it could be said that the “deposit” is more representative of individual particle-particle collisions and not a coating produced by the processing parameters. If one’s goal is to produce such a thin coating, then one might consider operating under the conditions of runs 3 and 7. For the goal of this research, however, runs 3 and 7 did not produce results that could be analyzed via ImageJ or have adequate polishing for microscopy performed. In the DOE, these two results were originally discarded however, the statistical analysis performed by the Design Expert software leveraged the resulting model and regression of the data against the remaining runs that were performed at the low voltage setting of 75% (**Table VIII**). The leveraging may have resulted in the statistics suggesting that travel speed is not significant to deposit porosity which goes against the findings of Tan et al. (2017), Nourian et al. (2022), and Klinkov et al. (2019), in which slower travel speeds reduced porosity due to an increase in the thermal energy associated with the substrate

and subsequent layers being formed. The interaction graph shows the effect of heating element voltage and standoff distance on the deposit porosity (**Figure 42**) and suggests that porosity decreased when heating element voltage was increased from 75% to 94% with a standoff distance of 13.0 mm. The graph indicates an increase in porosity when the heating element voltage was raised from 75% to 94% with a standoff distance of 6.5 mm. The interaction at close standoff behaves opposite of what is expected, where an increased temperature of the particles would make it easier for the particles to deform and close the pores produced from previous particle impacts.

Copper runs 8, 10, 11, 13, and 14, produced deposits with high thickness and exhibited more porosity along the build edge of the deposit not seen in the bulk of the material (**Figure 30**). Distinct porosities were not well observed within the model because of the averaging of the analysis. Runs 11, 13, and 14 all are the corner points of the design and in **Figure 30**, a trend of more pores being present towards the outside of the deposit, and the bulk inside of the deposit with less porosity were observed. The porosity makes sense, as particles deeper in the deposit have experienced more collisions and stresses resulting in more strain than particles on the outside of the deposit. Collisions and the induced strain close pores that form at the edges of deformed particles and material jetting. Additionally, the porosity observed (**Figure 32** and **Figure 33**) formed along particle boundaries. Pore formation along particle boundaries is expected due to poor deformation and adhesion occurring in particle-particle collisions which results in unclosed pores remaining in the deposit. The validation samples produced porosity data within the confidence interval in **Table XIII** and **Table XIV**, and confirmed the model as valid.

There is an additional effect that may be taking place, recrystallization, which takes place at approximately 40% of the absolute melting temperature of the metal. A thermocouple wired into a multimeter was moved around the exit of the CS nozzle and each heating element setting was checked, taking the highest value to appear on the multimeter after several minutes in the gas stream. The measured temperature is a rough approximation of the temperature of the gas stream, it provided important insight as to what might be occurring in sample microstructure and deposition. At 75% voltage to the heating element, the temperature of the gas stream was roughly 360 °C, well above the recrystallization temperature of zinc, approximately 168 °C, but below the recrystallization temperature of copper, approximately 434 °C. The high heating element settings, 94%, produced a gas stream temperature of roughly 640 °C, above the recrystallization temperature of copper. The particles, however, might not spend enough time in the gas stream to reach recrystallization temperature. The flying particles then collide with either the substrate or previously deposited particles, which increases the temperature of the deposit and substrate. For recrystallization to occur, the material would have to be held near the recrystallization temperature for an hour, with the time needed to recrystallize decreasing at higher temperatures. The high temperatures call into question the deposits produced with a high heat input versus a low heat input, i.e., the samples produced with either high voltage setting and/or samples produced with middle voltage setting but slow travel speed. The bulk of the deposits produced with high heat input settings could undergo some degree of recrystallization, relieving stresses produced from the particle impact, reforming grains that were previously deformed and could recrystallize in the space available in the pores. Recrystallization could potentially create less porous material in the bulk of a deposit, while the outside of the deposit would remain more porous as it would not be insulated and cooled at an increased rate. The

effect of recrystallization would also theoretically show up in the grain size data and the microhardness data, however, there is no thermal data collected in this study that would directly suggest a recrystallization phenomenon is occurring.

Recrystallization can also occur through strain on the crystal structure of a material. The strain reorients and reforms the crystal to accommodate the stress that is inducing the strain. CS is inherently a high strain rate process and so it could be that grains near the center of the deposit are reforming to accommodate the high strain of multiple particle deformation. Zhang and Zhang (2011) studied the possibility of strain induced recrystallization in the CS process and while they did not directly create movement in the grain boundary. They theorize that recrystallization is likely to occur when proper grain misorientation is achieved and that strain induced recrystallization could greatly improve the mechanical properties of a CS deposit from the new deformation free grains.

Particle collisions also add to the heating of the deposit and substrate as kinetic energy is partially converted to thermal energy upon impact. Particle collisions, in addition to the heat of the gas particles themselves, will heat the deposit and substrate. When the nozzle is traveling slower and the gas stream is allowed to have more time of a region of the substrate and deposit, more particle collisions are occurring in that region. The thermal energy from repeated particle collisions hinders the cooling of the deposit until the gas stream and nozzle are no longer over the deposited region. The hindering of the deposit cooling could insulate the deposit, keeping the temperature at or above the recrystallization temperature and allowing for recrystallization to occur.

Energy is needed for the metallurgical bond to be created between the CS material and the substrate. Larger particles require more energy to create enough bonds to adhere well to the

deposit and/or substrate. The energy required for adhesion would change as particle size gets smaller because a smaller mass and surface area colliding with the deposit and/or substrate means less bonds need to be formed to adhere well. Assuming all the particles that flow through the gas stream oriented normal to the substrate, then much of the kinetic energy would be imparted into the deposit and/or substrate. However, the gas plume out of the nozzle is more conical and particles will distribute themselves throughout the gas plume and collide with the substrate at non-normal angles. Additionally, the velocity near the edge of the gas plume is not going to be the same velocity near the center of the gas plume due to the pipe flow velocity profile and drag effects near the edge of the plume. The portion of the energy available to close pores in the deposit also changes depending on the angle of collision with the deposit. A shallower angle of impact means that less of the kinetic energy is imparted in the deposit and/or substrate and reduces the likelihood of successful deposition and there may not be enough force to close pores at non-normal angles.

5.3.2. Grain Size

Several interactions graphs were generated from the copper grain size analysis. For the interaction produced from the 75% heating element voltage (**Figure 45**), grain size increased as heating element voltage increased with a standoff of 13.0 mm but decreased when standoff was 6.5 mm standoff. The aforementioned behavior is not present in the analysis of the 80% heating element voltage data (**Figure 48**) which instead considers the effect of heating element voltage and travel speed. Grain size increased with heating element voltage for both high and low travel speeds and produced larger grains. Taking the heating element voltage interaction into consideration, a higher heat input per unit length, slow travel speed and high heating element voltage, produced large grains and as previously mentioned, under high gas temperatures

conditions, the particles are expected to deform more than in the presence of lower gas temperature conditions as the thermal input softens the material and increases the velocity of the particles. Thermal softening also applies to the grains in the particles and the grains are expected to deform in a similar fashion, refining and producing smaller grains in the microstructure. For a high heat input CS deposit to have larger grains than a low heat input CS deposit, some grain altering process must take place or some unaccounted-for particle geometry-based effect is preventing predictable deformation of the grains.

Grain refinement processes are methods to change the grain size of a material to improve mechanical properties. There are many ways to refine the grains in a metal, with common methods being sintering, work hardening, and recrystallization. In CS research, particle collisions are considered to primarily affect the grain structure in a work hardening fashion (Hussain et al., 2009; Sudharshan et al., 2007; Yin et al., 2018), where grains are compacted forming an anisotropy in the grain structure and producing higher strengths in the direction normal to the direction of the compaction (Prashar and Vasudev, 2021). Material flow can usually be seen without the need of an etchant in the form of slip lines or shear lines. In copper, there is another microstructural indicator of deformation which is the presence of twin grains. Twin grains, or grain boundaries, form during strain where a section of a larger grain is shifted out of orientation and forms grains with identical grain orientation. Twin grains can be found in CS copper deposits (Koivuluoto et al., 2010). Attempts to find these features in the present study were unfruitful due to the fine grain sizes.

When the validation samples were examined, their grain size did not fall between the 95% confidence interval range for grain size models produced with the 75% heating element

voltage or the models produced with the 80% heating element voltage (**Table XIII** and **Table XIV**). The produced grain size models should not be used as predictive models.

As previously mentioned, recrystallization can affect the grain size of a material. In the instance of CS deposits, if the inner bulk of the material underwent recrystallization, then the deformation of the particles and grains during collision would be undone. The resulting grains would exhibit little to no deformation or aspect ratio, and any trends based on deposit thickness would not appear as the inner grains but would be reformed into new grains and the outer grains remain deformed. Recrystallization would also undo the twin grains that could form during the straining of the material.

In **Figure 50**, grain size was compared to the Feret ratio, which remained relatively static while grain size varied. For the in-house system with the settings that were chosen, this deformation ratio was approximately 1.91:1, meaning that particles, on average, deformed to be twice as long as they were thick. The Feret ratio could also be a result of the original particle shape, having a pinecone like structure as can be seen in **Figure 24**.

5.3.3. Microhardness

Microhardness results for copper are comparable with each other in this study but are lower than previously reported microhardness values for both wrought copper and other CS copper deposits in research, of 100 HV (Davis et al., 2007; Sudharshan et al., 2007). The lower microhardness produced in this study could be because the higher porosity of the deposits, allows for material to deform when the indent is made during microhardness testing, as opposed to the material resisting the indent and putting stress into the crystal lattice. If the porosity is uniform across the deposit, then the effect of the pores on microhardness can be averaged to achieve a bulk hardness of the deposit. The statistical analysis did not find a significant

correlation among the tested parameters and microhardness data. None of the tested variables being significant could mean that microhardness is not significantly changed within the testing parameters of the study, one might still expect a trend of microhardness from the bulk of the deposit to the outside of the deposit because the inner bulk of the deposit would have experienced more collisions and stresses than the outer layer and would have a higher cold working effect. As such, the sufficiently thick samples were microhardness tested going away from the substrate. The microhardness data can be seen in **Figure 53**. Runs 8, 11, 13, and 14's rerun, all showed an increase in microhardness moving away from the substrate while runs 10 and 14 decreased away from the substrate. The behavior of runs 10 and 14 are consistent with the idea that particles and grains in the bulk of the deposit have more stress than particles on the outside of the deposit (Rokni et al., 2017). The behavior of run 8 cannot be accurately described with the trendline shown in **Figure 53**, as the error associated with the microhardness measurements suggests a uniform microhardness across the entire deposit. For runs 11 and 13, there is a trend of increasing in microhardness when moving away from the substrate. An increasing trend is counter-intuitive to what one might expect, as more porosity can be observed near the outer portion of deposits. While porosity plays a large role in determining the material properties of a deposit, it does not explain why the more porous outside of a deposit is harder than the less porous inside. For the more porous outside of the deposit to be harder than the inside, the conditions affecting the crystal lattice and grains must be considered, especially in the case of the CS process producing high strain in the material. To produce lower internal hardness, the stress located inside of the deposit must be relieved or the inside of the deposit may have a complex internal stress state due to poor adhesion to the substrate which could result in lower microhardness measurements.

In recrystallization, grains are reforming and are redistributing the stress that is held within the crystal structure of the grain. Recrystallization will undo the work hardening effect that is present in most CS deposits and as a result, create a material that is easier to strain as no stress is present in the crystal lattice, and cause low microhardness values.

There is a slight trend of the inside bulk of the material being softer than the outside of the material. The inside being softer is only possible if the inner bulk had more porosity which would decrease the microhardness (Perkins et al, 2019), or if the inner bulk had somehow relieved the stresses induced from the high strain rate of particle collisions.

Tension in the center of the deposit might also be affecting the microhardness results, making them lower than expected and lower in the bulk of the material. Despite CS being a primarily compression-based process where the particles are deformed via compression onto the substrate, the compressive forces must be balanced by tension forces. Conventionally, the tensional forces are shared between the substrate and the deposit but for the copper samples produced in this study, the gap between the deposit and the substrate poses the question that the bottom, deposit is balancing both the compression and tension forces. A complex stress state might also explain the hardness behavior observed in runs 11 and 13.

5.3.4. Thickness

The statistical analysis of the thickness data provided a good model with an adjusted R^2 value of 0.8755 for the 75% heating element voltage data and 0.9139 for the 80% heating element voltage data (**Table IX** and **Table X**). All the investigated processing parameters were deemed important in determining the resulting thickness of the deposit. Interaction plots (**Figure 57** and **Figure 64**) suggest that deposit thickness decreased as travel speed increased and that a standoff of 6.5 mm produced a slightly thicker deposit under slow travel speeds. The effect of

travel speed can be directly observed in **Figure 29** and **Figure 30**, where the travel speed decreased from one figure to the next and due to the nozzle traveling slower along the spray path, and the gas plume and particle stream spending more time over an area of the substrate.

Assuming particles adhere, the more time spent over one area, the more particles will deposit to create thicker deposit. Increasing the nozzle travel speed reduces the amount of time spent in one area and relates to less particle collisions per area and creating thinner deposits.

Figure 61 shows the interaction between heating element voltage and standoff distance and suggests that deposit thickness increased as heating element voltage increased, for both low (6.5 mm) and high (13.0 mm) standoff distances. The interaction also suggests that the 6.5 mm standoff distance created slightly thicker deposits than the 13.0 mm standoff distance. Longer standoff distances increase the time a particle spends in flight, allowing it to exit the jet core of the supersonic gas stream, and the particle begins to decelerate to a velocity below critical velocity (Pattison et al., 2008; Schmidt et al., 2006; Yin et al., 2014). However, there was no velocimetry collected data to support this claim but is a known effect in CS research.

The last interaction plot (**Figure 62**) between heating element voltage and travel speed suggests that deposit thickness increases as heating element voltage increased and the slower travel speed produced much thicker deposits than faster travel speeds. The effect of heating element voltage can be observed in **Figure 29** and **Figure 30** as well, where heating element voltage increased from image 1 to image 2 and travel speed decreased from **Figure 29** to **Figure 30**. The interaction relates back to the idea that the gas plume and particle stream spend more time over an area allowing for more particle collisions. As the heating element's voltage increases, so does the temperature of the gas stream. When heating element voltage is paired with a slower travel speed, the gas stream can heat up the substrate and previously deposited

particles, more particles deform and adhere to the substrate and/or previously deposited particles because deformation is easier due to the thermal softening of the material. (Assadi et al., 2003; Bae et al., 2009). The validation samples produced thickness data within the confidence interval of **Table XIII** but not **Table XIV**, however, the low range 95% confidence interval of **Table XIV** is 0.56% different than thickness data for validation sample 2 and the model is valid with slightly less than 95% confidence.

5.4. Zinc

Unlike copper, the zinc deposits were more comparable to one another because all the deposits were produced with the possibility of recrystallization taking place. As such, there is more certainty in the zinc samples that there is not a temperature-based phenomenon affecting only a portion of the samples.

5.4.1. Porosity

The produced model for zinc porosity considers heating element voltage and travel speed important. Heating element voltage and travel speed are consistent with previously mentioned research in which slower travel speeds reduce porosity due to an increase in the thermal energy associated with the substrate and subsequent layers being formed. Travel speeds effect can be observed in both **Figure 68** and **Figure 69**. The heating element voltage plays an important role in determining not only the particle temperature, but also the substrate temperature and particle velocity as well. Both travel speed and heating element voltage are important to the deformation mechanism that closes off the pores that form through particle collision and subsequent deformation. The model was set to find the settings that would produce minimal porosity and it recommends the processing parameters of 94% heating element voltage, 69 mm/min travel speed and 9.7 mm standoff distance to produce a porosity of 1.4%, however the lowest observed

porosity, 0.6%, came from run 8 which operated at 84% heating element voltage, 33 mm/min travel speed, and a standoff distance of 9.7 mm.

Kinetic and thermal energy transfer considerations remain present with the zinc system, like the Cu system. Instead of the potential for recrystallization, there is the potential for melting to occur in the zinc deposits. Zinc's melting temperature (approximately 420 °C) is surpassed by gas temperature when the heating element voltage exceeds 80% (**Figure 11**). The deposit temperature would possibly be greater than the melting temperature of zinc through a high gas stream temperature, before considering the added thermal energy from repeated particle collisions.

The zinc deposits exhibit relatively low porosity (average 3.6%) but have large pores on the scale of 50+ μm across most of the samples. The formation of large pores is not understood for this system but an idea can be made considering the particle size distribution in Table V and the particle shape (**Figure 25**). If a larger particle, in the size range of +53-106 μm from the sieve analysis, were to collide and deposit on either the substrate or a layer of zinc particles, subsequent smaller particle impacts may deform the first larger particle and create a rolling effect that seals itself due to further collisions. Another theory to explain the large pores is that larger particles are accelerated only enough to achieve critical velocity for deposition and adhere weakly to the deposit. A weakly adhered particle may have come out of the substrate during sectioning or polishing, resulting in a cavity. The validation samples produced porosity data within the confidence interval in **Table XVII** and confirmed the model as valid.

5.4.2. Grain Size and Microhardness

Although the grain size and microhardness data collected in this study was not able to be modeled within the bounds of the variables, statements about the data could still be made. The

zinc deposits exhibited rounder grains when compared to those found in the copper samples (**Figure 37** and **Figure 38**) and the zinc deposits had an average grain size of 6.0 μm . The zinc deposits had an average Vickers microhardness of 34.1 HV with a standard deviation of 2.4. Results coincides with other CS research (Vinay et al., 2021) that found CS deposits exhibiting a higher microhardness than conventionally wrought materials.

5.4.3. Thickness

The thickness of the produced CS zinc deposits was able to be modeled using heating element voltage, travel speed, and a quadratic effect of travel speed. **Figure 76** and **Figure 77** show that increasing the heating element voltage produced thicker deposits, regardless of travel speed and that slower travel speeds produced much thicker deposits. The effect of travel speed, mentioned previously in the copper thickness section, is due to the nozzles slower travel along the spray path, with the gas plume and particle stream spending more time per unit area of the substrate. The more time spent over one area, the more particles will deposit to create thicker deposit. The validation samples produced thickness data within the confidence interval in **Table XVII** and confirmed the model as valid.

6. Conclusions

By varying gas temperature, nozzle travel speed, and standoff distance, CS deposits have been made having different thickness and mechanical properties. Therefore, processing parameters play a significant role in successfully producing CS deposits with acceptable final mechanical properties. CS copper samples were created using copper powder with a d50 of 21.8 μm and d80 of 24.2 μm and a feed rate of 2.2 g/min. CS zinc samples were created with a zinc powder with a d50 of 22.0 μm and d80 of 49.8 μm and a feed rate of 1.7 g/min.

A zinc porosity model was produced, which included variables consistent with other CS research, heating element voltage, and travel speed. The zinc porosity model predicted a porosity of approximately 1.4% using a heating element voltage of 94% and a travel speed of 69 mm/min which was identical to the porosity observed, 1.4%. However, the lowest porosity observed, approximately 0.6%, came from the slowest travel speed tested and a star point of the central-composite model, 33 mm/min, at 84% heating element power. The difference between predicted and observed values means the model can be improved.

The porosity of the copper deposits played a role in the resulting microhardness and a complex internal stress state could be hiding a trend or lack thereof, resulting in the high variance of microhardness between identical runs. Zinc microhardness measurements were all within the measurement error and considered uniform for this study.

Copper and zinc deposit thickness was affected by heating element voltage and travel speed. Slower travel speeds allow for more particle collisions to occur per unit area underneath the CS nozzle. Heating element voltage increases particle velocity as well as thermally softens both the deposit and substrate. The increased thermal energy, caused by higher heating element voltages, allows more particles to have the energy necessary to deform and adhere to the substrate.

7. Future Work

Due to the complex thermal nature of the experiments performed in the study, it would be beneficial to perform thermal modeling of the copper CS system under similar conditions, where the temperature range passes over the recrystallization temperature.

The effect of particle geometry on the produced microstructure and deposit is not well understood for low pressure CS. Particle geometry affects the drag experienced by the particle in

flight but also could change the dynamics of collision with the substrate. By changing the orientation of the particle during collision, the way forces attributed with the collision will propagate through the particle will be different.

The porosity of CS deposits can also be improved by sintering the samples (Spencer and Zhang 2009; K. Yang et al., 2018; Yin et al., 2018; Zahiri et al., 2009). Sintering provides ample room for study and manipulation of the deposit material properties as the process will reduce porosity and relieve some of the stresses from particle collisions. Sintered CS deposits of copper were found to be stronger than before. While sintering would aid in the creation of smaller pieces and components that could be produced via AM CS, it would limit the size and geometry specification considerations would greatly increase as sintering can decrease the volume of the sintered part.

Lastly, computational fluid dynamics of the gas stream with particle velocimetry should be performed to better understand the effect of the K205 nozzle geometry on the particle velocity. Understanding the effect of nozzle geometry on the in-flight particle characteristics would prove valuable in developing a better understanding of how particles distribute themselves to create a deposit.

8. Bibliography

- Akin, Semih, et al. "Fabrication of Electrically Conductive Patterns on ABS Polymer Using Low-Pressure Cold Spray and Electroless Plating." *Volume 2: Manufacturing Processes; Manufacturing Systems; Nano/Micro/Meso Manufacturing; Quality and Reliability*, 3 Sept. 2020, <https://doi.org/10.1115/msec2020-8437>. Accessed 26 Apr. 2023.
- Alkhimov, A. P., et al. *Doklady Akademii Nauk SSSR*, vol. 260, no. 4, 1981, pp. 821–25.
- ASM International. Handbook Committee. *ASM Handbook 24*. Materials Park, Oh, Asm International, 2020.
- Assadi, Hamid, et al. "Bonding Mechanism in Cold Gas Spraying." *Acta Materialia*, vol. 51, no. 15, Sept. 2003, pp. 4379–94, doi:[https://doi.org/10.1016/s1359-6454\(03\)00274-x](https://doi.org/10.1016/s1359-6454(03)00274-x).
- "ASTM E11-20: Specification for Woven Wire Test Sieve Cloth and Test Sieves." *ASTM*, vol. 14.02, 6 May 2020, <https://doi.org/10.1520/e0011-20>. Accessed 26 Apr. 2023.
- Bae, Gyuyeol, et al. "Bonding Features and Associated Mechanisms in Kinetic Sprayed Titanium Coatings." *Acta Materialia*, vol. 57, no. 19, Nov. 2009, pp. 5654–66, doi:<https://doi.org/10.1016/j.actamat.2009.07.061>.
- Bagherifard, Sara, et al. "Cold Spray Deposition for Additive Manufacturing of Freeform Structural Components Compared to Selective Laser Melting." *Materials Science and Engineering: A*, vol. 721, Apr. 2018, pp. 339–50, doi:<https://doi.org/10.1016/j.msea.2018.02.094>.
- Barton, Dallin J., et al. "Laser Assisted Cold Spray of AISI 4340 Steel." *Surface and Coatings Technology*, vol. 400, Oct. 2020, p. 126218, doi:<https://doi.org/10.1016/j.surfcoat.2020.126218>.
- Breuninger, P., et al. "Microstructuring of Titanium Surfaces with Plasma-Modified Titanium

- Particles by Cold Spraying.” *Particuology*, vol. 44, June 2019, pp. 90–104, doi:<https://doi.org/10.1016/j.partic.2018.08.002>.
- Cai, Zhenhua, et al. “The Effect of Spray Distance and Scanning Step on the Coating Thickness Uniformity in Cold Spray Process.” *Journal of Thermal Spray Technology*, vol. 23, no. 3, Oct. 2013, pp. 354–62, doi:<https://doi.org/10.1007/s11666-013-0002-0>.
- Che, Hanqing, et al. “Cold Spray of Mixed Metal Powders on Carbon Fibre Reinforced Polymers.” *Surface and Coatings Technology*, vol. 329, Nov. 2017, pp. 232–43, doi:<https://doi.org/10.1016/j.surfcoat.2017.09.052>.
- Davis, Joseph R, et al. *Properties and Selection: Nonferrous Alloys and Special-Purpose Materials*. Metals Park, Oh, Asm International, 2007.
- Faizan-Ur-Rab, M., et al. “Application of a Holistic 3D Model to Estimate State of Cold Spray Titanium Particles.” *Materials & Design*, vol. 89, Jan. 2016, pp. 1227–41, doi:<https://doi.org/10.1016/j.matdes.2015.10.075>.
- Foley, Ryan P. “Microstructural Analysis of Additively Manufactured 308L Stainless Steel Produced by Plasma Arc Welding”. 2019.
- Fukumoto, M., et al. “Effect of Substrate Temperature on Deposition Behavior of Copper Particles on Substrate Surfaces in the Cold Spray Process.” *Journal of Thermal Spray Technology*, vol. 16, no. 5-6, Oct. 2007, pp. 643–50, doi:<https://doi.org/10.1007/s11666-007-9121-9>.
- Gilbert, Thomas R, et al. *Chemistry: The Science in Context*. New York, W. W. Norton & Company, 2020.
- Gilmore, D. L., et al. “Particle Velocity and Deposition Efficiency in the Cold Spray Process.” *Journal of Thermal Spray Technology*, vol. 8, no. 4, Dec. 1999, pp. 576–82,

doi:<https://doi.org/10.1361/105996399770350278>.

Goldbaum, Dina, et al. “The Effect of Deposition Conditions on Adhesion Strength of Ti and Ti6Al4V Cold Spray Splats.” *Journal of Thermal Spray Technology*, vol. 21, no. 2, Dec. 2011, pp. 288–303, doi:<https://doi.org/10.1007/s11666-011-9720-3>.

Guan, Kai, et al. “Effects of Processing Parameters on Tensile Properties of Selective Laser Melted 304 Stainless Steel.” *Materials & Design*, vol. 50, Sept. 2013, pp. 581–86, doi:<https://doi.org/10.1016/j.matdes.2013.03.056>.

Guillem-Marti, Jordi, et al. “Porous Titanium-Hydroxyapatite Composite Coating Obtained on Titanium by Cold Gas Spray with High Bond Strength for Biomedical Applications.” *Colloids and Surfaces B: Biointerfaces*, vol. 180, Aug. 2019, pp. 245–53, doi:<https://doi.org/10.1016/j.colsurfb.2019.04.048>.

Herrmann, Konrad. *Hardness Testing*. ASM International, 2011.

Hetzner, Harald, et al. “Empirical-Statistical Study on the Relationship between Deposition Parameters, Process Variables, Deposition Rate and Mechanical Properties of A-C:H:W Coatings.” *Coatings*, vol. 4, no. 4, 15 Dec. 2014, pp. 772–795, <https://doi.org/10.3390/coatings4040772>. Accessed 1 Dec. 2021.

Hou, Juan, et al. “Microstructure, Tensile Properties and Mechanical Anisotropy of Selective Laser Melted 304L Stainless Steel.” *Journal of Materials Science & Technology*, vol. 48, July 2020, pp. 63–71, doi:<https://doi.org/10.1016/j.jmst.2020.01.011>.

Huang, C. J., et al. “Advanced Brassbased Composites via Coldspray Additivemanufacturing and Its Potential in Component Repairing.” *8th Rencontres Internationales de La Projection Thermique*, vol. 371, 2019, pp. 211–23, doi:<https://doi.org/10.1016/j.surfcoat.2019.02.034>.

- Huang, C. J., et al. "Microstructures and Wear-Corrosion Performance of Vacuum Plasma Sprayed and Cold Gas Dynamic Sprayed Muntz Alloy Coatings." *Surface and Coatings Technology*, vol. 371, Aug. 2019, pp. 172–84, doi:<https://doi.org/10.1016/j.surfcoat.2018.09.058>.
- Hussain, T., et al. "Bonding Mechanisms in Cold Spraying: The Contributions of Metallurgical and Mechanical Components." *Journal of Thermal Spray Technology*, vol. 18, no. 3, Feb. 2009, pp. 364–79, doi:<https://doi.org/10.1007/s11666-009-9298-1>.
- Hutasoit, Novana, et al. "Effects of Build Orientation and Heat Treatment on Microstructure, Mechanical and Corrosion Properties of Al6061 Aluminium Parts Built by Cold Spray Additive Manufacturing Process." *International Journal of Mechanical Sciences*, vol. 204, 2021, p. 106526, doi:<https://doi.org/10.1016/j.ijmecsci.2021.106526>.
- Jodoin, B. "Cold Spray Nozzle Mach Number Limitation." *Journal of Thermal Spray Technology*, vol. 11, no. 4, Dec. 2002, pp. 496–507, doi:<https://doi.org/10.1361/105996302770348628>.
- Kim, Young-Kyun, and Kee-Ahn Lee. "Effect of Carrier Gas Species on the Microstructure and Compressive Deformation Behaviors of Ultra-Strong Pure Copper Manufactured by Cold Spray Additive Manufacturing." *Journal of Materials Science & Technology*, vol. 97, Jan. 2022, pp. 264–71, doi:<https://doi.org/10.1016/j.jmst.2021.04.062>.
- King, Peter C., et al. "Microstructural Refinement within a Cold-Sprayed Copper Particle." *Metallurgical and Materials Transactions A*, vol. 40, no. 9, June 2009, pp. 2115–23, doi:<https://doi.org/10.1007/s11661-009-9882-5>.
- Klinkov, S. V., et al. "Influence of Nozzle Velocity and Powder Feed Rate on the Coating Mass and Deposition Efficiency in Cold Spraying." *Surface and Coatings Technology*, vol.

- 367, June 2019, pp. 231–43, doi:<https://doi.org/10.1016/j.surfcoat.2019.04.004>.
- Koivuluoto, Heli, et al. “Cold-Sprayed Copper and Tantalum Coatings — Detailed FESEM and TEM Analysis.” *Surface and Coatings Technology*, vol. 204, no. 15, Apr. 2010, pp. 2353–61, doi:<https://doi.org/10.1016/j.surfcoat.2010.01.001>.
- Kuelper, Kristofer. “Dynamic Mechanical Response of Additively Manufactured 316L and AlSi10Mg”. 2019.
- Kumar, S., et al. “Estimation of Inter-Splat Bonding and Its Effect on Functional Properties of Cold Sprayed Coatings.” *Surface and Coatings Technology*, vol. 420, Aug. 2021, p. 127318, doi:<https://doi.org/10.1016/j.surfcoat.2021.127318>.
- Lapushkina, E., et al. “Contribution in Optimization of Zn Cold-Sprayed Coating Dedicated to Corrosion Applications.” *Surface and Coatings Technology*, vol. 400, Oct. 2020, p. 126193, doi:<https://doi.org/10.1016/j.surfcoat.2020.126193>.
- Legoux, J. G., et al. “Effect of Substrate Temperature on the Formation Mechanism of Cold-Sprayed Aluminum, Zinc and Tin Coatings.” *Journal of Thermal Spray Technology*, vol. 16, no. 5-6, Oct. 2007, pp. 619–26, doi:<https://doi.org/10.1007/s11666-007-9091-y>.
- Li, Chang-Jiu, and Wen-Ya Li. “Deposition Characteristics of Titanium Coating in Cold Spraying.” *Surface and Coatings Technology*, vol. 167, no. 2-3, Apr. 2003, pp. 278–83, doi:[https://doi.org/10.1016/s0257-8972\(02\)00919-2](https://doi.org/10.1016/s0257-8972(02)00919-2).
- Lienhard, Jasper, et al. “Tin and Zinc Microparticle Impacts above the Critical Adhesion Velocity.” *Surface and Coatings Technology*, vol. 432, Feb. 2022, p. 128053, doi:<https://doi.org/10.1016/j.surfcoat.2021.128053>.
- Ling, H. J., et al. “Microstructure and Improved Tribological Performance of Graphite/Copper-Zinc Composite Coatings Fabricated by Low Pressure Cold Spraying.”

- Surface and Coatings Technology*, vol. 364, Apr. 2019, pp. 256–64,
doi:<https://doi.org/10.1016/j.surfcoat.2019.03.007>.
- Liu, Zhiying, et al. “Prediction of Heterogeneous Microstructural Evolution in Cold Sprayed Copper Coatings Using Local Zener-Hollomon Parameter and Strain.” *Acta Materialia*, vol. 193, July 2020, pp. 191–201, doi:<https://doi.org/10.1016/j.actamat.2020.04.041>.
- Li, Wenya, et al. “Solid-State Cold Spraying of Ti and Its Alloys: A Literature Review.” *Progress in Materials Science*, vol. 110, May 2020, p. 100633,
doi:<https://doi.org/10.1016/j.pmatsci.2019.100633>.
- Li, W. -Y ., et al. “Effect of Standoff Distance on Coating Deposition Characteristics in Cold Spraying.” *Materials & Design*, vol. 29, no. 2, Jan. 2008, pp. 297–304,
doi:<https://doi.org/10.1016/j.matdes.2007.02.005>.
- Li, Zhiming, et al. “Microstructure Evolution and Mechanical Behavior of Cold-Sprayed, Bulk Nanostructured Titanium.” *Metallurgical and Materials Transactions A*, vol. 45, no. 11, July 2014, pp. 5017–28, doi:<https://doi.org/10.1007/s11661-014-2434-7>.
- Luo, Xiao-Tao, et al. “Microstructure and Mechanical Property of Ti and Ti6Al4V Prepared by an In-Situ Shot Peening Assisted Cold Spraying.” *Materials & Design*, vol. 85, Nov. 2015, pp. 527–33, doi:<https://doi.org/10.1016/j.matdes.2015.07.015>.
- Mahmood, Muhammad Arif, et al. “Grain Refinement and Mechanical Properties for AISI304 Stainless Steel Single-Tracks by Laser Melting Deposition: Mathematical Modelling versus Experimental Results.” *Results in Physics*, vol. 22, Mar. 2021, p. 103880,
doi:<https://doi.org/10.1016/j.rinp.2021.103880>.
- Marzbanrad, Bahareh, et al. “Characterization of Single- and Multilayer Cold-Spray Coating of Zn on AZ31B.” *Surface and Coatings Technology*, vol. 416, June 2021, p. 127155,

doi:<https://doi.org/10.1016/j.surfcoat.2021.127155>.

Meyer, M. C., et al. “Feed Rate Effect on Particulate Acceleration in Cold Spray under Low Stagnation Pressure Conditions.” *Surface and Coatings Technology*, vol. 304, Oct. 2016, pp. 237–45, doi:<https://doi.org/10.1016/j.surfcoat.2016.07.017>.

Ning, Xian-Jin, et al. “Cold Spraying of Al–Sn Binary Alloy: Coating Characteristics and Particle Bonding Features.” *Surface and Coatings Technology*, vol. 202, no. 9, Feb. 2008, pp. 1681–87, doi:<https://doi.org/10.1016/j.surfcoat.2007.07.026>.

Nourian, Ahmad, et al. “Effects of Process Parameters on Cold Spray Deposition of Al-6061 Alloy.” *Journal of Thermal Spray Technology*, Sept. 2022, doi:<https://doi.org/10.1007/s11666-022-01456-3>.

Novoselova, T., et al. “Formation of TiAl Intermetallics by Heat Treatment of Cold-Sprayed Precursor Deposits.” *Journal of Alloys and Compounds*, vol. 436, no. 1-2, June 2007, pp. 69–77, doi:<https://doi.org/10.1016/j.jallcom.2006.06.101>.

“Particle Shape.” *Sympatec*, www.sympatec.com/en/particle-measurement/glossary/particle-shape/#. Accessed 21 May 2023.

Pattison, J., et al. “Standoff Distance and Bow Shock Phenomena in the Cold Spray Process.” *Surface and Coatings Technology*, vol. 202, no. 8, Jan. 2008, pp. 1443–54, doi:<https://doi.org/10.1016/j.surfcoat.2007.06.065>.

Perkins, Allen, et al. *FINITE ELEMENT ANALYSIS of the EFFECT of POROSITY on the PLASTICITY and DAMAGE BEHAVIOR of MG AZ31 and al 6061 T651 ALLOYS*. 2019.

Prashar, Gaurav, and Hitesh Vasudev. “A Comprehensive Review on Sustainable Cold Spray Additive Manufacturing: State of the Art, Challenges and Future Challenges.” *Journal of Cleaner Production*, vol. 310, Aug. 2021, p. 127606,

doi:<https://doi.org/10.1016/j.jclepro.2021.127606>.

- Rafaja, David, et al. "Microstructural Characterisation of Titanium Coatings Deposited Using Cold Gas Spraying on Al₂O₃ Substrates." *Surface and Coatings Technology*, vol. 203, no. 20-21, July 2009, pp. 3206–13, doi:<https://doi.org/10.1016/j.surfcoat.2009.03.054>.
- Rawn, Penn. "3D Printing of 316L Stainless Steel and Its Effect on Microstructure and Mechanical Properties". 2017.
- Rokni, M.R., et al. "Microstructure and Mechanical Properties of Cold Sprayed 6061 al in As-Sprayed and Heat Treated Condition." *Surface and Coatings Technology*, vol. 309, Jan. 2017, pp. 641–650, <https://doi.org/10.1016/j.surfcoat.2016.12.035>. Accessed 1 Apr. 2022.
- Roy, Kevin, et al. "2.6 – Kinetic-Molecular Theory of Gases (Ideal Gas Behaviours)." *Ecampusontario.pressbooks.pub*, 2021, ecampusontario.pressbooks.pub/genchemforgeegees/chapter/2-6-kinetic-molecular-theory-of-gases-ideal-gas-behaviours/#:~:text=Gases%20composed%20of%20lighter%20molecules. Accessed 26 Apr. 2023.
- Salisbury, Tyler. *Fabrication and Characterization of Porous 420 Stainless Steel Substrates Produced Using Rapid Prototyping Technology and Thermally Strengthened Using Solid State Sintering*. 2011.
- Schmidt, Tobias, et al. "Development of a Generalized Parameter Window for Cold Spray Deposition." *Acta Materialia*, vol. 54, no. 3, Feb. 2006, pp. 729–42, doi:<https://doi.org/10.1016/j.actamat.2005.10.005>.
- Singh, R., et al. "Effects of Substrate Roughness and Sprayangle on Deposition Behavior of

- Coldsprayed Inconel 718.” *Surface and Coatings Technology*, vol. 319, no. C, 2017, pp. 249–59, doi:<https://doi.org/10.1016/j.surfcoat.2017.03.072>.
- Sone, Yoshio. *Kinetic Theory and Fluid Dynamics*. Springer Science & Business Media, 6 Dec. 2012.
- Sova, A., et al. “Deposition of Aluminum Powder by Cold Spray Micronozzle.” *The International Journal of Advanced Manufacturing Technology*, vol. 95, no. 9-12, Dec. 2017, pp. 3745–52, doi:<https://doi.org/10.1007/s00170-017-1443-2>.
- Sova, Aleksey, et al. “Velocity of the Particles Accelerated by a Cold Spray Micronozzle: Experimental Measurements and Numerical Simulation.” *Journal of Thermal Spray Technology*, vol. 22, no. 1, Nov. 2012, pp. 75–80, doi:<https://doi.org/10.1007/s11666-012-9846-y>.
- Spencer, K., and M. -X . Zhang. “Heat Treatment of Cold Spray Coatings to Form Protective Intermetallic Layers.” *Scripta Materialia*, vol. 61, no. 1, July 2009, pp. 44–47, doi:<https://doi.org/10.1016/j.scriptamat.2009.03.002>.
- Stokes, Michael A., et al. “Fundamental Physics Effects of Background Gas Species and Pressure on Vapor Plume Structure and Spatter Entrainment in Laser Melting.” *Additive Manufacturing*, vol. 55, July 2022, p. 102819, doi:<https://doi.org/10.1016/j.addma.2022.102819>.
- Sudharshan Phani, P., et al. “Effect of Process Parameters and Heat Treatments on Properties of Cold Sprayed Copper Coatings.” *Journal of Thermal Spray Technology*, vol. 16, no. 3, June 2007, pp. 425–34, doi:<https://doi.org/10.1007/s11666-007-9048-1>.
- Sun, Yuchen, et al. “The Transition from Rebound to Bonding in High-Velocity Metallic Microparticle Impacts: Jetting-Associated Power-Law Divergence.” *Journal of Applied*

- Mechanics*, vol. 87, no. 9, May 2020, doi:<https://doi.org/10.1115/1.4047206>.
- Suo, Xinkun, et al. “Strong Effect of Carrier Gas Species on Particle Velocity during Cold Spray Processes.” *Surface and Coatings Technology*, vol. 268, Apr. 2015, pp. 90–93, doi:<https://doi.org/10.1016/j.surfcoat.2014.04.039>.
- Suttey, Luke Joseph. “Evaluation of Metallurgical and Mechanical Properties of AlSi10Mg Produced by Selective Laser Melting”. 2018.
- Tan, Adrian Wei-Yee, et al. “Effects of Traverse Scanning Speed of Spray Nozzle on the Microstructure and Mechanical Properties of Cold-Sprayed Ti6Al4V Coatings.” *Journal of Thermal Spray Technology*, vol. 26, no. 7, Aug. 2017, pp. 1484–97, doi:<https://doi.org/10.1007/s11666-017-0619-5>.
- Tsai, Jung-Ting, et al. “Adhesion of Rough Cold Sprayed Metal Coatings on Polymers.” *Surface Engineering*, 24 Apr. 2023, pp. 1–13, <https://doi.org/10.1080/02670844.2023.2202005>. Accessed 26 Apr. 2023.
- Tsai, Jung-Ting, et al. “Establishing a Cold Spray Particle Deposition Window on Polymer Substrate.” *Journal of Thermal Spray Technology*, vol. 30, no. 4, 18 Mar. 2021, pp. 1069–1080, <https://doi.org/10.1007/s11666-021-01179-x>. Accessed 1 Nov. 2021.
- Vander, George F. *ASM Handbook. Volume 9, Metallography and Microstructures*. Materials Park, Ohio Asm International, 2004, pp. 297, 304–7, 778, 933.
- Van Steenkiste, T., and J. R. Smith. “Evaluation of Coatings Produced via Kinetic and Cold Spray Processes.” *Journal of Thermal Spray Technology*, vol. 13, no. 2, June 2004, pp. 274–82, doi:<https://doi.org/10.1361/10599630419427>.
- Vargas-Uscategui, Alejandro, et al. “Toolpath Planning for Cold Spray Additively Manufactured Titanium Walls and Corners: Effect on Geometry and Porosity.” *Journal of Materials*

Processing Technology, vol. 298, Dec. 2021, p. 117272,
doi:<https://doi.org/10.1016/j.jmatprotec.2021.117272>.

Vilardell, A. M., et al. “Functionalized Coatings by Cold Spray: An in Vitro Study of Micro- and Nanocrystalline Hydroxyapatite Compared to Porous Titanium.” *Materials Science and Engineering: C*, vol. 87, June 2018, pp. 41–49,
doi:<https://doi.org/10.1016/j.msec.2018.02.009>.

Vinay, Gidla, et al. “Generalised Bonding Criteria in Cold Spraying: Revisiting the Influence of In-Flight Powder Temperature.” *Materials Science and Engineering: A*, vol. 823, Aug. 2021, p. 141719, doi:<https://doi.org/10.1016/j.msea.2021.141719>.

---. “Improved Microstructure and Properties of Cold Sprayed Zinc Coatings in the as Sprayed Condition.” *Surface and Coatings Technology*, vol. 438, May 2022, p. 128392,
doi:<https://doi.org/10.1016/j.surfcoat.2022.128392>.

Wang, Hong-Ren, et al. “Effect of Process Conditions on Microstructure and Corrosion Resistance of Cold-Sprayed Ti Coatings.” *Journal of Thermal Spray Technology*, vol. 17, no. 5-6, Nov. 2008, pp. 736–41, doi:<https://doi.org/10.1007/s11666-008-9256-3>.

W. E. Frazier, "Metal Additive Manufacturing: A Review," ASM International, vol. 23, pp.1917-1928, 2014

Whang, Sung H. *Nanostructured Metals and Alloys*. Woodhead Publishing Limited, 2011.

WOLFE, D., and T. EDEN. “Cold Spray Particle Deposition for Improved Wear Resistance.” *The Cold Spray Materials Deposition Process*, 2007,
doi:<https://doi.org/10.1533/9781845693787.3.264>.

Wong, Wilson, et al. “Influence of Helium and Nitrogen Gases on the Properties of Cold Gas Dynamic Sprayed Pure Titanium Coatings.” *Journal of Thermal Spray Technology*, vol.

- 20, no. 1-2, Nov. 2010, pp. 213–26, doi:<https://doi.org/10.1007/s11666-010-9568-y>.
- Wu, Jingwei, et al. “Measurement of Particle Velocity and Characterization of Deposition in Aluminum Alloy Kinetic Spraying Process.” *Applied Surface Science*, vol. 252, no. 5, Dec. 2005, pp. 1368–77, doi:<https://doi.org/10.1016/j.apsusc.2005.02.108>.
- Yang, Kang, et al. “Characterizations and Anisotropy of Cold-Spraying Additive-Manufactured Copper Bulk.” *Journal of Materials Science & Technology*, vol. 34, no. 9, Sept. 2018, pp. 1570–79, doi:<https://doi.org/10.1016/j.jmst.2018.01.002>.
- Yang, Lijing, et al. “Nanocrystallization of Interfacial Microstructure of Deformed Particles in Cold Sprayed Ti6Al4V Deposits.” *Materials & Design*, vol. 210, Nov. 2021, p. 110117, doi:<https://doi.org/10.1016/j.matdes.2021.110117>.
- Yin, S., et al. “Significant Influence of Carrier Gas Temperature during the Cold Spray Process.” *Surface Engineering*, vol. 30, no. 6, Apr. 2014, pp. 443–50, doi:<https://doi.org/10.1179/1743294414y.0000000276>.
- Yin, Shuo, et al. “Cold Spray Additive Manufacturing and Repair: Fundamentals and Applications.” *Additive Manufacturing*, vol. 21, May 2018, pp. 628–50, doi:<https://doi.org/10.1016/j.addma.2018.04.017>.
- . “Effect of Injection Pressure on Particle Acceleration, Dispersion and Deposition in Cold Spray.” *Computational Materials Science*, vol. 90, July 2014, pp. 7–15, doi:<https://doi.org/10.1016/j.commatsci.2014.03.055>.
- . “Microstructure and Mechanical Anisotropy of Additively Manufactured Cold Spray Copper Deposits.” *Materials Science and Engineering: A*, vol. 734, Sept. 2018, pp. 67–76, doi:<https://doi.org/10.1016/j.msea.2018.07.096>.
- YU, Tianyu, et al. “Experimental and Numerical Study of Deposition Mechanisms for Cold

- Spray Additive Manufacturing Process.” *Chinese Journal of Aeronautics*, Mar. 2021, doi:<https://doi.org/10.1016/j.cja.2021.02.002>.
- Zahiri, Saden H., et al. “Elimination of Porosity in Directly Fabricated Titanium via Cold Gas Dynamic Spraying.” *Journal of Materials Processing Technology*, vol. 209, no. 2, Jan. 2009, pp. 922–29, doi:<https://doi.org/10.1016/j.jmatprotec.2008.03.005>.
- Zhang, Y. Y., and J. S. Zhang. “Recrystallization in the Particles Interfacial Region of the Cold-Sprayed Aluminum Coating: Strain-Induced Boundary Migration.” *Materials Letters*, vol. 65, no. 12, June 2011, pp. 1856–58, doi:<https://doi.org/10.1016/j.matlet.2011.04.014>.
- Zhou, Hongxia. “Microstructure Control and Properties of Cold-Sprayed Titanium and Its Alloy Coatings.” *Materials Science and Technology*, vol. 37, no. 2, Jan. 2021, pp. 121–43, doi:<https://doi.org/10.1080/02670836.2020.1868689>.

9. Appendix A: SEM Pore Analysis

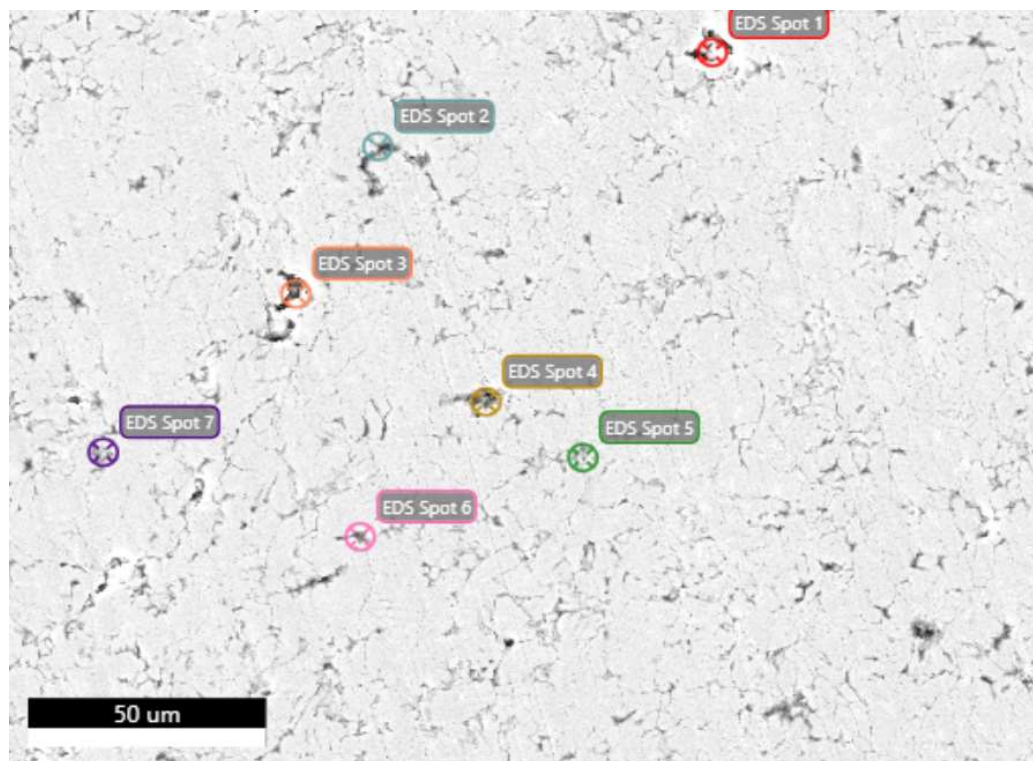
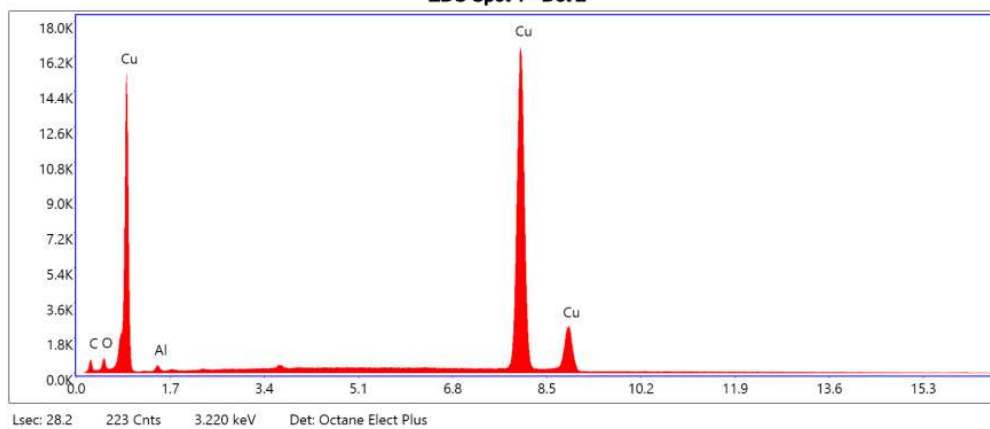


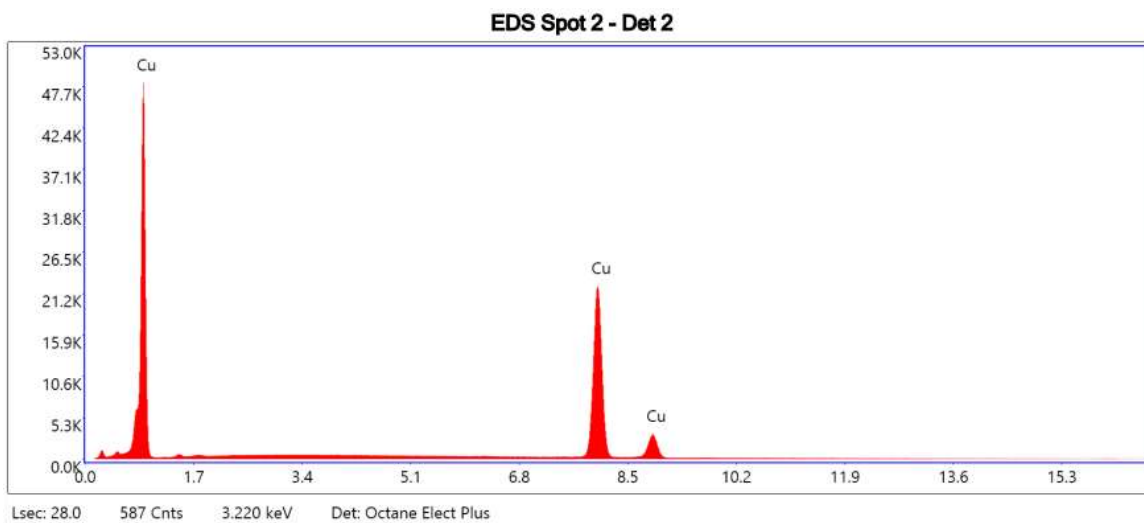
Figure 78: Cu run 8 SEM pore analysis area 1
EDS Spot 1 - Det 2



eZAF Smart Quant Results

Element	Weight %	Atomic %	Net Int.	Error %	Kratio	Z	A	F
C K	6.38	25.35	127.43	11.95	0.0144	1.2926	0.1750	1.0000
O K	1.55	4.63	119.99	11.99	0.0053	1.2487	0.2716	1.0000
AlK	0.85	1.50	72.82	15.03	0.0019	1.1295	0.1940	1.0023
CuK	91.22	68.52	9660.14	1.33	0.8866	0.9687	1.0025	1.0008

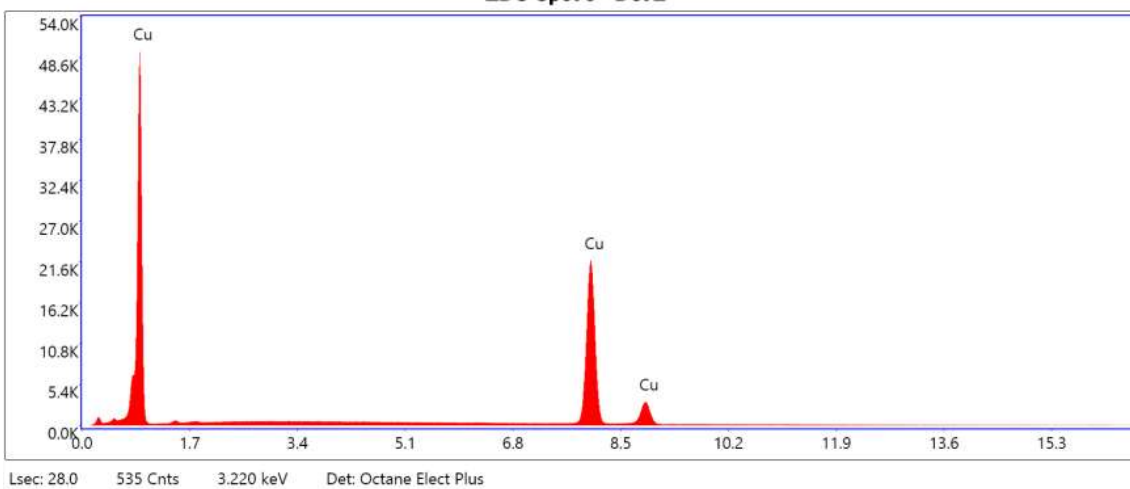
Figure 79: Cu run 8 SEM pore analysis area 1 spot 1



eZAF Smart Quant Results

Element	Weight %	Atomic %	Net Int.	Error %	Kratio	Z	A	F
CuK	100.00	100.00	12758.11	1.28	1.0000	1.0000	1.0000	1.0000

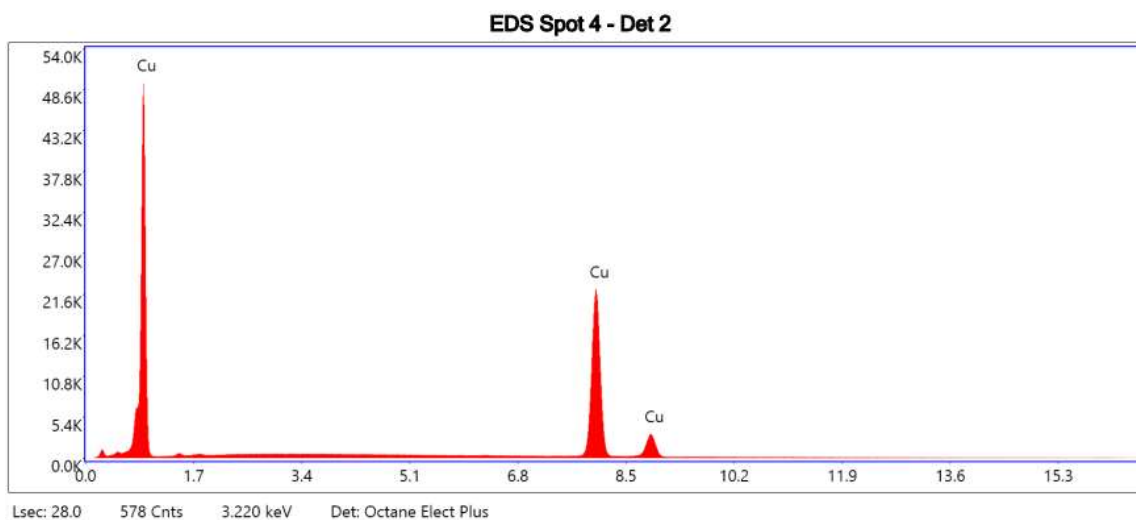
Figure 80: Cu run 8 SEM pore analysis area 1 spot 2
EDS Spot 3 - Det 2



eZAF Smart Quant Results

Element	Weight %	Atomic %	Net Int.	Error %	Kratio	Z	A	F
CuK	100.00	100.00	12519.03	1.28	1.0000	1.0000	1.0000	1.0000

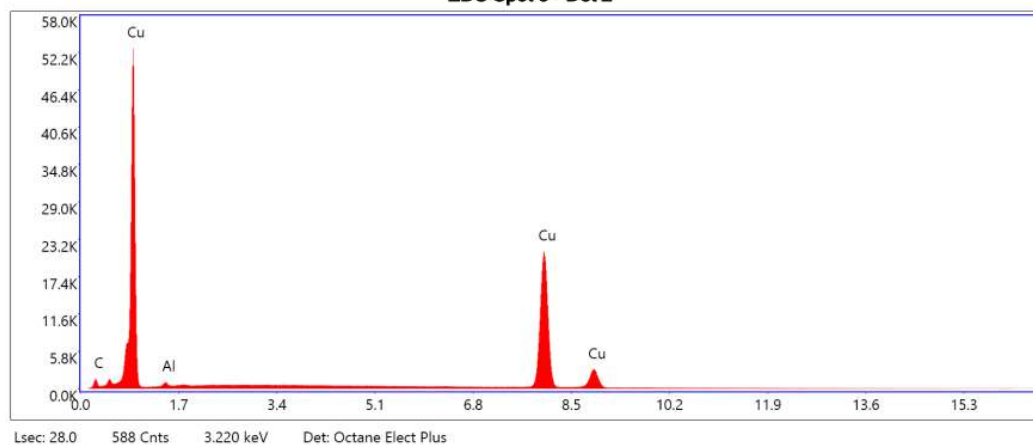
Figure 81: Cu run 8 SEM pore analysis area 1 spot 3



eZAF Smart Quant Results

Element	Weight %	Atomic %	Net Int.	Error %	Kratio	Z	A	F
CuK	100.00	100.00	12875.39	1.28	1.0000	1.0000	1.0000	1.0000

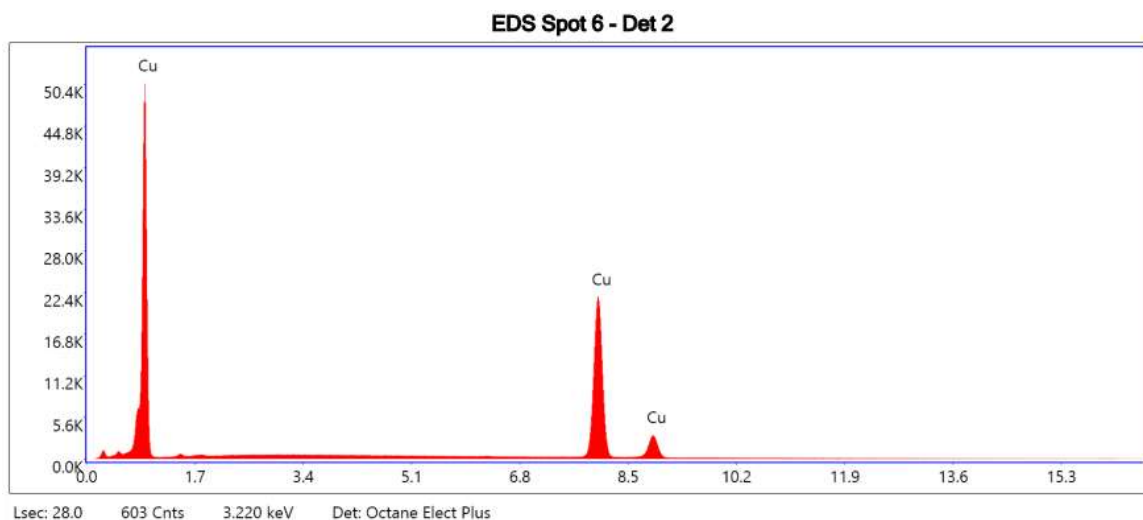
Figure 82: Cu run 8 SEM pore analysis area 1 spot 4
EDS Spot 5 - Det 2



eZAF Smart Quant Results

Element	Weight %	Atomic %	Net Int.	Error %	Kratio	Z	A	F
C K	10.45	37.62	280.77	10.85	0.0238	1.2781	0.1781	1.0000
AlK	1.59	2.54	185.90	14.32	0.0036	1.1168	0.2007	1.0023
CuK	87.96	59.84	12313.65	1.33	0.8457	0.9571	1.0035	1.0011

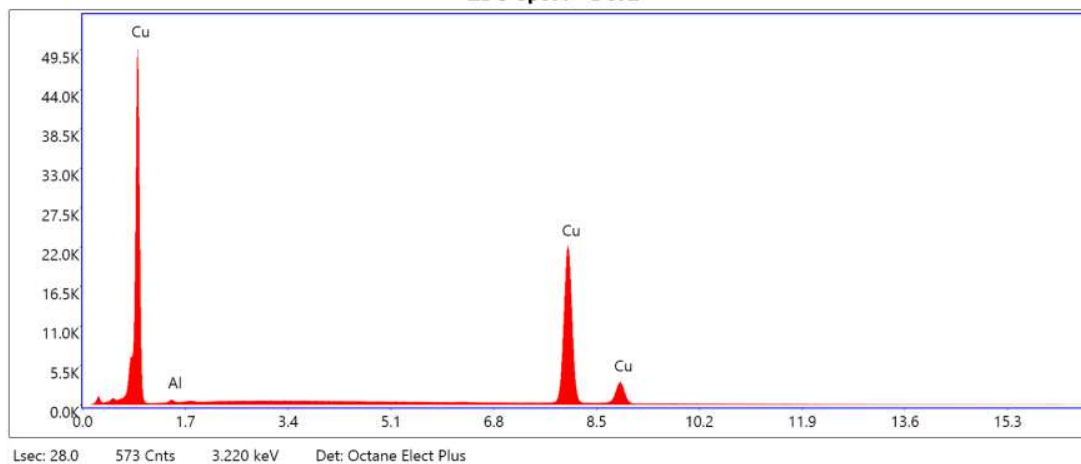
Figure 83: Cu run 8 SEM pore analysis area 1 spot 5



eZAF Smart Quant Results

Element	Weight %	Atomic %	Net Int.	Error %	Kratio	Z	A	F
CuK	100.00	100.00	12680.55	1.28	1.0000	1.0000	1.0000	1.0000

Figure 84: Cu run 8 SEM pore analysis area 1 spot 6
EDS Spot 7 - Det 2



eZAF Smart Quant Results

Element	Weight %	Atomic %	Net Int.	Error %	Kratio	Z	A	F
AlK	1.05	2.43	103.48	17.49	0.0022	1.1618	0.1819	1.0023
CuK	98.95	97.57	12855.56	1.28	0.9878	0.9981	1.0000	1.0001

Figure 85: Cu run 8 SEM pore analysis area 1 spot 7

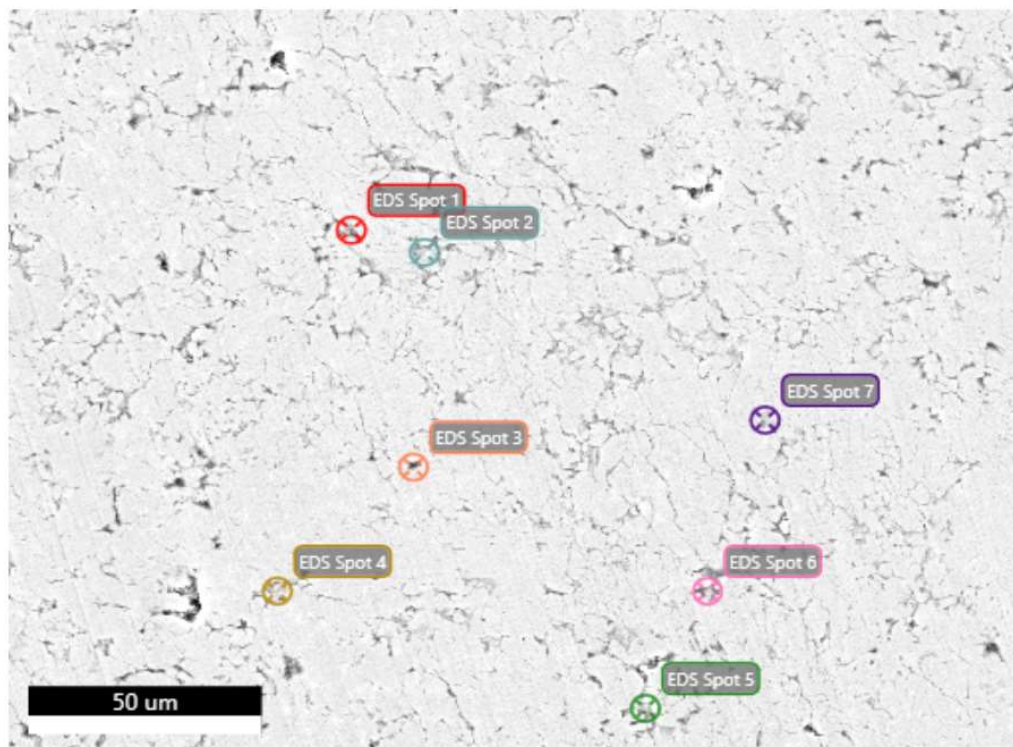
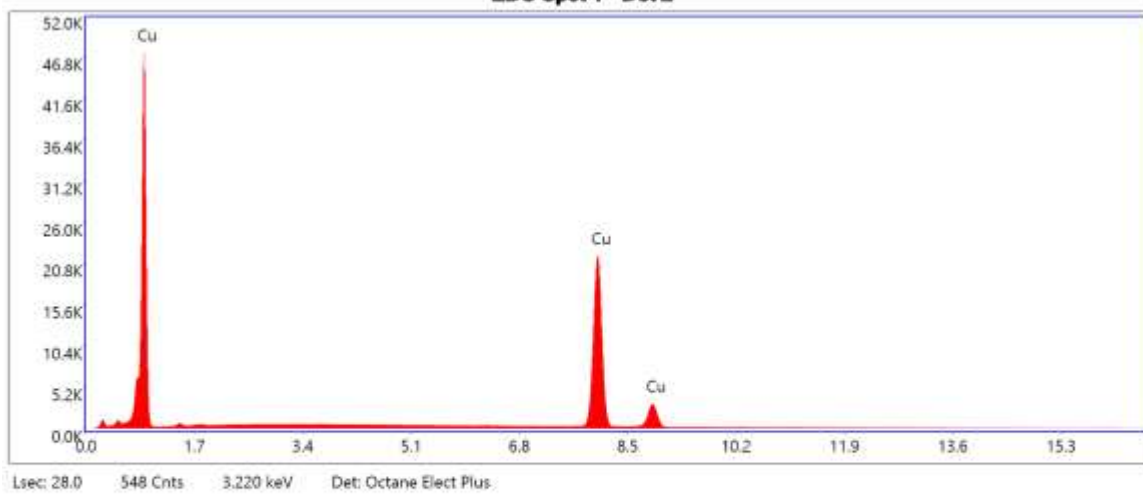


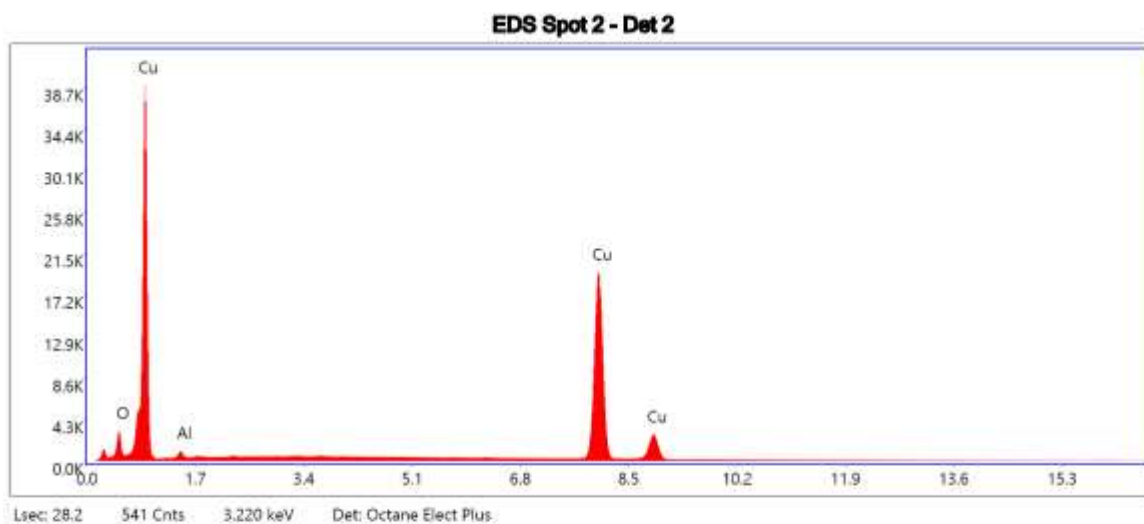
Figure 86: Cu run 8 SEM pore analysis area 2
EDS Spot 1 - Det 2



eZAF Smart Quant Results

Element	Weight %	Atomic %	Net Int.	Error %	Kratio	Z	A	F
CuK	100.00	100.00	12623.45	1.28	1.0000	1.0000	1.0000	1.0000

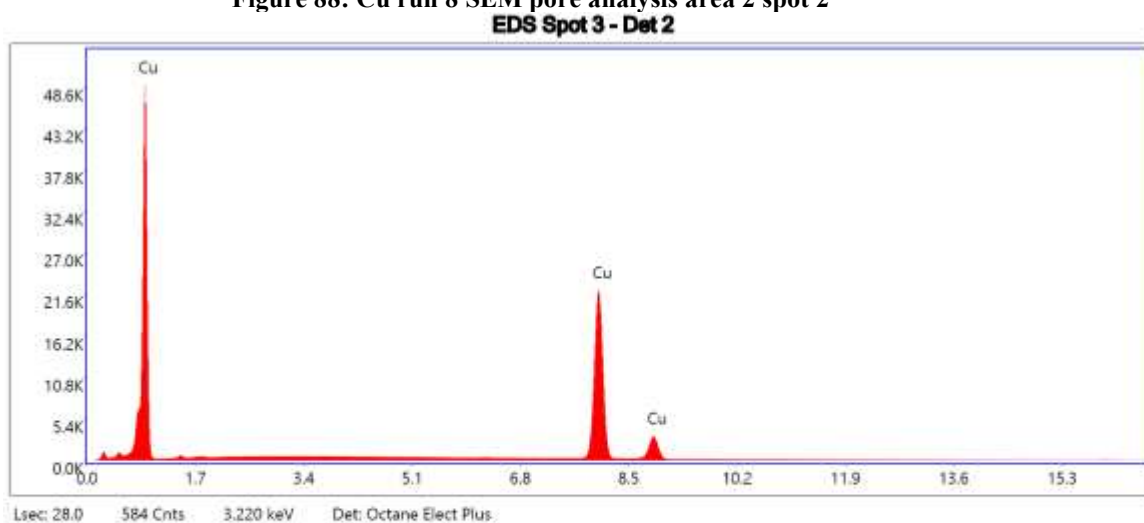
Figure 87: Cu run 8 SEM pore analysis area 2 spot 1



eZAF Smart Quant Results

Element	Weight %	Atomic %	Net Int.	Error %	Kratio	Z	A	F
O K	6.22	20.28	643.69	8.58	0.0246	1.2573	0.3142	1.0000
AlK	2.42	4.67	237.18	12.52	0.0053	1.1373	0.1922	1.0023
CuK	91.37	75.04	11184.40	1.31	0.8936	0.9754	1.0018	1.0010

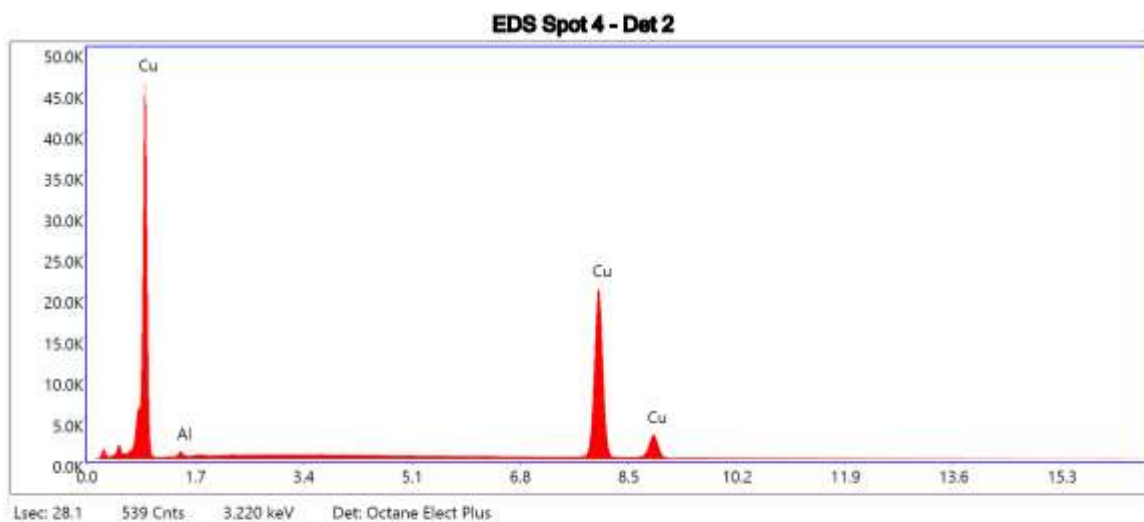
Figure 88: Cu run 8 SEM pore analysis area 2 spot 2



eZAF Smart Quant Results

Element	Weight %	Atomic %	Net Int.	Error %	Kratio	Z	A	F
CuK	100.00	100.00	12790.33	1.28	1.0000	1.0000	1.0000	1.0000

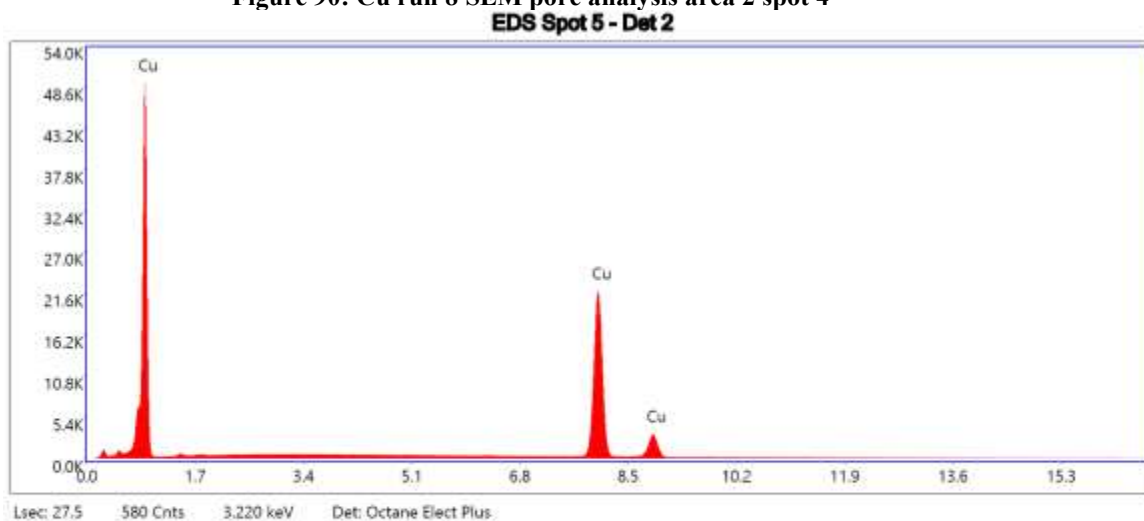
Figure 89: Cu run 8 SEM pore analysis area 2 spot 3



eZAF Smart Quant Results

Element	Weight %	Atomic %	Net Int.	Error %	Kratio	Z	A	F
AlK	1.85	4.26	174.38	14.16	0.0040	1.1602	0.1833	1.0023
CuK	98.15	95.74	12056.37	1.29	0.9784	0.9966	1.0000	1.0003

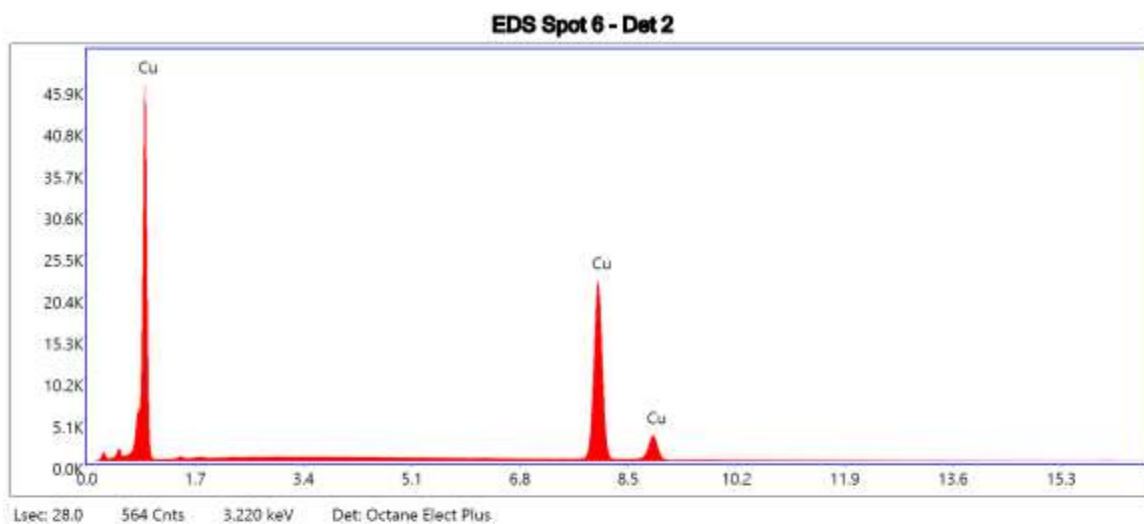
Figure 90: Cu run 8 SEM pore analysis area 2 spot 4



eZAF Smart Quant Results

Element	Weight %	Atomic %	Net Int.	Error %	Kratio	Z	A	F
CuK	100.00	100.00	12859.29	1.28	1.0000	1.0000	1.0000	1.0000

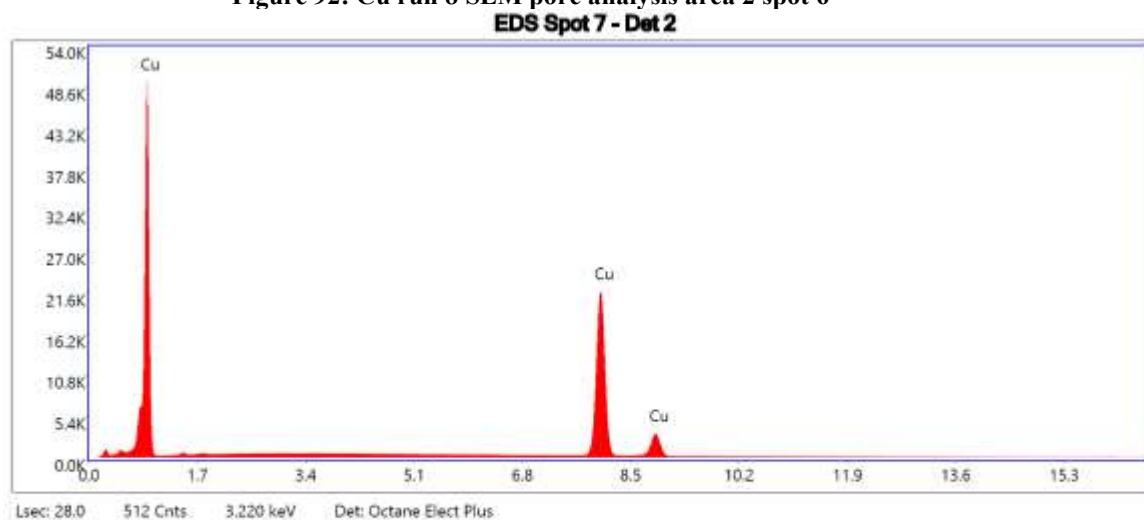
Figure 91: Cu run 8 SEM pore analysis area 2 spot 5



eZAF Smart Quant Results

Element	Weight %	Atomic %	Net Int.	Error %	Kratio	Z	A	F
CuK	100.00	100.00	12694.96	1.28	1.0000	1.0000	1.0000	1.0000

Figure 92: Cu run 8 SEM pore analysis area 2 spot 6



eZAF Smart Quant Results

Element	Weight %	Atomic %	Net Int.	Error %	Kratio	Z	A	F
CuK	100.00	100.00	12706.30	1.29	1.0000	1.0000	1.0000	1.0000

Figure 93: Cu run 8 SEM pore analysis area 2 spot 7

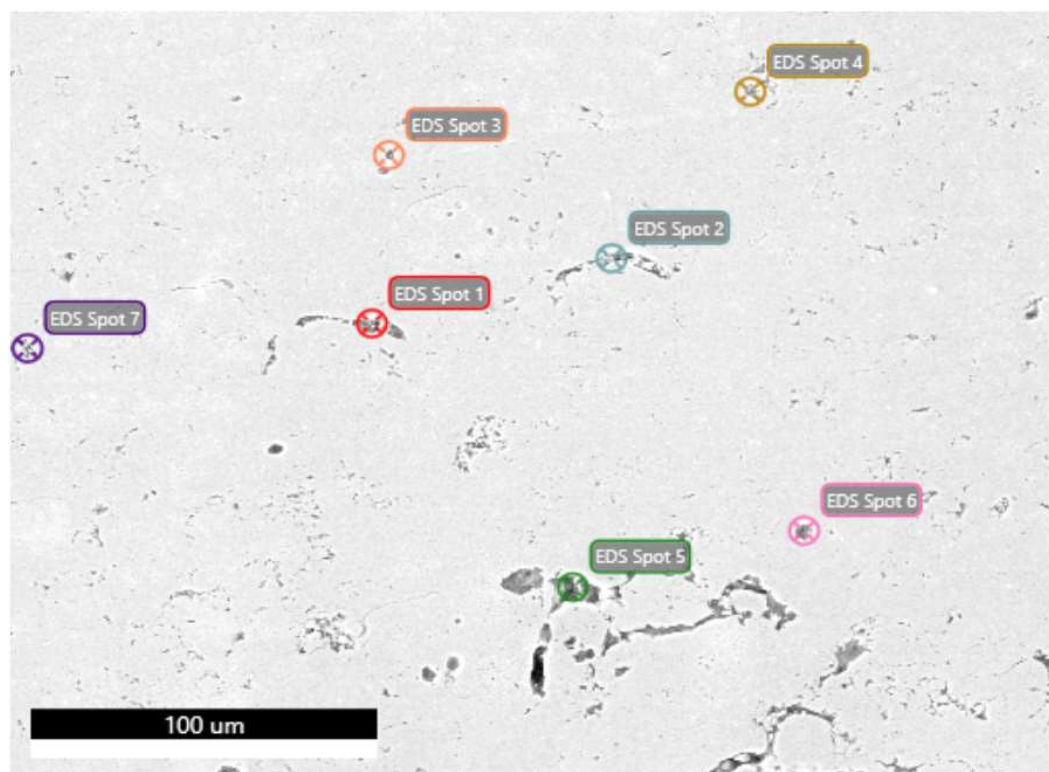
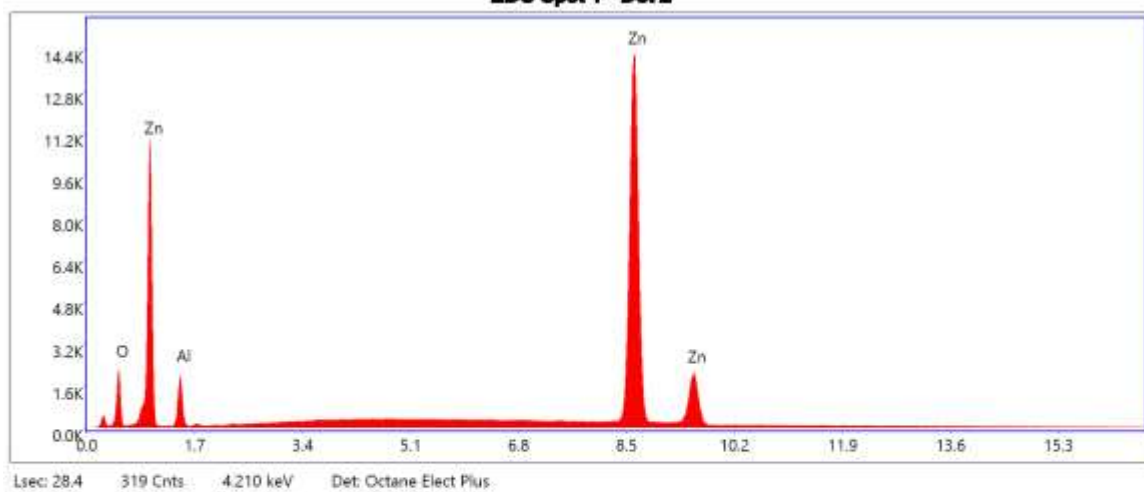


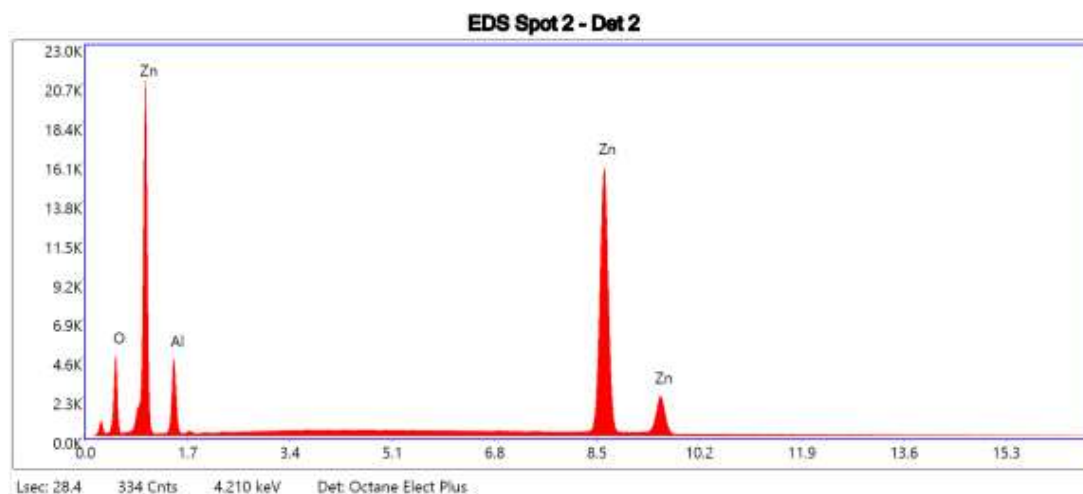
Figure 94: Zn run 11 SEM pore analysis area 1
EDS Spot 1 - Det 2



aZAF Smart Quant Results

Element	Weight %	Atomic %	Net Int.	Error %	Kratio	Z	A	F
O K	6.51	20.53	466.45	9.42	0.0195	1.2453	0.2411	1.0000
Al K	6.66	12.45	566.85	9.98	0.0139	1.1264	0.1852	1.0017
Zn K	86.83	67.02	8361.44	1.40	0.8430	0.9670	1.0021	1.0019

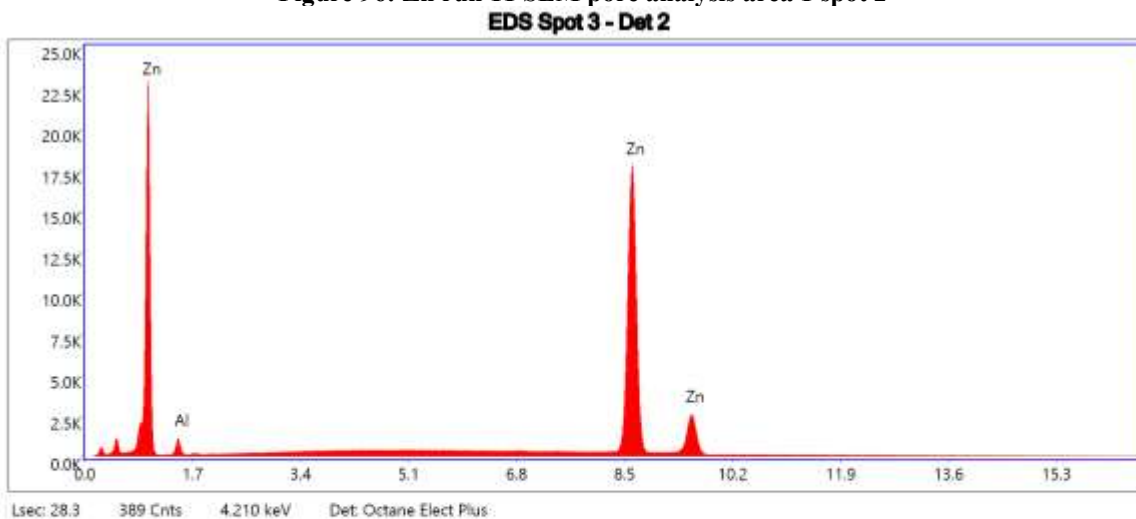
Figure 95: Zn run 11 SEM pore analysis area 1 spot 1



eZAF Smart Quant Results

Element	Weight %	Atomic %	Net Int.	Error %	Kratio	Z	A	F
O K	11.59	31.08	1076.36	9.00	0.0354	1.2181	0.2507	1.0000
AlK	11.63	18.50	1356.49	9.39	0.0261	1.1014	0.2037	1.0017
ZnK	76.78	50.42	9223.64	1.41	0.7295	0.9430	1.0036	1.0038

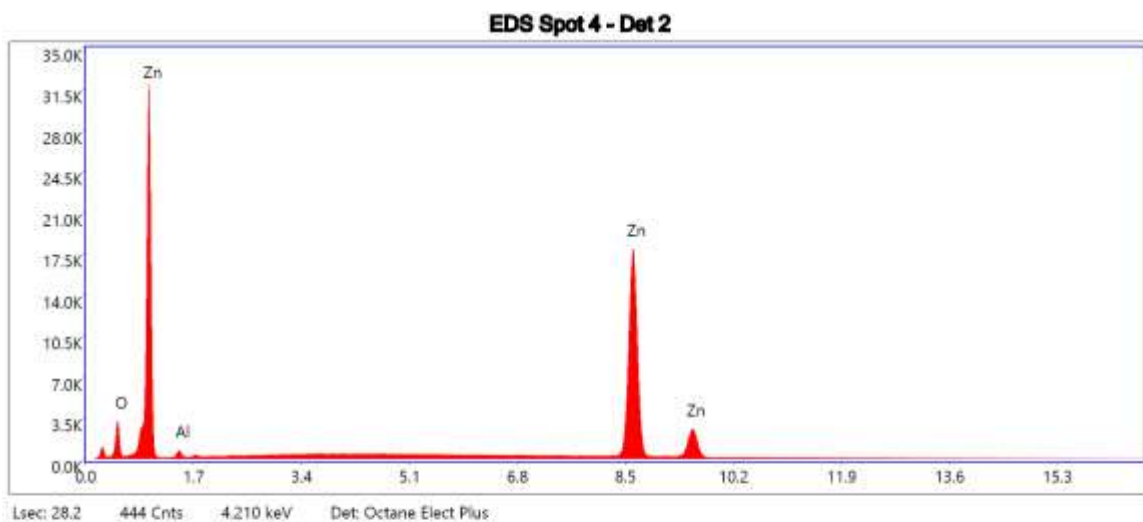
Figure 96: Zn run 11 SEM pore analysis area 1 spot 2



eZAF Smart Quant Results

Element	Weight %	Atomic %	Net Int.	Error %	Kratio	Z	A	F
AlK	3.49	8.06	312.73	10.84	0.0069	1.1544	0.1710	1.0018
ZnK	96.51	91.94	10580.95	1.34	0.9597	0.9937	1.0002	1.0005

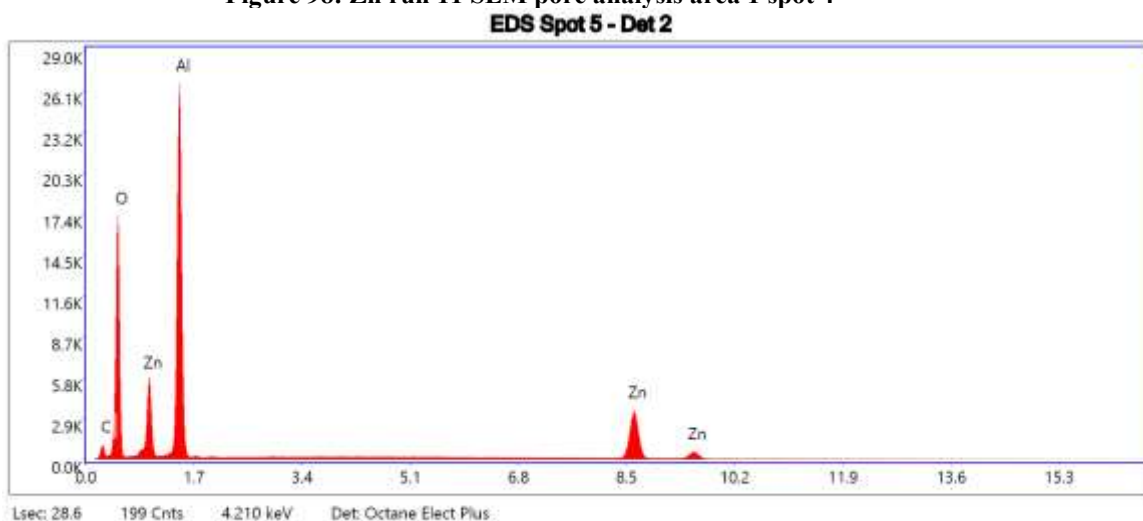
Figure 97: Zn run 11 SEM pore analysis area 1 spot 3



eZAF Smart Quant Results

Element	Weight %	Atomic %	Net Int.	Error %	Kratio	Z	A	F
O K	7.38	24.07	640.16	9.28	0.0225	1.2514	0.2439	1.0000
AlK	1.72	3.33	167.62	12.62	0.0035	1.1321	0.1770	1.0018
ZnK	90.90	72.60	10483.15	1.38	0.8872	0.9729	1.0020	1.0011

Figure 98: Zn run 11 SEM pore analysis area 1 spot 4

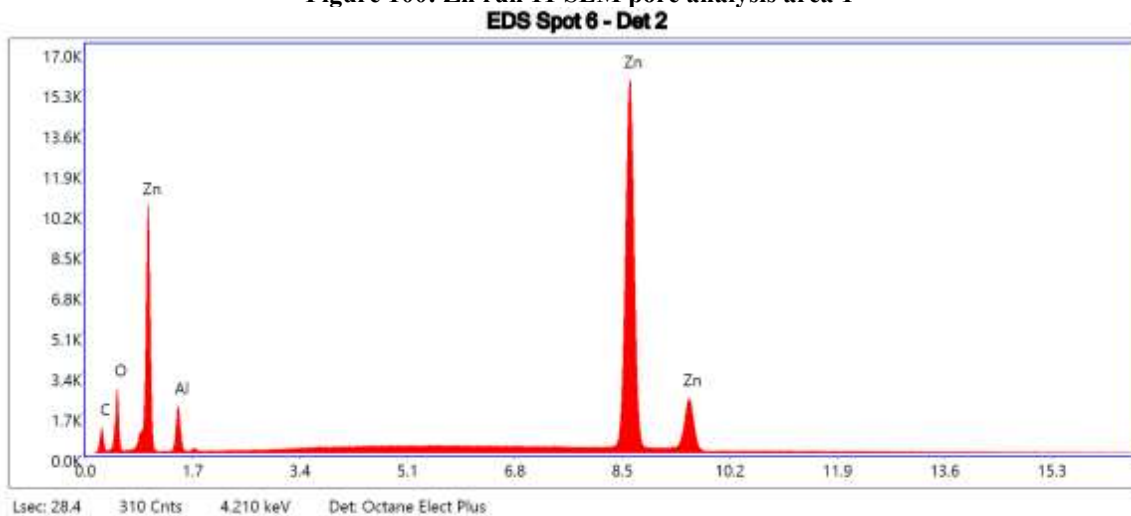


eZAF Smart Quant Results

Element	Weight %	Atomic %	Net Int.	Error %	Kratio	Z	A	F
C K	9.73	16.46	224.82	11.15	0.0166	1.1040	0.1548	1.0000
O K	43.46	55.21	4529.73	8.20	0.1298	1.0627	0.2810	1.0000
AlK	31.11	23.44	8106.77	6.40	0.1361	0.9545	0.4578	1.0011
ZnK	15.70	4.88	1953.90	2.14	0.1347	0.8026	1.0158	1.0520

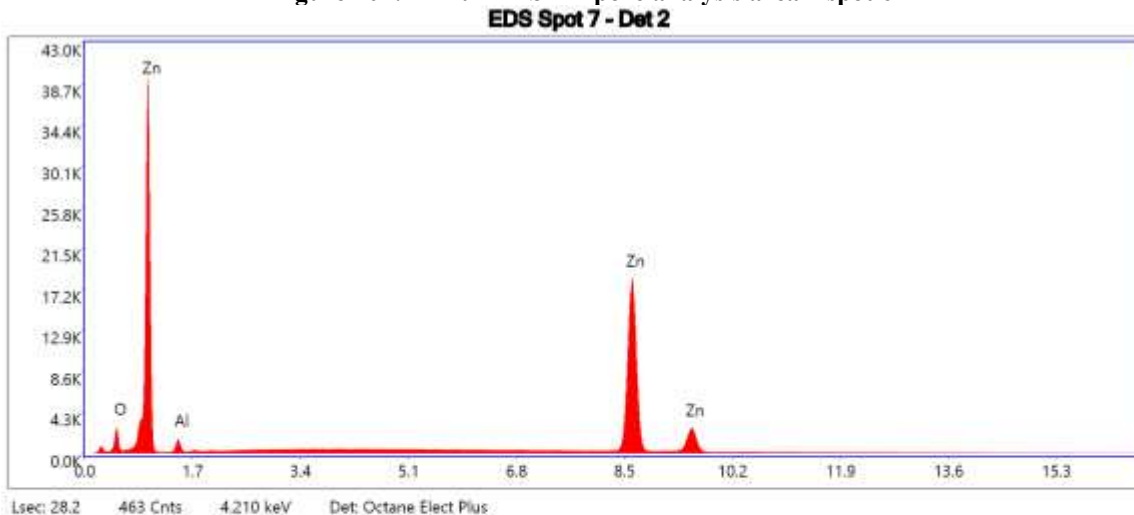
Figure 99: Zn run 11 SEM pore analysis area 1 spot 5

Figure 100: Zn run 11 SEM pore analysis area 1

**eZAF Smart Quant Results**

Element	Weight %	Atomic %	Net Int.	Error %	Kratio	Z	A	F
C K	10.41	32.07	212.72	11.36	0.0177	1.2423	0.1366	1.0000
O K	7.61	17.60	602.79	9.59	0.0194	1.2001	0.2124	1.0000
AlK	4.89	6.70	572.25	9.81	0.0108	1.0851	0.2031	1.0018
ZnK	77.08	43.62	9323.67	1.42	0.7221	0.9290	1.0053	1.0030

Figure 101: Zn run 11 SEM pore analysis area 1 spot 6

**eZAF Smart Quant Results**

Element	Weight %	Atomic %	Net Int.	Error %	Kratio	Z	A	F
O K	3.53	12.51	299.00	10.33	0.0105	1.2633	0.2359	1.0000
AlK	3.07	6.46	297.96	11.57	0.0061	1.1429	0.1746	1.0018
ZnK	93.40	81.03	10866.23	1.36	0.9198	0.9829	1.0011	1.0009

Figure 102: Zn run 11 SEM pore analysis area 1 spot 7

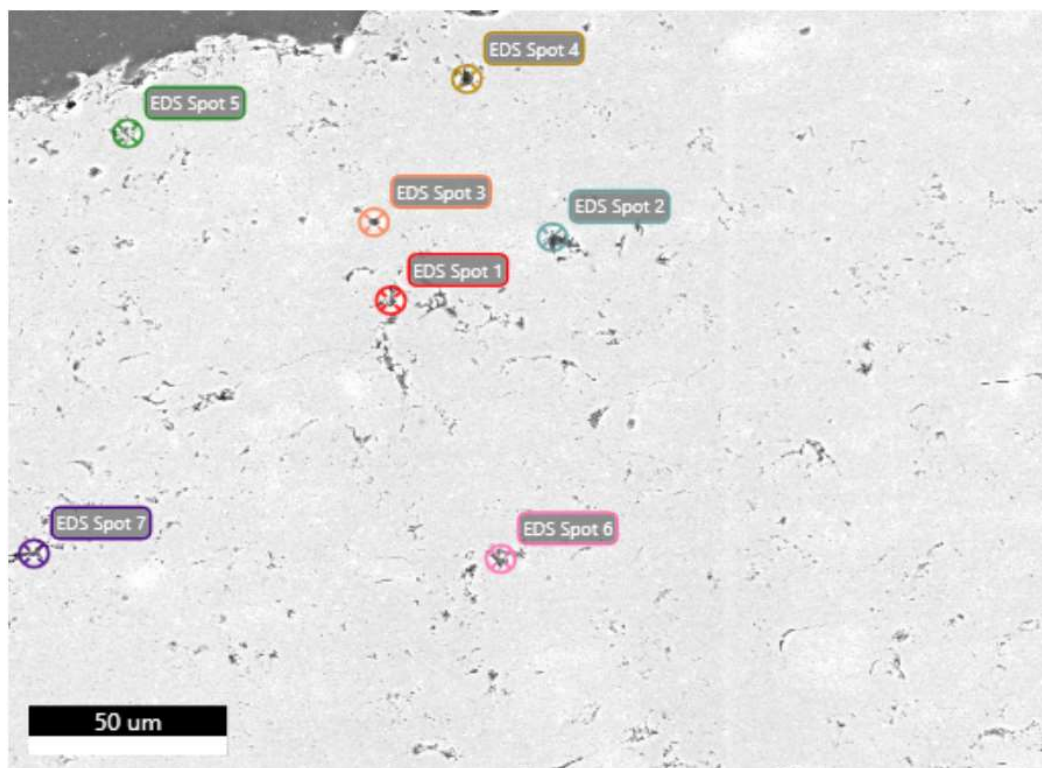
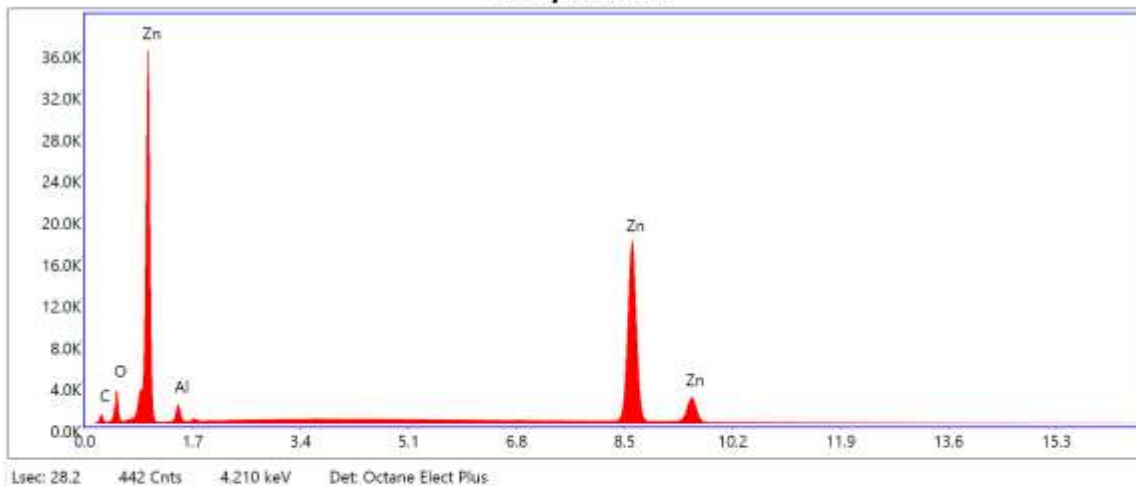


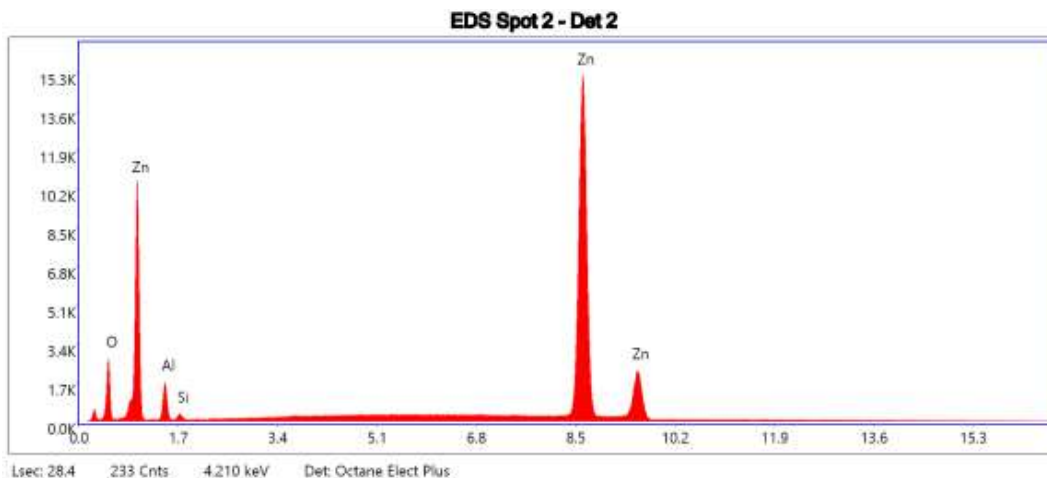
Figure 103: Zn run 11 SEM pore analysis area 2
EDS Spot 1 - Det 2



eZAF Smart Quant Results

Element	Weight %	Atomic %	Net Int.	Error %	Kratio	Z	A	F
C K	5.14	18.51	103.03	13.79	0.0085	1.2676	0.1301	1.0000
O K	7.13	19.25	620.13	9.47	0.0198	1.2246	0.2267	1.0000
Al K	4.49	7.20	509.37	10.32	0.0095	1.1076	0.1910	1.0018
Zn K	83.24	55.04	10361.99	1.40	0.7953	0.9498	1.0036	1.0022

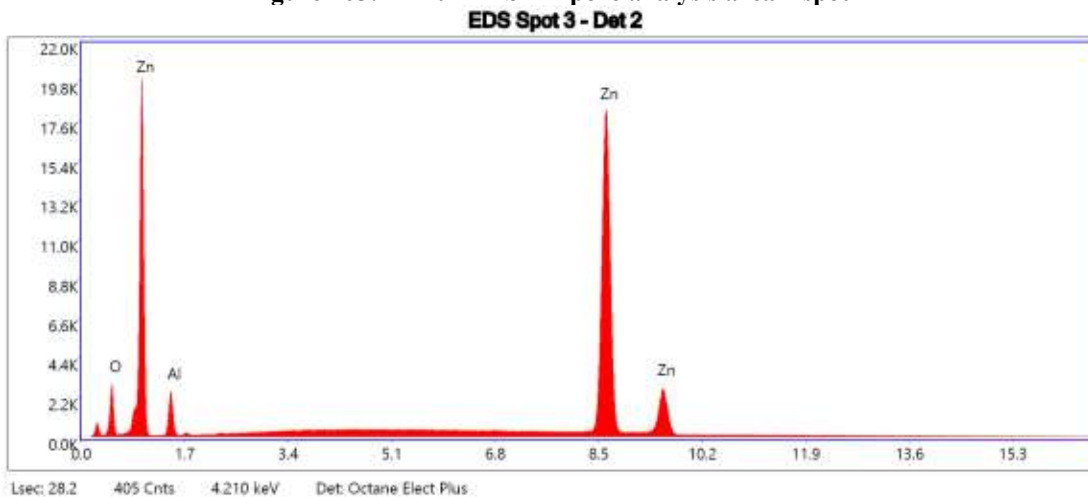
Figure 104: Zn run 11 SEM pore analysis area 2 spot 1



eZAF Smart Quant Results

Element	Weight %	Atomic %	Net Int.	Error %	Kratio	Z	A	F
OK	7.87	24.21	618.54	9.26	0.0238	1.2412	0.2437	1.0000
AlK	5.50	10.03	510.40	10.02	0.0115	1.1227	0.1860	1.0018
SiK	0.59	1.03	80.60	13.33	0.0018	1.1504	0.2587	1.0032
ZnK	86.03	64.73	8990.22	1.39	0.8326	0.9636	1.0024	1.0020

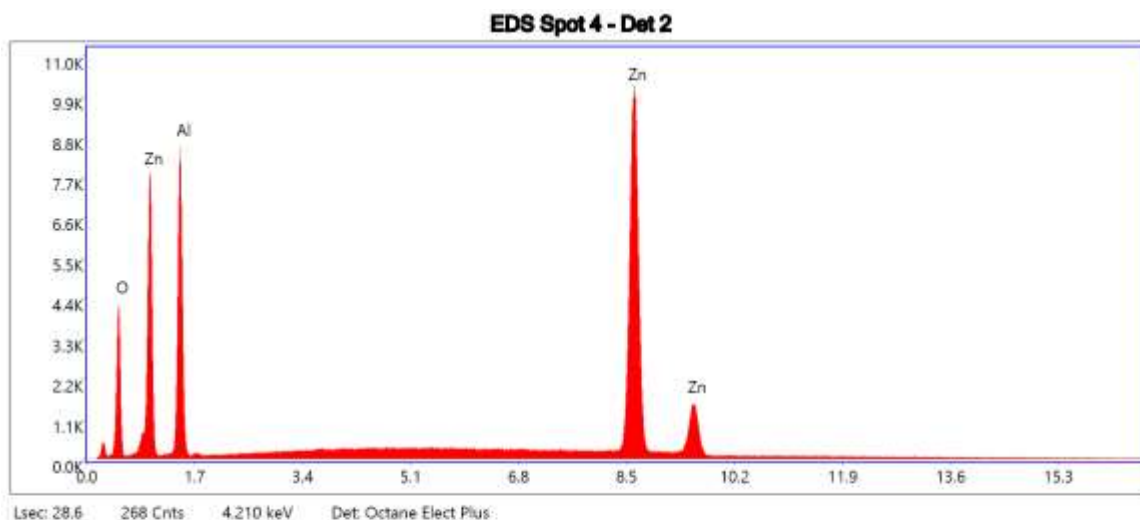
Figure 105: Zn run 11 SEM pore analysis area 2 spot 2



eZAF Smart Quant Results

Element	Weight %	Atomic %	Net Int.	Error %	Kratio	Z	A	F
OK	6.46	20.39	597.36	9.32	0.0194	1.2455	0.2410	1.0000
AlK	6.63	12.42	728.63	9.92	0.0139	1.1267	0.1851	1.0017
ZnK	86.91	67.19	10811.64	1.36	0.8440	0.9673	1.0020	1.0019

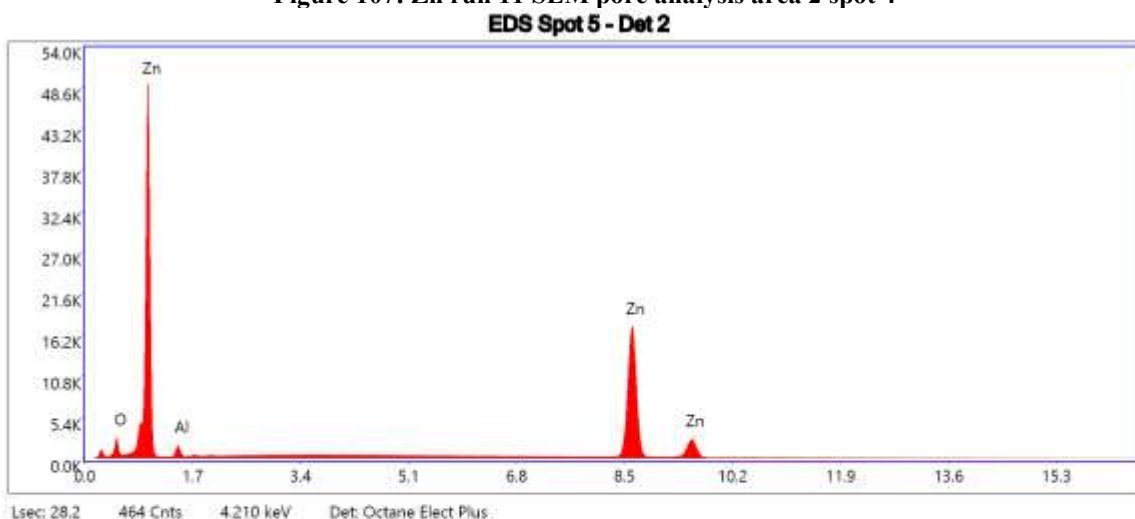
Figure 106: Zn run 11 SEM pore analysis area 2 spot 3



eZAF Smart Quant Results

Element	Weight %	Atomic %	Net Int.	Error %	Kratio	Z	A	F
O K	13.74	32.02	1031.06	8.84	0.0413	1.1908	0.2524	1.0000
AlK	23.16	32.00	2545.42	8.76	0.0598	1.0759	0.2394	1.0015
ZnK	63.09	35.98	6081.48	1.50	0.5862	0.9179	1.0048	1.0075

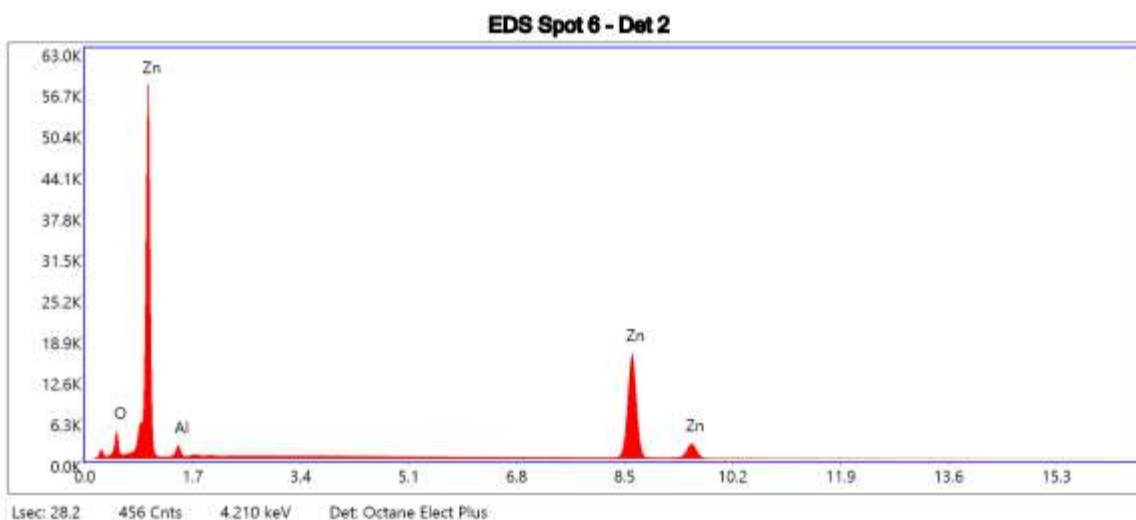
Figure 107: Zn run 11 SEM pore analysis area 2 spot 4



eZAF Smart Quant Results

Element	Weight %	Atomic %	Net Int.	Error %	Kratio	Z	A	F
O K	5.19	17.28	432.74	10.03	0.0156	1.2537	0.2388	1.0000
AlK	4.78	9.42	463.42	10.65	0.0098	1.1342	0.1798	1.0018
ZnK	90.03	73.30	10177.64	1.38	0.8800	0.9745	1.0016	1.0014

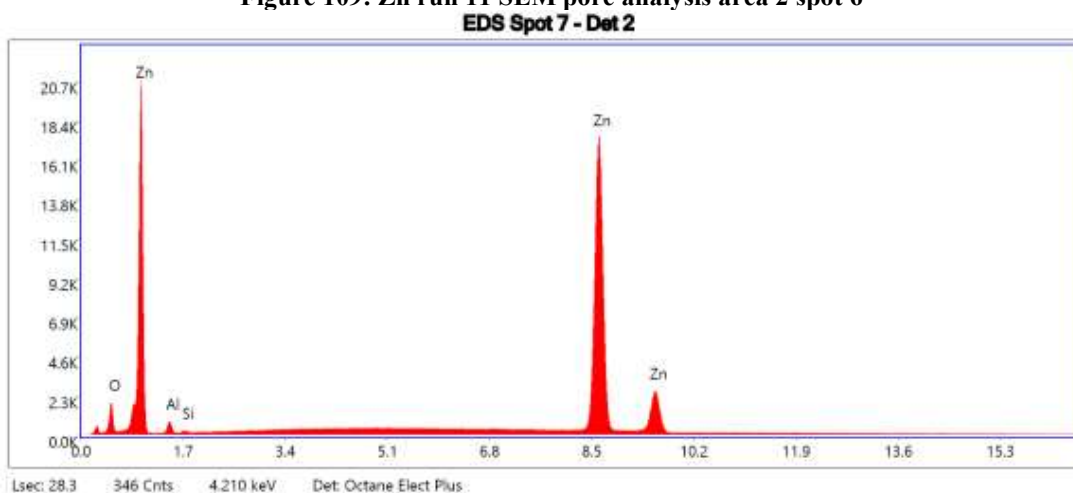
Figure 108: Zn run 11 SEM pore analysis area 2 spot 5



eZAF Smart Quant Results

Element	Weight %	Atomic %	Net Int.	Error %	Kratio	Z	A	F
O K	9.49	28.23	817.07	9.15	0.0290	1.2363	0.2476	1.0000
AlK	5.65	9.97	569.85	10.96	0.0119	1.1183	0.1874	1.0017
ZnK	84.86	61.79	9566.99	1.40	0.8182	0.9595	1.0028	1.0021

Figure 109: Zn run 11 SEM pore analysis area 2 spot 6



eZAF Smart Quant Results

Element	Weight %	Atomic %	Net Int.	Error %	Kratio	Z	A	F
O K	1.80	6.85	137.47	12.36	0.0053	1.2734	0.2329	1.0000
AlK	1.28	2.88	109.87	14.04	0.0025	1.1521	0.1694	1.0018
SiK	0.00	0.00	0.00	99.99	0.0000	1.1806	0.2472	1.0033
ZnK	96.92	90.27	10299.45	1.35	0.9621	0.9917	1.0005	1.0004

Figure 110: Zn run 11 SEM pore analysis area 2 spot 7

10. Appendix B: Model Diagnostic Graphs

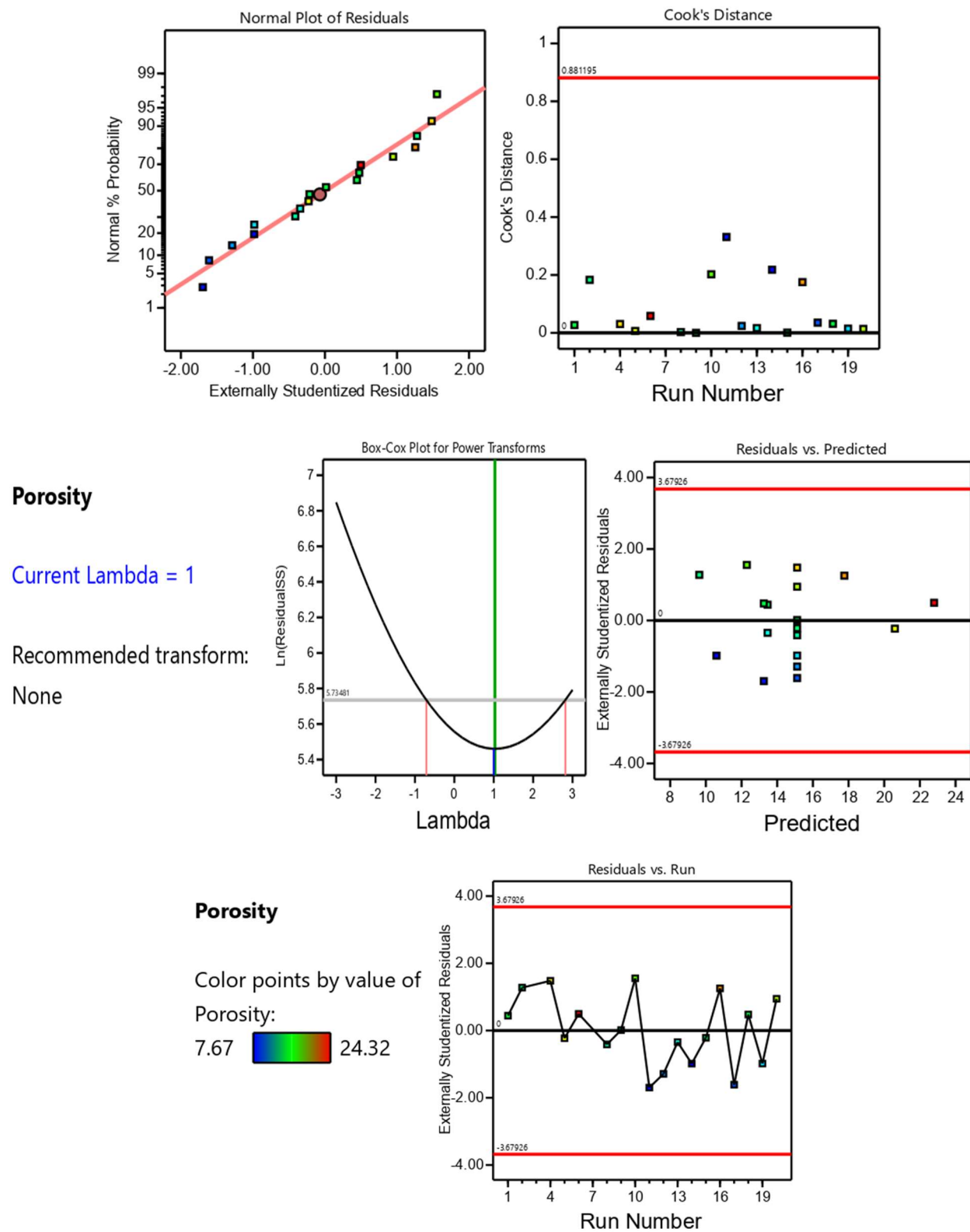


Figure 111: Cu Porosity Model Diagnostics

Grain size

Current Lambda = 1

Recommended transform:

None

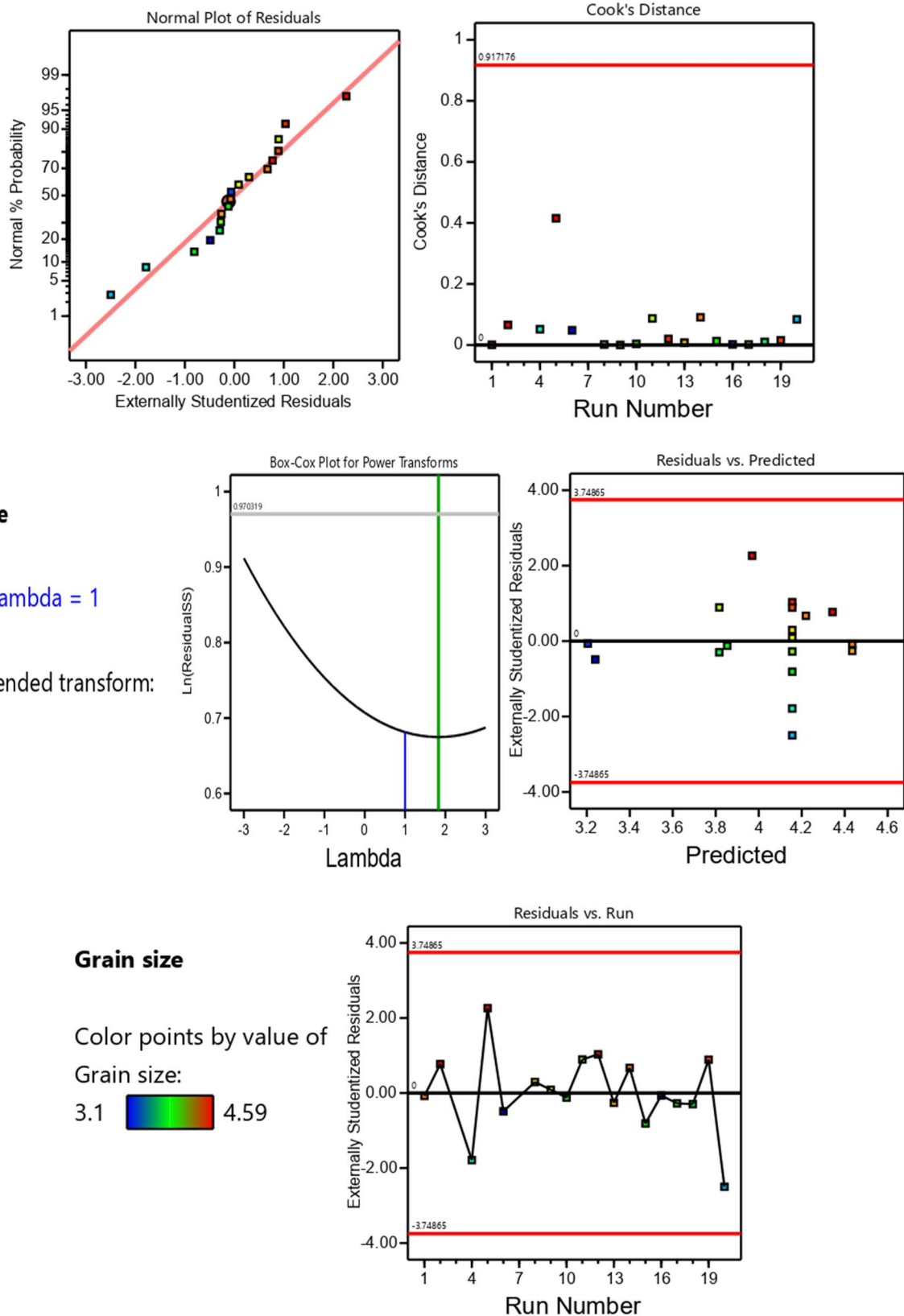


Figure 112: Cu Grain Size 75 Heating Element Voltage Model Diagnostics

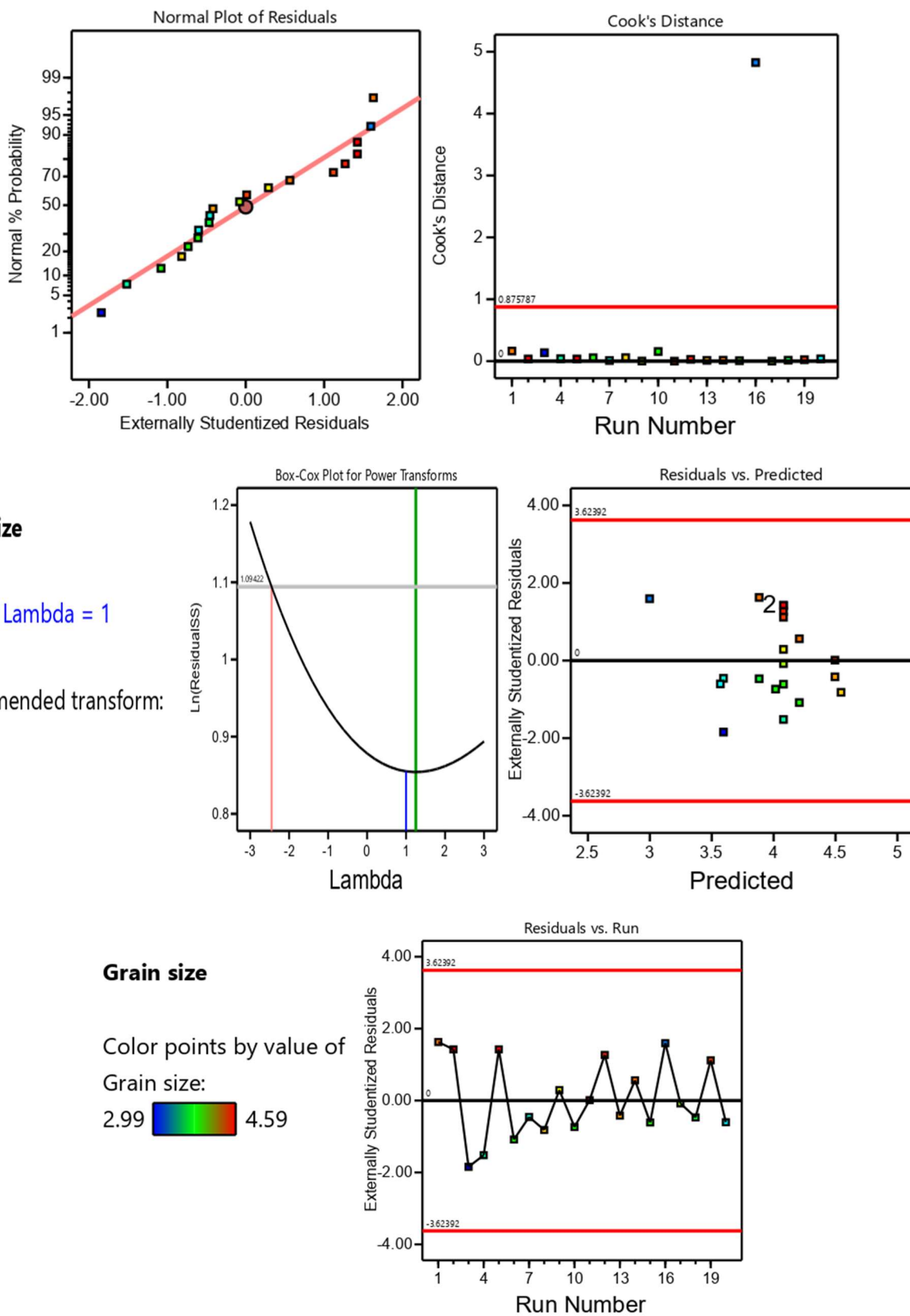
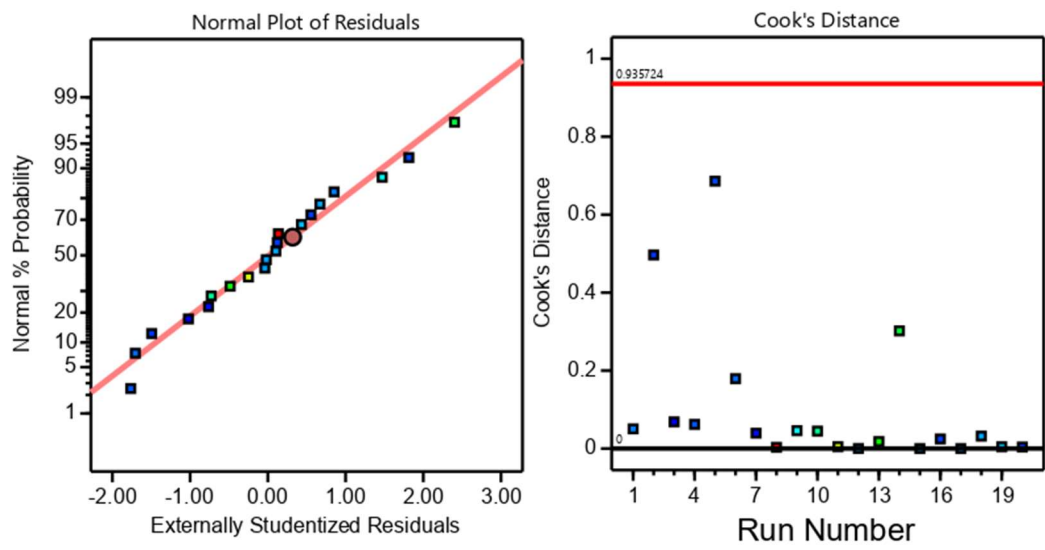


Figure 113: Cu Grain Size 80 Heating Element Voltage Model Diagnostics



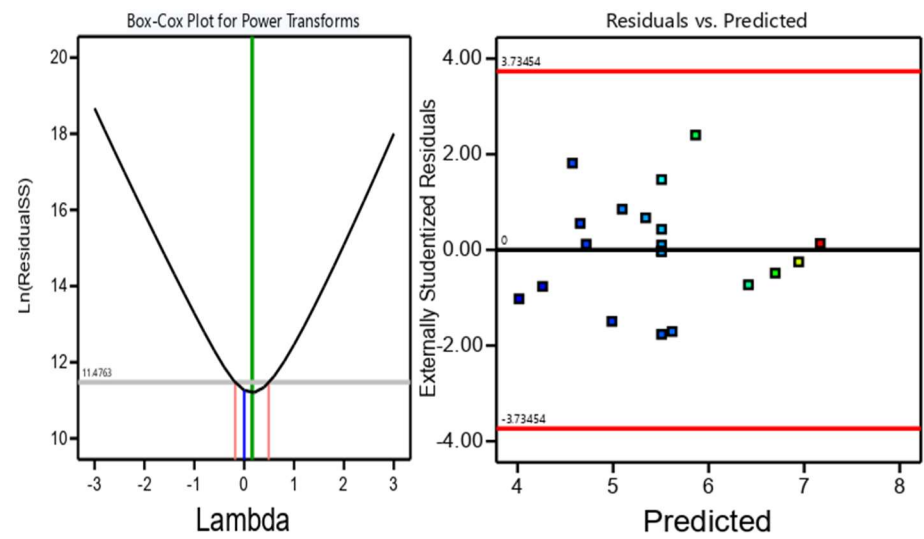
ln(Thickness)

Current Lambda = 0

Recommended transform:

Log

(Lambda = 0)



ln(Thickness)

Color points by value of

Thickness :

3.745  7.200

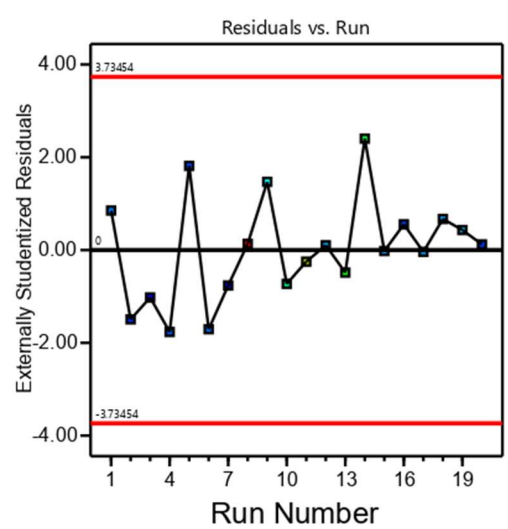
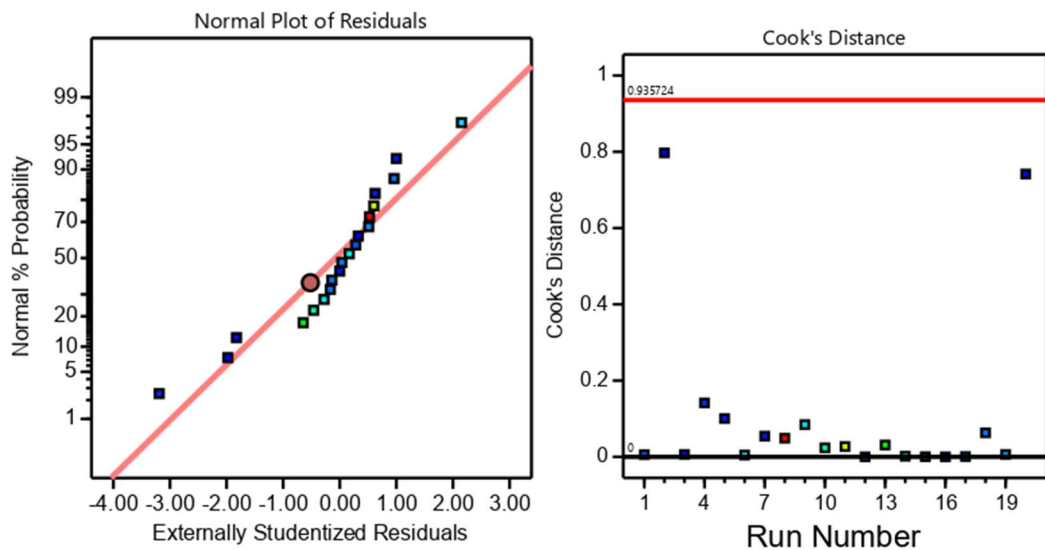


Figure 114: Cu Thickness 75 Heating Element Voltage Model Diagnostics



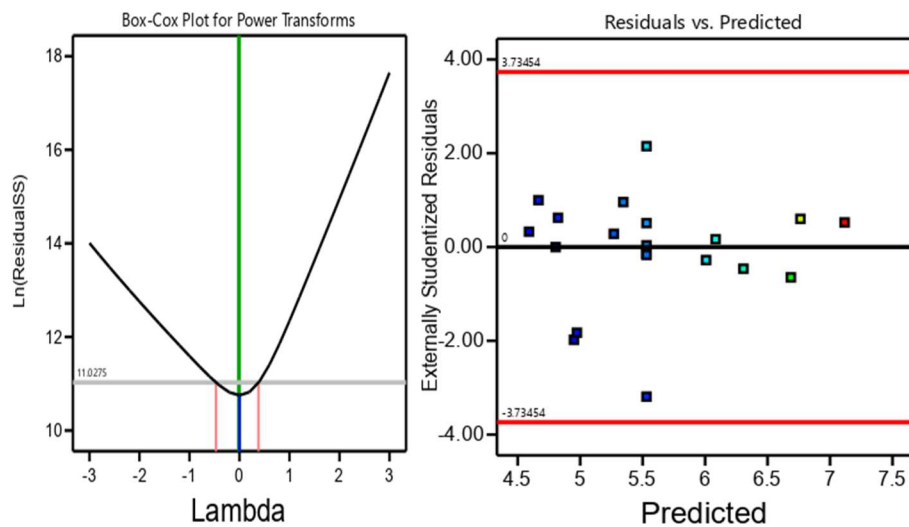
ln(Thickness)

Current Lambda = 0

Recommended transform:

Log

(Lambda = 0)



ln(Thickness)

Color points by value of

Thickness :

4.654  7.200

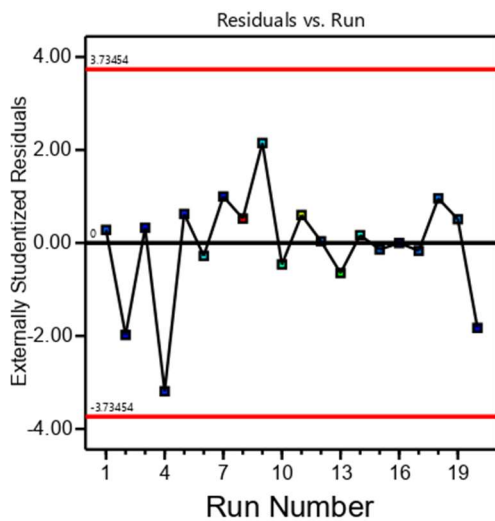


Figure 115: Cu Thickness 80 Heating Element Voltage Model Diagnostics

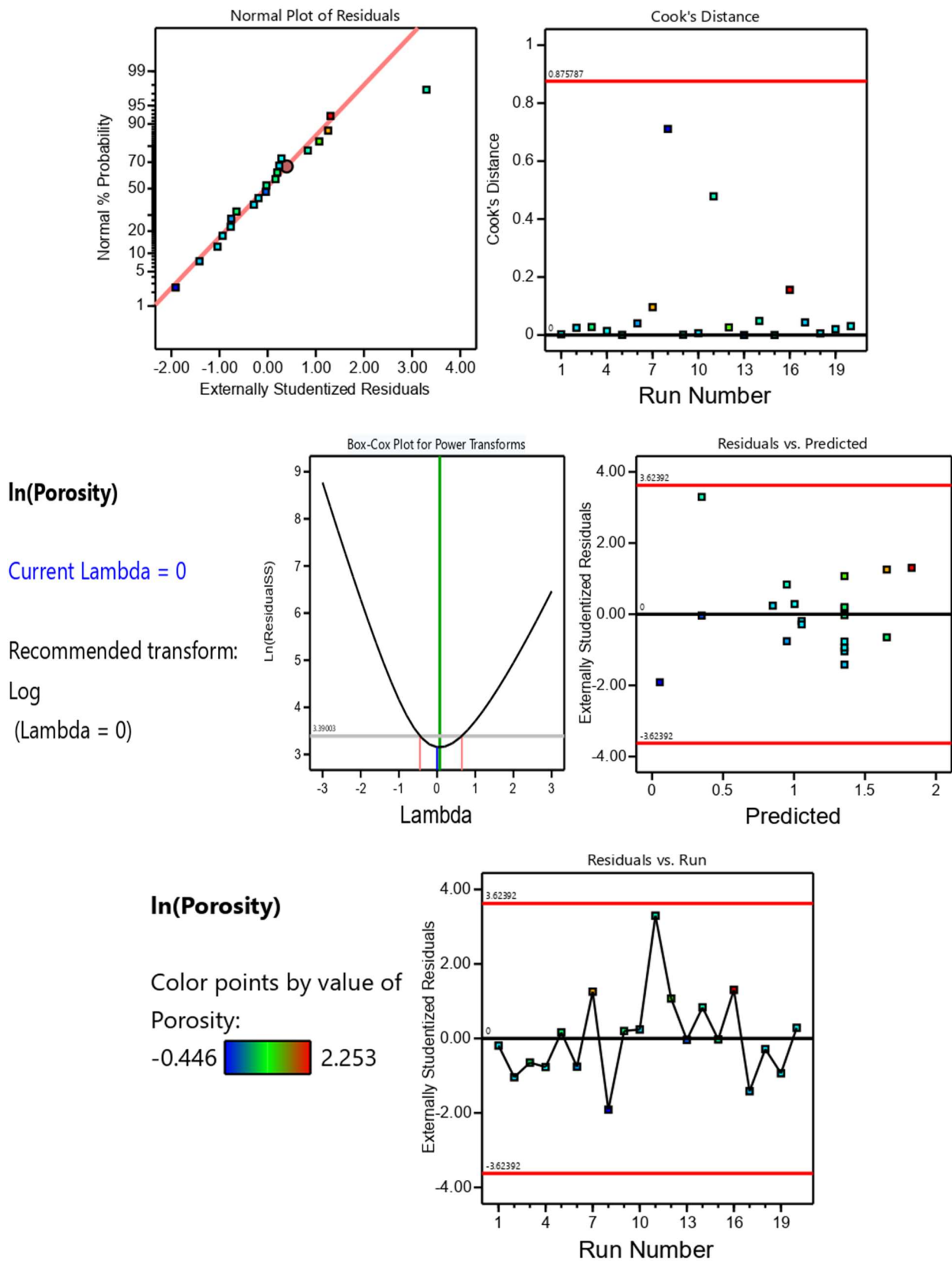


Figure 116: Zn Porosity Model Diagnostics

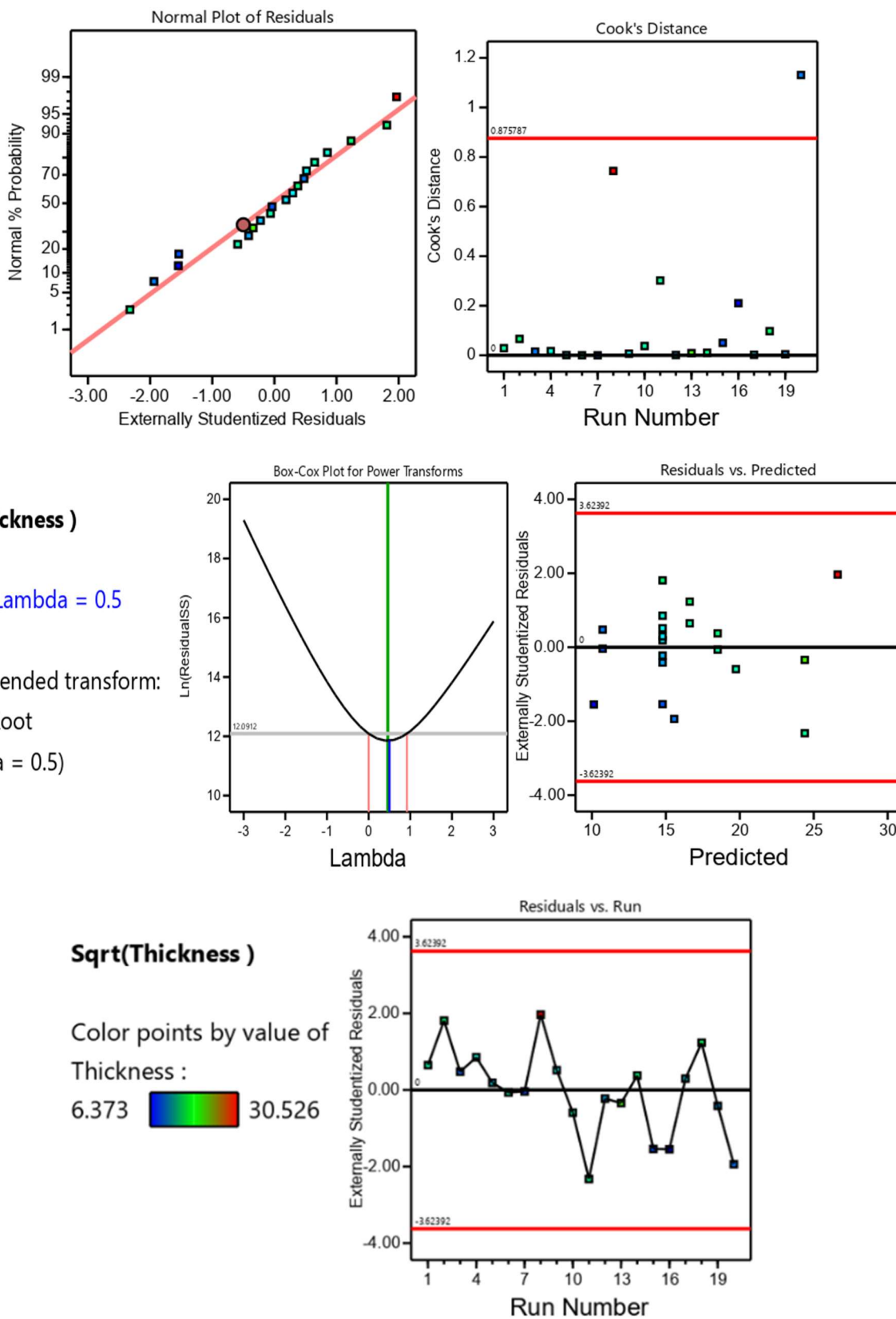


Figure 117: Zn Thickness Model Diagnostics

11. Appendix C: Raw Data

Table XVIII: Copper CS grain size analysis

Slice	Count	Average Size	%Area	Feret	Min Feret	Feret Ratio	Grain Size (um)
Cu Run 1 Etched Center x50.tif	218.00	53.45	37.56	16.10	8.93	1.80	4.12
Cu Run 1 Etched Left x50.tif	152.00	55.22	34.91	17.27	9.25	1.87	4.19
Cu Run 1 Etched LeftCenter x50.tif	169.00	66.90	38.07	17.83	10.06	1.77	4.61
Cu Run 1 Etched Right x50.tif	84.00	72.92	40.04	18.40	9.86	1.87	4.82
Cu Run 1 Etched RightCenter x50.tif	154.00	57.34	34.00	16.99	9.12	1.86	4.27
Cu Run 2 Etched Center x50.tif	85.00	55.69	23.13	16.16	9.11	1.77	4.21
Cu Run 2 Etched Left x50.tif	98.00	70.96	40.24	18.17	9.81	1.85	4.75
Cu Run 2 Etched Right x50.tif	71.00	71.61	33.95	17.25	10.15	1.70	4.77
NA RUN 3							
Cu Run 4 Etched Center x50.tif	55.00	37.94	10.58	14.52	7.34	1.98	3.47
Cu Run 4 Etched Left x50.tif	38.00	37.98	8.67	13.58	7.32	1.85	3.48
Cu Run 4 Etched Right x50.tif	46.00	41.88	9.90	15.56	7.23	2.15	3.65
Cu Run 5 Etched Center x50.tif	98.00	75.45	31.92	19.06	10.56	1.81	4.90
Cu Run 5 Etched Left x50.tif	72.00	63.30	21.63	16.92	9.97	1.70	4.49
Cu Run 5 Etched RightCenter x50.tif	90.00	60.17	32.71	16.04	8.87	1.81	4.38
Cu Run 6 Etched Center x50.tif	83.00	28.40	10.07	11.85	5.22	2.27	3.01
Cu Run 6 Etched CenterLeft x50.tif	67.00	36.25	11.35	13.38	6.33	2.11	3.40
Cu Run 6 Etched CenterRight x50.tif	48.00	30.51	8.51	12.21	5.89	2.07	3.12
Cu Run 6 Etched Left x50.tif	32.00	29.33	8.73	11.29	6.06	1.86	3.06
Cu Run 6 Etched Right x50.tif	25.00	25.99	5.88	11.21	5.33	2.10	2.88
NA RUN 7							
Cu Run 8 Etched Center Tip x50.tif	141.00	58.86	23.50	16.05	9.15	1.75	4.33
Cu Run 8 Etched Center x50.tif	258.00	51.36	31.77	16.16	8.72	1.85	4.04
Cu Run 8 Etched Left x50.tif	296.00	52.79	37.34	16.51	8.60	1.92	4.10
Cu Run 8 Etched LeftCenter Edge x50.tif	224.00	70.76	38.04	18.14	10.01	1.81	4.75
Cu Run 8 Etched LeftCenter x50.tif	290.00	49.47	34.48	15.89	8.50	1.87	3.97
Cu Run 8 Etched Right x50.tif	201.00	62.15	35.85	17.37	9.22	1.88	4.45
Cu Run 8 Etched RightCenter Edge x50.tif	299.00	58.32	41.65	16.52	9.15	1.81	4.31
Cu Run 8 Etched RightCenter x50.tif	267.00	54.05	34.46	16.41	8.67	1.89	4.15
Cu Run 9 Etched Center x50.tif	243.00	63.02	38.03	17.14	9.19	1.87	4.48
Cu Run 9 Etched Left x50.tif	156.00	48.19	25.44	15.45	8.10	1.91	3.92
Cu Run 9 Etched LeftCenter x50.tif	227.00	55.06	30.91	16.73	8.76	1.91	4.19
Cu Run 9 Etched Right x50.tif	159.00	52.76	28.14	17.01	8.55	1.99	4.10
Cu Run 9 Etched RightCenter x50.tif	233.00	56.19	32.29	16.65	8.88	1.88	4.23
Cu Run 10 Etched Center x50.tif	277.00	49.02	33.75	15.59	8.40	1.86	3.95
Cu Run 10 Etched Left x50.tif	169.00	42.23	19.88	14.20	7.04	2.02	3.67
Cu Run 10 Etched LeftCenter x50.tif	283.00	47.78	33.41	15.56	8.41	1.85	3.90
Cu Run 10 Etched Right x50.tif	86.00	44.42	18.98	14.93	7.30	2.05	3.76

Cu Run 10 Etched RightCenter x50.tif	233.00	46.15	26.69	15.20	7.85	1.94	3.83
Cu Run 11 Etched Center x50.tif	324.00	43.39	34.93	14.90	8.33	1.79	3.72
Cu Run 11 Etched CenterEdge x50.tif	176.00	56.15	32.32	16.80	8.85	1.90	4.23
Cu Run 11 Etched Left x50.tif	233.00	50.39	35.05	16.10	8.67	1.86	4.00
Cu Run 11 Etched LeftCenter x50.tif	283.00	50.32	35.49	15.80	8.55	1.85	4.00
Cu Run 11 Etched LeftCenterEdge x50.tif	271.00	56.03	37.66	17.27	8.88	1.95	4.22
Cu Run 11 Etched Right x50.tif	269.00	60.55	40.45	17.38	9.28	1.87	4.39
Cu Run 11 Etched RightCenter x50.tif	282.00	55.34	38.59	16.53	8.90	1.86	4.20
Cu Run 11 Etched RightCenterEdge x50.tif	197.00	51.26	36.74	16.26	8.49	1.92	4.04
Cu Run 12 Etched Center x50.tif	206.00	55.55	39.15	17.55	9.26	1.89	4.20
Cu Run 12 Etched Left x50.tif	56.00	63.93	29.53	16.82	9.13	1.84	4.51
Cu Run 12 Etched LeftCenter x50.tif	124.00	60.00	34.06	17.42	9.04	1.93	4.37
Cu Run 12 Etched Right x50.tif	110.00	74.42	44.44	18.49	9.57	1.93	4.87
Cu Run 12 Etched RightCenter x50.tif	120.00	70.32	35.93	18.25	9.62	1.90	4.73
Cu Run 13 Etched Center x50.tif	178.00	68.92	33.38	17.57	9.83	1.79	4.68
Cu Run 13 Etched Left x50.tif	120.00	56.74	16.91	16.71	8.80	1.90	4.25
Cu Run 13 Etched LeftCenter x50.tif	118.00	59.45	17.38	16.55	8.91	1.86	4.35
Cu Run 13 Etched Right x50.tif	131.00	54.06	17.53	15.76	9.02	1.75	4.15
Cu Run 13 Etched RightCenter x50.tif	135.00	57.80	19.31	15.97	9.30	1.72	4.29
Cu Run 14 Etched Center x50.tif	173.00	73.69	31.64	17.91	9.34	1.92	4.84
Cu Run 14 Etched Left x50.tif	133.00	66.21	25.63	17.63	8.95	1.97	4.59
Cu Run 14 Etched LeftCenter x50.tif	75.00	50.59	12.67	15.74	8.18	1.92	4.01
Cu Run 14 Etched Right x50.tif	80.00	77.29	37.02	17.75	8.98	1.98	4.96
Cu Run 14 Etched RightCenter x50.tif	79.00	38.40	9.75	12.95	7.23	1.79	3.50
Cu Run 15 Etched Center x50.tif	177.00	47.39	27.88	15.62	7.86	1.99	3.88
Cu Run 15 Etched Left x50.tif	100.00	40.96	20.71	14.64	7.21	2.03	3.61
Cu Run 15 Etched LeftCenter x50.tif	144.00	35.82	17.69	13.21	6.49	2.04	3.38
Cu Run 15 Etched Right x50.tif	118.00	57.17	38.36	16.75	8.67	1.93	4.27
Cu Run 15 Etched RightCenter x50.tif	158.00	51.99	32.09	16.01	8.20	1.95	4.07
Cu Run 16 Etched Attempt at Micro 1 x50.tif	25.00	27.46	1.56	11.49	6.12	1.88	2.96
Cu Run 16 Etched Attempt at Micro 2 x50.tif	16.00	38.45	1.39	13.39	7.60	1.76	3.50
Cu Run 16 Etched Attempt at Micro x50.tif	20.00	30.14	1.36	12.06	5.99	2.01	3.10
Cu Run 16 Etched No idea, sample turned bad 2.tif	6.00	39.72	0.54	14.04	7.96	1.76	3.56
Cu Run 16 Etched No idea, sample turned bad 3.tif	85.00	63.39	12.17	18.53	8.91	2.08	4.49
Cu Run 16 Etched No idea, sample turned bad.tif	6.00	29.61	0.40	11.68	6.66	1.75	3.07
Cu Run 17 Etched Center x50.tif	179.00	50.01	32.92	16.41	8.18	2.01	3.99
Cu Run 17 Etched Left x50.tif	156.00	52.67	37.34	17.00	8.42	2.02	4.09
Cu Run 17 Etched LeftCenter x50.tif	164.00	53.69	34.15	16.12	8.79	1.83	4.13
Cu Run 17 Etched Right x50.tif	76.00	44.67	22.61	15.75	7.29	2.16	3.77
Cu Run 17 Etched RightCenter x50.tif	141.00	56.27	37.01	17.49	8.65	2.02	4.23
Cu Run 18 Etched Center x50.tif	128.00	42.66	25.02	14.66	7.74	1.89	3.68

Cu Run 18 Etched Left x50.tif	101.00	39.35	19.91	13.86	7.35	1.89	3.54
Cu Run 18 Etched LeftCenter x50.tif	131.00	50.28	26.00	15.26	8.77	1.74	4.00
Cu Run 18 Etched Right x50.tif	66.00	44.49	17.46	15.69	7.75	2.02	3.76
Cu Run 18 Etched RightCenter x50.tif	125.00	40.04	16.78	14.24	6.99	2.04	3.57
Cu Run 19 Etched Center x50.tif	105.00	54.53	20.93	15.78	9.06	1.74	4.17
Cu Run 19 Etched Left x50.tif	110.00	68.23	27.95	16.78	10.06	1.67	4.66
Cu Run 19 Etched LeftCenter x50.tif	142.00	69.55	29.45	17.60	10.09	1.74	4.71
Cu Run 19 Etched Right x50.tif	88.00	60.90	33.67	18.29	9.28	1.97	4.40
Cu Run 19 Etched RightCenter x50.tif	135.00	63.26	33.40	17.61	10.30	1.71	4.49
Cu Run 20 Etched Center x50.tif	72.00	31.51	8.92	12.67	5.86	2.16	3.17
Cu Run 20 Etched Left x50.tif	60.00	37.95	13.67	12.43	6.57	1.89	3.48
Cu Run 20 Etched LeftCenter x50.tif	85.00	38.11	14.35	13.76	6.63	2.08	3.48
Cu Run 20 Etched Right x50.tif	28.00	35.27	8.88	14.04	6.38	2.20	3.35
Cu Run 20 Etched RightCenter x50.tif	50.00	35.42	11.03	12.64	6.14	2.06	3.36
Cu Run 8 Near Substrate-1 x50.tif	237.00	43.68	28.34	15.21	7.51	2.02	3.73
Cu Run 8 Near Substrate-2 x50.tif	291.00	43.78	30.16	15.73	7.75	2.03	3.73
Cu Run 8 Near Substrate-3 x50.tif	277.00	44.15	28.85	15.84	7.85	2.02	3.75
Cu Run 8 Near Substrate-4 x50.tif	265.00	39.85	24.92	14.85	7.70	1.93	3.56
Cu Run 8 Near Substrate-5 x50.tif	272.00	50.89	32.95	16.16	8.24	1.96	4.02
Cu Run 8 Near Substrate-6 x50.tif	265.00	56.15	35.06	16.48	8.49	1.94	4.23
Cu Run 8 Next line-1 x50.tif	231.00	44.01	28.02	15.71	7.30	2.15	3.74
Cu Run 8 Next line-2 x50.tif	306.00	38.73	27.99	14.62	7.38	1.98	3.51
Cu Run 8 Next line-3 x50.tif	272.00	39.97	25.74	14.69	7.70	1.91	3.57
Cu Run 8 Next line-4 x50.tif	262.00	46.63	29.13	15.81	7.98	1.98	3.85
Cu Run 8 Next line-5 x50.tif	274.00	49.40	32.17	15.77	8.37	1.88	3.97
Cu Run 8 Next line-6 x50.tif	281.00	48.60	32.33	15.90	8.31	1.91	3.93
Cu Run 8 Line 3 of 3 1 x50.tif	202.00	44.37	24.69	15.49	8.07	1.92	3.76
Cu Run 8 Line 3 of 3 2 x50.tif	288.00	43.24	29.40	15.49	7.85	1.97	3.71
Cu Run 8 Line 3 of 3 3 x50.tif	255.00	51.13	31.15	16.89	8.36	2.02	4.03
Cu Run 8 Line 3 of 3 4 x50.tif	251.00	49.58	29.77	16.34	8.39	1.95	3.97
Cu Run 8 Line 3 of 3 5 x50.tif	254.00	46.48	27.96	15.38	8.03	1.92	3.85
Cu Run 8 Line 3 of 3 6 x50.tif	274.00	51.06	33.11	15.96	8.43	1.89	4.03
Cu Run 10 Line 1-3 1 x50.tif	147.00	33.70	13.56	13.05	6.24	2.09	3.28
Cu Run 10 Line 1-3 2 x50.tif	216.00	46.97	23.94	14.93	8.06	1.85	3.87
Cu Run 10 Line 1-3 3 x50.tif	252.00	49.84	29.80	15.87	8.18	1.94	3.98
Cu Run 10 Line 2-3 1 x50.tif	130.00	34.12	12.19	12.96	6.34	2.04	3.30
Cu Run 10 Line 2-3 2 x50.tif	203.00	44.27	21.21	14.44	7.49	1.93	3.75
Cu Run 10 Line 2-3 3 x50.tif	221.00	44.59	23.49	15.11	7.95	1.90	3.77
Cu Run 10 Line 3-3 1 x50.tif	133.00	36.95	13.45	13.55	6.53	2.07	3.43
Cu Run 10 Line 3-3 2 x50.tif	240.00	43.95	24.93	15.01	7.99	1.88	3.74
Cu Run 10 Line 3-3 3 x50.tif	252.00	46.29	27.67	15.11	7.96	1.90	3.84

Cu Run 11 Line 1-3 1 x50.tif	97.00	43.00	16.17	14.96	7.94	1.88	3.70
Cu Run 11 Line 1-3 2 x50.tif	120.00	40.23	11.43	15.11	7.33	2.06	3.58
Cu Run 11 Line 1-3 3 x50.tif	186.00	39.24	17.29	14.11	7.18	1.96	3.53
Cu Run 11 Line 1-3 4 x50.tif	125.00	30.95	9.11	12.32	6.11	2.02	3.14
Cu Run 11 Line 2-3 1 x50.tif	79.00	36.19	10.47	13.69	6.71	2.04	3.39
Cu Run 11 Line 2-3 2 x50.tif	137.00	39.12	12.70	13.59	6.67	2.04	3.53
Cu Run 11 Line 2-3 3 x50.tif	119.00	31.36	8.88	13.23	6.34	2.08	3.16
Cu Run 11 Line 2-3 4 x50.tif	134.00	35.69	11.29	13.38	6.62	2.02	3.37
Cu Run 11 Line 3-3 1 x50.tif	79.00	26.62	6.59	11.81	5.98	1.98	2.91
Cu Run 11 Line 3-3 2 x50.tif	90.00	30.12	6.43	12.29	6.47	1.90	3.10
Cu Run 11 Line 3-3 3 x50.tif	114.00	29.61	7.97	12.26	6.03	2.03	3.07
Cu Run 11 Line 3-3 4 x50.tif	124.00	34.17	10.01	13.03	6.42	2.03	3.30
Cu Run 13 Line 1-3 1 x50.tif	140.00	45.16	22.07	15.69	7.94	1.98	3.79
Cu Run 13 Line 1-3 2 x50.tif	231.00	50.04	27.33	16.20	8.74	1.85	3.99
Cu Run 13 Line 1-3 3 x50.tif	242.00	47.72	27.28	16.58	8.57	1.93	3.90
Cu Run 13 Line 2-3 1 x50.tif	156.00	43.63	23.25	15.31	8.06	1.90	3.73
Cu Run 13 Line 2-3 2 x50.tif	153.00	49.84	20.77	16.52	8.32	1.99	3.98
Cu Run 13 Line 2-3 3 x50.tif	200.00	50.64	23.92	16.34	8.34	1.96	4.01
Cu Run 13 Line 3-3 1 x50.tif	128.00	52.33	24.19	16.17	8.46	1.91	4.08
Cu Run 13 Line 3-3 2 x50.tif	185.00	42.46	24.61	15.51	8.22	1.89	3.68
Cu Run 13 Line 3-3 3 x50.tif	240.00	44.54	25.27	15.80	8.22	1.92	3.77
Cu Run 14 line 1-3 1 x50.tif	194.00	59.25	31.72	17.77	9.07	1.96	4.34
Cu Run 14 line 1-3 2 x50.tif	234.00	58.61	32.15	18.26	8.95	2.04	4.32
Cu Run 14 line 1-3 3 x50.tif	241.00	53.13	30.26	16.70	8.50	1.96	4.11
Cu Run 14 line 2-3 1 x50.tif	160.00	51.70	25.95	16.73	8.16	2.05	4.06
Cu Run 14 line 2-3 2 x50.tif	185.00	65.52	39.96	18.67	9.42	1.98	4.57
Cu Run 14 line 2-3 3 x50.tif	188.00	51.26	25.06	16.31	8.36	1.95	4.04
Cu Run 14 line 3-3 1 x50.tif	210.00	49.40	29.41	16.79	8.08	2.08	3.97
Cu Run 14 line 3-3 2 x50.tif	275.00	54.55	37.51	17.45	8.75	1.99	4.17
Cu Run 14 line 3-3 3 x50.tif	249.00	50.97	30.12	16.76	8.52	1.97	4.03
Cu Etched Rerun 14 Center x50.tif	103.00	58.64	41.66	16.55	9.57	1.73	4.32
Cu Etched Rerun 14 Left x50.tif	85.00	65.48	43.06	17.91	9.91	1.81	4.57
Cu Etched Rerun 14 LeftCenter x50.tif	88.00	73.79	50.02	18.09	10.41	1.74	4.85
Cu Etched Rerun 14 Right x50.tif	71.00	57.11	30.24	17.32	9.23	1.88	4.26
Cu Etched Rerun 14 RightCenter x50.tif	86.00	63.16	45.63	17.76	10.39	1.71	4.48
Cu Etched Rerun 3 Center x50.tif	6.00	24.66	2.49	11.17	5.73	1.95	2.80
Cu Etched Rerun 3 LeftCenter x50.tif	8.00	24.18	4.15	10.34	6.00	1.72	2.77
Cu Etched Rerun 3 RightCenter x50.tif	3.00	35.65	2.38	13.99	5.36	2.61	3.37
Cu Etched Rerun 6 Center x50.tif	123.00	37.48	27.61	13.70	7.72	1.78	3.45
Cu Etched Rerun 6 Left x50.tif	78.00	41.98	19.71	13.78	7.91	1.74	3.66
Cu Etched Rerun 6 LeftCenter x50.tif	123.00	49.96	37.80	16.71	9.48	1.76	3.99

Cu Etched Rerun 6 Right x50.tif	17.00	38.01	10.12	12.65	7.28	1.74	3.48
Cu Etched Rerun 6 RightCenter x50.tif	59.00	62.85	28.02	17.42	9.16	1.90	4.47
Cu Etched Rerun 7 Center x50.tif	46.00	32.71	19.61	13.26	6.89	1.93	3.23
Cu Etched Rerun 7 LeftCenter x50.tif	56.00	50.29	32.25	16.43	7.27	2.26	4.00
Cu Etched Rerun 7 RightCenter x50.tif	26.00	27.75	10.96	11.62	5.93	1.96	2.97
Cu Etched Validation 1 Center x50.tif	75.00	31.17	15.38	12.66	6.46	1.96	3.15
Cu Etched Validation 1 Left x50.tif	28.00	23.62	8.12	9.89	5.27	1.88	2.74
Cu Etched Validation 1 LeftCenter x50.tif	52.00	30.49	13.47	12.09	6.16	1.96	3.12
Cu Etched Validation 1 Right x50.tif	19.00	24.56	6.54	11.17	5.19	2.15	2.80
Cu Etched Validation 1 RightCenter x50.tif	51.00	35.54	19.29	12.31	6.76	1.82	3.36
Cu Etched Validation 2 Center x50.tif	81.00	60.02	30.96	17.71	8.77	2.02	4.37
Cu Etched Validation 2 Left x50.tif	44.00	35.96	18.38	13.32	6.45	2.07	3.38
Cu Etched Validation 2 LeftCenter x50.tif	68.00	34.82	17.17	12.56	6.51	1.93	3.33
Cu Etched Validation 2 Right x50.tif	18.00	34.52	8.17	13.58	6.24	2.18	3.31
Cu Etched Validation 2 RightCenter x50.tif	50.00	35.33	15.89	12.76	6.68	1.91	3.35

Table XIX: Zinc CS grain size analysis

Slice	Count	Average Size	%Area	Feret	MinFeret	Feret Ratio
Zn Run 1 Etched Center x50.tif	50.00	88.22	10.56	22.06	11.98	1.84
Zn Run 1 Etched Left x50.tif	30.00	96.67	8.87	21.73	11.89	1.83
Zn Run 1 Etched LeftCenter x50.tif	48.00	92.86	13.83	23.83	12.11	1.97
Zn Run 1 Etched Right x50.tif	23.00	90.19	7.94	18.03	9.82	1.84
Zn Run 1 Etched RightCenter x50.tif	52.00	111.41	14.58	24.43	12.89	1.89
Zn Run 2 Etched Center x50.tif	48.00	118.61	16.32	25.14	13.74	1.83
Zn Run 2 Etched Left x50.tif	28.00	125.62	13.01	26.98	14.84	1.82
Zn Run 2 Etched LeftCenter x50.tif	42.00	151.64	17.95	29.82	15.50	1.92
Zn Run 2 Etched Right x50.tif	32.00	139.10	15.53	28.84	13.78	2.09
Zn Run 2 Etched RightCenter x50.tif	45.00	118.76	14.61	26.72	14.01	1.91
Zn Run 3 Etched Center x50.tif	43.00	110.02	25.46	21.63	10.83	2.00
Zn Run 3 Etched LeftCenter x50.tif	5.00	113.03	3.99	23.10	11.43	2.02
Zn Run 3 Etched RightCenter x50.tif	14.00	81.53	7.07	16.87	10.13	1.67
Zn Run 4 Etched Center x50.tif	45.00	122.69	13.72	24.27	13.59	1.79
Zn Run 4 Etched LeftCenter x50.tif	49.00	108.19	14.36	25.07	12.98	1.93
Zn Run 4 Etched RightCenter x50.tif	48.00	103.80	14.27	22.30	13.13	1.70
Zn Run 5 Etched Center x50.tif	17.00	116.24	5.31	21.81	11.66	1.87
Zn Run 5 Etched LeftCenter x50.tif	8.00	124.53	3.61	20.76	12.64	1.64
Zn Run 5 Etched RightCenter x50.tif	30.00	87.94	9.40	23.36	11.56	2.02
Zn Run 6 Etched Center x50.tif	26.00	99.86	6.19	23.54	12.27	1.92
Zn Run 6 Etched Left x50.tif	36.00	84.92	9.16	18.95	10.08	1.88
Zn Run 6 Etched LeftCenter x50.tif	30.00	141.81	10.15	26.73	14.67	1.82
Zn Run 6 Etched Right x50.tif	22.00	149.23	10.45	30.68	14.32	2.14
Zn Run 6 Etched RightCenter x50.tif	28.00	95.51	6.79	23.79	12.43	1.91

Zn Run 7 Etched Center x50.tif	29.00	90.39	32.70	19.76	9.98	1.98
Zn Run 7 Etched LeftCenter x50.tif	23.00	119.79	35.45	21.73	10.71	2.03
Zn Run 7 Etched RightCenter x50.tif	12.00	150.56	34.85	28.95	11.06	2.62
Zn Run 8 Etched Center x50.tif	12.00	105.81	2.92	26.58	12.89	2.06
Zn Run 8 Etched Left x50.tif	51.00	88.12	10.27	18.68	10.01	1.87
Zn Run 8 Etched LeftCenter x50.tif	30.00	131.78	10.68	24.99	14.24	1.76
Zn Run 8 Etched Right x50.tif	34.00	93.26	9.88	18.42	10.30	1.79
Zn Run 8 Etched RightCenter x50.tif	36.00	103.06	8.55	24.27	12.92	1.88
Zn Run 8 Etched Near substrate 1.tif	35.00	103.69	14.73	17.93	10.82	1.66
Zn Run 8 Etched Near substrate 2.tif	13.00	89.57	2.66	23.97	11.65	2.06
Zn Run 8 Etched Near substrate 3.tif	17.00	185.06	7.25	33.70	17.26	1.95
Zn Run 8 Etched Near substrate 4.tif	45.00	117.57	12.20	21.10	12.15	1.74
Zn Run 8 Etched Near substrate 5.tif	15.00	71.51	4.68	15.89	9.74	1.63
Zn Etched Run 9 Center x50.tif	25.00	93.17	16.29	23.22	11.91	1.95
Zn Etched Run 9 Left x50.tif	9.00	163.28	13.06	32.97	14.43	2.28
Zn Etched Run 9 LeftCenter x50.tif	24.00	152.62	22.63	29.45	15.96	1.85
Zn Etched Run 9 Right x50.tif	10.00	142.97	14.73	29.09	15.35	1.90
Zn Etched Run 9 RightCenter x50.tif	14.00	138.47	13.98	31.18	14.24	2.19
Zn Run 10 Etched Center x50.tif	47.00	132.07	15.43	26.80	13.54	1.98
Zn Run 10 Etched Left x50.tif	31.00	132.23	13.35	28.97	13.47	2.15
Zn Run 10 Etched LeftCenter x50.tif	36.00	112.61	10.66	24.95	12.91	1.93
Zn Run 10 Etched Right x50.tif	13.00	125.14	5.60	28.69	13.31	2.16
Zn Run 10 Etched RightCenter x50.tif	45.00	96.94	12.18	23.30	11.33	2.06
Zn Etched Run 11 Center x50.tif	26.00	110.77	18.47	26.26	13.20	1.99
Zn Etched Run 11 Left x50.tif	19.00	96.88	13.65	23.28	12.15	1.92
Zn Etched Run 11 LeftCenter x50.tif	33.00	94.12	20.30	23.80	12.32	1.93
Zn Etched Run 11 Right x50.tif	4.00	85.21	3.00	18.23	10.13	1.80
Zn Etched Run 11 RightCenter x50.tif	21.00	90.94	13.46	21.97	10.68	2.06
Zn Run Etched 12 Center x50.tif	8.00	137.32	7.18	27.62	13.66	2.02
Zn Run Etched 12 Left x50.tif	1.00	154.17	1.86	25.87	19.06	1.36
Zn Run Etched 12 LeftCenter x50.tif	4.00	152.55	4.95	24.45	14.74	1.66
Zn Run Etched 12 Right x50.tif	17.00	133.36	19.69	21.75	11.65	1.87
Zn Run Etched 12 RightCenter x50.tif	16.00	88.92	11.27	20.25	9.38	2.16
Zn Etched Run 13 Center x50.tif	23.00	123.63	18.72	26.81	13.81	1.94
Zn Etched Run 13 Left x50.tif	3.00	47.77	1.20	15.42	7.56	2.04
Zn Etched Run 13 LeftCenter x50.tif	22.00	79.50	11.27	23.33	12.04	1.94
Zn Etched Run 13 Right x50.tif	16.00	136.54	13.71	29.79	14.38	2.07
Zn Etched Run 13 RightCenter x50.tif	17.00	146.54	18.05	26.94	15.17	1.78
Zn Etched Run 14 Center x50.tif	43.00	94.48	9.49	23.31	11.71	1.99
Zn Etched Run 14 Left x50.tif	16.00	98.80	4.67	20.11	10.05	2.00
Zn Etched Run 14 LeftCenter x50.tif	56.00	92.60	13.56	23.14	12.75	1.82

Zn Etched Run 14 Right Centerx50.tif	45.00	92.87	10.50	23.47	12.28	1.91
Zn Etched Run 14 Right x50.tif	31.00	137.13	13.66	30.55	14.42	2.12
Zn Etched Run 15 Center x50.tif	21.00	109.18	14.57	19.13	10.50	1.82
Zn Etched Run 15 LeftCenter x50.tif	16.00	103.13	10.19	18.43	10.60	1.74
Zn Etched Run 15 RightCenter x50.tif	23.00	113.75	20.53	20.94	10.29	2.03
Zn Etched Run 16 Center x50.tif	10.00	136.23	41.01	19.92	12.24	1.63
Zn Etched Run 16 LeftCenter x50.tif	11.00	116.41	24.67	20.41	10.93	1.87
Zn Etched Run 16 RightCenter x50.tif	9.00	201.74	29.32	27.35	15.77	1.73
Zn Etched Run 17 Center x50.tif	10.00	143.68	3.99	27.35	14.34	1.91
Zn Etched Run 17 LeftCenter x50.tif	43.00	111.33	15.00	20.68	10.91	1.89
Zn Etched Run 17 RightCenter x50.tif	24.00	98.46	7.21	19.38	10.10	1.92
Zn Etched Run 18 Center x50.tif	21.00	111.30	5.45	25.42	12.40	2.05
Zn Etched Run 18 Left x50.tif	17.00	92.03	4.51	22.72	10.78	2.11
Zn Etched Run 18 LeftCenter x50.tif	30.00	131.58	9.26	28.29	12.93	2.19
Zn Etched Run 18 Right x50.tif	32.00	135.19	11.93	22.96	11.59	1.98
Zn Etched Run 18 RightCenter x50.tif	44.00	120.09	12.38	25.81	14.12	1.83
Zn Etched Run 19 Center x50.tif	13.00	95.78	3.43	20.20	9.33	2.16
Zn Etched Run 19 LeftCenter x50.tif	8.00	104.06	3.95	24.58	12.72	1.93
Zn Etched Run 19 RightCenter x50.tif	25.00	108.62	12.63	27.57	14.20	1.94
Zn Etched Run 20 Center x50.tif	25.00	84.09	7.98	16.52	10.02	1.65
Zn Etched Run 20 LeftCenter x50.tif	23.00	135.29	13.08	22.20	12.36	1.80
Zn Etched Run 20 RightCenter x50.tif	24.00	138.97	16.25	22.53	12.54	1.80
Zn Validation 1 Etched Center x50.tif	11.00	111.69	6.91	25.44	12.71	2.00
Zn Validation 1 Etched Left x50.tif	11.00	96.15	10.18	18.30	9.83	1.86
Zn Validation 1 Etched LeftCenter x50.tif	23.00	116.12	18.63	27.35	13.41	2.04
Zn Validation 1 Etched Right x50.tif	13.00	93.00	10.61	19.44	10.09	1.93
Zn Validation 1 Etched RightCenter x50.tif	8.00	132.41	7.44	22.71	11.73	1.94
Zn Validation 2 Etched Center x50.tif	19.00	108.61	14.74	26.31	12.80	2.06
Zn Validation 2 Etched Left x50.tif	7.00	208.09	11.31	37.53	17.46	2.15
Zn Validation 2 Etched LeftCenter x50.tif	10.00	84.90	5.53	23.39	12.31	1.90
Zn Validation 2 Etched Right x50.tif	13.00	75.15	8.33	17.70	9.79	1.81
Zn Validation 2 Etched RightCenter x50.tif	21.00	130.24	16.93	28.86	14.75	1.96

Table XX: CS Vickers microhardness data

Sample	Force (gf)	D1 (um)	D2 (um)	HV
Cu 1	50.00	36.79	38.62	65.20
Cu 1	50.00	35.31	37.99	69.00
Cu 1	50.00	34.99	36.08	73.40
Cu 1	50.00	39.00	38.96	61.00
Cu 1	50.00	37.35	38.61	64.20
Cu 1	300.00	92.19	96.04	62.80
Cu 1	300.00	96.57	90.65	63.40

Cu 1	300.00	94.59	96.96	60.60
Cu 1	300.00	85.31	85.32	76.40
Cu 1	300.00	87.03	91.25	70.00
Cu 2	50.00	34.41	36.91	72.90
Cu 2	50.00	36.11	35.70	71.90
Cu 2	50.00	38.34	38.36	63.00
Cu 2	300.00	106.69	98.01	53.10
Cu 2	300.00	90.61	91.77	66.90
Cu 2	300.00	92.24	90.94	66.30
Cu 3-2	10.00	16.88	16.36	67.10
Cu 3-2	10.00	15.20	16.00	76.10
Cu 3-2	10.00	16.22	16.64	68.60
Cu 3-2	10.00	18.21	18.95	53.70
Cu 3-2	10.00	14.81	15.95	78.30
Cu 4	50.00	36.13	37.62	68.10
Cu 4	50.00	35.99	36.03	71.50
Cu 4	50.00	33.42	34.93	79.30
Cu 4	50.00	34.38	35.45	76.00
Cu 4	50.00	36.71	36.84	68.50
Cu 5	300.00	95.60	92.85	62.60
Cu 5	300.00	94.36	93.93	62.70
Cu 5	300.00	94.49	93.43	63.00
Cu 5	50.00	32.46	34.46	82.80
Cu 5	50.00	33.15	34.70	80.50
Cu 5	50.00	34.36	38.27	70.30
Cu 5	50.00	37.58	36.75	67.10
Cu 5	50.00	35.34	38.81	67.40
Cu 6	300.00	102.54	99.47	54.50
Cu 6	300.00	111.36	112.94	44.20
Cu 6	300.00	105.62	102.83	51.20
Cu 6	50.00	43.07	42.31	50.80
Cu 6	50.00	42.08	40.78	54.00
Cu 6	50.00	37.70	40.29	60.90
Cu 6-2	50.00	37.99	38.75	62.90
Cu 6-2	50.00	38.48	39.92	60.30
Cu 6-2	50.00	35.68	37.59	69.00
Cu 6-2	50.00	36.10	35.75	71.80
Cu 6-2	50.00	39.67	41.13	56.08
Cu 7	10.00	18.79	19.55	50.40
Cu 7	10.00	18.78	20.01	49.20
Cu 7	10.00	19.20	19.85	48.60

Cu 7-2	10.00	19.58	18.74	50.50
Cu 7-2	10.00	17.93	17.96	57.50
Cu 7-2	10.00	19.94	21.16	43.90
Cu 8	300.00	86.76	87.61	73.10
Cu 8	300.00	91.97	90.94	66.50
Cu 8	300.00	97.58	101.62	56.00
Cu 8	300.00	90.01	91.23	67.70
Cu 8	300.00	95.61	97.42	59.70
Cu 8	300.00	95.27	96.22	60.60
Cu 8	300.00	94.16	98.87	59.70
Cu 8	300.00	94.72	94.72	62.00
Cu 8	300.00	91.20	91.20	66.80
Cu 8	300.00	93.23	93.23	64.00
Cu 8	300.00	93.26	93.35	63.90
Cu 8	300.00	86.61	89.52	71.70
Cu 8	300.00	95.92	96.74	59.90
Cu 8	300.00	86.58	88.98	72.10
Cu 8	300.00	93.05	93.05	64.20
Cu 8	300.00	95.80	95.80	60.60
Cu 8	300.00	92.18	92.71	65.00
Cu 8	300.00	88.87	87.56	71.40
Cu 8	50.00	34.74	35.78	74.50
Cu 8	50.00	38.43	37.32	64.60
Cu 8	50.00	37.90	39.04	62.60
Cu 8	50.00	36.61	37.77	67.00
Cu 8	50.00	35.06	36.04	73.30
Cu 8	50.00	36.24	37.36	68.40
Cu 8	50.00	35.20	35.00	75.00
Cu 8	50.00	36.65	36.43	69.40
Cu 8	50.00	34.76	35.45	75.20
Cu 8	50.00	39.54	39.63	59.10
Cu 8	50.00	40.64	41.01	55.60
Cu 8	50.00	35.33	36.52	71.80
Cu 8	50.00	36.40	38.09	66.80
Cu 8	50.00	39.09	41.38	57.20
Cu 8	50.00	39.84	39.81	58.40
Cu 8	50.00	36.10	37.80	67.90
Cu 8	50.00	33.37	37.57	73.60
Cu 8	50.00	39.36	40.06	58.70
Cu 8	50.00	34.66	35.49	75.30
Cu 8	50.00	35.21	36.08	72.90

Cu 8	50.00	35.10	35.95	73.40
Cu 8	50.00	38.38	39.01	61.90
Cu 9	50.00	39.45	38.48	61.00
Cu 9	50.00	37.20	37.42	66.60
Cu 9	50.00	35.78	35.54	72.90
Cu 9	50.00	34.14	34.55	78.60
Cu 9	50.00	36.94	37.49	66.90
Cu 9	50.00	37.62	37.54	65.60
Cu 10	50.00	33.75	33.75	81.40
Cu 10	50.00	32.33	33.18	86.40
Cu 10	50.00	35.76	36.58	70.80
Cu 10	50.00	36.78	38.34	65.70
Cu 10	50.00	34.07	34.86	78.00
Cu 10	50.00	36.96	34.25	73.10
Cu 10	50.00	33.57	33.71	81.90
Cu 10	50.00	39.87	39.87	58.30
Cu 10	50.00	36.87	35.78	70.20
Cu 10	50.00	37.43	37.44	66.10
Cu 11	50.00	35.64	35.58	73.10
Cu 11	50.00	41.77	42.32	52.40
Cu 11	50.00	39.76	39.97	58.30
Cu 11	50.00	43.41	43.39	49.20
Cu 11	50.00	40.57	40.98	55.70
Cu 11	50.00	37.81	37.70	65.00
Cu 11	50.00	37.60	38.37	64.20
Cu 11	50.00	40.18	38.94	59.20
Cu 11	50.00	37.43	38.72	64.10
Cu 11	50.00	35.21	34.59	76.10
Cu 11	50.00	46.90	46.97	42.00
Cu 11	50.00	37.21	38.48	64.70
Cu 11	50.00	39.62	42.23	54.00
Cu 11	50.00	35.11	34.77	75.90
Cu 11	50.00	32.64	33.92	83.70
Cu 11	50.00	42.11	41.33	53.20
Cu 11	50.00	46.97	46.25	42.60
Cu 11	50.00	41.41	41.01	54.50
Cu 11	50.00	34.46	34.46	78.00
Cu 11	50.00	35.56	36.54	71.30
Cu 12	50.00	36.43	35.95	70.70
Cu 12	50.00	35.72	36.40	71.30
Cu 12	50.00	36.55	38.63	65.60

Cu 12	50.00	35.24	35.70	73.60
Cu 12	50.00	37.26	37.66	66.00
Cu 13	50.00	34.68	33.64	79.40
Cu 13	50.00	32.44	33.19	86.10
Cu 13	50.00	41.67	41.67	53.30
Cu 13	50.00	33.72	37.12	73.90
Cu 13	50.00	35.09	34.92	75.60
Cu 13	50.00	37.24	37.80	65.80
Cu 13	50.00	37.66	38.40	64.10
Cu 13	50.00	41.36	40.27	55.66
Cu 13	50.00	35.53	36.12	72.20
Cu 13	50.00	35.24	36.24	72.50
Cu 13	50.00	36.77	38.04	66.20
Cu 13	50.00	35.36	35.66	73.50
Cu 13	50.00	37.27	38.66	64.30
Cu 13	50.00	37.70	39.52	62.10
Cu 13	50.00	38.23	39.09	62.00
Cu 13	50.00	35.21	35.21	74.70
Cu 14	50.00	39.10	41.77	56.70
Cu 14	50.00	40.90	41.77	54.20
Cu 14	50.00	37.91	38.64	63.20
Cu 14	50.00	36.39	36.89	69.00
Cu 14	50.00	36.44	38.62	65.80
Cu 14	50.00	35.50	35.59	73.50
Cu 14	50.00	57.10	57.10	28.40
Cu 14	50.00	44.53	44.07	47.20
Cu 14	50.00	42.55	42.55	51.20
Cu 14	50.00	51.24	53.18	34.00
Cu 14	50.00	44.82	45.95	45.00
Cu 14	50.00	37.38	39.39	62.90
Cu 14	50.00	38.64	40.01	59.90
Cu 14-2	50.00	39.15	39.80	59.50
Cu 14-2	50.00	39.20	40.56	58.20
Cu 14-2	50.00	41.94	42.79	51.60
Cu 14-2	50.00	38.73	39.70	60.20
Cu 14-2	50.00	33.60	34.09	80.90
Cu 14-2	50.00	34.22	35.59	76.10
Cu 14-2	50.00	38.83	40.70	58.60
Cu 14-2	50.00	35.20	35.20	74.80
Cu 14-2	50.00	39.34	37.92	62.10
Cu 14-2	50.00	38.58	38.41	62.50

Cu 14-2	50.00	33.65	33.65	81.80
Cu 14-2	50.00	38.24	38.83	62.40
Cu 14-2	50.00	38.51	40.30	49.70
Cu 14-2	50.00	34.22	34.59	78.30
Cu 15	50.00	39.76	41.56	56.00
Cu 15	50.00	36.42	37.77	67.30
Cu 15	50.00	37.10	37.37	66.80
Cu 15	50.00	37.80	38.56	63.60
Cu 15	50.00	37.50	39.91	61.80
Cu 16	50.00	33.08	34.09	82.20
Cu 16	50.00	31.70	34.56	84.40
Cu 16	50.00	37.59	40.46	60.80
Cu 17	50.00	34.35	37.58	71.60
Cu 17	50.00	35.96	36.19	71.20
Cu 17	50.00	36.09	38.58	66.50
Cu 17	50.00	33.86	35.52	77.00
Cu 17	50.00	34.30	37.74	71.40
Cu 18	50.00	35.26	36.34	72.30
Cu 18	50.00	35.87	36.61	70.50
Cu 18	50.00	36.82	38.66	65.00
Cu 18	50.00	37.40	38.04	65.10
Cu 18	50.00	32.75	33.05	85.60
Cu 18	50.00	31.58	32.58	90.00
Cu 18	50.00	33.26	33.09	84.20
Cu 19	50.00	35.09	35.97	73.40
Cu 19	50.00	33.07	33.07	84.70
Cu 19	50.00	34.10	34.91	77.80
Cu 19	50.00	35.81	36.80	70.30
Cu 19	50.00	36.15	36.55	70.10
Cu 19	50.00	37.86	37.86	64.60
Cu 20	50.00	37.55	40.08	61.50
Cu 20	50.00	25.48	27.44	66.20
Cu 20	50.00	29.89	31.56	49.10
Cu 20	50.00	27.16	27.16	62.80
Cu 20	50.00	26.71	25.55	67.80
Cu Val 1	50.00	31.74	32.23	90.60
Cu Val 1	50.00	33.48	34.84	79.30
Cu Val 1	50.00	35.09	36.26	72.80
Cu Val 1	50.00	35.44	35.31	74.00
Cu Val 1	50.00	33.26	33.43	83.30
Cu Val 2	10.00	15.46	16.12	74.30

Cu Val 2	10.00	16.20	16.49	69.40
Cu Val 2	10.00	16.53	16.49	68.00
Cu Val 2	10.00	16.46	16.41	68.60
Cu Val 2	10.00	15.29	15.76	76.90
Zn 1	25.00	35.76	35.76	36.20
Zn 1	25.00	22.95	23.44	34.40
Zn 1	25.00	34.85	35.06	37.90
Zn 1	25.00	35.87	36.36	35.50
Zn 1	25.00	36.11	36.54	35.10
Zn 1	25.00	35.31	36.39	36.00
Zn 2	25.00	35.35	35.22	37.20
Zn 2	25.00	38.09	37.96	32.00
Zn 2	25.00	35.06	35.41	37.30
Zn 2	25.00	36.47	36.29	35.00
Zn 2	25.00	35.84	36.27	35.60
Zn 3	10.00	25.80	26.89	26.70
Zn 3	10.00	24.16	24.66	31.10
Zn 3	10.00	25.52	25.82	28.10
Zn 4	25.00	38.01	38.78	31.40
Zn 4	25.00	38.60	40.53	29.60
Zn 4	25.00	35.66	36.25	35.80
Zn 4	25.00	35.46	35.82	36.40
Zn 4	25.00	36.16	36.95	34.60
Zn 5	25.00	34.17	35.50	38.20
Zn 5	25.00	35.79	36.47	35.50
Zn 5	25.00	35.44	36.03	36.30
Zn 5	25.00	34.82	35.36	37.60
Zn 5	25.00	35.95	35.97	35.80
Zn 6	25.00	36.11	35.31	36.30
Zn 6	25.00	35.95	35.46	36.30
Zn 6	25.00	36.15	37.08	34.50
Zn 6	25.00	34.97	35.60	37.20
Zn 6	25.00	36.15	35.83	35.70
Zn 7	10.00	23.71	24.42	32.00
Zn 7	10.00	24.10	23.92	32.10
Zn 7	10.00	23.25	23.19	34.30
Zn 8	25.00	40.02	40.21	28.80
Zn 8	25.00	39.59	39.33	29.70
Zn 8	25.00	34.71	35.61	37.40
Zn 8	25.00	34.96	34.88	38.00
Zn 8	25.00	35.33	35.03	37.40

Zn 8	25.00	38.66	37.45	32.00
Zn 8	25.00	35.94	35.66	36.10
Zn 8	25.00	36.42	35.47	35.80
Zn 8	25.00	35.98	36.94	34.80
Zn 8	25.00	35.47	36.18	36.10
Zn 8	25.00	35.15	35.50	37.10
Zn 8	25.00	35.88	36.90	35.00
Zn 8	25.00	36.16	36.30	35.30
Zn 8	25.00	35.54	36.15	36.00
Zn 8	25.00	35.37	36.61	35.70
Zn 8	25.00	36.00	36.64	35.10
Zn 8	25.00	36.13	36.91	34.70
Zn 8	25.00	34.59	35.57	37.60
Zn 8	25.00	36.98	36.60	34.20
Zn 8	25.00	36.16	36.02	35.50
Zn 9	25.00	36.73	37.50	33.60
Zn 9	25.00	38.33	40.13	30.10
Zn 9	25.00	36.22	36.06	35.40
Zn 9	25.00	35.67	36.85	35.20
Zn 9	25.00	37.05	37.42	33.40
Zn 10	25.00	38.56	39.01	30.80
Zn 10	25.00	38.20	39.07	31.00
Zn 10	25.00	38.71	40.14	29.80
Zn 10	25.00	39.30	39.46	29.80
Zn 10	25.00	39.20	38.91	30.30
Zn 10	25.00	37.71	38.99	31.50
Zn 10	25.00	37.00	37.62	33.30
Zn 10	25.00	36.95	38.58	32.50
Zn 10	25.00	37.87	38.19	32.00
Zn 10	25.00	37.76	39.20	31.30
Zn 10	25.00	38.27	39.60	30.50
Zn 10	25.00	38.20	38.44	31.50
Zn 10	25.00	36.83	37.03	33.90
Zn 11	25.00	35.90	35.48	36.30
Zn 11	25.00	37.40	38.10	32.50
Zn 11	25.00	35.61	36.79	35.30
Zn 11	25.00	36.94	37.15	33.70
Zn 11	25.00	34.89	35.64	37.20
Zn 11	25.00	34.80	35.70	37.30
Zn 11	25.00	35.88	36.51	35.30
Zn 11	25.00	35.03	35.80	36.90

Zn 11	25.00	37.07	37.60	33.20
Zn 11	25.00	35.39	35.51	36.80
Zn 11	25.00	35.35	36.22	36.20
Zn 11	25.00	35.42	36.18	36.10
Zn 11	25.00	36.05	34.25	37.50
Zn 12	25.00	35.53	34.68	37.60
Zn 12	25.00	37.08	36.91	33.80
Zn 12	25.00	38.65	37.85	31.60
Zn 12	25.00	35.58	36.43	35.70
Zn 12	25.00	35.34	34.65	37.80
Zn 13	25.00	34.94	36.70	36.10
Zn 13	25.00	35.77	37.43	34.60
Zn 13	25.00	37.03	37.20	33.60
Zn 13	25.00	36.50	37.48	33.80
Zn 13	25.00	35.22	36.18	36.30
Zn 13	25.00	36.92	37.30	33.60
Zn 13	25.00	37.46	37.95	32.60
Zn 13	25.00	36.92	38.24	32.80
Zn 13	25.00	37.14	37.56	33.20
Zn 13	25.00	35.87	37.12	34.80
Zn 13	25.00	36.51	37.27	34.00
Zn 13	25.00	36.02	37.35	34.40
Zn 13	25.00	38.85	38.81	30.70
Zn 13	25.00	36.27	37.25	34.30
Zn 13	25.00	37.33	37.12	33.40
Zn 13	25.00	33.89	36.14	37.80
Zn 14	25.00	36.14	36.76	34.80
Zn 14	25.00	35.50	36.24	36.00
Zn 14	25.00	35.58	36.76	35.40
Zn 14	25.00	35.83	36.14	35.80
Zn 14	25.00	36.95	37.23	33.60
Zn 14	25.00	35.31	36.23	36.20
Zn 14	25.00	35.83	36.44	35.50
Zn 14	25.00	35.27	36.44	36.00
Zn 14	25.00	36.55	37.54	33.70
Zn 14	25.00	35.53	35.34	36.90
Zn 14	25.00	36.99	36.44	34.30
Zn 14	25.00	35.92	36.87	34.90
Zn 14	25.00	35.64	35.99	36.10
Zn 15	10.00	25.39	26.11	27.90
Zn 15	10.00	24.24	24.17	31.60

Zn 15	10.00	27.89	28.68	23.10
Zn 16	10.00	24.55	24.22	31.10
Zn 16	10.00	23.72	22.41	34.80
Zn 16	10.00	20.63	21.91	40.90
Zn 17	25.00	36.19	36.73	34.90
Zn 17	25.00	34.80	36.69	36.20
Zn 17	25.00	36.04	36.45	35.20
Zn 18	25.00	37.94	38.04	32.10
Zn 18	25.00	37.34	37.38	33.20
Zn 18	25.00	37.00	38.14	32.80
Zn 18	25.00	36.86	37.22	33.70
Zn 18	25.00	37.13	37.41	33.30
Zn 19	25.00	34.98	34.41	38.50
Zn 19	25.00	34.57	33.74	39.70
Zn 19	25.00	34.43	34.43	39.00
Zn 19	25.00	35.43	35.07	37.30
Zn 19	25.00	37.15	36.78	33.90
Zn 20	25.00	36.64	36.74	34.40
Zn 20	25.00	38.41	37.36	32.30
Zn 20	25.00	36.16	36.61	35.00
Zn Val 1	25.00	36.18	36.86	34.70
Zn Val 1	25.00	35.77	37.89	34.10
Zn Val 1	25.00	36.48	36.40	34.90
Zn Val 1	25.00	35.91	36.22	35.60
Zn Val 1	25.00	35.81	38.69	33.40
Zn Val 2	25.00	36.94	37.42	33.50
Zn Val 2	25.00	37.57	37.51	32.80
Zn Val 2	25.00	36.38	37.33	34.10
Zn Val 2	25.00	37.45	37.88	32.60
Zn Val 2	25.00	38.82	37.78	31.60

Table XXI: CS Porosity Analysis Data

Slice	Area	%	Min thresh	Max thresh	image size	lower thresh	upper thresh
Cu Run 1 Center x50.tif	479925.00	16.64	0.00	255.00	479925.00	0.00	59.00
Cu Run 1 DownCenter x50.tif	438192.00	12.63	0.00	255.00	438192.00	0.00	59.00
Cu Run 1 FarLeft x50.tif	124600.00	19.69	0.00	255.00	124600.00	0.00	59.00
Cu Run 1 FarRight x50.tif	189552.00	11.96	0.00	255.00	189552.00	0.00	59.00
Cu Run 1 Left x50.tif	29036.00	13.84	255.00	255.00	209788.00	0.00	59.00
Cu Run 1 Right x50.tif	358930.00	15.09	0.00	255.00	358930.00	0.00	59.00
Cu Run 2 Center x50.tif	361984.00	15.73	0.00	255.00	361984.00	0.00	59.00
Cu Run 2 Left x50.tif	310373.00	11.94	0.00	255.00	310373.00	0.00	59.00
Cu Run 2 Right x50.tif	33577.00	13.91	255.00	255.00	241400.00	0.00	59.00

Sample not thick enough to image							
Cu Run 4 Center x50-1.tif	81989.00	24.14	255.00	255.00	339586.00	255.00	255.00
Cu Run 4 LeftCenter x50.tif	269555.00	10.14	0.00	255.00	269555.00	0.00	59.00
Cu Run 4 RightCenter x50.tif	195888.00	28.04	0.00	255.00	195888.00	0.00	59.00
Cu Run 5 Center x50.tif	446832.00	14.34	0.00	255.00	446832.00	129.00	255.00
Cu Run 5 Left x50.tif	204036.00	12.08	0.00	255.00	204036.00	0.00	59.00
Cu Run 5 LeftCenter x50.tif	692416.00	45.25	0.00	255.00	692416.00	0.00	59.00
Cu Run 5 Right x50.tif	20426.00	14.99	255.00	255.00	136240.00	0.00	59.00
Cu Run 5 RightCenter x50.tif	321088.00	12.32	0.00	255.00	321088.00	0.00	59.00
Cu Run 6 Center x50.tif	389760.00	21.44	0.00	255.00	389760.00	129.00	255.00
Cu Run 6 Left x50.tif	96939.00	26.61	255.00	255.00	364356.00	129.00	255.00
Cu Run 6 Right x50.tif	185832.00	24.92	0.00	255.00	185832.00	129.00	255.00
Cu Run 7 Center x50.tif	137309.00	38.24	0.00	255.00	137309.00	255.00	255.00
Cu Run 7 Left x50.tif	40499.00	37.38	255.00	255.00	108345.00	255.00	255.00
Cu Run 7 Right x50.tif	61666.00	46.32	255.00	255.00	133127.00	-1.00	-1.00
Cu Run 8 Center Tip x50.tif	527100.00	13.65	0.00	255.00	527100.00	0.00	59.00
Cu Run 8 LeftCenterEdge x50.tif	70622.00	13.38	255.00	255.00	527800.00	0.00	59.00
Cu Run 8 LeftEdge x50.tif	526347.00	12.41	0.00	255.00	526347.00	0.00	59.00
Cu Run 8 RightCenterEdge x50.tif	526932.00	12.83	0.00	255.00	526932.00	0.00	59.00
Cu Run 8 RightEdge x50.tif	522640.00	19.06	0.00	255.00	522640.00	0.00	59.00
Cu Run 8 Center x50.tif	529200.00	9.73	0.00	255.00	529200.00	0.00	59.00
Cu Run 8 Left x50.tif	527745.00	15.02	0.00	255.00	527745.00	0.00	59.00
Cu Run 8 LeftCenter x50.tif	527100.00	13.40	0.00	255.00	527100.00	0.00	59.00
Cu Run 8 Right x50.tif	523447.00	15.22	0.00	255.00	523447.00	0.00	59.00
Cu Run 8 RightCenter x50.tif	528500.00	13.76	0.00	255.00	528500.00	0.00	59.00
Cu Run 9 Center x50.tif	525594.00	20.30	0.00	255.00	525594.00	0.00	59.00
Cu Run 9 Left x50.tif	57303.00	11.05	255.00	255.00	518614.00	0.00	59.00
Cu Run 9 LeftCenter x50.tif	524250.00	16.51	0.00	255.00	524250.00	0.00	59.00
Cu Run 9 Right x50.tif	524896.00	10.86	0.00	255.00	524896.00	0.00	59.00
Cu Run 9 RightCenter x50.tif	529200.00	17.19	0.00	255.00	529200.00	0.00	59.00
Cu Run 10 Center x50.tif	520555.00	18.15	0.00	255.00	520555.00	0.00	59.00
Cu Run 10 Left x50.tif	526235.00	14.39	0.00	255.00	526235.00	0.00	59.00
Cu Run 10 LeftCenter x50.tif	523392.00	20.47	0.00	255.00	523392.00	0.00	59.00
Cu Run 10 Right x50.tif	475338.00	19.69	0.00	255.00	475338.00	0.00	59.00
Cu Run 10 RightCenter x50.tif	520708.00	14.75	0.00	255.00	520708.00	0.00	59.00
Cu Run 11 Center x50.tif	554048.00	7.29	0.00	255.00	554048.00	0.00	59.00
Cu Run 11 EdgeCenter x50.tif	482220.00	8.58	0.00	255.00	482220.00	0.00	59.00
Cu Run 11 Left x50.tif	552015.00	7.38	0.00	255.00	552015.00	0.00	59.00
Cu Run 11 LeftCenter x50.tif	550449.00	8.24	0.00	255.00	550449.00	0.00	59.00
Cu Run 11 LeftEdgeCenter x50.tif	394944.00	7.32	0.00	255.00	394944.00	0.00	59.00
Cu Run 11 Right x50.tif	472276.00	9.00	0.00	255.00	472276.00	0.00	59.00

Cu Run 11 RightCenter x50.tif	554288.00	7.91	0.00	255.00	554288.00	0.00	59.00
Cu Run 11 RightEdgeCenter x50.tif	46626.00	10.02	255.00	255.00	465254.00	0.00	59.00
Cu Run 12 Center x50.tif	527296.00	8.33	0.00	255.00	527296.00	0.00	59.00
Cu Run 12 Left x50.tif	379080.00	10.88	0.00	255.00	379080.00	0.00	59.00
Cu Run 12 LeftCenter x50.tif	37303.00	7.57	255.00	255.00	492788.00	0.00	59.00
Cu Run 12 Right x50.tif	351500.00	10.34	0.00	255.00	351500.00	0.00	59.00
Cu Run 12 RightCenter x50.tif	411929.00	13.45	0.00	255.00	411929.00	0.00	59.00
Cu Run 13 Center x50.tif	525480.00	6.58	0.00	255.00	525480.00	0.00	59.00
Cu Run 13 Left x50.tif	527152.00	14.17	0.00	255.00	527152.00	0.00	59.00
Cu Run 13 LeftCenter x50.tif	523447.00	13.31	0.00	255.00	523447.00	0.00	59.00
Cu Run 13 Right x50.tif	524144.00	15.05	0.00	255.00	524144.00	0.00	59.00
Cu Run 13 RightCenter x50.tif	527250.00	12.30	0.00	255.00	527250.00	0.00	59.00
Cu Run 14 Center x50.tif	549746.00	6.26	0.00	255.00	549746.00	0.00	59.00
Cu Run 14 Left x50.tif	244998.00	7.96	0.00	255.00	244998.00	0.00	59.00
Cu Run 14 LeftCenter x50.tif	550449.00	5.79	0.00	255.00	550449.00	0.00	59.00
Cu Run 14 Right x50.tif	350176.00	9.42	0.00	255.00	350176.00	0.00	59.00
Cu Run 14 RightCenter x50.tif	554510.00	8.94	0.00	255.00	554510.00	0.00	59.00
Cu Run 15 Center x50.tif	523447.00	11.92	0.00	255.00	523447.00	0.00	59.00
Cu Run 15 LeftCenter x50.tif	320620.00	18.85	0.00	255.00	320620.00	0.00	59.00
Cu Run 15 RightCenter x50.tif	278103.00	11.95	0.00	255.00	278103.00	0.00	59.00
Cu Run 16 Center x50.tif	61968.00	19.94	255.00	255.00	310744.00	0.00	59.00
Cu Run 16 LeftCenter x50.tif	52454.00	22.98	255.00	255.00	228231.00	0.00	59.00
Cu Run 16 RightCenter x50.tif	31163.00	22.86	255.00	255.00	136320.00	0.00	59.00
Cu Run 17 Center x50.tif	443928.00	7.85	0.00	255.00	443928.00	0.00	59.00
Cu Run 17 Left x50.tif	424384.00	11.02	0.00	255.00	424384.00	0.00	59.00
Cu Run 17 LeftCenter x50.tif	30951.00	6.71	255.00	255.00	461480.00	0.00	59.00
Cu Run 17 Right x50.tif	265419.00	13.09	0.00	255.00	265419.00	0.00	59.00
Cu Run 17 RightCenter x50.tif	461959.00	6.58	0.00	255.00	461959.00	0.00	59.00
Cu Run 18 Center x50.tif	483025.00	18.56	0.00	255.00	483025.00	0.00	59.00
Cu Run 18 Left x50.tif	42222.00	12.94	255.00	255.00	326424.00	0.00	59.00
Cu Run 18 LeftCenter x50.tif	489984.00	13.50	0.00	255.00	489984.00	0.00	59.00
Cu Run 18 Right x50.tif	27906.00	10.44	255.00	255.00	267264.00	0.00	59.00
Cu Run 18 RightCenter x50.tif	487204.00	18.95	0.00	255.00	487204.00	0.00	59.00
Cu Run 19 Center x50.tif	457929.00	8.35	0.00	255.00	457929.00	0.00	59.00
Cu Run 19 LeftCenter x50.tif	46326.00	13.55	255.00	255.00	341848.00	0.00	59.00
Cu Run 19 RightCenter x50.tif	285104.00	11.74	0.00	255.00	285104.00	0.00	59.00
Cu Run 20 Center x50.tif	29512.00	12.44	255.00	255.00	237320.00	0.00	59.00
Cu Run 20 RightCenter x50.tif	148135.00	19.12	0.00	255.00	148135.00	0.00	59.00
Cu Run 20 LeftCenter x50.tif	194880.00	25.14	0.00	255.00	194880.00	255.00	255.00
Cu Rerun 3 Center x50.tif	241001.00	17.70	0.00	255.00	241001.00	0.00	32.00
Cu Rerun 3 LeftCenter x50.tif	226954.00	18.29	0.00	255.00	226954.00	0.00	12.00

Cu Rerun 3 RightCenter x50.tif	199732.00	16.58	0.00	255.00	199732.00	0.00	17.00
Cu Rerun 6 Center Edge x50.tif	475200.00	19.01	0.00	255.00	475200.00	0.00	23.00
Cu Rerun 6 Center Near Substrate x50.tif	464294.00	2.10	0.00	255.00	464294.00	0.00	24.00
Cu Rerun 6 Left x50.tif	538380.00	15.18	0.00	255.00	538380.00	0.00	18.00
Cu Rerun 6 LeftCenter Edgex50.tif	493185.00	24.49	0.00	255.00	493185.00	0.00	14.00
Cu Rerun 6 LeftCenter Near Substrate x50.tif	15045.00	3.81	255.00	255.00	394460.00	0.00	29.00
Cu Rerun 6 Right x50.tif	335797.00	14.05	0.00	255.00	335797.00	0.00	20.00
Cu Rerun 6 RightCenter Edgex50.tif	117034.00	23.16	255.00	255.00	505440.00	0.00	11.00
Cu Rerun 6 RightCenter Near Substrate x50.tif	27807.00	7.33	255.00	255.00	379200.00	0.00	21.00
Cu Rerun 7 Center x50.tif	42660.00	11.91	255.00	255.00	358172.00	0.00	12.00
Cu Rerun 7 LeftCenter x50.tif	19193.00	7.54	255.00	255.00	254560.00	0.00	14.00
Cu Rerun 7 RightCenter x50.tif	21421.00	9.54	255.00	255.00	224580.00	0.00	15.00
Cu Rerun 14 Center x50.tif	536136.00	14.46	0.00	255.00	536136.00	0.00	27.00
Cu Rerun 14 Left x50.tif	111121.00	20.60	255.00	255.00	539496.00	0.00	21.00
Cu Rerun 14 LeftCenter x50.tif	546235.00	12.17	0.00	255.00	546235.00	0.00	18.00
Cu Rerun 14 Right x50.tif	459030.00	12.87	0.00	255.00	459030.00	0.00	12.00
Cu Rerun 14 RightCenter x50.tif	535830.00	14.61	0.00	255.00	535830.00	0.00	14.00
Cu Validation 1 Center x50.tif	539540.00	7.40	0.00	255.00	539540.00	0.00	15.00
Cu Validation 1 Left x50.tif	387177.00	8.11	0.00	255.00	387177.00	0.00	15.00
Cu Validation 1 LeftCenter x50.tif	421070.00	5.12	0.00	255.00	421070.00	0.00	17.00
Cu Validation 1 Right x50.tif	21449.00	6.60	255.00	255.00	324964.00	0.00	9.00
Cu Validation 1 RightCenter x50.tif	426132.00	8.19	0.00	255.00	426132.00	0.00	12.00
Cu Validation 2 Center x50.tif	65945.00	13.98	255.00	255.00	471868.00	0.00	12.00
Cu Validation 2 Left x50.tif	248886.00	13.94	0.00	255.00	248886.00	0.00	17.00
Cu Validation 2 LeftCenter x50.tif	350439.00	14.21	0.00	255.00	350439.00	0.00	11.00
Cu Validation 2 Right x50.tif	301070.00	16.77	0.00	255.00	301070.00	0.00	12.00
Cu Validation 2 RightCenter x50.tif	66414.00	14.75	255.00	255.00	450288.00	0.00	9.00
Zn Run 1 Center x50.tif	595794.00	2.45	0.00	255.00	595794.00	255.00	255.00
Zn Run 1 Left x50.tif	10996.00	2.46	255.00	255.00	447924.00	0.00	18.00
Zn Run 1 LeftCenter x50.tif	640900.00	3.45	0.00	255.00	640900.00	0.00	8.00
Zn Run 1 Right x50.tif	385728.00	2.98	0.00	255.00	385728.00	0.00	14.00
Zn Run 1 RightCenter x50.tif	517450.00	2.08	0.00	255.00	517450.00	0.00	11.00
Zn Run 2 Center x50.tif	25715.00	3.98	255.00	255.00	645480.00	255.00	255.00
Zn Run 2 Left x50.tif	367510.00	2.12	0.00	255.00	367510.00	255.00	255.00
Zn Run 2 LeftCenter x50.tif	645830.00	2.10	0.00	255.00	645830.00	0.00	14.00
Zn Run 2 Right x50.tif	360680.00	1.86	0.00	255.00	360680.00	0.00	15.00
Zn Run 2 RightCenter x50.tif	20014.00	3.09	255.00	255.00	647140.00	0.00	8.00
Zn Run 3 Center x50.tif	19577.00	6.20	255.00	255.00	315900.00	14.00	255.00
Zn Run 3 LeftCenter x50.tif	252399.00	2.89	0.00	255.00	252399.00	0.00	9.00
Zn Run 3 RightCenter x50.tif	219390.00	3.35	0.00	255.00	219390.00	0.00	12.00
Zn Run 4 Center x50.tif	678300.00	2.21	0.00	255.00	678300.00	0.00	15.00

Zn Run 4 LeftCenter x50.tif	483505.00	1.99	0.00	255.00	483505.00	0.00	12.00
Zn Run 4 RightCenter x50.tif	541080.00	4.49	0.00	255.00	541080.00	0.00	8.00
Zn Run 5 Center x50.tif	540090.00	2.17	0.00	255.00	540090.00	0.00	11.00
Zn Run 5 LeftCenter x50.tif	335580.00	7.31	0.00	255.00	335580.00	0.00	14.00
Zn Run 5 RightCenter x50.tif	350797.00	2.92	0.00	255.00	350797.00	0.00	11.00
Zn Run 6 Center x50.tif	466560.00	1.32	0.00	255.00	466560.00	0.00	17.00
Zn Run 6 Left x50.tif	405631.00	0.80	0.00	255.00	405631.00	0.00	8.00
Zn Run 6 LeftCenter x50.tif	594690.00	4.03	0.00	255.00	594690.00	0.00	15.00
Zn Run 6 Right x50.tif	441936.00	2.31	0.00	255.00	441936.00	0.00	12.00
Zn Run 6 RightCenter x50.tif	7370.00	1.42	255.00	255.00	518894.00	0.00	26.00
Zn Run 7 Center x50.tif	229830.00	12.79	0.00	255.00	229830.00	0.00	9.00
Zn Run 7 LeftCenter x50.tif	140778.00	5.02	0.00	255.00	140778.00	0.00	6.00
Zn Run 7 RightCenter x50.tif	212772.00	6.32	0.00	255.00	212772.00	0.00	12.00
Zn Run 8 Center x50 Near Substrate 2.tif	2785.00	0.43	255.00	255.00	646485.00	0.00	18.00
Zn Run 8 Left x50.tif	649116.00	0.63	0.00	255.00	649116.00	0.00	21.00
Zn Run 8 LeftCenter x50.tif	647140.00	0.40	0.00	255.00	647140.00	0.00	23.00
Zn Run 8 Right x50.tif	646152.00	0.93	0.00	255.00	646152.00	0.00	12.00
Zn Run 8 RightCenter x50.tif	648459.00	0.82	0.00	255.00	648459.00	0.00	24.00
Zn Run 9 Center x50.tif	542995.00	2.46	0.00	255.00	542995.00	0.00	11.00
Zn Run 9 Left x50.tif	443576.00	5.91	0.00	255.00	443576.00	0.00	12.00
Zn Run 9 LeftCenter x50.tif	502810.00	3.17	0.00	255.00	502810.00	0.00	12.00
Zn Run 9 Right x50.tif	313446.00	6.32	0.00	255.00	313446.00	0.00	11.00
Zn Run 9 RightCenter x50.tif	514044.00	3.09	0.00	255.00	514044.00	0.00	14.00
Zn Run 10 Center x50.tif	634725.00	2.02	0.00	255.00	634725.00	0.00	20.00
Zn Run 10 Left x50.tif	437526.00	1.31	0.00	255.00	437526.00	0.00	11.00
Zn Run 10 LeftCenter x50.tif	14129.00	3.20	255.00	255.00	441404.00	0.00	23.00
Zn Run 10 Right x50.tif	407550.00	1.39	0.00	255.00	407550.00	0.00	18.00
Zn Run 10 RightCenter x10.tif	493324.00	4.80	0.00	255.00	493324.00	0.00	12.00
Zn Run 11 Center x50.tif	509212.00	2.60	0.00	255.00	509212.00	0.00	11.00
Zn Run 11 Left x50.tif	449264.00	1.91	0.00	255.00	449264.00	0.00	3.00
Zn Run 11 LeftCenter x50.tif	524860.00	4.19	0.00	255.00	524860.00	0.00	11.00
Zn Run 11 Right x50.tif	17836.00	6.07	255.00	255.00	293970.00	0.00	5.00
Zn Run 11 RightCenter x50.tif	463740.00	2.60	0.00	255.00	463740.00	0.00	5.00
Zn Run 12 Center x50.tif	473612.00	4.45	0.00	255.00	473612.00	0.00	9.00
Zn Run 12 Left x50.tif	264180.00	5.92	0.00	255.00	264180.00	0.00	12.00
Zn Run 12 LeftCenter x50.tif	368024.00	4.79	0.00	255.00	368024.00	0.00	11.00
Zn Run 12 Right x50.tif	22989.00	11.85	255.00	255.00	193936.00	0.00	8.00
Zn Run 12 RightCenter x50.tif	331103.00	1.89	0.00	255.00	331103.00	0.00	6.00
Zn Run 13 Center x50.tif	635369.00	1.35	0.00	255.00	635369.00	0.00	12.00
Zn Run 13 Left x50.tif	601680.00	2.09	0.00	255.00	601680.00	0.00	12.00
Zn Run 13 LeftCenter x50.tif	622008.00	1.09	0.00	255.00	622008.00	0.00	12.00

Zn Run 13 Right x50.tif	567440.00	1.51	0.00	255.00	567440.00	0.00	11.00
Zn Run 13 RightCenter x50.tif	637315.00	0.95	0.00	255.00	637315.00	0.00	23.00
Zn Run 14 Center x50.tif	544236.00	1.83	0.00	255.00	544236.00	0.00	18.00
Zn Run 14 Left x50.tif	535665.00	4.00	0.00	255.00	535665.00	0.00	12.00
Zn Run 14 LeftCenter x50.tif	543172.00	2.92	0.00	255.00	543172.00	0.00	15.00
Zn Run 14 Right x50.tif	483360.00	5.22	0.00	255.00	483360.00	0.00	18.00
Zn Run 14 RightCenter x50.tif	536136.00	3.31	0.00	255.00	536136.00	0.00	18.00
Zn Run 15 Center x50.tif	225624.00	6.03	0.00	255.00	225624.00	0.00	21.00
Zn Run 15 CenterLeft x50.tif	151580.00	2.19	0.00	255.00	151580.00	0.00	23.00
Zn Run 15 CenterRight x50.tif	147472.00	3.67	0.00	255.00	147472.00	0.00	20.00
Zn Run 15 Left x50.tif	111228.00	2.67	0.00	255.00	111228.00	0.00	11.00
Zn Run 15 Right x50.tif	144536.00	4.63	0.00	255.00	144536.00	0.00	14.00
Zn Run 16 Center x50.tif	4525.00	8.01	255.00	255.00	56520.00	0.00	20.00
Zn Run 16 LeftCenter x50.tif	56242.00	8.92	0.00	255.00	56242.00	0.00	15.00
Zn Run 16 RightCenter x50.tif	67545.00	11.62	0.00	255.00	67545.00	0.00	15.00
Zn Run 17 Center x50.tif	540684.00	4.44	0.00	255.00	540684.00	0.00	19.00
Zn Run 17 LeftCenter x50.tif	431365.00	1.43	0.00	255.00	431365.00	0.00	12.00
Zn Run 17 RightCenter x50.tif	421596.00	1.08	0.00	255.00	421596.00	0.00	14.00
Zn Run 18 Center x50.tif	601524.00	1.67	0.00	255.00	601524.00	0.00	14.00
Zn Run 18 CenterLeft x50.tif	700964.00	3.79	0.00	255.00	700964.00	0.00	12.00
Zn Run 18 CenterRight x50.tif	635369.00	2.12	0.00	255.00	635369.00	0.00	14.00
Zn Run 18 Left x50.tif	15215.00	3.10	255.00	255.00	490304.00	0.00	12.00
Zn Run 18 Right x50.tif	513911.00	2.26	0.00	255.00	513911.00	0.00	15.00
Zn Run 19 Center x50.tif	432795.00	3.41	0.00	255.00	432795.00	0.00	14.00
Zn Run 19 LeftCenter x50.tif	320271.00	3.08	0.00	255.00	320271.00	0.00	32.00
Zn Run 19 RightCenter x50.tif	269892.00	1.71	0.00	255.00	269892.00	0.00	17.00
Zn Run 20 Center x50.tif	322140.00	2.23	0.00	255.00	322140.00	0.00	18.00
Zn Run 20 LeftCenter x50.tif	293043.00	2.73	0.00	255.00	293043.00	0.00	18.00
Zn Run 20 RightCenter x50.tif	201761.00	3.86	0.00	255.00	201761.00	0.00	20.00
Zn Validation 1 Center x50.tif	540600.00	5.22	0.00	255.00	540600.00	0.00	26.00
Zn Validation 1 Left x50.tif	547256.00	4.88	0.00	255.00	547256.00	0.00	12.00
Zn Validation 1 LeftCenter x50.tif	19491.00	3.58	255.00	255.00	544680.00	0.00	18.00
Zn Validation 1 Right x50.tif	464462.00	5.08	0.00	255.00	464462.00	0.00	11.00
Zn Validation 1 RightCenter x50.tif	542151.00	2.60	0.00	255.00	542151.00	0.00	14.00
Zn Validation 2 Center x50.tif	540558.00	1.93	0.00	255.00	540558.00	0.00	39.00
Zn Validation 2 Left x50.tif	435461.00	1.99	0.00	255.00	435461.00	0.00	20.00
Zn Validation 2 LeftCenter x50.tif	545214.00	1.38	0.00	255.00	545214.00	0.00	32.00
Zn Validation 2 Right x50.tif	319590.00	3.08	0.00	255.00	319590.00	0.00	35.00
Zn Validation 2 RightCenter x50.tif	506680.00	4.00	0.00	255.00	506680.00	0.00	23.00